



IntechOpen

Two-dimensional Materials

Synthesis, Characterization
and Potential Applications

Edited by Pramoda Kumar Nayak



WEB OF SCIENCE™



TWO-DIMENSIONAL MATERIALS - SYNTHESIS, CHARACTERIZATION AND POTENTIAL APPLICATIONS

Edited by **Pramoda Kumar Nayak**

Two-dimensional Materials - Synthesis, Characterization and Potential Applications

<http://dx.doi.org/10.5772/64760>

Edited by Pramoda Kumar Nayak

Contributors

Ramakrishna Podila, Apparao Rao, Pooja Puneet, Sriparna Bhattacharya, Sai Sunil Kumar Mallineni, Anurag Srivastava, Fengjiao Liu, Jose Jaime Taha-Tijerina, Laura Peña-Paras, Demofilo Maldonado-Cortes, Ming Hu, Guangzhao Qin, Yazeed Alaskar, Shamsul Arafin, Kang L. Wang, Qijin Chi, Mianqi Xue, Fengwang Li, Rebecca Cheung, Rui Zhang, Grzegorz Sobon, Rafael Vargas-Bernal, Mercedes Velázquez, Teresa Alejo, David López-Díaz, Beatriz Martín-García, Maria Dolores Merchan, Li, Wang Jianghao, Li Guangshe

© The Editor(s) and the Author(s) 2016

The moral rights of the and the author(s) have been asserted.

All rights to the book as a whole are reserved by INTECH. The book as a whole (compilation) cannot be reproduced, distributed or used for commercial or non-commercial purposes without INTECH's written permission.

Enquiries concerning the use of the book should be directed to INTECH rights and permissions department (permissions@intechopen.com).

Violations are liable to prosecution under the governing Copyright Law.



Individual chapters of this publication are distributed under the terms of the Creative Commons Attribution 3.0 Unported License which permits commercial use, distribution and reproduction of the individual chapters, provided the original author(s) and source publication are appropriately acknowledged. If so indicated, certain images may not be included under the Creative Commons license. In such cases users will need to obtain permission from the license holder to reproduce the material. More details and guidelines concerning content reuse and adaptation can be found at <http://www.intechopen.com/copyright-policy.html>.

Notice

Statements and opinions expressed in the chapters are those of the individual contributors and not necessarily those of the editors or publisher. No responsibility is accepted for the accuracy of information contained in the published chapters. The publisher assumes no responsibility for any damage or injury to persons or property arising out of the use of any materials, instructions, methods or ideas contained in the book.

First published in Croatia, 2016 by INTECH d.o.o.

eBook (PDF) Published by IN TECH d.o.o.

Place and year of publication of eBook (PDF): Rijeka, 2019.

IntechOpen is the global imprint of IN TECH d.o.o.

Printed in Croatia

Legal deposit, Croatia: National and University Library in Zagreb

Additional hard and PDF copies can be obtained from orders@intechopen.com

Two-dimensional Materials - Synthesis, Characterization and Potential Applications

Edited by Pramoda Kumar Nayak

p. cm.

Print ISBN 978-953-51-2554-9

Online ISBN 978-953-51-2555-6

eBook (PDF) ISBN 978-953-51-4186-0

We are IntechOpen, the first native scientific publisher of Open Access books

3,350+

Open access books available

108,000+

International authors and editors

114M+

Downloads

151

Countries delivered to

Our authors are among the
Top 1%

most cited scientists

12.2%

Contributors from top 500 universities



WEB OF SCIENCE™

Selection of our books indexed in the Book Citation Index
in Web of Science™ Core Collection (BKCI)

Interested in publishing with us?
Contact book.department@intechopen.com

Numbers displayed above are based on latest data collected.
For more information visit www.intechopen.com



Meet the editor



Pramoda Kumar Nayak is currently a senior researcher at the Centre for Low Dimensional Carbon Materials, Ulsan National Institute of Science and Technology, Republic of Korea. He received his doctoral degree in physics from the Indian Institute of Technology, Guwahati, India. After completion of his Ph.D, he worked as a postdoctoral researcher and visiting scientist in several institutions around the globe such as the Institute for Plasma Research, India; National Cheng Kung University, Taiwan; and National Tsing Hua University, Hsinchu, Taiwan, before coming to South Korea. His research interest is focused on two-dimensional materials, including transition metal dichalcogenides (TMD), graphene and hexagonal boron nitride (*h*-BN). He has published more than 40 international journals, 5 book chapters and 1 book.

Contents

Preface XI

- Chapter 1 **Synthesis Strategies about 2D Materials 1**
Jianghao Wang, Guangshe Li and Liping Li
- Chapter 2 **Langmuir-Blodgett Methodology: A Versatile Technique to Build 2D Material Films 21**
María Mercedes Velázquez, Teresa Alejo, David López-Díaz, Beatriz Martín-García and María Dolores Merchán
- Chapter 3 **Heteroepitaxial Growth of III–V Semiconductors on 2D Materials 43**
Yazeed Alaskar, Shamsul Arafin, Isaac Martinez-Velis and Kang L. Wang
- Chapter 4 **Two-Dimensional Transition Metal Dichalcogenides for Electrocatalytic Energy Conversion Applications 63**
Fengwang Li and Mianqi Xue
- Chapter 5 **Defect Engineered 2D Materials for Energy Applications 83**
Sai Sunil Kumar Mallineni, Sriparna Bhattacharya, Fengjiao Liu, Pooja Puneet, Apparao Rao, Anurag Srivastava and Ramakrishna Podila
- Chapter 6 **Graphene against Other Two-Dimensional Materials: A Comparative Study on the Basis of Electronic Applications 103**
Rafael Vargas-Bernal
- Chapter 7 **Application of 2D Materials to Ultrashort Laser Pulse Generation 123**
Grzegorz Sobon

- Chapter 8 **2D-Based Nanofluids: Materials Evaluation and Performance 153**
Jaime Taha-Tijerina, Laura Peña-Parás and Demófilo Maldonado-Cortés
- Chapter 9 **Diverse Thermal Transport Properties of Two-Dimensional Materials: A Comparative Review 199**
Guangzhao Qin and Ming Hu
- Chapter 10 **Mechanical Properties and Applications of Two-Dimensional Materials 219**
Rui Zhang and Rebecca Cheung
- Chapter 11 **Design, Assembly, and Fabrication of Two-Dimensional Nanomaterials into Functional Biomimetic Device Systems 247**
Chengyi Hou, Minwei Zhang and Qijin Chi

Preface

There are only few discoveries and new technologies in material science that have the potential to dramatically alter and revolutionize our material world. Discovery of two-dimensional (2D) materials, the thinnest form of materials to ever occur in nature, is one of them. After isolation of graphene from graphite in 2004, a whole other class of atomically thin materials, dominated by surface effects and showing completely unexpected and extraordinary properties, has been created. Research on 2D materials, such as graphene and its cousins (silicene, germanene, phosphorene etc.), transition metal dichalcogenides (TMD), other layered semiconductors, MXenes, and so on, now involves thousands of researchers worldwide in the cutting-edge fields of physics, chemistry, engineering and biology, and extending from fundamental science to novel applications. The class of 2D materials possesses layered structure with strong in-plane chemical bonds and weak out-of-plane coupling between layers. These layered structures provide the opportunity to be cleaved into individual freestanding atomic layers. When the thickness of layered material is reduced to a single or only a few layers, some extraordinary variations occur in their electronic properties due to quantum confinement. While identifying the uniqueness/individuality of the 2D materials, people may think that these layered materials will expose novel and unpredicted properties, allowing for many innovative openings.

The book “Two-dimensional Materials - Synthesis, Characterization and Potential Applications” is meant to provide a comprehensive view and state-of-the-art knowledge about 2D materials. It consists of 11 chapters contributed by a team of experts in this exciting field and provides latest synthesis techniques, characterization of 2D materials and their potential applications in energy conservation, electronics, optoelectronics, biotechnology, and so on.

Chapter 1 starts with an overview of the recent progress in the synthetic techniques for 2D materials, in which the authors introduce experimental scheme, advantages and disadvantages and applications of these synthetic strategies. Chapter 2 introduces the Langmuir-Blodgett Methodology, a versatile technique to build 2D material films including graphene oxides, quantum dots and silver nanowires. Chapter 3 presents the epitaxial growth of III-V nanowires and thin films on 2D layered materials.

2D TMDs have attracted considerable interest as alternatives to noble metal catalysts owing to their unique electronic structure and high catalytic activity. Chapter 4 provides an overview of recent progress in 2D TMDs for electrocatalytic energy conversion applications. The presence of intrinsic defects in the form of vacancies and grain boundaries and extrinsic defects such as dopants in 2D materials results in new electronic states to endow unique functionalities. In this aspect, Chapter 5 presents the review of defect-induced phenomena in 2D materials for electronic and energy applications. Chapter 6 provides a comparative study

between graphene against other 2D materials based on electronic applications. Chapter 7 discusses the recent achievements in the area of ultrafast fiber lasers utilizing 2D materials such as graphene, topological insulators, TMDs and black phosphorus.

Thermal energy management plays a crucial role from high-payload electrical instruments to ultrasmall electronic circuitries. The advent of nanofluids could successfully address the low thermal efficiency of conventional fluids in a significant manner. Chapter 8 narrates the advances in thermal nanofluids using 2D materials. Chapter 9 reviews the state-of-the-art theoretical and experimental investigations of phonon transport properties of broad 2D nanostructures. Special attention is given to the effect of different physical factors, such as sample size, strain and layer thickness.

By exploiting the unique mechanical and mechanoelectric transduction properties, 2D materials can be used in a wide range of applications such as: flexible electronics, strain sensors, nanogenerators and innovative nanoelectromechanical systems (NEMS). In this aspect, the authors review mechanical properties of different 2D materials, varying from conductors, semiconductors to insulators in Chapter 10. In Chapter 11, the recent efforts on fabrication and assembly of 2D nanomaterials into functional biomimetic systems have been presented.

I hope that this book will be useful to a large number of researchers in various disciplines, both in academia and industry, seeking to gain update knowledge in the field of 2D materials.

I am very pleased to have gotten the opportunity to have served as the Editor of this book, which contains a wide variety of studies from authors all around the world. I would like to thank all the authors for their efforts in sending their best research papers to the attention of the audiences, including students, scientists and engineers, throughout the world.

I would also like to acknowledge the help given by InTech Open Access Publisher, in particular, publishing process manager, Mr. Edi Lipović, for his assistance, patience and support throughout the whole process of this book project.

Dr. Pramoda Kumar Nayak

Low Dimensional Carbon Materials Centre,
Ulsan National Institute of Science and Technology,
Ulsan, Republic of Korea

Synthesis Strategies about 2D Materials

Jianghao Wang, Guangshe Li and Liping Li

Additional information is available at the end of the chapter

<http://dx.doi.org/10.5772/63918>

Abstract

In recent years, more and more attentions have been paid to two-dimensional (2D) materials due to the excellent electrical, optical, thermal and mechanical properties. To characterize the layer-dependent changes in properties and to provide pathways for their integration into a multitude of applications, it is essential to explore the reliable syntheses of single- and few-layer 2D materials. Therefore, many strategies, such as micromechanical exfoliation, ultrasonic exfoliation, hydrothermal method, topochemical transformation, chemical vapor deposition method and so on, have been developed to synthesize high-quality and ultrathin nanosheets showing their own merits and demerits in preparing 2D nanomaterials. Herein, an overview of the recent progress in the synthetic techniques is presented for 2D materials, in which we would introduce their experimental scheme, advantages and disadvantages, and applications of these synthetic strategies. Eventually, the potential trends and future directions for synthesizing technology for 2D materials are proposed.

Keywords: two-dimensional, nanosheets, top down, bottom up, synthesis strategy

1. Introduction

The discovery of single-layer graphene in 2004 by Novoselov and Geim has shown that it is highly possible to exfoliate stable, single-atom or single-polyhedral-thick two-dimensional (2D) materials from van der Waals solids, and these 2D materials could exhibit unique and fascinated physical properties, such as ultrahigh carrier mobility at room temperature ($\sim 10,000 \text{ cm}^2\text{V}^{-1}\text{s}^{-1}$), quantum hall effect, large theoretical specific surface area ($2630 \text{ m}^2\text{g}^{-1}$), excellent optical transparency ($\sim 97.7\%$) and so on [1, 2]. This great discovery helps Novoselov and Geim win Nobel Prize in 2010. The success of graphene arouses intensive interests in 2D materials in the

world. As a consequence, more and more 2D materials have been synthesized successfully, showing great promise for in many applications.

Ideal 2D materials belong to those with only one atom or several atoms thickness and infinite lateral size. The reliable synthesis of single- and few-layer 2D materials is an essential first step for characterizing the layer-dependent changes in their properties, as well as for providing pathways of their integration into a multitude of applications [1]. For instances, when the thickness of metal Co was reduced to only one or several atoms, the catalytic activity of carbon dioxide reduction would be improved greatly when comparing to bulk metal Co [3]. Single-layer MoS_2 has been synthesized by mechanical exfoliation strategy and exhibits excellent performance in the field of gas sensors and phototransistors. It is worth noting that when bulk MoS_2 is exfoliated into monolayer, the type of band gap would change from indirect type to direct one [1, 4]. Another important example is that single-layered $\text{Co}(\text{OH})_2$ can realize an ultrahigh energy density in all-solid-state asymmetric supercapacitor [5].

The emergence of these novel properties is the driving force for the rapid development of research in ultrathin 2D nanosheets, which has been on the forefront of scientific disciplines including chemistry, physics, materials, science, medicine and biology. However, the quest for methods of producing 2D materials with controlled thickness and lateral size has been always a challenging subject. This may be caused by the anisotropic crystal growth and strong chemical bonds in crystal structure. The common classification of crystalline structures according to the type of chemical bonds could be divided into van der Waals solids, layered ionic solids and nonlayered materials [1]. Every synthetic strategy has its own merits and demerits in preparing different kind of materials. Therefore, in this chapter, we concentrate on the different synthetic methods for synthesizing two-dimensional crystals. According to the principle of generating two-dimensional materials, we can divide the synthetic strategies into top-down and bottom-up strategies. The distinction between these two general classifications is based on the processes involved in the creation of the nanometer-sized structures [6]. In the bottom-up approach, nanoscale materials are constructed from atomic or molecular precursors that are allowed to react and grow in size or self-assemble into more complex structures. By contrast, the top-down approach carves nanoscale structures by controlled removal of materials from larger or bulk solids.

2. Top-down strategy

In top-down nanofabrication, the crafting of ultrathin nanosheets is achieved through physical-based or through chemical-based process. The physical top-down approach employs the use of mechanical force or ultrasonic wave to exfoliate layered van der Waals solids into single- and few-layer 2D materials, whereas the chemical top-down strategy relies essentially on chemical reaction that brought about by ion exchange or by the application of heat and so on. In this section, a brief overview is presented of the top-down synthetic process for 2D nanostructures, including their advantages and limitations.

2.1. Micromechanical exfoliation

Micromechanical exfoliation has been used to exfoliate graphite into single-layer graphene by Novoselov and Geim for the first time [2]. Mechanical exfoliation is a straightforward method to obtain only one- or few-layer nanosheets, which well maintains the crystal structure and properties. Beside this, versatility and low cost of this method make it highly popular for synthesizing 2D materials and extremely convenient for fundamental research. Even so, this method is limited to the laboratory research and seems impossible to scale up for industrial production. Although large size and high quality of ultrathin nanosheets can be obtained by this way, this method is applicable only for layered van der Waals solids. The nanosheets of layered ionic solids and nonlayered materials cannot be obtained by this strategy. Additionally, several other factors (stoichiometry and stacking orders) play the key roles in successful fabrication of monolayer MX_2 nanostructures by mechanical exfoliation. Herein, we take graphene as an example to introduce this method.

Graphene is a monolayer sheet of carbon, showing only one atom thickness but extending indefinitely in two dimensions, which is the typical representative of 2D materials. Many astonishing properties have been discovered for graphene, which include better electrical and thermal conductivity, mechanical strength and optical purity. The procedure of micromechanical exfoliation is very simple. **Figure 1** illustrates the process of mechanical exfoliation [7].

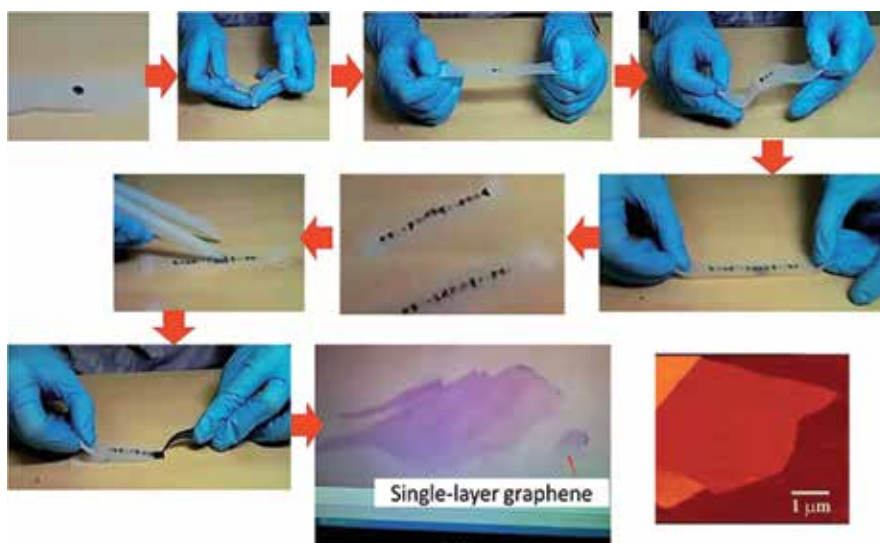


Figure 1. An illustrative procedure of the Scotch-tape-based micromechanical cleavage for graphene [7].

The exfoliation mechanics of this method are utilization of mechanical force to exfoliate graphite from Scotch tape. If one takes great pain to repeat this normal force over and over, the graphitic layer would become thinner and thinner, and eventually one can obtain single-layer graphene.

2.2. Ultrasonic exfoliation

Ultrasonic exfoliation is an effective strategy to delaminate van der Waals solids into single- or few-layer nanosheet. Compared to the mechanical exfoliation, this method is more effective and higher productive. The details for ultrasonic exfoliation process are shown in **Figure 2** [8]. As indicated in **Figure 2a**, sonication time and suitable solvents play the key roles in exfoliation. Suitable solvents are those with appropriate surface energies. In good solvents, the exfoliated nanosheets are stabilized against reaggregation. Otherwise, for “bad” solvents, reaggregation and sedimentation will occur. In recent reports, different types of organic solvents have been used as a dispersing medium for delaminating van der Waals solids (listed in **Table 1**) [8–14]. Although this method has many advantages, it is hard to get high-purity single-layer 2D material, which is a primary need for electronic applications. To make readers understand this method more in-depth, in the following, we will take black phosphorus (BP) as an example to introduce this strategy.

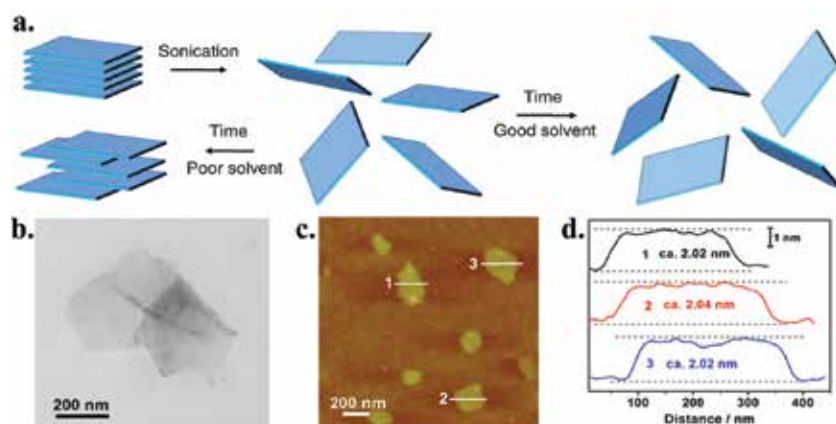


Figure 2. (a) An illustrative procedure of sonication-assisted exfoliation. The layered crystal is sonicated in a solvent, resulting in exfoliation and nanosheet formation [8]. (b) TEM image of ultrathin BP nanosheets. (c–d) AFM image and corresponding height image of ultrathin BP nanosheets [13].

BN	MoS ₂		WS ₂		
Solvent	A/I (AU) [†] 300 nm	Solvent	A/I (AU) 670 nm	Solvent	A/I (AU) 630 nm
1 Cyclohexylpyrrolidone (CHP)	100	NVP	100	DMSO	100
2 N-dodecyl-pyrrolidone (N12P)	61	N8P	98	NVP	92
3 Benzyl benzoate	44	N12P	97	NMF	90
4 Isopropanol	44	CHP	88	N12P	84
5 N-Octyl-pyrrolidone (N8P)	44	NMP	80	DMEU	75
6 N-vinylpyrrolidone (NVP)	41	DMEU	73	DMF	73

BN		MoS ₂		WS ₂	
Solvent	A/l (AU) ¹ 300 nm	Solvent	A/l (AU) 670 nm	Solvent	A/l (AU) 630 nm
7 Benzyl ether	40	DMSO	61	Benzyl benzoate	71
8 Dimethyl-imidazolidinone (DMEU)	36	DMF	54	CHP	69
9 Cyclohexanone	29	DMA	54	Cyclohexanone	63
10 Chlorobenzene	28	Benzaldehyde	51	Benzonitrile	59
11 Dimethylsulphoxide (DMSO)	27	Benzonitrile	47	N8P	59
12 Benzonitrile	26	Benzyl benzoate	46	Isopropanol	59
13 Chlorobenzene	25	NMF	41	DMA	57
14 Chloroform	23	Cyclohexanone	38	Benzylether	55
15 Bromobenzene	23	Isopropanol	32	Chlorobenzene	45
16 N-Methyl-pyrrolidone(NMP)	23	Quinoline	26	Methanol	45
17 N-Methylformamide (NMF)	21	Acetone	24	Formamide	40
18 Dimethylformamide (DMF)	18	Benzylether	23	Bromobenzene	29
19 Dimethylacetamide (DMA)	16	Cyclohexane	22	Quinoline	26
20 Formamide	9	Methanol	21	Acetone	17

¹A is absorbance; l is the path length of the beam of light through the material sample. A/l at fixed wavelength was used to estimate the mass remaining in the supernatant.

Table 1. The best 20 solvents for each material [9].

Single-layer BP is a very promising two-dimensional material that can be the substitution of graphene due to its exceptional electronic properties. The direct band gap of BP can be tuned from 0.3 eV in the bulk to 1.5 eV in the monolayer. Recently, Xie's group successfully prepared pristine 2D black phosphorus through direct ultrasonic exfoliation in organic solvent [13]. Briefly, they dispersed 50 mg of bulk black phosphorus in 100 mL of distilled water, which was bubbled with argon to eliminate the dissolved oxygen molecules for avoiding the oxidation. Then, sonicating the mixture solution in ice water for 8 h (Note: keeping the system at a relatively low temperature is important). After ultrasonic treatment, the resultant dispersions were centrifuged at 1500 rpm for 10 min to remove the unexfoliated component and the supernatant was collected for further use.

Ultrathin nanosheet thus obtained show lateral size of about several hundred nanometers (see TEM image in **Figure 2b**), and the ultrathin thickness is indicated by the near transparency of the sheets. AFM image and the corresponding height distribution (**Figure 2c** and **2d**) show that the measured height is about 2.0 nm, consistent with the four individual black phosphorus

layers. The black phosphorus nanosheets show excellent photodegradation of organic components such as DPBF and MO.

2.3. Lithium-intercalated and exfoliation

Ultrasonic exfoliation is incapable of peeling off a single layer of 2D nanostructure; herein, lithium (Li) intercalation process is introduced for synthesizing single sheets. The scheme of lithium-intercalated exfoliation strategy is shown in **Figure 3a** [15]. The formation of Li_xXS_2 compound is a key step in lithium intercalation process, and this reaction can be tuned to control the yield of single layers [16, 17]. The yield of this strategy for obtaining single-layer transition metal dichalcogenide is nearly 100%, while some challenges still remain. The first one is that the experiment is carried out at high temperature for long durations. Also, the lithium intercalation must be controlled carefully to obtain single-layer nanosheets, while preventing the formation of metal nanoparticles and precipitation of Li_2S . To make readers understand this method more in-depth, in the following, we would take MoS_2 as an example to introduce this strategy.

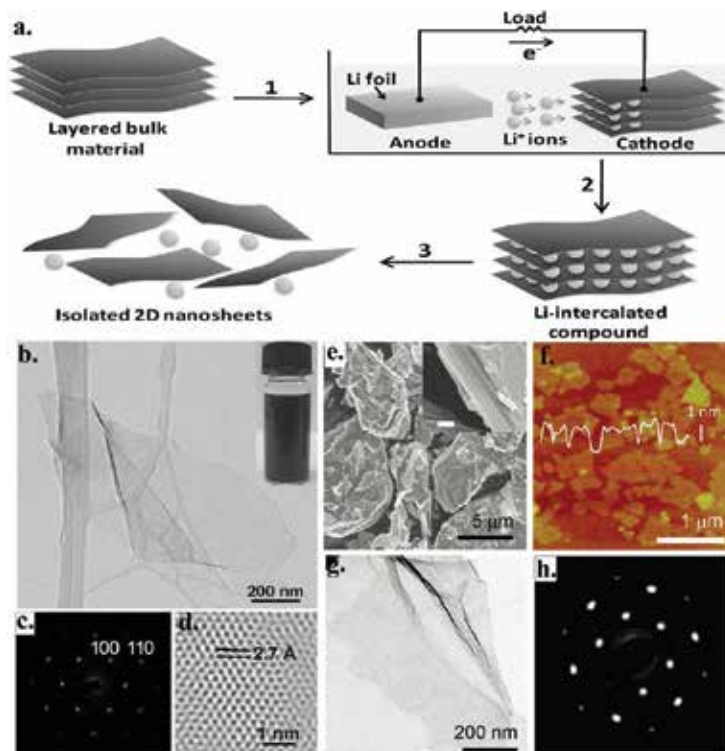


Figure 3. (a) Electrochemical lithiation process for the fabrication of 2D nanosheets from the layered bulk material. (b–d) Morphology characterization of MoS_2 exfoliated by electrochemical lithium-intercalated and exfoliation process [15]. (e–h) Morphology characterization of MoS_2 exfoliated by lithium-intercalated exfoliation process. [18].

2.3.1. Ultrathin nanosheets of MoS₂ through electrochemical lithium-intercalated exfoliation process

To control the step of the formation of Li_xMoS₂ compound, Zhang's group developed a simple method—electrochemical lithiation process—to control Li-intercalated and subsequent exfoliation in water or ethanol [15]. Lithium intercalation of MoS₂ is performed in a test cell. The bulk MoS₂ is prepared as cathode. The electrochemical intercalation is performed using galvanostatic discharge at a current density of 0.05 mA. After the discharge process, the product is washed with acetone to remove any residual electrolyte, followed by exfoliation and ultrasonication in distilled water or ethanol. Eventually, the suspension is centrifuged and washed many times with water.

As shown in **Figure 3b–d**, high-quality and ultrathin MoS₂ nanosheets can be obtained by this simple method. The lateral size of nanosheets is about several hundred nanometers with a near transparency. Electron diffraction pattern of a flat area of the nanosheet (**Figure 3c**) and the corresponding high-resolution transmission electron microscope (HRTEM) image (**Figure 3d**) show that the hexagonal lattice structure is formed by this method, showing clearly a lattice spacing of 2.7 Å assigned to the (100) planes. This strategy can also be applied to prepare other single-layer semiconducting nanosheets, such as WS₂, TiS₂, TaS₂ or graphene.

2.3.2. Ultrathin nanosheets of MoS₂ through lithium-intercalated exfoliation

Recently, Chhowalla's group successfully prepared monolayer MoS₂ through lithium-intercalated and exfoliation [18]. In detail, they immersed 3 g bulk MoS₂ crystals in certain concentration of butyllithium solution in hexane for 2 days in a flask filled with argon gas to obtain lithium intercalation compound. Exfoliation is achieved immediately after this process (within 30 min to avoid deintercalation) by ultra-sonicating Li_xMoS₂ in water for 1 h. The mixture is centrifuged several times to remove excess lithium in the form of LiOH and unexfoliated material.

Commercial MoS₂ powder (**Figure 3e**) was used to prepare highly monodisperse monolayer MoS₂ nanosheets through Li intercalation and exfoliation. As shown in **Figure 3f** and **g**, the lateral size of product is 300~800 nm and the average thickness is about 1~1.2 nm, which is larger than the dimension of 0.65~0.7 nm reported for mechanically exfoliated MoS₂ monolayers. This discrepancy may be explained by surface corrugation due to the distortions and the presence of adsorbed or trapped molecules. The absence of any sheets below the thickness values and no evidence of step edges on the nanosheets surface suggest that they consist of monolayers. The selected area electron diffraction (SAED) patterns indicate hexagonal symmetry of the atomic arrangement and that individual sheets consist of a single-crystal domain (**Figure 3h**). All of the results undoubtedly confirm that MoS₂ with monolayer thickness has been successfully synthesized.

2.4. Ion-change exfoliation

Although the exfoliation strategy mentioned previously is convenient to delaminate van der Waals solids into ultrathin nanostructure, it is hard to exfoliate layered ionic solids such as LiCoO₂ or LDHs. This is because these ionic solids have strong ionic bonds in the layers. Ion-

change exfoliation is a normal method to get this kind of 2D materials [19–23]. The scheme of ion-change exfoliation is shown in **Figure 4a** [19]. In the next section, we will take LiCoO_2 and $(\text{Co}^{2+}\text{-Co}^{3+})\text{-LDHs}$ as examples to illuminate this method [23, 24].

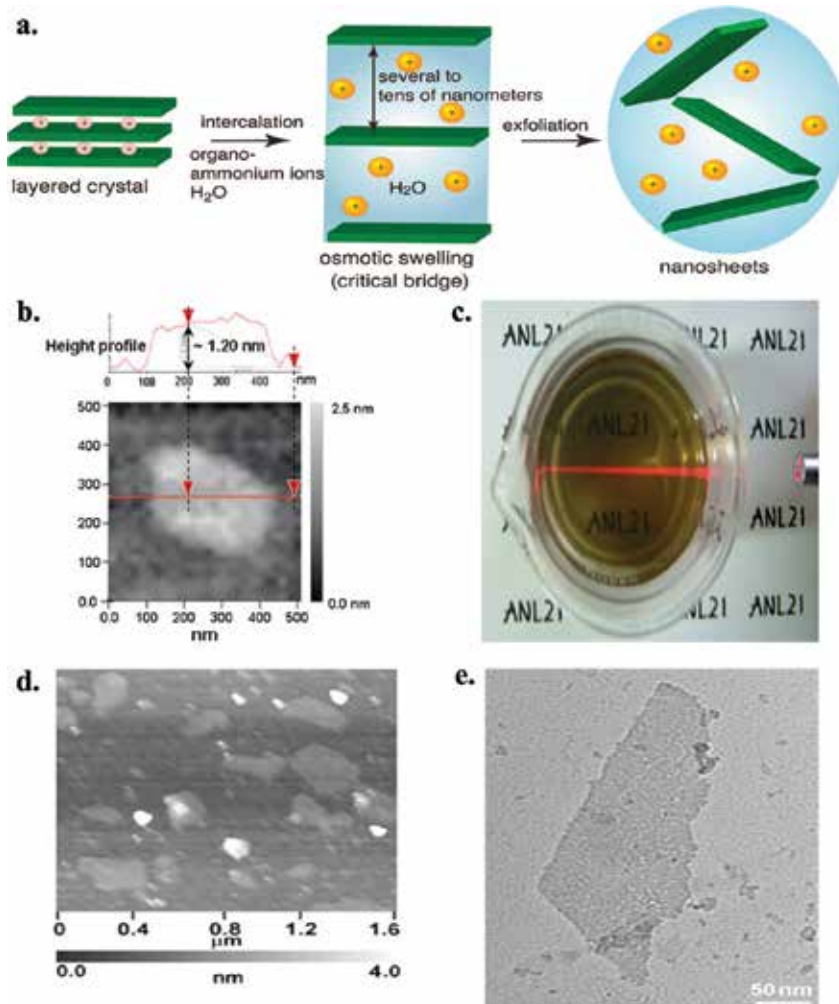


Figure 4. (a) Schematic illustration of the osmotic swelling to exfoliation process [19]. (b) AFM image and height profile of the exfoliated cobalt oxide adsorbed onto PEI-coated mica substrate. Photograph of the colloidal suspension of cobalt oxide. (c) The visible light is illuminated from the side of the beaker to demonstrate the Tyndall scattering effect [23]. $\text{Co}^{2+}\text{-Co}^{3+}$ LDH nanosheets: (d) AFM image; (e) TEM image [24].

2.4.1. LiCoO_2

LiCoO_2 is a kind of cation-exchange layered metal oxides. Seong-Ju's group delaminated LiCoO_2 into monolayer recently [23]. The procedure of exfoliating could be described as follows: A proton-exchange reaction for the generation of layered $\text{Li}_x\text{H}_{1-x}\text{CoO}_2$ is carried out

in an aqueous solution of HCl (1 M, 1 mg mL⁻¹ of LiCoO₂) at room temperature for 3 days. During the proton-exchange reaction, HCl solution is replaced with fresh solution every day. Exfoliation of the layered cobalt oxide is achieved by the intercalation of tetrabutylammonium (TBA) cation into the layers of Li_xH_{1-x}CoO₂. After the reaction, incompletely exfoliated particles were separated from the colloidal suspension through centrifugation (6000 rpm for 10 min), resulting in a pure colloidal suspension. The powdered samples of completely exfoliated nanosheets are collected from the pure colloidal suspension through high-speed centrifugation at 17,000 rpm for 30 min.

AFM of the as-obtained sample provides direct evidence for the exfoliation of layered cobalt oxide nanosheets (**Figure 4b**). The thickness of LiCoO₂ nanosheets is about 1.2 nm, which is slightly thicker than the crystallographic thickness of individual cobalt oxide layers. The observation of Tyndall phenomenon from the pure suspension, characteristic of colloidal suspensions, provides strong evidence for the exfoliation of layered cobalt oxide nanosheets too (**Figure 4c**).

2.4.2. (Co²⁺-Co³⁺)-LDHs

According to Sasaki's report [24], 0.5 g of the sample is dispersed into an aqueous solution (500 mL) that contains 2.5 M NaClO₄ and 2.5 mM HCl. This mixed solution is carefully degassed by purging with nitrogen gas for conversion into ClO₄⁻-LDH (addition of HCl is crucial for preventing carbonate, CO₃²⁻ contamination from air). After purging with nitrogen gas, the reaction vessel is tightly capped and shaken for 1 day at room temperature. The sample is filtered, washed with degassed water and air-dried. The obtained ClO₄⁻ LDH (0.1 g) is mixed with formamide (100 mL) in a conical beaker. After an ultrasonic treatment for 30 min, a translucent colloidal suspension is obtained. The suspension is further centrifuged to remove possible nonexfoliated particles. AFM and TEM images shown in **Figure 4d** and **e** provided direct evidence for successfully exfoliation of the samples.

3. Bottom-up strategy

Top-down strategy is useful in preparing ultrathin and high-quality nanosheets with large lateral size. Even so, it has to be mentioned that all exfoliation methods as mentioned before are only suitable to those materials whose bulk crystals are layered [25]. The mass production by methods mentioned earlier is usually very low. When using bottom-up approach, nanoscale materials are constructed from atomic or molecular precursors that are suitable to react and grow in size, or self-assemble into more complex structures. Then, 2D materials can be enlarged easily [6]. In this section, a brief overview is presented for the bottom-up synthetic process to 2D nanostructures.

3.1. Wet chemical strategy

Wet chemical method is promising for preparing all types of 2D materials owing to its high-yield, low-cost and mass production. Wet chemical strategy is a big kind of synthesis method, which includes hydro/solvothermal synthesis and template synthesis. In this section, we introduce various types of wet-chemical synthesis strategies for preparing 2D nanomaterials.

3.1.1. Hydro/solvothermal synthesis

Hydro/solvothermal method is a common strategy used for the synthesis of inorganic materials. Advantages of hydro/solvothermal method over other types of crystal growth include low temperature (generally in a temperature range of 100–240°C) and convenience of adjusting reaction conditions. Many factors play the key roles in the synthesis of ultrathin nanostructure, which include temperature, reaction time, reactant ratio and so on. Many 2D materials have been prepared by this method, just like MoS₂, TiO₂, ZnO, Co₃O₄, MnO₂ and Rh [26–29]. In the following, we will take Li's work as an example to explain this strategy.

Ultrathin Rh nanosheets were synthesized successfully through solvothermal method by Li et al. recently [29]. For detailed steps, Rh(acac)₃ and PVP are dissolved in solvent mixed by benzyl alcohol and formaldehyde. The mixture is stirred vigorously for 1 h and then transferred to a Teflon-lined stainless steel autoclave. The autoclave is sealed and maintained at 180°C for 8 h and then cooled to room temperature. The resulted black product is precipitated with acetone (10 mL), separated in a centrifuge and washed three times with ethanol (10 mL) and finally dried under vacuum.

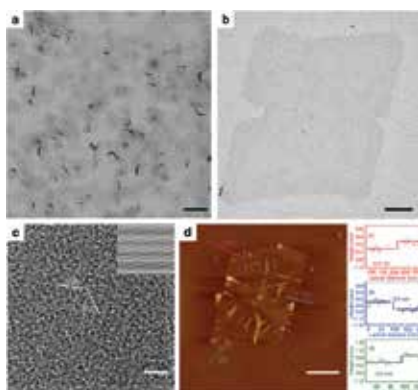


Figure 5. (a) Low-magnification TEM image of PVP-capped Rh nanosheet, (b) high-magnification TEM image of PVP-capped Rh NSs, (c) aberration-corrected microscopy image of PVP-capped Rh NS (inset, the corresponding filtered image using crystallographic average method to improve signal-to-noise ratio), (d) AFM image and the corresponding height profiles of a bare Rh NS [29].

Detailed structure information for the synthesized atomically thick Rh nanosheets is indicated by TEM, HRTEM and AFM. TEM image clearly shows that ultrathin nanosheet has a dimension lateral size of about 500 nm, while the near transparency of the sheets indicates the

ultrathin thickness (**Figure 5a, b**). As shown in **Figure 5c**, Rh nanosheets have a single crystalline nature of Rh nanosheets, which possesses a hexagonal structure, with a lattice parameter of ca. 2.6 Å, closer to the atomic distance of Rh (2.69 Å) in the (111) plane of the bulk Rh phase. AFM image of Rh NS shows that the sheet-like features are consistent with TEM images (see **Figure 5a, b**) Section analysis and height profile (**Figure 5d**) reveal that the height of Rh NS is about 4 Å. This is closer to the diameter of Rh atoms (the radius of Rh atomic is about 1.73 Å). All of these results undoubtedly confirm the successful synthesis of Rh nanosheets with an atomic thickness.

3.1.2. Template synthesis

A typical procedure of template method includes complicating morphology of template by growing crystal confined in specific dimension and then removing template through high temperature or adjusting pH. By this way, nearly all types of nanostructure including quantum dot (0D), nanowire (1D) and nanosheets (2D) can be prepared. The suitable template and condition of removing template are important. Many nonlayered structure 2D nanomaterials can be synthesized using the as-prepared 2D nanomaterials as the template, such as Fe₂O₃, Au, CuInS₂ and so on [30–32]. Herein, we take α-Fe₂O₃ as an example to illuminate this method.

3.1.2.1. Half-unit-cell thickness of alpha-Fe₂O₃ semiconductor nanosheets

Recently, Wei's group successfully synthesized free-standing half-unit-cell α-Fe₂O₃ nanosheets using CuO nanoplate as the template [30]. The layered iron hydroxide nanosheets are first prepared on CuO template surface by the mutually promoted slow interfacial reactions of Fe²⁺ hydrolysis and CuO-etching process at a low temperature of 25°C for a whole day, which

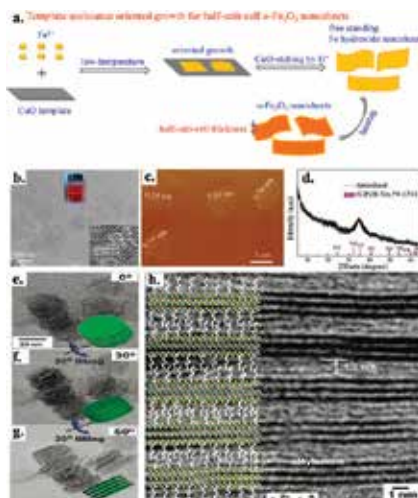


Figure 6. (a) Schematic of synthesis strategy of α-Fe₂O₃ nanosheets. (b) TEM image of the α-Fe₂O₃ nanosheets. The insets show the HRTEM image and the Tyndall effect of the α-Fe₂O₃ nanosheets. (c) AFM image and (d) XRD pattern of the α-Fe₂O₃ nanosheets [30]. (e–g) TEM images of the assembled ultrathin ZrS₂ nanodiscs obtained by rotating TEM holder under different angle. (h) HRTEM side-view image of multiply stacked 1.6-nm-thick ZrS₂ nanodiscs [33].

is beneficial for the synthesis of ultrathin nanosheets. When CuO template is etched out, a heat treatment is carried out for the dehydrogenation of Fe hydroxide nanosheets, which leads to the formation of the stable and free-standing α -Fe₂O₃ nanosheets.

AFM and TEM image provide direct evidence for successful exfoliation of the sample. As shown in **Figure 6b, c**, the lateral size of α -Fe₂O₃ nanosheets is up to about 1 μ m, and thickness is about 0.55–0.59 nm. The XRD pattern of the α -Fe₂O₃ shown in **Figure 6d** exhibits only a broad and weak diffraction peak corresponding to the (110) orientation plane of α -Fe₂O₃. It is interesting to note that ultrathin α -Fe₂O₃ nanosheet shows an intrinsic ferromagnetism of 0.6 μ _B/atom at 100 K and remains ferromagnetism at room temperature.

3.1.2.2. Ultrathin zirconium disulfide nanodiscs

Except for hard template, soft colloidal templated synthesis is used to prepare two-dimensional 2D materials frequently. The long-chain oleylamine and/or oleic acid surfactants are often used as the soft colloidal templates for directing the crystal growth. Cheon et al. used this method to synthesize ultrathin ZrS₂ nanodiscs [36]. Intermediate lamellar complexes composed of 2D arrays of ZrCl₄ and alkyl amine are first obtained, in which alkyl amine serves as the soft colloidal template. Then, CS₂ is injected into the mixture aforementioned to form ultrathin ZrS₂ nanodiscs dispersed in solution.

As indicated in **Figure 6e–h**, the resultant ultrathin ZrS₂ nanodiscs possess radius of \sim 15 nm and thickness of 0.5 nm. The spacing between the discs is \sim 1.5 nm (**Figure 6h**), which corresponds to the length of the oleylamine surfactant layers. When compared to bulk ZrS₂, ultrathin ZrS₂ discs show the unique nanoscale size effects, enhanced discharge capacity by 230% and greatly improved stability.

3.2. Microwave-assisted method

In recent years, microwave-assisted chemical synthesis strategy has become a well-established technique to promote and enhance chemical reactions. The main advantages of this method are represented by much shorter reaction time (generally in only a few minutes) and higher energy efficiency when comparing to other conventional strategies. Due to these advantages, some 2D nanomaterials can be prepared by this way conveniently, such as SnO₂, α -Ni(OH)₂, K_{0.17}MnO₂ and CuSe [33–37].

To understand it more clearly, let us take α -Ni(OH)₂ as an example (**Figure 7**) [36]: firstly, precursors were prepared by starting materials of Ni(NO₃)₂·6H₂O, urea, deionized water and ethylene glycol at given proportions. Then, the resulting solution is transferred into a home-made round-bottomed flask and treated under microwave irradiation in a microwave reactor at 700 W for several minutes. Finally, the green powder is obtained by centrifugation and washed several times with distilled water and absolute ethanol. After that, the powder was dried in vacuum at 80°C for 12 h. Detailed structure information for the synthesized Ni(OH)₂ nanosheets is unraveled by FESEM and TEM images in **Figure 7b–d**. In comparison with traditional wet-chemical syntheses, the microwave-assisted liquid-phase growth can

shorten the reaction time to less than 20 min. Particularly, the ultrathin α -Ni(OH)₂ nanosheets exhibit a maximum specific capacitance of 4172.5 Fg⁻¹ at a current density of 1 Ag⁻¹.

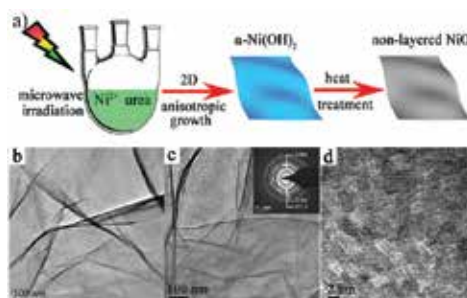


Figure 7. (a) Schematic illustration for the synthesis of nanosheets. (b) High magnification FESEM images of α -Ni(OH)₂ nanosheets, (c) TEM image (the inset showing SAED pattern) and (d) a planar HRTEM image [36].

3.3. Topochemical transformation

Topological conversion is a strategy in which the product's morphology is inherited from their precursor through nucleation and growth inside the precursors. The key to success is the degree of lattice match between precursor and their product. From the viewpoint of anisotropy of layered compounds, it is easier to obtain 2D nanostructure of hydroxide rather than oxides. This method is applicable of preparing nonlayer 2D nanostructure oxides, such as Co₃O₄, CeO₂ and δ -FeOOH [38–40]. In the following, we will take Co₃O₄ and Ni as examples to illuminate this method [38, 41].

3.3.1. Atomically thick Co₃O₄ nanosheets through topotactic oxidation transformation

The schematic illustration of the preparation of ultrathin Co₃O₄ nanosheets is shown in **Figure 8**. As illustrated in **Figure 8a**, the thickness of (001)-oriented few layered α -Co(OH)₂ is

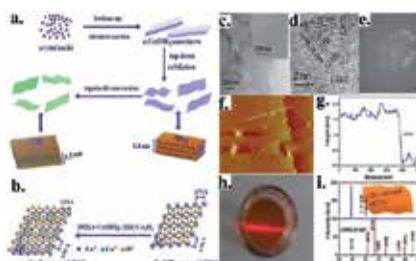


Figure 8. (a) Schematic illustration of the preparation of ATCNs. (b) Schematic model of the top-view illustrating the topochemical transformation from α -Co(OH)₂ (001) plane to Co₃O₄ (111) plane. (c–e) TEM image, HRTEM image and the corresponding fast Fourier transform pattern of ATCNs. (f and g) Tapping model AFM image and corresponding height profile of as-obtained nanosheets deposited on a silicon substrate. (h) Photograph of a colloidal suspension of the ATCNs displaying the Tyndall effect. (i) XRD pattern of ATCNs-based film displaying highly preferred [111] orientation [38].

closer to the thickness of (111)-oriented Co_3O_4 nanosheets. More specifically, the discrepancies between $\alpha\text{-Co}(\text{OH})_2$ {100} ($d=2.76 \text{ \AA}$) and Co_3O_4 {220} ($d=2.84 \text{ \AA}$) are calculated to be below 3%. Moreover, Co^{2+} atomic arrangement in $\alpha\text{-Co}(\text{OH})_2$ (001) plane and Co_3O_4 (111) plane is very closer (**Figure 8b**). These features enable atomically thick Co_3O_4 nanosheets to preserve the thickness of the precursor possible.

Atomically thick Co_3O_4 nanosheets were prepared by this method, as confirmed by TEM, AMF and XRD. From TEM image, one could clearly see ultrathin nanosheets with lateral size of about 400 nm with the near transparency of the sheets (**Figure 8c**). HRTEM image, and the corresponding fast Fourier transform (FFT) pattern in **Figure 8d** and **e** for the as-obtained product depicts its [111] preferential orientation. The thickness of the as-synthesized Co_3O_4 nanosheets is also evaluated by tapping-mode atomic force microscopy (AFM). AFM image and the corresponding height distribution (**Figure 8f, g**) show that the measured height is about 1.5 nm. Microscopically, the colloidal suspension of the product displays the Tyndall phenomenon (**Figure 8h**), so that the formation of homogeneous ultrathin nanosheets in ethanol can be inferred. As shown in **Figure 8i**, XRD pattern of the atomically thick nanosheet-based films can be readily indexed to be pure Co_3O_4 (JCPDS no. 42-1467) and also displays the highly preferred [111] orientation, which is corresponding to the result of HRTEM. All of the results undoubtedly confirm that Co_3O_4 nanosheets with ultrathin thickness have been successfully synthesized. The oriented growth of ATCNs is attributed to $\alpha\text{-Co}(\text{OH})_2$ -to- Co_3O_4 topochemical conversion with the relationship of [001] $\alpha\text{-Co}(\text{OH})_2$ and [111] Co_3O_4 .

3.3.2. Ultrathin nickel nanosheets through topotactic reduction transformation

Except for topotactic oxidation, toporeduction is also frequently used to prepare nonlayered materials. Sun [41] used this method and synthesized ultrathin nickel nanosheets array recently. $\text{Ni}(\text{OH})_2$ nanosheet array on a metal substrate is prepared first. And then, ethylene glycol is used as the reduction agent to get Ni nanosheets. The slow conversion kinetics keeps the ultrathin nanosheet morphology and atomic thickness.

Figure 9 reveals the morphology inheritance between Ni and $\text{Ni}(\text{OH})_2$ nanosheet array. **Figure 9a, b** shows SEM and HRTEM of $\text{Ni}(\text{OH})_2$ sheet array. It is seen that the thickness of $\text{Ni}(\text{OH})_2$ is about 5.8 nm (10–12 layers), whereas the thickness of Ni nanosheet shown in

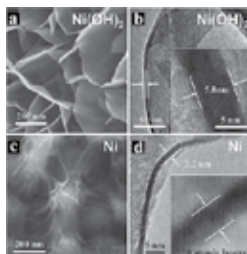


Figure 9. (a and c) SEM images of the as-synthesized $\text{Ni}(\text{OH})_2$ nanowall array and Ni-NSA. (b and d) HRTEM image of a scrolled $\text{Ni}(\text{OH})_2$ nanowall and a vertically laid Ni nanosheet. The inset shows the thickness of $\text{Ni}(\text{OH})_2$ nanowall and Ni nanosheet [41].

Figure 9c, d is about 2.2 nm (10 atomic layers). This provides strong evidence that Ni nano-sheets are obtained by toporeduction transformation.

3.4. Chemical vapor deposition (CVD)

Recently, CVD technique has shown promise to generate high-quality TMD layers with a scalable size, controllable thickness and excellent electronic properties. CVD is a high-temperature chemical synthesis process by which a desired material is deposited on substrates. CVD processes have been extensively studied for synthesizing thin film coatings of a wide range of materials, including metals, semiconductors, and insulators. The scheme of CVD method is shown in **Figure 10a** [1]. The precursor vapor is introduced from outside or generated inside the tube furnace. The main advantages of CVD synthesis process are represented by the accesses to high quality, high purity 2D nanomaterials with controlled properties, which allow one to control the morphology, crystallinity and defects of 2D nanostructures by tuning the process parameters [42]. Due to these advantages, some 2D nanomaterials have been prepared by this way conveniently, such as graphene, MoS₂, h-BN [43–49]. CVD method is also another annealing strategy for the growth of high-quality single-crystalline 2D sheet on substrates. Even so, CVD suffers from the requirement of high temperature, high vacuum and specific substrates. In the following, we will take h-BN and MoS₂ as an example to elaborate this strategy.

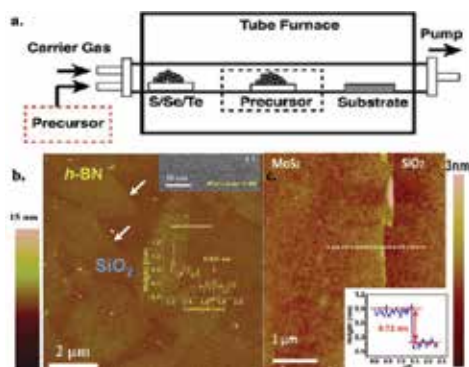


Figure 10. (a) Schematic illustration of experimental setup for the 2D materials synthesis by a noncatalytic vapor deposition process. The precursor vapor can be introduced from outside or generated inside the tube furnace [1]. (b) AFM images of the initial flakes of h-BN. White arrows point to the sharp edges of these flakes. Inset: TEM image of the folded edge of a monolayer h-BN [43]. (c) AFM image of a monolayer MoS₂ film on a SiO₂/Si substrate. Inset: corresponding height profile of as-obtained nanosheets [46].

Hexagonal BN is called “white graphite” due to its similar lamellar structure to graphite. h-BN possesses many unique properties such as chemical stability, strong mechanical strength, high-thermal conductivity and low dielectric constant. What is more, the band gap of h-BN can be tuned with thickness. To produce BN precursor, the first heating zone is ramped up to $T_1=60\sim 90^\circ\text{C}$ with a heating belt. Turn on the on-off valve between the first and second heating zone only during CVD process, one can prevent the undesired growth. The second heating

zone is heated up to $T_2 = 1000^\circ\text{C}$ for typically 10~90 min under 10 sccm hydrogen atmosphere at a pressure of 350 mTorr after mounting the copper foil. Copper foil (25 μm , Alfa Aesar) is used as the metal catalyst substrate. Before the growth of h-BN, copper foil is annealed at 1000°C for 20 min under 10 sccm H_2 to grow the copper grain and to obtain a smooth surface. AFM of as-obtained sample provides direct evidence for single-layer h-BN synthesized by chemical vapor deposition method (**Figure 10b**). AFM image and the corresponding height distribution inset in **Figure 10b** show that the measured height is about 0.42 nm, consistent with monolayer thickness (c-axis spacing for h-BN is ~ 0.32 nm). In addition, TEM image of monolayer h-BN clearly demonstrates that the number of layer of h-BN is one (**Figure 10c**). Moreover, for a complete h-BN layer (**Figure 10d**), the wrinkles of h-BN film (indicated by a yellow arrow) under scanning electron microscopy (SEM) can be clearly seen. These wrinkles are characteristic of h-BN and graphene films due to the negative thermal expansion coefficients of h-BN and graphene. All of the results undoubtedly confirm that h-BN with monolayer thickness have been successfully synthesized.

Synthesis of transition metal dichalcogenides (TMDs) using CVD is the cutting edge research area in recent years. Lee [46] synthesized single-layer MoS_2 by this method recently. As shown in **Figure 10c**, ultrathin MoS_2 nanosheets with smooth surface are observed with AFM. The cross-sectional height in inset of **Figure 10c** reveals that the thickness of MoS_2 film is ~ 0.72 nm, which corresponds to a monolayer MoS_2 .

4. Perspective and conclusions

With the advantages of very high surface-to-volume ratios and special electronic properties in two-dimensional materials, ultrathin nanosheets are very promising in catalysis, supercapacitors, photoconductive materials, batteries and magneto-optical components. Therefore, it is imperative to exploit more technologically advanced synthesis strategies to obtain high quality, large size, ultrathin two-dimensional materials. At present, thinner, larger size, high productive and quality nanosheets are still the chief purpose for scientists. Usually, the thinner nanosheets give a higher catalytic performance and other special properties. Besides these, controllable thickness, architectures assembled by nanosheets and composite nanostructure, such as quantum-dot/nanosheets, sandwich structure and modification on two-dimensional nanosheets, also provide new opportunities for material science.

In summary, synthetic strategies, such as top-down and bottom-up method, have been employed for synthesizing two-dimensional crystals. The top-down strategy includes micro-mechanical exfoliation, ultrasonic exfoliation, lithium-intercalated and exfoliation and ion-change exfoliation. Using top-down strategies, one is able to obtain high-quality and large-size two-dimensional crystal conveniently. Even so, this method is only appropriate for those materials whose bulk crystals are layered. Comparatively, bottom-up strategy could overcome this shortage. Bottom-up strategy is composed of wet chemical method, microwave-assisted chemical, topological conversion strategy and chemical vapor deposition method. All these strategies may present different features and questions for preparing two-dimensional

materials. In the future, scientists should take more and more efforts to develop new synthetic technologies for high-quality 2D material and the relevant applications.

Author details

Jianghao Wang¹, Guangshe Li² and Liping Li^{1*}

*Address all correspondence to: Lipingli@fjirsm.ac.cn

1 Key Laboratory of Design and Assembly of Functional Nanostructures, Fujian Institute of Research on the Structure of Matter, Fuzhou, P.R. China

2 State Key Laboratory of Inorganic Synthesis and Preparative Chemistry, College of Chemistry, Jilin University, Changchun, P.R. China

References

- [1] Joshua EG. Progress, challenges, and opportunities in two-dimensional materials beyond graphene. *ACS Nano*. 2014;7(4): 2898–2962. DOI: 10.1021/nn400280c
- [2] Novoselov KS. Electric field effect in atomically electric field effect in atomically. *Science*. 2004;306(5696): 666–669. DOI: 10.1126/science.1102896
- [3] Xie Y. Partially oxidized atomic cobalt layers for carbon dioxide electroreduction to liquid fuel. *Nature*. 2016;529(7484): 68–71. DOI: 10.1038/nature16455
- [4] Zhang H. Single-layer MoS₂ phototransistors. *ACS Nano*. 2012;6(1): 74–80. DOI: 10.1021/nn2024557
- [5] Gao S. Ultrahigh energy density realized by a single-layer beta-Co(OH)₂ all-solid-state asymmetric supercapacitor. *Angew Chem Int Ed Engl*. 2014;53(47): 12789–12793. DOI: 10.1002/anie.201407836
- [6] Han MY. Chemical routes to top-down nanofabrication. *Chem Soc Rev*. 2013;42(14): 6006–6018. DOI: 10.1039/c3cs60113g
- [7] Shen ZG. A review on mechanical exfoliation for the scalable production of graphene. *J. Mater. Chem. A*. 2015;3(22):11700–11715. DOI: 10.1039/c5ta00252d
- [8] Coleman JN. Liquid exfoliation of layered materials. *Science*. 2013;334(6052): 72–75. DOI: 10.1126/science.1208891
- [9] Coleman JN. Two-dimensional nanosheets produced by liquid exfoliation of layered materials. *Science*. 2011;331(6017): 568–571. DOI: 10.1126/science.1194975

- [10] Coleman JN. Large-scale exfoliation of inorganic layered compounds in aqueous surfactant solutions. *Adv Mater.* 2011;23(34): 3944–3948. DOI: 10.1002/adma.201102584
- [11] Zhang HL. A Mixed-solvent strategy for efficient exfoliation of inorganic graphene analogues. *Angew Chem Int Ed Engl.* 2011;50(46): 10839–10842. DOI: 10.1002/anie.201105364
- [12] Coleman JN. Preparation of high concentration dispersions of exfoliated MoS₂ with increased flake size. *Chem Mater.* 2012;24(12): 2414–2421. DOI: 10.1021/Cm301515z
- [13] Xie Y. Ultrathin black phosphorus nanosheets for efficient singlet oxygen generation. *J Am Chem Soc.* 2015;137(35): 11376–11382. DOI: 10.1021/jacs.5b06025
- [14] Hersam MC. Solvent exfoliation of electronic-grade, two-dimensional black phosphorus. *ACS Nano.* 2015;9(4):3596–3604. DOI: 10.1021/acsnano.5b01143
- [15] Zhang H. Single-layer semiconducting nanosheets: high-yield preparation and device fabrication. *Angewandte Chemie.* 2011;50(47): 11093–11097. DOI: 10.1002/anie.201106004
- [16] Zhang H. The chemistry of two-dimensional layered transition metal dichalcogenide nanosheets. *Nat Chem.* 2013;5(4): 263–275. DOI: 10.1038/nchem.1589
- [17] Chen M. Chemically exfoliated ReS₂ nanosheets. *Nanoscale.* 2014;6(21): 12458–12462. DOI: 10.1039/c4nr03740e
- [18] Chhowalla M. Photoluminescence from chemically exfoliated MoS₂. *Nano Lett.* 2011;11(12): 5111–5116. DOI: 10.1021/nl201874w
- [19] Sasaki T. Two-dimensional oxide and hydroxide nanosheets: controllable high-quality exfoliation, molecular assembly, and exploration of functionality. *Acc Chem Res.* 2014;48(1): 136–143. DOI: 10.1021/ar500311w
- [20] Hwang SJ. Composition-tailored 2 D Mn(1-x)Ru(x)O(2) nanosheets and their reassembled nanocomposites: improvement of electrode performance upon Ru substitution. *Chem Eur J.* 2014;20(17): 5132–5140. DOI: 10.1002/chem.201304009
- [21] Sasaki T. Exfoliated oxide nanosheets: new solution to nanoelectronics. *J Mater Chem.* 2009;19(17): 2503. DOI: 10.1039/b820160a
- [22] Sasaki T. Osmotic swelling to exfoliation. Exceptionally high degrees of hydration of a layered titanate. *J Am Chem Soc.* 1998;120(19): 4682–4689. DOI: 10.1021/Ja974262l
- [23] Hwang SJ. Soft-chemical exfoliation route to layered cobalt oxide monolayers and its application for film deposition and nanoparticle synthesis. *Chem Eur J.* 2009;15(41): 10752–10761. DOI: 10.1002/chem.200901590
- [24] Sasaki T. Topochemical synthesis of monometallic (Co²⁺-Co³⁺) layered double hydroxide and its exfoliation into positively charged Co(OH)₂ nanosheets. *Angew Chem Int Ed Engl.* 2008;47(1): 86–89. DOI: 10.1002/anie.200703941

- [25] Zhang H. Wet-chemical synthesis and applications of non-layer structured two-dimensional nanomaterials. *Nat Commun.* 2015;6:7873. DOI: 10.1038/ncomms8873
- [26] Xue JM. Ultrasmall Fe₃O₄ nanoparticle/MoS₂ nanosheet composites with superior performances for lithium ion batteries. *Small.* 2014;10(8): 1536–1543. DOI: 10.1002/sml.201302879
- [27] Bai H. Large-scale, ultrathin and (001) facet exposed TiO₂ nanosheet superstructures and their applications in photocatalysis. *J Mater Chem A.* 2014;2(7): 2040. DOI: 10.1039/c3ta14343k
- [28] Dou SX. Generalized self-assembly of scalable two-dimensional transition metal oxide nanosheets. *Nat Commun.* 2014;5: 3813. DOI: 10.1038/ncomms4813
- [29] Li J. Ultrathin rhodium nanosheets. *Nat Commun.* 2014;5: 3039. DOI: 10.1038/ncomms4093
- [30] Wei S. Half-unit-cell alpha-Fe₂O₃ semiconductor nanosheets with intrinsic and robust ferromagnetism. *J Am Chem Soc.* 2014;136(29): 10393–10398. DOI: 10.1021/ja504088n
- [31] Zhang H. Synthesis of hexagonal close-packed gold nanostructures. *Nat Commun.* 2011;2: 292. DOI: 10.1038/ncomms1291
- [32] Xie Y. CuInSe₂ ultrathin nanoplatelets: novel self-sacrificial template-directed synthesis and application for flexible photodetectors. *Chem Commun.* 2012;48(73): 9162–9164. DOI: 10.1039/c2cc34727j
- [33] Xie Y. Ultra-rapid microwave-assisted synthesis of layered ultrathin birnessite K_{0.17}MnO₂ nanosheets for efficient energy storage. *J Mater Chem A.* 2013;1(28): 8154–8159. DOI: 10.1039/C3ta11194f
- [34] Cheon J. Ultrathin zirconium disulfide nanodiscs. *J Am Chem Soc.* 2011;133(20): 7636–7639. DOI: 10.1021/ja200400n
- [35] Cao C. Microwave-assisted and gram-scale synthesis of ultrathin SnO₂ nanosheets with enhanced lithium storage properties. *ACS Appl Mater Interfaces.* 2015;7(4):2745–2753. DOI: 10.1021/am507826d
- [36] Li YD. Ultrathin nickel hydroxide and oxide nanosheets: synthesis, characterizations and excellent supercapacitor performances. *Sci Rep.* 2014;4:5787. DOI: 10.1038/srep05787
- [37] Pan GB. Facile microwave-assisted synthesis of Klockmannite CuSe nanosheets and their exceptional electrical properties. *Sci Rep.* 2014;4:5998. DOI: 10.1038/srep05998
- [38] Xie Y. Topochemical transformation route to atomically thick Co₃O₄ nanosheets realizing enhanced lithium storage performance. *Nanoscale.* 2013;5(12):5241–5246. DOI: 10.1039/c3nr01178j

- [39] Sun Y. Pits confined in ultrathin cerium (IV) oxide for studying catalytic centers in carbon monoxide oxidation. *Nat Commun.* 2013;4:2899. DOI: 10.1038/ncomms3899
- [40] Chen PZ. Ultrathin nanosheets of ferropyhyte: a new two-dimensional material with robust ferromagnetic behavior. *Chem Sci.* 2014;5(6):2251. DOI: 10.1039/c3sc53303d
- [41] Sun X. Single-crystalline ultrathin nickel nanosheets array from in situ topotactic reduction for active and stable electrocatalysis. *Angew Chem Int Ed Engl.* 2016;55(2): 693–697. DOI: 10.1002/anie.201509616
- [42] Li LJ. Recent advances in controlled synthesis of two-dimensional transition metal dichalcogenides via vapour deposition techniques. *Chem Soc Rev.* 2014;DOI: 10.1039/c4cs00256c
- [43] Kong J. Synthesis of monolayer hexagonal boron nitride on Cu foil using chemical vapor deposition. *Nano Lett.* 2012;12(1):161–166. DOI: 10.1021/nl203249a
- [44] Rodney SR. Large-area synthesis of high-quality and uniform graphene films on copper foils. *Science.* 2009;324(5932):1312–1314. DOI: 10.1126/science.117124
- [45] Kong J. Role of the seeding promoter in MoS₂ growth by chemical vapor deposition. *ACS Nano.* 2014;14(2):464–472. DOI: 10.1021/nl4033704
- [46] Lee YH. Synthesis of large-area MoS₂ atomic layers with chemical vapor deposition. *Adv Mater.* 2012;24(17):2320–2325. DOI: 10.1002/adma.201104798
- [47] Nayak PK. Robust room temperature valley polarization in monolayer and bilayer WS₂. *Nanoscale.* 2016;8:6035–6042. DOI: 10.1039/C5NR08395H
- [48] Shaw JC. Chemical vapor deposition growth of monolayer MoSe₂ nanosheets. *Nano Res.* 2014;7(4):511–517. DOI: 10.1007/s12274-014-0417-z
- [49] Huang JK. Large-area synthesis of highly crystalline WSe₂ monolayers and device applications. *ACS Nano.* 2014;8(1):923–930. DOI: 10.1021/nn405719x

Langmuir-Blodgett Methodology: A Versatile Technique to Build 2D Material Films

María Mercedes Velázquez, Teresa Alejo,
David López-Díaz, Beatriz Martín-García and
María Dolores Merchán

Additional information is available at the end of the chapter

<http://dx.doi.org/10.5772/63495>

Abstract

The Langmuir-Blodgett (LB) methodology is based on the transfer process of a monolayer adsorbed at the water interface, Langmuir film, from the air-water interface onto solids by vertical dipping of the substrate immersed on the subphase. The technique allows the continuous variation of material density, packing, and arrangement by compressing or expanding the film by using barriers. Consequently, it provides the possibility of preparing films with the control of interparticle distance necessary to exploit the two-dimensional (2D) materials in technological applications. In this chapter, we present some examples of fabrication of thin films of 2D material using this methodology. We show some methodologies based on this technique to build thin films of graphene oxides, Quantum Dots (QDs), and silver nanowires.

Keywords: Langmuir-Blodgett films, graphene oxide, silver nanowires, CdSe Quantum Dots, AFM, TEM, FESEM

1. Introduction

Dimensionality is one of the most fundamental material parameters because it defines the atomic structure of materials and determines its main properties. Thus, one chemical element or compound can exhibit different properties in different dimensions. Some interesting examples about size effect are surface plasmon resonance in metal nanoparticles, quantum confinement in semiconductor particles, and superparamagnetism in magnetic nanomaterials.

If one dimension is restricted, we have two-dimensional (2D) or layered shape material. An interesting example of this kind of materials is graphene. This material is a monolayer of carbon atoms tightly packed into 2D honeycomb lattice that has attracted worldwide attention since it was discovered in 2004 [1, 2]. This new material has emerged with a promising future due to its amazing properties such as transparency, high-charge mobility, thermal conductivity, and mechanical resistance. Due to these unique properties, graphene has been proposed as a good candidate for manufacturing transparent-conducting electrodes, transistors, hydrogen-storage devices, and gas sensors [3, 4]. The growing interest on graphene has highlighted the importance of another 2D material in technological applications such as transition metal chalcogenides (TMC) and layered ionic solids.

Several 2D materials can be obtained by exfoliation of a layered bulk crystal. However, this procedure is often difficult because the van der Waals interactions between adjacent layers must be overcome. Mechanical exfoliation provides good results, but mostly applied for fundamental research because it is arduous and expensive to produce the material at industrial scale by this way. Other methodologies such as solvent-assisted ultrasound exfoliation [5] or chemical synthesis [6] allow obtaining large amounts of materials at low cost, although they present several disadvantages against mechanical exfoliation. One important disadvantage is related with the deposition of materials onto solids. Hence, for several technological applications, it is necessary to support 2D materials onto solid substrates [7, 8] and since the properties of 2D materials deposited onto solids are strongly affected by the film morphology, a deposition methodology becomes necessary, which allows a great control of the material density and packing. Several techniques such as drop casting [9] or spin coating [10] have been used to integrate these materials onto novel devices; however, they often lead to nonuniform films or films with aggregated materials due to uncontrolled capillary flow and dewetting processes during solvent evaporation. These aggregates decrease the specific properties of each material [2, 11]. An illustrative example of the aggregation produced by solvent evaporation can be seen in **Figure 1**. The figure shows a field emission scanning electron microscopy (FESEM) image of a graphene oxide (GO) film deposited onto silicon by drop casting.

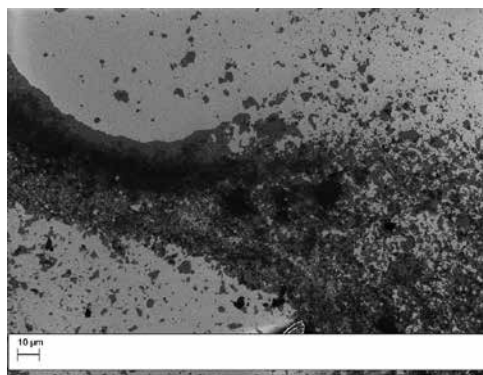


Figure 1. FESEM image of graphene oxide deposited onto silicon by drop casting.

An alternative technique is the Langmuir-Blodgett (LB) methodology. This method consists on the transfer process of a water-insoluble material from the air-water interface onto a solid substrate by vertical dipping of the solid in the Langmuir monolayer [12]. This technique allows continuous variation of material density, packing, and arrangement by compressing or expanding the film using barriers. Consequently, it offers the possibility of preparing films with the control of interparticle distance necessary to exploit the 2D materials in technological applications. Despite this methodology being successfully used for transferring water-insoluble molecules [12–14] and nanoparticles [15], it has been less employed to transfer graphene derivatives [16–19] or TMC materials onto solid substrates.

This chapter reviews some strategies to build 2D material films by means of the LB methodology. The content is organized into three main sections. The first one introduces the LB methodology. The second one summarizes the production of thin films of graphene oxide derivatives by using this methodology [17–20]. The last section describes some representative results concerning thin films of Quantum Dots (QDs) of transition metal chalcogenides [21–26] and silver nanowires (AgNWs) [27]. All sections are focused on the possibility of tuning the morphology of the 2D material by modifying the surface composition of the Langmuir monolayer and the deposition methodology.

2. Langmuir-Blodgett methodology

The LB methodology consists on the transfer process from the air-water interface onto a solid substrate of a monomolecular layer of amphiphilic material adsorbed at the air-water interface [12]. The amphiphilic material is dissolved in a volatile solvent and dropped on the air-water interface. For optimal results, the solvent should have a positive spreading coefficient and be insoluble in the subphase [28]. After the spreading, the solvent evaporates and the material forms a monolayer. When the monolayer reaches the thermodynamic equilibrium, it is symmetrically compressed by using two barriers. The sequential isothermal compression changes the structure of the monomolecular film, which passes through a series of 2D states, referred to as gas, expanded and compressed liquids, and solid state. Consequently, knowing the 2D phase diagram of the film, it is possible to control its structure and associated physical and chemical properties. To transfer the film onto the solid, a flat substrate is immersed into the aqueous subphase and then extracted in a controlled way with the film adsorbed onto it, see **Figure 2a**. The transfer process can be repeated many times to obtain multilayers [12, 29] of different thickness and composition. During the transfer process, the surface pressure is maintained constant by barrier compression in order to compensate the loss of molecules transferred onto the solid. One variant of this methodology is the horizontal deposition technique, referred as Langmuir-Schaefer (LS) method. In the latter, the solid substrate is placed parallel to the air-water interface and deposition is done by contacting the substrate horizontally with the floating monolayer, see **Figure 2b**.



Figure 2. Langmuir-Blodgett (a) and Langmuir-Schaefer (b) transfer processes.

When the monolayer is transferred, its structure is often modified; therefore, to construct high-quality films, a careful control of experimental parameters, such as stability and homogeneity of the monolayer, subphase properties (composition, pH, presence of electrolytes, and temperature), substrate nature, speed of immersion/emersion of substrate, surface pressure during the deposition process, and the number of transferred monolayers, is required [12, 29].

3. The Langmuir-Blodgett films of graphene oxide derivatives

As commented previously, due to its unique properties graphene has been suggested to be used in a great number of technological applications. Nevertheless, each application requires a different set of properties. Thus, graphene synthesized by chemical vapor deposition (CVD) or micromechanical exfoliation renders high-quality sheets suitable for electronic applications; however, these sheets cannot be used for the fabrication of composites or water-soluble materials, because they do not contain functionalized groups. In these situations, graphene oxides [30] are preferred because they contain reactive oxygen functional groups that can attach small molecules, polymers, or nanoparticles to the graphitic surfaces for potential use in polymer composites [31], gas sensors [32], or photovoltaic cells [33, 34].

Another important issue of the use of graphene in technological applications is related to its implementation in devices. In the particular case of graphene oxide derivatives, conventional deposition techniques such as drop casting [9] or spin coating [10] not only induce aggregation of flakes, as can be seen in **Figure 1**, but also force the sheets to fold and wrinkle, losing its excellent properties [2]. Therefore, to overcome these limitations other deposition techniques such as LB have been recently proposed [16, 35].

Graphene oxide can be considered as an amphiphilic material [36] because it is constituted by two different domains. The hydrophobic one corresponds to π -conjugated sp^2 carbon while the hydrophilic domain is constituted by O-groups attached at the basal plane [37]. The existence of two regions allows obtaining stable water-insoluble monolayers of the material. Accordingly, several properties such as rheological properties, morphology, and stability of GO monolayers have been recently reported [11, 16, 18, 19]. Several works seem to indicate a great influence of the chemical composition on the film properties [19, 38].

Concerning the chemical synthesis, graphene oxide is usually obtained by graphite oxidation [17, 19, 39] or carbon nanofibers [18–20, 40] by means of the Staudenmaier [41] or the Hummers [42] reactions. Then, graphene oxides are often reduced by chemical agents [17, 43, 44] or thermal annealing [45, 46] to restore the graphene structure. However, both the GO reduced by chemical agents, referred as reduced graphene oxide (RGO), and the thermally reduced retain some O-groups attached to the basal plane of GO. These O-groups decrease the amazing properties of graphene such as transparency and high electric conductivity.

Despite the interest raised by GO, the knowledge of its chemical structure remains still a challenge. The best-known graphene oxide structure consists of two different carbon domains constituted by Csp^2 corresponding to aromatic groups and Csp^3 of alcohol and epoxy groups attached at the basal plane. The carboxylic acid groups are located at the edge of the sheets [37]. However, the main origin of the controversy is the percentage of each group into the flakes. Several are the causes of discrepancies, although the variability of the starting material and the oxidation process seem to be the most important ones [47]. On the other hand, the chemical structure of graphene oxide was recently revisited because it has been proved that the oxidation of carbon-based materials originates highly oxidized fragment, named as oxidative debris (OD) [47–49]. The oxidized fragments remain strongly adsorbed onto the graphitic sheets due to π - π staking interactions but can be removed by alkaline washing of graphene oxide. The purified GO contains lower O/C ratio than the non-purified one, and consequently its chemical structure and solubility properties are quite different [47, 49].

It is necessary to consider that in nanocomposites built with GO, the second component, polymers, nanoparticles, or small molecules, often interacts with the O-groups of graphene oxide; therefore, to improve the quality of the composite, it is crucial to have knowledge of the chemical structure of graphene oxide to control interactions between components which have a great influence on the properties of nanocomposites. However, there is no systematic study related to the effect of the oxidation procedure, nature of the starting material, and purification process on the chemical structure and properties of graphene oxides. Recently, we have started the systematic study of the effect of the starting material, reduction protocol, and purification process on the chemical structure of graphene oxides and on the film morphology. With this objective in mind, we have synthesized graphene oxides using graphite, and GANF[®] nanofibers from the Grupo Antolín Ingeniería (Burgos, Spain) as starting materials. The oxidation procedure was Hummer's reaction modified to obtain more oxidized samples [17, 18–20]. As reducing agents, we used hydrazine, vitamin C, and sodium borohydride. The purification process consisted of alkaline washing of graphene oxide and is previously reported [48, 49].

To quantify the oxidation degree of different materials, X-ray photoelectron spectroscopy (XPS) was employed. In all samples, the C1s core-level spectrum is an asymmetric band that can be fitted to three components centered at 284.8, 286.4, and 287.9 eV. These peaks are assigned to C-C bonds of the aromatic network, C-O bonds of alcohol or epoxide groups, and COOH groups, respectively [50]. From the area of these peaks, the percentage of the different groups in each sample was calculated. Results obtained for different kinds of graphene oxides are collected in **Figure 3**. Data shown in **Figure 3** were taken from references [17–19].

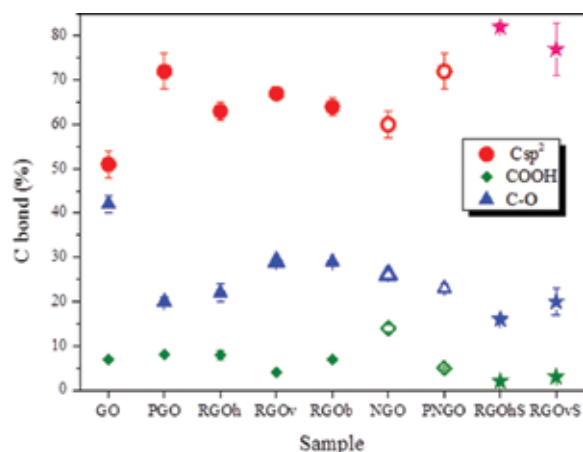


Figure 3. Chemical composition of graphene oxides determined by XPS measurements. Data were taken from references [17–19]. Solid symbols correspond to graphene oxides obtained from graphite and open symbols from GANF[®] nanofibers. Stars are results of surfactant-functionalized graphene oxides.

Results in **Figure 3** clearly show differences between the chemical composition of graphene oxides synthesized by the oxidation of graphite (GO) and nanofibers (NGO). Thus, the percentage of Csp² is slightly higher for NGO than for GO, while the percentage of C-O groups at the basal plane is higher for GO than for NGO and the percentage of COOH groups attached to NGO is twice that of GO. This behavior was attributed to the different size of nanoplatelets [18, 19]. In the case of NGO, dynamic light-scattering measurements (DLS) and the statistical analysis of FESEM images demonstrated that nanoplatelets of NGO are smaller than the GO ones; therefore, since the carboxylic groups are mainly localized at the edge of sheets the smallest sheets contain the highest proportions of COO⁻ groups [19]. As far as the influence of the purification procedure on the chemical composition, our results indicated that the percentage of Csp² increases after the alkaline washing. Moreover, the purification process drives to graphene oxides of similar chemical composition although the chemical structure of non-purified graphene oxides is quite different.

Another interesting result is that the percentage of Csp² of reduced graphene oxide is almost independent on the reducing agent, and the averaged value of 65 ± 2 is lower than the value found for purified graphene oxide, 72 ± 4 . This fact was previously reported for graphene oxide reduced by hydrazine [47] and was interpreted as follows: due to the basic nature of hydrazine, it cleans oxidative debris and simultaneously reduces the oxygen groups of graphene oxide; however, nitrogen atoms remain attached to RGO sheets decreasing the percentage of Csp². This C-N bond identified by XPS as a peak centered at 400 eV is responsible for the increase of Csp³ percentage. The balance of these processes leads to RGO sheets of intermediate composition between purified PGO and GO [17]. Similar situations were observed for graphene oxides reduced by vitamin C and borohydride, respectively. In these cases, oxygen and boron atoms of the oxidized product of vitamin C and borohydride remain attached to the network decreasing the aromatic degree of graphene derivatives. According to our results,

we postulate that alkaline washing must be the preferred procedure to increase the C_{sp^2} percentage on graphene oxide nanoplatelets.

Graphene oxide nanoplatelets are insulators and to increase the electric conductivity chemical reduction has been postulated. However, RGO films prepared by conventional deposition methodologies present low electrical conductivity values. This is probably due to the platelet aggregation induced by dewetting processes. We have explored the Langmuir-Blodgett methodology to obtain non-aggregated and ordered reduced graphene oxide films. To prepare the LB film, it is necessary to select the proper surface state, which will be transferred. To identify the surface state of materials at the interface, the compressional modulus, ϵ , has been widely used. The parameter can be calculated from the surface-pressure isotherm using Eq. (1):

$$\epsilon = -A \left(\frac{\delta \Pi}{\delta A} \right)_{T,P} \quad (1)$$

In Eq. (1), A represents the surface area and π the surface pressure value. We have recorded the surface pressure isotherms of each material and a representative example is plotted in **Figure 4a**. The compressional elastic modulus value is plotted against the surface pressure in **Figure 4b**.

The isotherm morphology is similar to that of surfactant molecules and can be interpreted as follows: monolayers of surface pressure close to zero correspond to low values of compress-

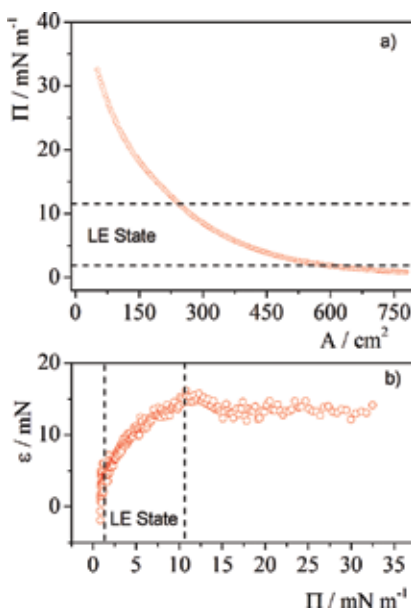


Figure 4. (a) Surface pressure and (b) compressional elastic modulus isotherms of graphene oxide reduced by borohydride at 293 K.

sional modulus and were assigned to surface states in which the nanoplatelets are isolated in a two-dimensional gas state. When the surface area decreases, the nanoplatelets are pushed closer to each other, resulting in small domains in which ϵ grows until it reaches a maximum value. This two-dimensional region is commonly assigned to the liquid-expanded (LE) state and corresponds to close-packed sheets. Beyond the compressional elastic modulus maximum, the nanoplatelets form wrinkles, overlaps, and three-dimensional (3D) structures [16].

In a previous work, the LE state of the GO monolayer [38] has been modeled by Volmer's model adapted to nanoparticles [51]. We have used this model to interpret the isotherms of different nanoplatelets of GO at the LE state. Our results demonstrated strong interactions between carboxylic acids at the edge of sheets through hydrogen bonds [18, 19].

Because we are interested to build GO films of closely packed and nonoverlapped nanoplatelets, we transferred graphene oxide monolayers at the LE state by the LB methodology [18, 19]. Representative atomic force microscopy (AFM) and FESEM images of these films are collected in **Figure 5**.

As can be seen in **Figure 5**, the solid coverage is higher for GO, **Figure 5a**, than for reduced graphene oxides, **Figure 5b**. Low coverage was also reported for purified graphene oxides [18,

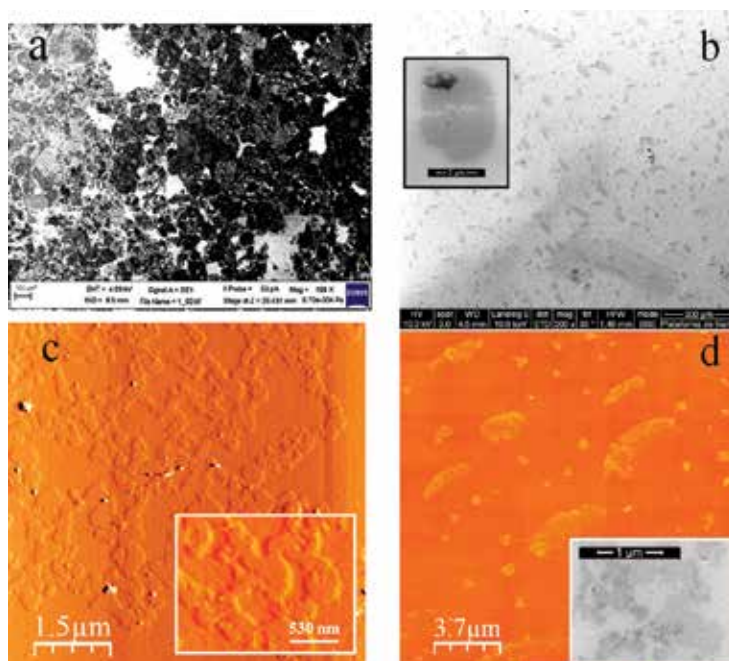


Figure 5. Representative images of different graphene oxides films: (a) SEM image of graphene oxide obtained by oxidation of graphite; (b) TEM image of graphene oxide reduced by vitamin C. The inset is a magnification to show the morphology of RGOv nanoplatelets; (c) graphene oxide functionalized with DDPS and reduced by hydrazine. The inset shows a magnification of the AFM image; (d) graphene oxide functionalized with DDPS and reduced by vitamin C. The inset is a TEM image to show details of the film morphology. Reduced graphene oxides were obtained using graphite as starting materials. The surface pressure of the Langmuir monolayer precursor of the LB film was 1 mN m^{-1} .

19] and was attributed to the low percentage of O-groups attached to sheets of purified oxides [19]. A high percentage of O-groups favor the contact between silanol groups of the silicon wafer and sheets increasing the adhesion of nanoplatelets to silicon. Since the chemical composition of reduced and purified graphene oxides is almost the same, the low percentage of O-groups at reduced samples can be responsible for the low coverage observed for RGO films.

In an attempt to improve the solid coverage, the reduced graphene oxides were functionalized with the zwitterionic surfactant N dodecyl-N,N-dimethyl-3-ammonio-1-propanesulfonate (DDPS). We have proved that the surfactant remains adsorbed onto graphene oxide platelets playing two important roles: as surface active molecule, it favours attractive interactions between the silicon and the reduced graphene oxide and because it is attached at sheets minimizing the restacking of flakes. It is interesting to note that the surfactant is attached to sheets in a non-covalent way, and consequently the chemical structure of graphene oxide is not significantly altered [52].

The AFM images of functionalized reduced graphene oxide films, **Figure 5c** and **d**, show that the functionalization with the DDPS surfactant increases the solid coverage; however, it is lower than that for graphene oxide, **Figure 5a**. The AFM images of RGOhS, **Figure 5c**, also show the formation of the chained sheets suggesting lateral attractive interactions between flakes. These attractive interactions can be likely induced by the surfactant molecules attached to the sheets [17].

We have great interest to study the effect of GO chemical composition on the electrical conductivity of GO films. However, in the case of reduced graphene oxide the electrical conductivity value is too small to detect significant differences; therefore, we employed an alternative method widely used by other authors. The method consists of measuring the conductivity of paper-like graphene oxide films [53]. To analyze the electrical conductivity dependence with the chemical composition, we have plotted the electrical conductivity against the Csp² and C-O group percentages shown in **Figure 6a** and **b**, respectively.

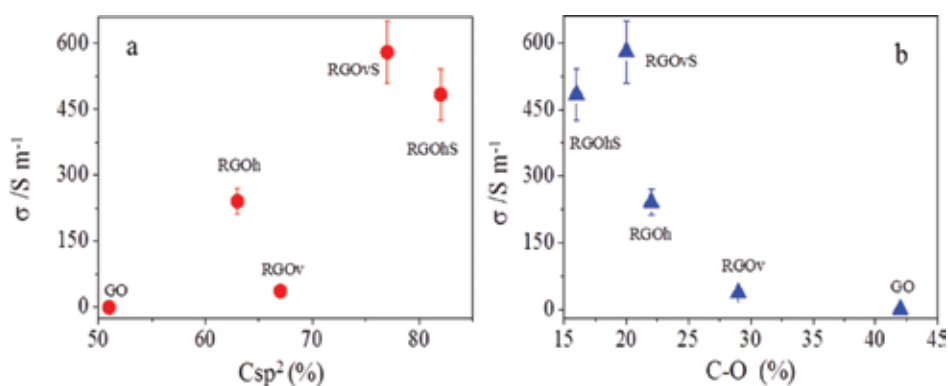


Figure 6. Variation of the electrical conductivity values of paper-like graphene oxide films with the Csp² (a) and (b) C-O group percentages, respectively. Data were taken from Reference [16].

Results in **Figure 6a** show that the electrical conductivity increases as the C_{sp^2} percentage. Moreover, the highest conductivity value is obtained for graphene oxide functionalized with the zwitterionic surfactant. In addition, samples with the lowest percentage of C-O and COOH groups, see **Figure 3**, correspond with reduced graphene oxides functionalized with the surfactant DDPS. All these facts suggest that the surfactant molecules can eliminate high amount of O-groups of samples increasing the electrical conductivity of flakes as can be seen in **Figure 6b**.

On summarizing, the LB technique can be presented as a good methodology of building graphene oxide films because it renders high-coverage and ordered films. On the other hand, the conductivity of our surfactant-functionalized RGO samples is higher than the values found in the literature for paper-like films of reduced graphene oxide [5, 54] functionalized with ionic surfactants, although more efforts must be done to improve the solid coverage and to increase the electrical conductivity values of graphene oxide films.

4. The Langmuir-Blodgett films of 2D materials: QDs and nanowires

Nanoparticles of CdSe Quantum Dots are semiconductors which show size dependence in their optoelectronic properties with attractive applications in the fabrication of solar cells or light-emitting diodes (LEDs) due to their band-gap tunability.

The most important optical advantages are a broad and continuous absorbance spectrum and a narrow emission spectrum whose maximum position and dynamic emission properties depend on its QD size. However, optoelectronic device applications based on nanoparticles require QDs assembly in controllable architecture to avoid the deterioration of the quantum film efficiency. Therefore, the thickness and uniformity of the assembled QD films are crucial factors in the emission properties of films [7, 55–58].

In the particular case of CdSe QDs, the hydrophobic nanoparticles present the highest quantum efficiency. However, when these nanoparticles are transferred from the air-water interface onto substrates such as glass, silicon, or mica without treatment to become the solid surface, hydrophobic, low coverage and nanoparticle agglomeration have been observed [59, 60]. These undesirable results decrease the quantum yield of nanoparticle films. To solve this problem, some approaches have been proposed. One of the most widely used strategies consists of mixing nanoparticles with surfactants or polymers and then transferring the mixture from the air-water interface onto the solid substrate [61–63]. This approach seeks to control the assembly of hydrophobic nanoparticles at the air-water interface. With this purpose, we have proposed three amphiphilic molecules of distinct nature, the copolymers poly(octadecene-co-maleic anhydride), PMAO, and poly(styrene-co-maleic anhydride) partial 2-butoxyethyl ester cumene terminated, PS-MA-BEE, and the Gemini surfactant ethyl-bis(dimethyl octadecylammonium bromide), 18-2-18. All these molecules present surface activity and can anchor to substrates such as mica, glass, or silicon, through their hydrophilic moieties [13, 14] favoring the QDs' adhesion across its hydrophobic part. We have chosen the polymer PMAO because it interacts effectively with hydrophobic nanoparticles leading to excellent stability by

avoiding 3D aggregation [64, 65]. In the case of the polymer PS-MA-BEE, it was chosen because it is a good component to organize hybrid nanomaterials used in submicrometric electronic devices [66]. This is due to its mechanical rigidity and good adhesion on solids [67]. Finally, the Gemini surfactant was chosen since it has been proposed in combination with DNA for biotechnological applications [68, 69].

Our results demonstrated that the QD aggregation is avoided by the addition of these polymer and surfactant molecules. Attractive interactions between the chains of these molecules and the hydrophobic moieties of the QD stabilizer, trioctylphosphine oxide (TOPO), favor the adsorption of QDs on the matrices, while the hydrophilic groups of polymer or surfactant molecules increase the QDs' adhesion in solid substrates, avoiding the nanoparticle agglomeration.

We also found two different film features depending on the film composition. To illustrate this behavior, **Figure 7** collects some AFM, transmission electron microscopy (TEM), and scanning electron microscopy (SEM) images of QD films prepared with different matrix compositions.

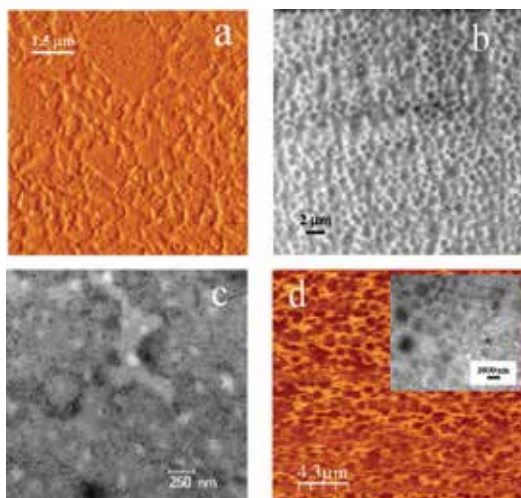


Figure 7. (a) AFM image of a Gemini/QD film at the surfactant mole fraction of 0.98, (b) SEM image of a PMAO/QD LB film onto mica at the polymer mole fraction of 0.50. The Langmuir monolayers were transferred at the surface pressure of 30 mN m^{-1} , (c) TEM image of mixed PS-MA-BEE/QD LB film of polymer mole fraction of 0.5 and deposited at the surface pressure of 14 mN m^{-1} , and (d) AFM image of a mixed PS-MA-BEE/QD film of polymer mole fraction of 0.96 and deposited at the surface pressure of 30 mN m^{-1} . The inset corresponds to the TEM image of the film.

Images in **Figure 7** show two different morphologies, hexagonal networks and domains of different shapes, depending on the film composition. Thus, mixed films of QDs and PS-MA-BEE of high polymer mole fraction, $X_p \geq 0.95$, and deposited at 30 mN m^{-1} [22] and PMAO/QDs films are constituted by hexagonal networks [21], **Figure 7b** and **d**. It is interesting to note that the height of rims around the holes was 4 nm, which is compatible with the diameter of the nanoparticles dissolved in chloroform (3.4 nm). This result indicates that QDs are mainly confined in rims and do not form 3D aggregates. On the other hand, all the Gemini/

QDs films and PS-MA-BEE/QDs films of polymer mole fraction below 0.95 deposited at low-surface pressure (14 mN m^{-1}) are constituted by domains of different morphologies, **Figure 7a** and **c**. The domain height determined by AFM measurements ($\sim 3 \text{ nm}$) is consistent with the diameter of QDs dissolved in chloroform. This fact indicates that there is no 3D aggregation in these films.

Differences between film morphologies were interpreted according to dewetting mechanisms [21, 22]. The two dewetting mechanisms considered in these cases are known as nucleation, growth, and coalescence of holes [70] and spinodal [71]. In the former, the gravity contribution predominates and the dewetting process starts with the nucleation of holes at film-defect sites followed by the material displacement away from the nucleus. The material is accumulated in the rims of holes delimiting a mosaic [70]. Conversely, in the spinodal dewetting mechanism, the capillary waves break the film into nanostructures when the amplitude of the capillary waves exceeds the thickness of the film. Taking into account that the molecular weight of the polymer PMAO is around 50 times higher than the surfactant one, it becomes clear that the gravitational effect prevailed over the capillary waves even in films with small amount of the polymer PMAO. Therefore, the PMAO/QDs film morphology is driven by the mechanism of nucleation, growth, and coalescence of holes, while spinodal dewetting mechanism prevails in Gemini/QD films [21]. In the case of PS-MA-BEE/QD films, the interpretation of the behavior observed is not so evident and it is necessary to analyze the balance between the driving forces involved in the surface arrangement: gravitational and capillary forces. Thus, the elasticity values go through a minimum for PS-MA-BEE/QDs monolayers at the surface pressure of 30 mN m^{-1} and for polymer mole ratio above 0.95, while it reaches maximum values for monolayers at the surface pressure value of 14 mN m^{-1} and $X_p < 0.95$ [22]. Taking into account that the damping coefficient passes through a maximum at low elasticity values and decreases when the elasticity modulus increases [22], it is easy to understand that in PS-MA-BEE/QD films of low elasticity values ($\pi = 30 \text{ mN m}^{-1}$ and $X_p \geq 0.95$), the capillary waves are quickly damped and the film breaks in domains separated by holes due to gravitational effects. Conversely, the capillary waves for monolayers with the highest elasticity values ($\pi = 14 \text{ mN m}^{-1}$ and $X_p < 0.95$) do not damp so quickly and they drive the dewetting mechanism. In these situations, the spinodal dewetting mechanism predominates against the growth of holes process leading to QD domains of different shapes [22].

Another interesting example is the preparation of silver nanowire films for manufacturing modern devices such as photovoltaic cells, touch panels, and light-emitting diodes. Although the development of new materials is mainly by the requirements of each application [72], high transparency and electrical conductivity always constitute required requisites.

Indium tin oxide (ITO) currently dominates the field of transparent conductive electrodes as a result of its excellent optoelectronic properties [73]; however, it suffers important limitations due to the scarcity of indium, brittleness of its electrodes, and high manufacturing cost. Several materials such as carbon nanotubes [74, 75], graphene films [76, 77], conducting polymers, and metal nanowires [72, 78] are being analyzed to replace ITO. However, the properties of these materials, in terms of electrical resistance and transparency, are still inferior to ITO [78]. Among all, the silver nanowires arouse great interest due to the high conductivity of silver ($6.3 \times 10^7 \text{ S}$

m^{-1}) [79]. Since the nanowires are usually synthesized in solution, an important issue is the control of the transfer process from solutions onto the substrate. This is because to achieve low electrical resistance and high transparency, it is necessary to optimize the morphology, the placement of nanowires, and the junction resistance between them in the network. As commented previously, spin-coating and drop-casting methodologies present several disadvantages since water evaporation leaves discontinuous films with typical coffee rings that significantly decrease the quality of AgNW films [80, 81]. To overcome these limitations, we have reported a strategy based on the Langmuir-Schaefer methodology to transfer hydrophobic AgNW from the air-water interface onto Lexan polycarbonate substrate in an ordered and controlled way [27].

The first step for building LB films is to obtain stable monolayers of hydrophobic materials. Therefore, it is necessary to synthesize hydrophobic nanowires, since the commercial ones are water soluble since they use polyvinyl pyrrolidone molecules as capping agents. To synthesize hydrophobic AgNW, polyvinyl pyrrolidone was replaced by octyl thiol molecules. The surface modification is achieved through the surface ligand exchange procedure reported by Tao [82]. After the synthesis of AgNW, they were deposited at the air-water interface and different surface states were transferred onto the solid substrate by the LS methodology. The surface states of nanowire monolayers are characterized by the surface compressional modulus, ϵ , calculated from the surface pressure isotherm and Eq. (1), and ϵ -values are plotted against the surface concentration, Γ , in **Figure 8a**. As can be seen in **Figure 8a**, when the surface concentration is small, the elasticity modulus value is close to zero. In this region, named as low-surface density state (LD), nanowires are randomly orientated. When the surface density is further increased and ϵ reaches a value of 10 mN m^{-1} , the monolayer is highly packed; we referred to this state as the high-surface density state (HD) [83].

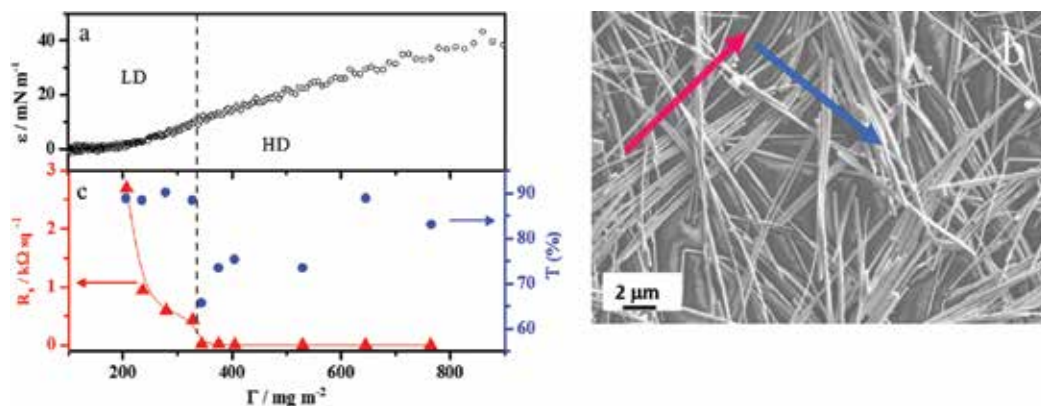


Figure 8. (a) Elasticity isotherm of silver nanowires capped with octyl thiol at 20°C , (b) FESEM image of a bilayer of AgNW of 645 mg m^{-2} . Arrows indicate the orientation of the first (red) and second (blue) layers, and (c) variation of sheet resistance and transmittance with the nanowire surface concentration of LS films.

We have transferred AgNW Langmuir monolayers at LD and HD states by the Langmuir-Schaefer methodology. With the purpose of achieving a network of nanowires, a second layer

in which the nanowires are oriented perpendicular to the first layer was deposited. In the first and second layers, the surface density of the transferred Langmuir monolayer was the same [27]. The surface density is controlled by the surface pressure value. **Figure 8b** shows a representative FE-SEM image of a nanowire film obtained by this methodology.

The sheet resistance, R_s , measured in $\Omega \text{ sq}^{-1}$ and the transmittance measured at 550 nm are plotted against the surface concentration in **Figure 8c**. Data in **Figure 8c** show that the monolayers at the LD state present high R_s values which decrease when the surface concentration increases, while the transmittance value is almost independent on surface concentration and remains constant at 88%. The behavior is opposite for films built from Langmuir monolayers at the HD state. In this case, the sheet resistance is maintained at $8 \Omega \text{ sq}^{-1}$ while the transmittance value changes from 65 to 89% when the surface concentration was modified between 345 to 770 mg m^{-2} . According to the resistance and transparency values, our AgNW films can be employed as substitutes for ITO as components of devices such as touch screens, electromagnetic shielding, and defrosted windows [27]. Moreover, our results proved that the Langmuir-Schaefer methodology is a versatile technique, which allows modifying the transmittance keeping the sheet resistance or tuning the sheet resistance, maintaining the transparency of films constant by properly selecting the surface state and the nanowire mass transferred onto the solid substrate.

Results analyzed in this chapter allow us to discuss the ability of the Langmuir-Blodgett and Langmuir-Schaefer methodologies to build thin films of 2D materials such as graphene oxides, transition metal chalcogenide nanoparticles, CdSe Quantum Dots, and silver nanowires. We discuss the advantages of these methods against the most conventional ones such as drop and spin coating for built-in 2D material films with applications in the fabrication of solar cells, LEDs, sensors, and transparent electrodes.

We also review some strategies for improving the solid coverage, avoiding the nanoparticle aggregation, and modulating the film morphology. All these issues are crucial for increasing the quality of films and to modulate its properties according to the properties required for each application.

Results analyzed in this chapter indicate that the Langmuir-Blodgett and Langmuir-Schaefer methodologies combined with self-assembled materials can be proposed as a non-template reproducible technique for patterning at the nanoscale. However, most efforts have to be done for achieving more homogeneous films, higher coverage, and a greater control of the material arrangements to build good-quality films to be used in technological applications.

Acknowledgements

The authors thank financial support from the European Regional Development Fund, ERDF, Ministerio de Educación y Ciencia (MAT 2010-19727), and Ministerio de Economía y Competitividad (IPT-2012-0429-420000). TA and BMG wish to thank the European Social Fund and Consejería de Educación de la Junta de Castilla y León for their FPI grants. We also thank Ultra-

Intense Lasers Pulsed Center of Salamanca (CLPU) for the AFM measurements, to Microscopy Service (Universidad de Salamanca) for the TEM measurements, and Sala Blanca de Nanotecnología (USAL) for FE-SEM facility. We thank Dr. García Fierro (Instituto de Catálisis y Petroleoquímica, Madrid) for XPS measurements.

Author details

María Mercedes Velázquez*, Teresa Alejo, David López-Díaz, Beatriz Martín-García and María Dolores Merchán

*Address all correspondence to: mvsal@usal.es

Department of Physical Chemistry, Faculty of Chemistry, University of Salamanca, Salamanca, Spain

References

- [1] Novoselov K S, Geim A K, Morozov S V, Jiang D, Zhang Y, Dubonos S V, Grigorieva I V, Firsov A A. Electric Field Effect in Atomically Thin Carbon Films. *Science*. 2004; 306: 666–669. DOI: 10.1126/science.1102896
- [2] Geim A K, Novoselov K S. The Rise of Graphene. *Nature Materials*. 2007; 6: 183–191. DOI: 10.1038/nmat1849
- [3] Geim A K. Graphene: Status and Prospects. *Science*. 2009; 324: 1530–1534. DOI: 10.1126/science.1158877
- [4] Castro Neto A H, Guinea F, Peres N M R, Novoselov K S, Geim A K. The Electronic Properties of Graphene. *Reviews of Modern Physics*. 2009; 81: 109–162.
- [5] Lotya M, Hernandez Y, King P J, Smith R J, Nicolosi V, Karlsson L S, Blighe F M, De S, Wang Z, McGovern I T, Duesberg G S, Coleman J N. Liquid Phase Production of Graphene by Exfoliation of Graphite in Surfactant/Water Solutions. *Journal of the American Chemical Society*. 2009; 131: 3611–3620. DOI: 10.1021/ja807449u
- [6] Park S, Ruoff R S. Chemical Methods for the Production of Graphenes. *Nature Nanotechnology*. 2009; 4: 217–224. DOI: 10.1038/nnano.2009.58
- [7] Talapin D V, Lee J-S, Kovalenko M V, Shevchenko E V. Prospects of Colloidal Nanocrystals for Electronic and Optoelectronic Applications. *Chemical Reviews*. 2010; 110: 389–458. DOI: 10.1021/cr900137k
- [8] Wang J, Vernerberg D, Lin Z. Quantum Dot Sensitized Solar Cells. *Journal of Nanotechnology and Nanomanufacturing*. 2011; 1: 155–171. DOI: 10.1166/jnan.2011.1057

- [9] Gilje S, Han S, Wang M, Wang K L, Kaner R B. A Chemical Route to Graphene for Device Applications. *Nano Letters*. 2007; 7: 3394–3398. DOI: 10.1021/nl0717715
- [10] Becerril H A, Mao J, Liu Z, Stoltenberg R M, Bao Z, Chen Y. Evaluation of Solution-Processed Reduced Graphene Oxide Films as Transparent Conductors. *ACS Nano*. 2008; 2: 463–470. DOI: 10.1021/nn700375n
- [11] Zheng Q, Li Z, Yang J, Kim J-K. Graphene Oxide-based Transparent Conductive Films. *Progress in Materials Science*. 2014; 64: 200–247. DOI: 10.1016/j.pmatsci.2014.03.004
- [12] Roberts G G. *Langmuir-Blodgett Films*. New York: Springer US; 1990. 425 p. DOI: 10.1007/978-1-4899-3716-2
- [13] Martín-García B, Velázquez M M, Pérez-Hernandez J A, Hernandez-Toro J. Langmuir and Langmuir-Blodgett Films of a Maleic Anhydride Derivative: Effect of Subphase Divalent Cations. *Langmuir*. 2010; 26: 14556–14562. DOI: 10.1021/la101736e
- [14] Alejo T, Merchán M D, Velázquez M M. Specific Ion Effects on the Properties of Cationic Gemini Surfactant Monolayers. *Thin Solid Films*. 2011; 519: 5689–5695. DOI: 10.1016/j.tsf.2011.03.018
- [15] Collier C P, Saykally R J, Shiang J J, Henrichs S E, Heath J R. Reversible Tuning of Silver Quantum Dot Monolayers Through the Metal-Insulator Transition. *Science*. 1997; 277: 1978–1981. DOI: 10.1126/science.277.5334.1978
- [16] Cote L J, Kim F, Huang J. Langmuir-Blodgett Assembly of Graphite Oxide Single Layers. *Journal of the American Chemical Society*. 2008; 131: 1043–1049. DOI: 10.1021/ja806262m
- [17] Martín-García B, Velázquez M M, Rossella F, Bellani V, Diez E, García Fierro J L, Pérez-Hernández J A, Hernández-Toro J, Claramunt S, Cirera A. Functionalization of Reduced Graphite Oxide Sheets with a Zwitterionic Surfactant. *ChemPhysChem*. 2012; 13: 3682–3690. DOI: 10.1002/cphc.201200501
- [18] López-Díaz D, Mercedes Velázquez M, Blanco de La Torre S, Pérez-Pisonero A, Trujillano R, Fierro J L G, Claramunt S, Cirera A. The Role of Oxidative Debris on Graphene Oxide Films. *ChemPhysChem*. 2013; 14: 4002–4009. DOI: 10.1002/cphc.201300620
- [19] Hidalgo R S, López-Díaz D, Velázquez M M. Graphene Oxide Thin Films: Influence of Chemical Structure and Deposition Methodology. *Langmuir*. 2015; 31: 2697–2705. DOI: 10.1021/la5029178
- [20] Orna J, López-Díaz D, Pérez A, Rodríguez M J, Lagunas A R, Velázquez M M, Blanco S, Merino C. GRAnPH®: High Quality Graphene Oxide Obtained from GANF® Carbon Nanofibres. In: *eNanonewsletter*. Antonio Correia, Madrid, Spain: Phantoms Foundation; 2013. pp 33–37

- [21] Alejo T, Merchán M D, Velázquez M M, Pérez-Hernández J A. Polymer/Surfactant Assisted Self-assembly of Nanoparticles into Langmuir-Blodgett Films. *Materials Chemistry and Physics*. 2013; 138: 286–294. DOI: 10.1016/j.matchemphys.2012.11.058
- [22] Martín-García B, Velázquez M M. Block Copolymer Assisted Self-assembly of Nanoparticles into Langmuir-Blodgett Films: Effect of Polymer Concentration. *Materials Chemistry and Physics*. 2013; 141: 324–332. DOI: 10.1016/j.matchemphys.2013.05.017
- [23] Martín-García B, Paulo P M R, Costa S M B, Velázquez M M. Photoluminescence Dynamics of CdSe QD/Polymer Langmuir-Blodgett Thin Films: Morphology Effects. *The Journal of Physical Chemistry C*. 2013; 117: 14787–14795. DOI: 10.1021/jp311492z
- [24] Alejo T, Martín-García B, Merchán M D, Velázquez M M. QDs Supported on Langmuir-Blodgett Films of Polymers and Gemini Surfactant. *Journal of Nanomaterials*. 2013; 2013: 1–10. DOI: 10.1155/2013/287094
- [25] Alejo T, Merchán M D, Velázquez M M. Adsorption of Quantum Dots onto Polymer and Gemini Surfactant Films: A Quartz Crystal Microbalance Study. *Langmuir*. 2014; 30: 9977–9984. DOI: 10.1021/la5024955
- [26] Martín-García B, Velázquez M M. Nanoparticle Self-assembly Assisted by Polymers: The Role of Shear Stress in the Nanoparticle Arrangement of Langmuir and Langmuir-Blodgett Films. *Langmuir*. 2014; 30: 9977–9984. DOI: 10.1021/la404834b
- [27] Lopez-Diaz D, Merino C, Velázquez M. Modulating the Optoelectronic Properties of Silver Nanowires Films: Effect of Capping Agent and Deposition Technique. *Materials*. 2015; 8: 5405. DOI: 10.3390/ma8115405
- [28] Gaines G L J. *Insoluble Monolayers at Liquid-Gas Interfaces*. New York: Interscience; 1966.
- [29] Petty M C. *Langmuir-Blodgett Films: An Introduction*. New York: Cambridge University Press; 1996. DOI: 10.1017/CBO9780511622519
- [30] Zhu Y, Murali S, Cai W, Li X, Suk J W, Potts J R, Ruoff R S. Graphene and Graphene Oxide: Synthesis, Properties, and Applications. *Advanced Materials*. 2010; 22: 3906–3924. DOI: 10.1002/adma.201001068
- [31] Potts J R, Dreyer D R, Bielawski C W, Ruoff R S. Graphene-Based Polymer Nanocomposites. *Polymer*. 2011; 52: 5–25. DOI: 10.1016/j.polymer.2010.11.042
- [32] Prezioso S, Perrozzi F, Giancaterini L, Cantalini C, Treossi E, Palermo V, Nardone M, Santucci S, Ottaviano L. Graphene Oxide as a Practical Solution to High Sensitivity Gas Sensing. *The Journal of Physical Chemistry C*. 2013; 117: 10683–10690. DOI: 10.1021/jp3085759
- [33] Eda G, Chhowalla M. Chemically Derived Graphene Oxide: Towards Large-Area Thin-Film Electronics and Optoelectronics. *Advanced Materials*. 2010; 22: 2392–2415. DOI: 10.1002/adma.200903689

- [34] Loh K P, Bao Q, Eda G, Chhowalla M. Graphene oxide as a Chemically Tunable Platform for Optical Applications. *Nature Chemistry*. 2010; 2: 1015–1024.
- [35] Zheng Q, Ip W H, Lin X, Yousefi N, Yeung K K, Li Z, Kim J-K. Transparent Conductive Films Consisting of Ultralarge Graphene Sheets Produced by Langmuir–Blodgett Assembly. *ACS Nano*. 2011; 5: 6039–6051. DOI: 10.1021/nn2018683
- [36] Kim J, Cote L J, Huang J. Two Dimensional Soft Material: New Faces of Graphene Oxide. *Accounts of Chemical Research*. 2012; 45: 1356–1364. DOI: 10.1021/ar300047s
- [37] Lerf A, He H, Forster M, Klinowski J. Structure of Graphite Oxide Revisited. *The Journal of Physical Chemistry B*. 1998; 102: 4477–4482. DOI: 10.1021/jp9731821
- [38] Imperiali L, Liao K-H, Clasen C, Fransaer J, Macosko C W, Vermant J. Interfacial Rheology and Structure of Tiled Graphene Oxide Sheets. *Langmuir*. 2012; 28: 7990–8000. DOI: 10.1021/la300597n
- [39] Dreyer D R, Park S, Bielawski C W, Ruoff R S. The Chemistry of Graphene Oxide. *Chemical Society Reviews*. 2010; 39: 228–240. DOI: 10.1039/b917103g
- [40] Varela-Rizo H, Rodriguez-Pastor I, Merino C, Martin-Gullon I. Highly Crystalline Graphene Oxide Nano-Platelets Produced from Helical-Ribbon Carbon Nanofibers. *Carbon*. 2010; 48: 3640–3643. DOI: 10.1016/j.carbon.2010.05.033
- [41] Staudenmaier L. Verfahren zur Darstellung der Graphitsäure. *Methods for synthesizing graphite acid*. 1898; 31: 1481–1487. DOI: 10.1002/cber.18980310237
- [42] Hummers W S, Offeman R E. Preparation of Graphitic Oxide. *Journal of the American Chemical Society*. 1958; 80: 1339–1339. DOI: 10.1021/ja01539a017
- [43] Stankovich S, Dikin D A, Piner R D, Kohlhaas K A, Kleinhammes A, Jia Y, Wu Y, Nguyen S T, Ruoff R S. Synthesis of Graphene-Based Nanosheets via Chemical Reduction of Exfoliated Graphite Oxide. *Carbon*. 2007; 45: 1558–1565. DOI: 10.1016/j.carbon.2007.02.034
- [44] Fernández-Merino M J, Guardia L, Paredes J I, Villar-Rodil S, Solís-Fernández P, Martínez-Alonso A, Tascón J M D. Vitamin C Is an Ideal Substitute for Hydrazine in the Reduction of Graphene Oxide Suspensions. *The Journal of Physical Chemistry C*. 2010; 114: 6426–6432. DOI: 10.1021/jp100603h
- [45] Bagri A, Mattevi C, Acik M, Chabal Y J, Chhowalla M, Shenoy V B. Structural Evolution During the Reduction of Chemically Derived Graphene Oxide. *Nature Chemistry*. 2010; 2: 581–587. DOI: 10.1038/nchem.686
- [46] Claramunt S, Varea A, López-Díaz D, Velázquez M M, Cornet A, Cirera A. The Importance of Interbands on the Interpretation of the Raman Spectrum of Graphene Oxide. *The Journal of Physical Chemistry C*. 2015; 119: 10123–10129. DOI: 10.1021/acs.jpcc.5b01590

- [47] Thomas H R, Day S P, Woodruff W E, Vallés C, Young R J, Kinloch I A, Morley G W, Hanna J V, Wilson N R, Rourke J P. Deoxygenation of Graphene Oxide: Reduction or Cleaning? *Chemistry of Materials* 2013; 25: 3580–3588 DOI: 10.1021/cm401922e
- [48] Wang Z, Shirley M D, Meikle S T, Whitby R L D, Mikhailovsky S V. The Surface Acidity of Acid Oxidised Multi-Walled Carbon Nanotubes and the Influence of In-situ Generated Fulvic Acids on Their Stability in Aqueous Dispersions. *Carbon*. 2009; 47: 73–79. DOI: 10.1016/j.carbon.2008.09.038
- [49] Rourke J P, Pandey P A, Moore J J, Bates M, Kinloch I A, Young R J, Wilson N R. The Real Graphene Oxide Revealed: Stripping the Oxidative Debris from the Graphene-like Sheets. *Angewandte Chemie International Edition*. 2011; 50: 3173–3177. DOI: 10.1002/anie.201007520
- [50] Hontoria-Lucas C, López-Peinado A J, López-González J D D, Rojas-Cervantes M L, Martín-Aranda R M. Study of Oxygen-Containing Groups in a Series of Graphite Oxides: Physical and Chemical Characterization. *Carbon*. 1995; 33: 1585–1592. DOI: 10.1016/0008-6223(95)00120-3
- [51] Fainerman V B, Kovalchuk V I, Lucassen-Reynders E H, Grigoriev D O, Ferri J K, Leser M E, Michel M, Miller R, Möhwald H. Surface-Pressure Isotherms of Monolayers Formed by Microsize and Nanosize Particles. *Langmuir*. 2006; 22: 1701–1705. DOI: 10.1021/la052407t
- [52] Qi X, Pu K-Y, Li H, Zhou X, Wu S, Fan Q-L, Liu B, Boey F, Huang W, Zhang H. Amphiphilic Graphene Composites. *Angewandte Chemie International Edition*. 2010; 49: 9426–9429. DOI: 10.1002/anie.201004497
- [53] Gao W, Alemany L B, Ci L, Ajayan P M. New Insights into the Structure and Reduction of Graphite Oxide. *Nature Chemistry*. 2009; 1: 403–408.
- [54] Fernández-Merino M J, Paredes J I, Villar-Rodil S, Guardia L, Solís-Fernández P, Salinas-Torres D, Cazorla-Amorós D, Morallón E, Martínez-Alonso A, Tascón J M D. Investigating the Influence of Surfactants on the Stabilization of Aqueous Reduced Graphene Oxide Dispersions and the Characteristics of Their Composite Films. *Carbon*. 2012; 50: 3184–3194. DOI: doi:10.1016/j.carbon.2011.10.039
- [55] Rogach A L. *Semiconductor Nanocrystal Quantum Dots: Synthesis, Assembly, Spectroscopy and Applications*. New York: Springer-Verlag Wien; 2008. 372 p. DOI: 10.1007/978-3-211-75237-1
- [56] Tomczak N, Jańczewski D, Han M, Vancso G J. Designer Polymer–Quantum Dot Architectures. *Progress in Polymer Science*. 2009; 34: 393–430. DOI: 10.1016/j.progpolymsci.2008.11.004
- [57] Kim T-H, Cho K-S, Lee E K, Lee S J, Chae J, Kim J W, Kim D H, Kwon J-Y, Amaratunga G, Lee S Y, Choi B L, Kuk Y, Kim J M, Kim K. Full-Colour Quantum Dot Displays

- Fabricated by Transfer Printing. *Nature Photonics*. 2011; 5: 176–182. DOI: 10.1038/nphoton.2011.12
- [58] Selinsky R S, Ding Q, Faber M S, Wright J C, Jin S. Quantum Dot Nanoscale Heterostructures for Solar Energy Conversion. *Chemical Society Reviews*. 2013; 42: 2963–2985. DOI: 10.1039/C2CS35374A
- [59] Lambert K, Capek R K, Bodnarchuk M I, Kovalenko M V, Van Thourhout D, Heiss W, Hens Z. Langmuir-Schaefer Deposition of Quantum Dot Multilayers. *Langmuir*. 2010; 26: 7732–7736. DOI: 10.1021/la904474h
- [60] Dabbousi B O, Murray C B, Rubner M F, Bawendi M G. Langmuir-Blodgett Manipulation of Size-Selected CdSe Nanocrystallites. *Chemistry of Materials*. 1994; 6: 216–219. DOI: 10.1021/cm00038a020
- [61] Gupta S, Singh N, Sastry M, Kakkar R, Pasricha R. Controlling the Assembly of Hydrophobized Gold Nanoparticles at the Air–Water Interface by Varying the Interfacial Tension. *Thin Solid Films*. 2010; 519: 1072–1077. DOI: 10.1016/j.tsf.2010.08.046
- [62] Pohjalainen E, Pohjakallio M, Johans C, Kontturi K, Timonen J V, Ikkala O, Ras R H, Viitala T, Heino M T, Seppala E T. Cobalt Nanoparticle Langmuir-Schaefer Films on Ethylene Glycol Subphase. *Langmuir*. 2010; 26: 13937–13943. DOI: 10.1021/la101630q
- [63] Gattas-Asfura K M, Constantine C A, Lynn M J, Thimann D A, Ji X, Leblanc R M. Characterization and 2D Self-Assembly of CdSe Quantum Dots at the Air-Water Interface. *Journal of the American Chemical Society*. 2005; 127: 14640–14646. DOI: 10.1021/ja0514848
- [64] Shtykova E V, Huang X, Gao X, Dyke J C, Schmucker A L, Dragnea B, Remmes N, Baxter D V, Stein B, Konarev P V, Svergun D I, Bronstein L M. Hydrophilic Monodisperse Magnetic Nanoparticles Protected by an Amphiphilic Alternating Copolymer. *The Journal of Physical Chemistry C*. 2008; 112: 16809–16817. DOI: 10.1021/jp8053636
- [65] Bronstein L M, Shtykova E V, Malyutin A, Dyke J C, Gunn E, Gao X, Stein B, Konarev P V, Dragnea B, Svergun D I. Hydrophilization of Magnetic Nanoparticles with Modified Alternating Copolymers. Part 1: The Influence of the Grafting. *The Journal of Physical Chemistry C*. 2010; 114: 21900–21907. DOI: 10.1021/jp107283w
- [66] Jones R, Winter C S, Tredgold R H, Hodge P, Hoorfar A. Electron-Beam Resists from Langmuir-Blodgett Films of Poly(styrene/maleic anhydride) Derivatives. *Polymer*. 1987; 28: 1619–1626. DOI: 10.1016/0032-3861(87)90001-2
- [67] John Collins S, L. Mary N, Radhakrishnan G, Dhathathreyan A. Studies of Spread Monolayers of Derivative of Styrene-maleic Anhydride Copolymers. *Journal of the Chemical Society, Faraday Transactions*. 1997; 93: 4021–4023. DOI: 10.1039/A704115B
- [68] Chen X, Wang J, Shen N, Luo Y, Li L, Liu M, Thomas R K. Gemini Surfactant/DNA Complex Monolayers at the Air-Water Interface: Effect of Surfactant Structure on the

- Assembly, Stability, and Topography of Monolayers. *Langmuir*. 2002; 18: 6222–6228. DOI: 10.1021/la025600l
- [69] Chen Q, Kang X, Li R, Du X, Shang Y, Liu H, Hu Y. Structure of the Complex Monolayer of Gemini Surfactant and DNA at the Air/Water Interface. *Langmuir*. 2012; 28: 3429–3438. DOI: 10.1021/la204089u
- [70] Gentili D, Foschi G, Valle F, Cavallini M, Biscarini F. Applications of Dewetting in Micro and Nanotechnology. *Chemical Society Reviews*. 2012; 41: 4430–4443. DOI: 10.1039/c2cs35040h
- [71] Reiter G. Dewetting of Thin Polymer Films. *Physical Review Letters*. 1992; 68: 75–78. DOI: 10.1103/PhysRevLett.68.75
- [72] Langley D, Giusti G, Mayousse C, Celle C, Bellet D, Simonato J-P. Flexible Transparent Conductive Materials Based on Silver Nanowire Networks: A Review. *Nanotechnology*. 2013; 24: 452001. DOI: 10.1088/0957-4484/24/45/452001
- [73] Alam M J, Cameron D C. Investigation of Annealing Effects on Sol–Gel Deposited Indium Tin Oxide Thin Films in Different Atmospheres. *Thin Solid Films*. 2002; 420–421: 76–82. DOI: 10.1016/S0040-6090(02)00737-X
- [74] Wu Z, Chen Z, Du X, Logan J M, Sippel J, Nikolou M, Kamaras K, Reynolds J R, Tanner D B, Hebard A F, Rinzler A G. Transparent, Conductive Carbon Nanotube Films. *Science*. 2004; 305: 1273–1276. DOI: 10.1126/science.1101243
- [75] Doherty E M, De S, Lyons P E, Shmeliov A, Nirmalraj P N, Scardaci V, Joimel J, Blau W J, Boland J J, Coleman J N. The Spatial Uniformity and Electromechanical Stability of Transparent, Conductive Films of Single Walled Nanotubes. *Carbon*. 2009; 47: 2466–2473. DOI: 10.1016/j.carbon.2009.04.040
- [76] Moon I K, Kim J I, Lee H, Hur K, Kim W C, Lee H. 2D Graphene Oxide Nanosheets as an Adhesive Over-Coating Layer for Flexible Transparent Conductive Electrodes. *Scientific Reports*. 2013; 3: 1–7. DOI: 10.1038/srep01112
- [77] Yun Y S, Kim D H, Kim B, Park H H, Jin H J. Transparent Conducting Films Based on Graphene Oxide/Silver Nanowire Hybrids with High Flexibility. *Synthetic Metals*. 2012; 162: 1364–1368. DOI: 10.1016/j.synthmet.2012.05.026
- [78] Madaria A, Kumar A, Ishikawa F, Zhou C. Uniform, Highly Conductive, and Patterned Transparent Films of a Percolating Silver Nanowire Network on Rigid and Flexible Substrates Using a Dry Transfer Technique. *Nano Research*. 2010; 3: 564–573. DOI: 10.1007/s12274-010-0017-5
- [79] Serway R A. *Principles of Physics*. 2nd Ed. Fort Worth, Texas: Saunder Colloge Pub.; 1998. p. 602.

- [80] Deegan R D, Bakajin O, Dupont T F, Huber G, Nagel S R, Witten T A. Capillary Flow as the Cause of Ring Stains from Dried Liquid Drops. *Nature*. 1997; 389: 827–829. DOI: 10.1038/39827
- [81] Huang J, Fan R, Connor S, Yang P. One-Step Patterning of Aligned Nanowire Arrays by Programmed Dip Coating. *Angewandte Chemie International Edition*. 2007; 46: 2414–2417. DOI: 10.1002/anie.200604789
- [82] Tao A, Kim F, Hess C, Goldberger J, He R, Sun Y, Xia Y, Yang P. Langmuir-Blodgett Silver Nanowire Monolayers for Molecular Sensing Using Surface-Enhanced Raman Spectroscopy. *Nano Letters*. 2003; 3: 1229–1233. DOI: 10.1021/nl0344209
- [83] Gonçalves da Silva A M, Romão R S, Lucero Caro A, Rodriguez Patino J M. Memory Effects on the Interfacial Characteristics of Dioctadecyldimethylammonium Bromide Monolayers at the Air–Water Interface. *Journal of Colloid and Interface Science*. 2004; 270: 417–425. DOI: 10.1016/j.jcis.2003.11.002

Heteroepitaxial Growth of III–V Semiconductors on 2D Materials

Yazeed Alaskar, Shamsul Arafin,
Isaac Martinez-Velis and Kang L. Wang

Additional information is available at the end of the chapter

<http://dx.doi.org/10.5772/64419>

Abstract

Quasi van der Waals epitaxy (QvdWE) of III-V semiconductors on two-dimensional layered material, such as graphene, is discussed. Layered materials are used as a lattice mismatch/thermal expansion coefficient mismatch-relieving layer to integrate III-V semiconductors on any arbitrary substrates. In this chapter, the epitaxial growth of both III–V nanowires and thin films on two-dimensional layered materials is presented. Also, the growth challenges of thin film on two-dimensional materials using QvdWE are discussed through density functional theory calculations. Furthermore, optoelectronic devices of III-V semiconductors integrated on two-dimensional layered material based on QvdWE are overviewed to prove the future potential and importance of such type of epitaxy.

Keywords: van der Waals, heteroepitaxy, graphene, III–V semiconductor, thin films, nanostructures

1. Introduction to van der Waals epitaxy

Heteroepitaxial growth of III–V semiconductor on complementary metal-oxide-semiconductor (CMOS)-compatible substrates has been a subject of research over the last 40 years [1–10]. Unfortunately, these long-period and extensive scientific efforts devoted to the direct growth of III–V materials on such target substrates have resulted in little success. The primary obstacle to success is the lattice and thermal expansion mismatches between semiconductor compounds of interest and the substrate materials. Therefore, the heteroepitaxy of high-quality three-dimensional (3D) materials requires an alternative technique, which can eliminate the limitation of inherent lattice matching [11–15].

Thanks to the two-dimensional (2D)-layered materials whose unique and promising properties enable to open up a new route of heteroepitaxy without the aforementioned constraints. Recently, the so-called van der Waals epitaxy (vdWE), a new paradigm of epitaxial growth for III–V semiconductors, has been the focus of significant research interest, which is evidenced by a search in Google Scholar, leading to 12,200 hits in the years 2011 through 2015 [16–21]. Needless to say, this new research area of heteroepitaxy is mainly dictated by the surface properties of emerging 2D materials, which also have many novel electrical, optical, thermal, and mechanical properties [22–34].

Recently, different research groups already used few 2D atomic-layered materials as a semiconductor substrate for the growth of 3D semiconductors [35–37]. Among them, graphene, hexagonal boron nitride (hBN), transition metal dichalcogenides (TMDs), and topological insulator materials are the most frequently used ones. The main reason why these 2D materials are advantageous to be used as a semiconductor substrate is that the overgrown film materials float on top of the dangling-bonds-free 2D substrate surface instead of being rigidly bound to it, thereby mitigating lattice and thermal mismatch between 3D materials and the underlying 2D substrate. Besides, due to the crystalline surface with triangular lattice or honeycomb atomic arrangement, 2D materials are structurally compatible with many 3D semiconductors of zinc-blend (ZB), wurtzite (WZ), and diamond crystal structures. Furthermore, most of the 2D materials are thermally stable, which exhibit high decomposition temperature, thus making it an ideal material of choice for many fabrication processes.

The integration of III–V semiconductors on 2D materials is feasible using the epitaxial growth by molecular beam epitaxy (MBE) or metal organic chemical vapor phase deposition (MOCVD). Layered materials can be grown directly on the target substrates using either chemical vapor deposition (CVD) or MBE [38, 39]. Then, the layered material can be mechanically transferred onto any substrate after being grown if needed. Graphene is found to be one of the most popular 2D materials for van der Waals (vdW) epitaxial growth. A number of studies are undertaken to achieve high-quality MBE-grown GaAs nanowires (NWs) on a graphene/silicon substrate. High-density, vertical, coaxially heterostructured InAs/InGaAs NWs on graphene over a wide tunable ternary compositional range is demonstrated using MOCVD.

Using graphene as a 2D material for relieving thermal/lattice mismatch, the proof-of-principle demonstrations for the epitaxial growth of GaAs [36, 40], InAs [41], and GaN [23, 42, 43] on silicon substrates are already presented in several studies. Hence, these early demonstrations show a great promise of vdW heteroepitaxy for integrating III–V semiconductors on silicon using 2D materials as a buffer layer. Both nanostructures and thin films of these compound semiconductors are addressed by these preliminary studies. Most importantly, the results obtained from these studies motivate to realize high-quality epitaxial thin film or nanostructures of other III–V semiconductors, for example, InP, GaSb, InAs on silicon using graphene buffer layers. In such a way, the epitaxial growth on 2D material platform will have significant implications for a wide variety of optoelectronic devices, such as light-emitting devices [26, 42] and a new generation of solar cells for flexible applications [44].

Given the significant research interest in vdW heteroepitaxy for III–V compound semiconductors utilizing 2D materials, there is an obvious need for a comprehensive book chapter, which describes the recent progress and research activities. The aim of this chapter is to give a precise picture of the current status of vdW heteroepitaxy for 3D semiconductors on 2D materials, targeting mainly for optoelectronic device applications.

In this chapter, the difference between vdWE associated with layered materials and conventional epitaxy is first briefly discussed in Section 2. The work of several groups worked on nanowires grown on graphene using vdW epitaxial growth is then described in Section 3. Different types of grown 3D III–V thin films on 2D materials already demonstrated are mentioned in Section 4. Finally, a summary on the future prospects of the vdW epitaxy concept in case of growth of 3D materials on a layered material substrate is presented in Section 5.

2. vdWE vs. conventional epitaxy

VdWE was first introduced by Koma in 1984 where he successfully grew NbSe₂/MoS₂ system using vdW weak interactions [18, 45]. In this type of epitaxy, the growth is driven by the vdW forces between the 2D layers with neither surface dangling bonds nor passivation. These weak vdW interactions between the layers during the epitaxy releases any stress stored in the strained films, yielding high-quality material with reduced threading dislocation densities. This kind of epitaxy is different from the conventional growth where lattice-matching conditions are very important to have high-quality single-crystal semiconductors. As an intermediate type of epitaxy between vdWE and the conventional epitaxy, quasi van der Waals epitaxy (QvdWE) emerged recently by integrating 3D conventional semiconductors on layered substrates. In QvdWE, the interface interactions are not purely based on the vdW interaction but a midpoint where the dangling bonds of the grown 3D semiconductor have an effect on the epitaxial growth [46]. Importantly, the concept of QvdWE can be applied for the deposition of different types of grown structures including nanowires and thin films, as schematically shown in **Figure 1**. In the following sections, several demonstrations by different research teams worldwide for such structures utilizing QvdWE are discussed.

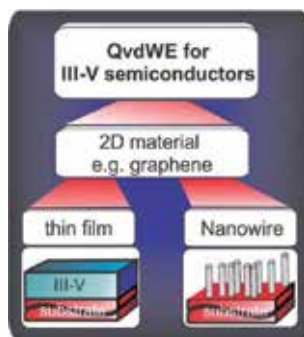


Figure 1. Different types of growth structures.

3. III-V nanowires QvdWE on layered materials

Munshi et al. proposed a generic atomic model that relates the epitaxial growth configurations of various III-V nanowires on graphene to the lattice mismatch between graphene and the grown semiconductor, as in **Figure 2(a–d)** [47]. The experimental verification of the model was undertaken through the use of molecular beam epitaxy (MBE). In this study, the self-catalyzed vapor liquid technique was used to create regular hexagonal cross-sectional shapes with

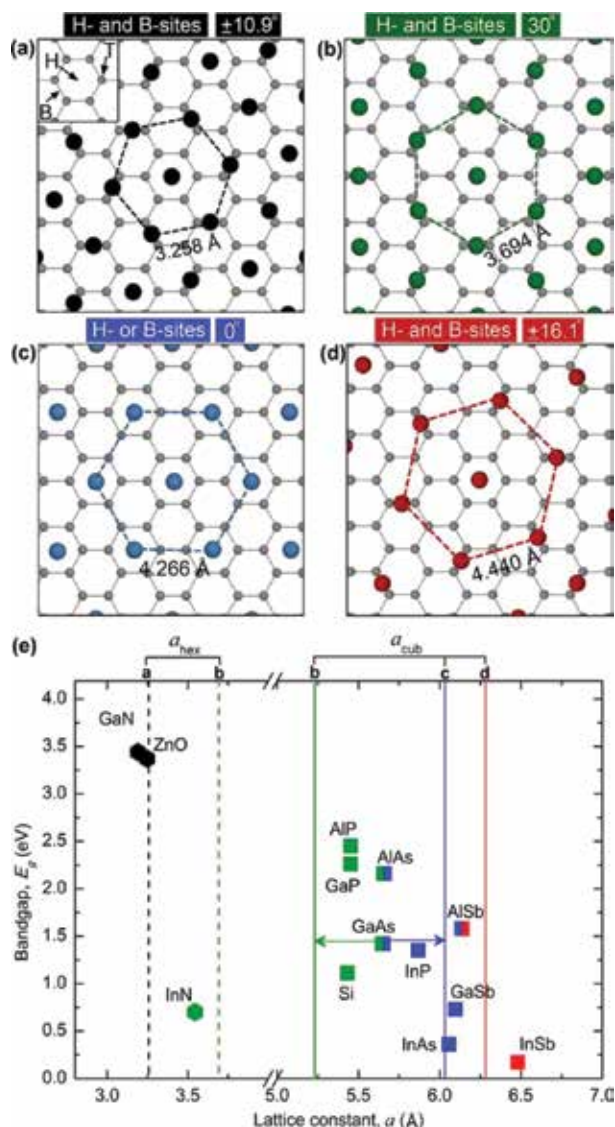


Figure 2. (a–d) Different possible arrangements of semiconductor atoms in the (111) plane of cubic crystal on graphene. (b) III/V semiconductor bandgaps versus lattice. The vertical lines represent the lattice matching condition for different III/V semiconductor arrangements in (a–d) on graphene. Reproduced with permission from Ref. [47].

uniformity in diameter and length. To increase the nanowire density on graphene, two-temperature growth strategy was used to facilitate the nucleation prior to the nanowire growth. A TEM image of GaAs nanowire grown on graphene shows that the bottom part of the nanowire has a mixture of ZB and WZ segments with twins and stacking faults, whereas the rest of the nanowire is nearly defect-free ZB configuration. In this demonstration, authors showed that despite the quite large mismatch in two different configurations, that is, cubic GaAs on graphene, 6.3% lattice mismatch for blue configuration and 8.2% for the green configuration (**Figure 2e**), they were still able to achieve high quality epitaxial growth, hinting that QvdWE can overcome the lattice mismatch constraints.

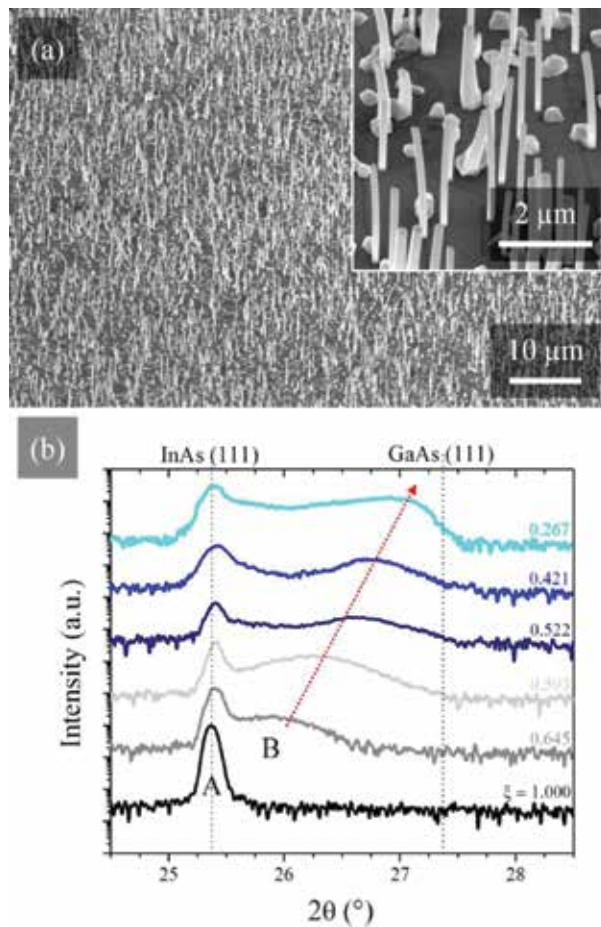


Figure 3. (a) Tilted scanning electron microscopy (SEM) image of $\text{In}_{0.39}\text{Ga}_{0.61}\text{As}$ NWs, with a higher magnification image shown in the inset. (b) Normalized XRD rocking curves of different In compositions plotted on a logarithmic scale. The B peak represents the position of the InGaAs peak. Reproduced with permission from Ref. [48].

Mohseni et al. have reported a self-organized method for the formation of coaxially heterostructured $\text{InAs}/\text{In}_x\text{Ga}_{1-x}\text{As}$ NWs, over a wide tunable ternary compositional range grown

directly on graphene substrates [48]. In this growth, metalorganic chemical vapor deposition (MOCVD) was used to integrate the III-V semiconductor on the graphene. The growth of InGaAs nanowires led to spontaneous separation of phase from the start of the growth, which eventually led to a well-defined InAs/In_xGa_{1-x}As ($0.2 < x < 1$) core-shell structure. The axial growth of InAs-In_xGa_{1-x}As ($0.2 < x < 1$) started without change in diameter of nanowires. After about 2 μm in height, those nanowires were grown in the form of core-shell structures. The shell composition of InAs-In_xGa_{1-x}As changes as a function of indium flow; however, the thickness of the shell and core and the start of nonsegregated InAs-In_xGa_{1-x}As are independent of the composition of indium (**Figure 3**). Moreover, the authors found out that no InGaAs phase segregation was observed when growing on MoS₂ or through the Au-assisted vapor-liquid-solid (VLS) technique on graphene. This work demonstrated that QvdWE of InAs on graphene could facilitate phase segregation phenomenon causing a self-organized InAs core/InGaAs shell nanowires. This phase segregation is driven mainly by lack of strain between InAs and graphene layers interface due to the weak vdW forces at this interface.

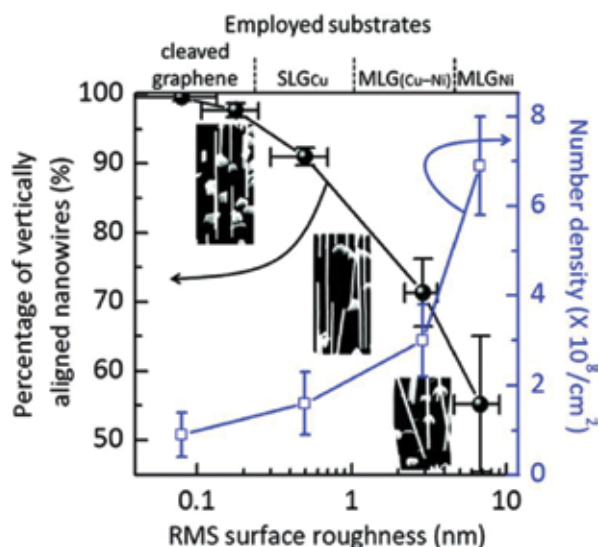


Figure 4. The percentage of vertically well-aligned InAs nanowires (black solid circles) and the density of nanowires (blue empty squares) relationship to the rms surface roughness of the graphene substrates. Reproduced with permission from Ref. [41].

Hong et al. found out that the density of InAs nanowires arrays integrated on graphene films increases with the number of graphene layers [41]. This is mainly because the nucleation of InAs is more likely on the surface potential wells formed by surface ledges in the graphene. However, the use of single-layer graphene as a substrate will encourage the growth of vertically well-aligned InAs arrays of nanowires with high levels of strong vdW attraction (**Figure 4**). The QvdW epitaxial relationship between InAs and graphene is confirmed by the InAs's hexagonal morphology with six ZB sidewall facets, aligned in a sixfold within a single domain of graphene.

QvdWE of III–V nanowires on 2D materials has brought a new momentum due to the introduction of new and attractive properties to the grown 1D nanostructure. However, the increased speed of investigation in developing nanostructures on 2D materials does not lack its issues and drawbacks. There is a challenge in accurate regulation of dopant circulation inside the semiconductor nanostructures, the direction of growth, dimensionality, and consistency in size. In addition, high surface recombination, poor thermal management, and highly resistive ohmic contacts are other few inherent aspects of nanostructures, which must be overcome to realize the potential of nanowires [49].

4. III–V thin films by QvdWE on 2D materials

4.1. GaAs thin films

The integration of III–V thin films on 2D materials opened a new and unique opportunity by releasing the lattice/thermal expansion mismatches between any 3D semiconductors and 2D material. Moreover, the weak vdW force of the layered materials allows reusing the 2D substrate multiple times by peeling off the grown semiconductors from the layered materials [42]. The demonstration of III–As-based thin films growth on graphene was reported by Alaskar et al. where ultra-smooth planar GaAs was deposited on silicon substrate using graphene as a buffer layer was performed, as presented in **Figure 5** [36]. In addition, the challenges that face the epitaxial growth of III–V semiconductors atop 2D materials, especially graphene, were highlighted. From a thermodynamics perspective of the growth, the low surface free energy of the layered materials yields an island growth mode where the surface of the layered 2D substrate is nonwetting.

The surface free energies of 3D semiconductors are two orders of magnitude higher than layered materials (**Table 1**), which make this type of epitaxial growth challenging. Indeed, engineering tricks are needed to overcome this issue [50–52].

The adsorption and migration energies of III–V-based atoms on graphene, as listed in **Table 2**, indicate that the growth of GaAs on graphene should be initiated with gallium for its higher adsorption and migration energies compared to arsenic, indium, or aluminum.

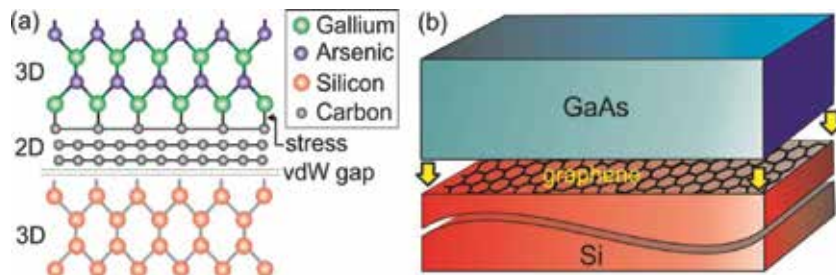
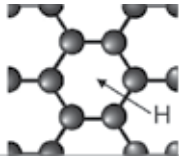
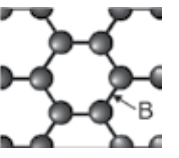
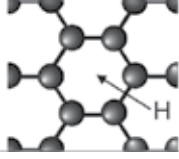
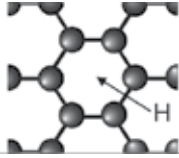


Figure 5. (a) The atomic geometry of GaAs/graphene/Si structure using (b) the schematic view of multilayered graphene used as a buffer layer for GaAs on silicon. Reproduced with permission from Ref. [36].

Materials	Surface free energy (mJ m^{-2})
Si (111)	1467 [53]
GaAs (111)	1697 [53]
Graphene	48
Multilayer graphene (MLG)	52
Bismuth selenide (Bi_2Se_3)	180 [54]

Note: Reproduced with permission from Ref. [36].

Table 1. The surface free energies of different 3D semiconductors and layered semiconductors.

Atom	Favored adsorption site	Adsorption energy E_b (eV)	Migration energy E_m (eV)
Gallium		1.5	0.05
Arsenic		1.3	0.21
Indium		1.3	0.06
Aluminum		1.7	0.03

Note: Reproduced with permission from Ref. [36].

Table 2. Adsorption and migration energies of Ga, As, In, and Al adatoms adsorbed on most favorable site of bilayer graphene based on density functional theory (DFT) calculation, taking into account vdW forces.

Utilizing the superior kinetic properties of gallium, the growth was initiated by two monolayers of Ga atoms at room temperature. This was followed by arsenic overpressure while elevating the growth temperature to 400°C and the deposition of 25 nm GaAs atop graphene

at a rate of 0.15 Å/s. The GaAs morphology showed a smooth surface with an RMS value of 0.6 nm. The crystal quality was characterized using both Raman spectroscopy and X-ray diffraction (XRD) [40]. The two GaAs Raman signature peaks at 268 (TO) and 292 (LO) cm^{-1} can be seen in the micro-Raman spectrum (**Figure 6a**). **Figure 6b** shows the rocking curve full width at half maximum (FWHM) value for the GaAs(111) plane around 245 arcsec (0.068°), indicating high defect density. This is still encouraging since the direct growth of GaAs with the same thickness shows much higher defect density [2].

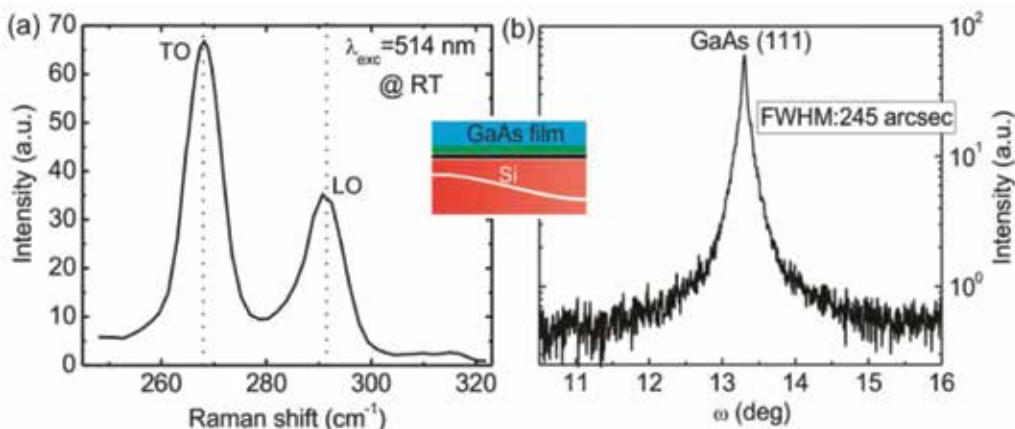


Figure 6. (a) Room temperature micro-Raman spectrum of GaAs on graphene/silicon shows TO and LO peaks at 268 and 292 cm^{-1} , respectively, where the TO peak is the dominant one. (b) XRD rocking-curve of GaAs (111) peak. Reproduced with permission from Ref. [36].

4.2. GaN thin films

So far, the thin-film growth of nitride-based semiconductors on graphene is more successful and promising compared to III-As semiconductors. This is mainly because of the high adsorption energy of nitrogen on graphene of (4.6 eV) compared to arsenic or phosphide [55, 56].

An IBM research group demonstrated the QvdWE growth of high-quality GaN on graphene/SiC substrates. The weak vdW forces between GaN and graphene help to reuse an expensive graphene/SiC substrate for multiple transfers and direct bonding to GaN/Si substrate enhanced by atomically smooth-released interface [42]. Compared to the conventional laser lift-off process, this novel technique is more advantageous since the extra surface treatment after releasing GaN layer on graphene is not required for further repetition. In addition, the high roughness of released surfaces out of laser lift-off process does not allow the released layer for direct bonding to other substrates. By using graphene grown on silicon carbide (SiC) substrate, the edged steps on the graphene surface were used to nucleate GaN on the inert graphene (**Figure 7**).

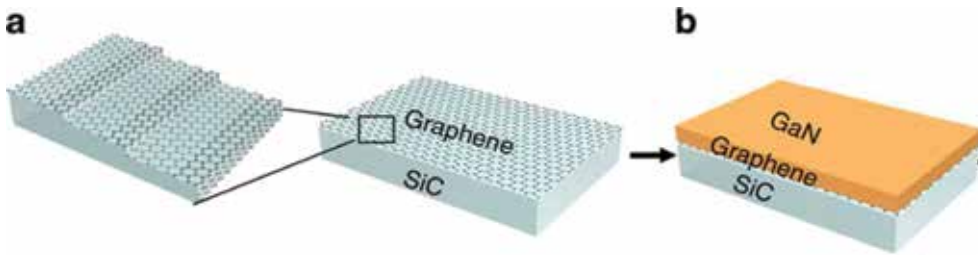


Figure 7. (a) Schematic showing the edged steps on the graphene/SiC surface. (b) Schematic of the final structure after GaN growth on graphene/SiC substrate. Reproduced with permission from Ref. [42].

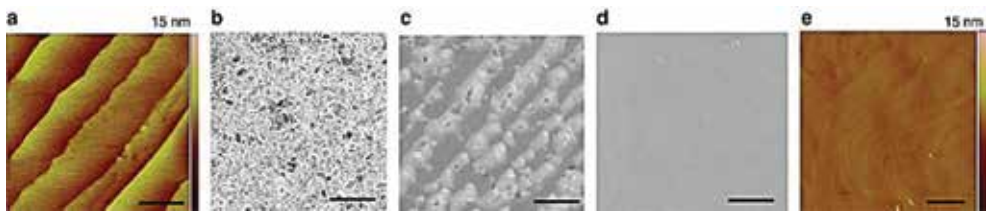


Figure 8. (a) AFM image of graphene/SiC surface. (b) SEM image of GaN films grown on graphene by two-step growth (580 and 1150°C). (c) SEM image of GaN films grown on graphene by one-step growth at 1100°C. (d) SEM image of GaN films grown on graphene by modified two-step growth (1100 and 1250°C). (e) AFM image of GaN films using the modified two-step method with RMS roughness of 3 Å. (scale bar, 10 μm). Reproduced with permission from Ref. [42].

Material	Substrate	Epitaxial mismatch (%)	Threading dislocation density (cm^{-3})	AFM RMS roughness (Å)	XRD (0002) $2\theta/\omega$ scan	
					2θ peak ($^\circ$)	FWHM (arcsec)
GaN	GaN	0	3×10^6	1.18	34.86	90 [57]
GaN	Al_2O_3	14	9×10^8	1.74	34.54	220 [58, 59]
GaN/AlN	Al_2O_3	14	6×10^8	2.14	34.22	380 [60]
GaN/AlN	Si(111)	17	3×10^9	>6.0	34.56	380 [60, 61]
GaN/AlN	SiC	3	2×10^9	1.80	34.55	200 [62]
GaN	Graphene/SiC	23	1×10^9	2.98	34.57	222 [42]

Note: Reproduced with permission from Ref. [42].

Table 3. Comparison of GaN/graphene crystalline quality to GaN films grown on other substrates.

Direct QvdWE of high-quality single-crystalline GaN on epitaxial graphene/SiC substrates was performed through an optimized two-step growth temperature. Using low nucleation temperature (580°C) will form 3D-faceted GaN clusters while using one-step growth of high temperature (1100°C) will form continuous GaN stripes aligned along the SiC steps. To obtain a smooth GaN surface, the nucleation preferentially formed at 1100°C along the periodic step

edges, that are 5–10 nm height and 5–10 μm apart, then the growth advanced laterally to coalesce at a higher temperature of 1250°C (**Figure 8a–d**). The resulted GaN has a root mean square surface roughness of 3 Å (**Figure 8e**). The average dislocation density of the grown GaN on graphene was reported to be $\sim 1 \times 10^9 \text{ cm}^{-2}$, which is comparable to AlN-buffer-assisted GaN films that were grown on other substrates using MOCVD (**Table 3**).

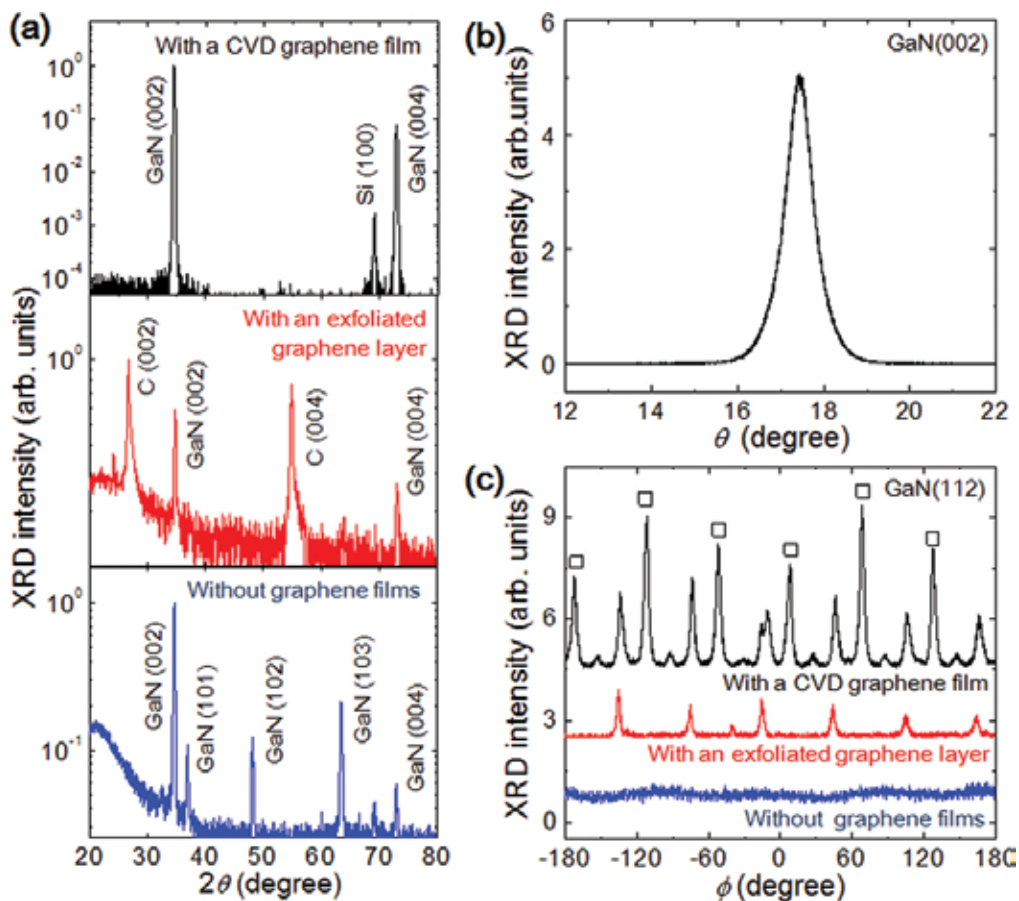


Figure 9. X-ray diffraction (XRD) scans of GaN films grown on (a) CVD graphene/SiO₂ substrates, (b) grown on exfoliated graphene layer/SiO₂ and (c) grown directly on SiO₂. (d) XRD rocking curve of GaN films grown on CVD graphene/SiO₂. (e) ϕ -Scans of GaN films grown on CVD graphene SiO₂, on exfoliated graphene layers/SiO₂, and directly on SiO₂ without graphene layers. Reproduced with permission from Ref. [43].

Chung et al. reported the growth of GaN layer on graphene/fused silica substrate. Compared to the growth of GaN on fused silica directly, GaN grown on graphene using interlayer ZnO nanowalls as a buffer layer showed a significant improvement [43]. To facilitate the growth on graphene, it was exposed to oxygen plasma at 30 W and 100 mT of oxygen for 1 s. This treatment increased the wettability of the graphene surface for a proceeding GaN/ZnO layers. In this study, MOCVD was used to grow ZnO walls first followed by three-step growth of GaN. The

height and density of the ZnO nanowalls were 200–400 nm and 10^{10} cm², respectively. The first step of GaN was at a low temperature 560–600°C to prevent the reaction between GaN and underlayer ZnO. Second step was to grow at a higher temperature of 1100°C to promote lateral growth of GaN under hydrogen ambient gas. Finally, the growth at 1200°C was to smoothen the surface and achieve a good-quality GaN layers. The crystal quality of GaN grown on graphene, GaN grown on exfoliated graphene and GaN grown on SiO₂ were examined by XRD. XRD spectra of the GaN/graphene peaks correspond to the (002) and (004) orientations of WZ GaN. However, multiple peaks were observed when no graphene layer was used. For GaN films grown on the substrates with CVD graphene films, the FWHM value of the X-ray diffraction rocking curves was as small as 0.8°, as shown in **Figure 9**.

5. Applications of QvdWE of III/V semiconductors on layered materials

Optoelectronic devices have been fabricated based on the integration of III/V semiconductors on 2D materials [26, 44]. In the following, two examples of such devices are presented. The first is the demonstration of a blue light-emitting diode (LED) in which an IBM group successfully reused the same substrate of graphene/SiC multiple times to grow GaN by depositing a nickel (Ni) stressor on top of the GaN that has stronger adhesion to the GaN than the weak vdW attraction to graphene/SiC substrate [42]. Multiple quantum wells (MQW) of InGaN/GaN sandwiched between p-GaN and n-GaN layers were grown to create the blue LED device. The transmission electron microscope (TEM) image of the LED stack is shown in **Figure 10(a–d)**. The *I–V* curve of the device shows a diodic behavior. Moreover, the electroluminescence spectrum confirming the blue emission at 440 nm of the LED is shown in **Figure 10f–g**.

The second application is a solar cell demonstrated by other group used radial and axial junctions of InGaAs/InAs nanowires grown epitaxially on multilayer graphene [63]. This solar cell is based on dense arrays of InGaAs nanowires, where graphene serves as the conductive back contact and growth template for vdW epitaxial assembly of vertical nanowires. In this study, three different junctions are schematically represented in **Figure 11a–c**. The first set shows an axial junction of n-InGAs and p-InGAs doped by Si and Zn, respectively. The second set is fabricated using radial InGaAs p-n junction. Finally, the third set is same as the second but with a shell of p-GaAs passivation layer. The device contacts are shown in **Figure 11d**. Among the three sets, the last one demonstrates a core-shell p-n junction In_{0.25}Ga_{0.75}As nanowire arrays with conversion efficiency of 2.51%. The figures of merits, such as open circuit voltage (V_{oc}), short circuit current density (J_{sc}), fill factor (FF), the power conversion efficiency (PCE), and the ideality factor (n) for these three sets of devices are summarized in **Table 4**. Radial junction has higher short circuit currents hinting that carriers generated at various lengths along the NW are effectively swept by the p-n junction built-in electric field. Furthermore, the GaAs passivation shell quenched surface defects and the SRH recombination centers.

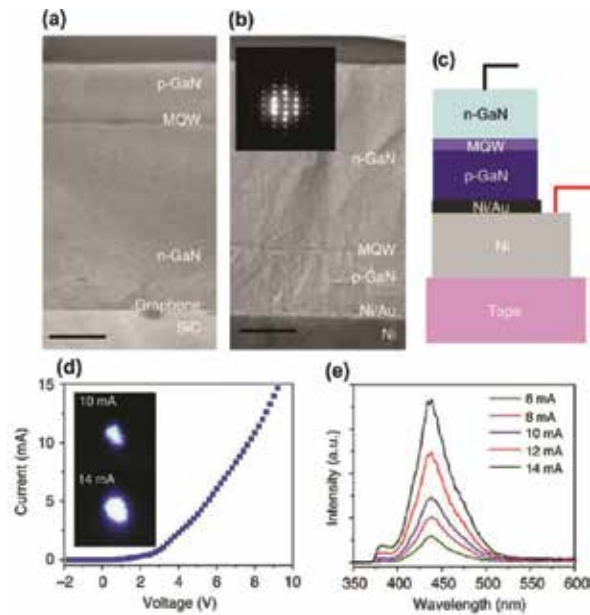


Figure 10. (a) Cross-sectional TEM image shows (p-GaN/MQW/n-GaN) LED stacks grown on a graphene/SiC substrate (scale bar, 1 μm). (b) TEM image of a released LED stack from a graphene/SiC substrate: n-GaN/MQW/p-GaN/Ni. A selected area electron diffraction pattern is displayed in an inset. (c) Schematic of a transferred visible LED device on the tape. (d) I–V curve of a transferred LED stack. (e) Electroluminescence (EL) spectra of a transferred LED stack as a function of injection current. Reproduced with permission from Ref. [42].

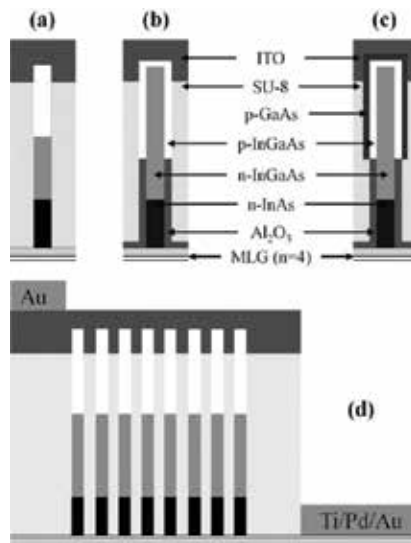


Figure 11. (a–c) Schematic structure of the three different nanowires based solar cell junctions. (d) Schematic structure of the device including the metallic contacts. Reproduced with permission from Ref. [63].

Device group	Device structure	V_{oc} (V)	J_{sc} (mA/cm ²)	FF (%)	PCE (%)	n
A	Axial junction	0.18	13.14	38.43	0.91	1.93
B	Radial junction	0.20	16.20	40.24	1.32	1.91
C	Radial junction with passivation	0.26	17.16	55.32	2.51	1.54

Note: Reproduced with permission from Ref. [63].

Table 4. The main performance and figure of merits obtained from the NW array on graphene solar cell presented in this study.

6. Future directions and conclusion

In summary, this chapter has provided a detailed overview of the recent progress of the QvdW heteroepitaxial growth of III–V semiconductors on layered materials. The growth demonstrations of several III–V semiconductors, such as GaAs, GaN, InAs, are mainly included in this chapter. Most of these demonstrations used graphene as a buffer 2D material. Many studies have reported nonplanar nanostructures, for example nanowire arrays, whereas few of them are focused on planar structures, for example thin films. The suitability of such grown structures in various applications in electronics, photonics, and optoelectronics is also discussed in this chapter.

The more versatility of the vdWE over conventional heteroepitaxy is the possibility to achieve epitaxial growth of III–V semiconductors without the strict requirements of lattice matching. On top of that, the idea of vdWE can be applied to rather a wide variety of materials. The materials extend from 1D to 3D and even to organic. In such a way, it is possible to integrate 3D/2D to create new types of junctions. Such inherent features of vdWE could have widespread consequences and real-life applications. These are the reasons why the research area of vdWE is gaining extensive interest recently in the research community.

In spite of great technological advances and efforts, nanostructure-based devices are still suffering from several carrier loss mechanisms, surface-states induced band bending, Fermi level pinning, poor ohmic contacts, and controlled incorporation of n - and p -type dopants. Due to the poor performance caused by these aforementioned issues, thin films or planar structures are still gaining more attention. In this context, vdWE, historically developed for planar structures, can be a great solution on the way toward successful heteroepitaxial growth on a target substrate. However, the main challenge is the low surface energy of the 2D materials. Therefore, finding a way to increase the wettability and the surface free energy of the 2D materials will make integration much easier in the future.

Although most of the literature studies so far are focusing on using graphene, we consider other 2Ds such as TMDs have the potential to be a good fit for this integration, as long as they are stable at high temperature. The reason is that they have higher surface free energy, can be monolithically integrated at UHV chamber making the interfaces purer from any organics, and

would open a new window for creating new type of junctions between III-V and 2D materials without the need for unpractical transfer processes.

Author details

Yazeed Alaskar^{1,2*}, Shamsul Arafin³, Isaac Martinez-Velis¹ and Kang L. Wang¹

*Address all correspondence to: alaskar@ucla.edu

1 Department of Electrical Engineering, University of California at Los Angeles, CA, USA

2 National Nanotechnology Research Center, King Abdulaziz City for Science and Technology, Riyadh, Saudi Arabia

3 Department of Electrical and Computer Engineering, University of California at Santa Barbara, CA, USA

References

- [1] Akiyama M, Kawarada Y, Ueda T, Nishi S, Kaminishi K: Growth of high quality GaAs layers on Si substrates by MOCVD. *Journal of Crystal Growth*. 1986;77:490–7. DOI: 10.1016/0022-0248(86)90342-8
- [2] Bolkhovityanov YB, Pchelyakov OP: III–V compounds-on-Si: heterostructure fabrication, application and prospects. *Open Nanoscience Journal*. 2009;3:20–33. DOI: 10.2174/1874140100903010020
- [3] Bringans RD, Biegelsen DK, Swartz L-E, Ponce FA, Tramontana JC: Use of ZnSe as an interlayer for GaAs growth on Si. *Applied Physics Letters*. 1992;61:195–7. DOI: 10.1063/1.108216
- [4] Bringans RD, Olmstead MA, Uhrberg RIG, Bachrach RZ: Formation of the interface between GaAs and Si: implications for GaAs-on-Si heteroepitaxy. *Applied Physics Letters*. 1987;51:523–5. DOI: 10.1063/1.98386
- [5] Bringans RD, Olmstead MA, Ponce FA, Biegelsen DK, Krusor BS, Yingling RD: The effect of a Ga prelayer on the beginning of GaAs epitaxy on Si. *Journal of Applied Physics*. 1988;64:3472–5. DOI: 10.1063/1.341481
- [6] Lee MK, Horng RH, Wu DS, Chen PC: Improvements in the heteroepitaxy of GaAs on Si by incorporating a ZnSe buffer layer. *Applied Physics Letters*. 1991;59:207–9. DOI: 10.1063/1.105967

- [7] Wang WI: Molecular beam epitaxial growth and material properties of GaAs and AlGaAs on Si (100). *Applied Physics Letters*. 1984;44:1149–51. DOI: 10.1063/1.94673
- [8] Xu HY, Guo YN, Wang Y, Zou J, Kang JH, Gao Q, Tan HH, Jagadish C: Effects of annealing and substrate orientation on epitaxial growth of GaAs on Si. *Journal of Applied Physics*. 2009;106:083514. DOI: 10.1063/1.3248372
- [9] Yamaguchia M: Dislocation density reduction in heteroepitaxial III–V compound films on Si substrates for optical devices. *Journal of Material Research*. 1991;6:376–84. DOI: 10.1557/JMR.1991.0376
- [10] del Alamo JA: Nanometre-scale electronics with III–V compound semiconductors. *Nature*. 2011;479:317–23. DOI: 10.1038/nature10677
- [11] Palmer JE, Saitoh T, Yodo T, Tamura M: Growth and characterization of GaSe and GaAs/GaSe on As-passivated Si(111) substrates. *Journal of Applied Physics*. 1993; 74:7211–22. DOI: 10.1063/1.355038
- [12] Palmer JE, Saitoh T, Yodo T, Tamura M: Growth and characterization of GaAs/GaSe/Si heterostructures. *Japanese Journal of Applied Physics*. 1993;32:1126–9. DOI: 10.1143/JJAP.32.L1126
- [13] Palmer JE, Saitoh T, Yodo T, Tamura M, In: Gumbs G, Luryi S, Weiss B, Wicks GW, editors. Growth and characterization of GaSe and GaAs/GaSe heterostructures on As-passivated Si substrates. In: *MRS Symposium Proceedings*. 1994;326:33–38. DOI: 10.1557/PROC-326-33.
- [14] Palmer JE, Saitoh T, Yodo T, Tamura M: GaAs on Si(111) with a layered structure GaSe buffer layer. *Journal of Crystal Growth*. 1995;150:685–90. DOI: 10.1016/0022-0248(95)80296-O
- [15] Rumaner LE, Olmstead MA, Ohuchi FS: Interaction of GaSe with GaAs(111): formation of heterostructures with large lattice mismatch. *Journal of Vacuum Science and Technology B*. 1998;16:977–88. DOI: 10.1116/1.590055
- [16] Jaegermann W, Klein A, Pettenkofer C. Electronic properties of van der Waals-epitaxy films and interfaces. In: Hughes HP, Starnberg HI, editors. *Electron Spectroscopies Applied to Low-Dimensional Materials. Physics and Chemistry of Materials with Low-Dimensional Structures*. 24: Kluwer, Dordrecht, The Netherlands; 2002. pp. 317–402.
- [17] Utama MI, Zhang Q, Zhang J, Yuan Y, Belarrie FJ, Arbiol J, Xiong Q: Recent developments and future directions in the growth of nanostructures by van der Waals epitaxy. *Nanoscale*. 2013;5:3570–88. DOI: 10.1039/c3nr34011b
- [18] Koma A, Sunouchi K, Miyajima T: Nanometer structure electronics fabrication and characterization of heterostructures with subnanometer thickness. *Microelectronic Engineering*. 1984;2:129–36. DOI: 10.1016/0167-9317(84)90057-1

- [19] Ueno K, Takeda N, Sasaki K, Koma A: Investigation of the growth mechanism of layered semiconductor GaSe. *Applied Surface Science*. 1997;113–114:38–42. DOI: 10.1016/S0169-4332(96)00837-9
- [20] Ueno T, Yamamoto H, Saiki K, Koma A: Van der Waals epitaxy of metal dihalide. *Applied Surface Science*. 1997;113–114:33–7. DOI: 10.1016/S0169-4332(96)00770-2
- [21] Koma A: Van der Waals epitaxy for highly lattice-mismatched systems. *Journal of Crystal Growth*. 1999;201–202:236–41. DOI: 10.1016/S0022-0248(98)01329-3
- [22] Bonaccorso F, Sun Z, Hasan T, Ferrari AC: Graphene photonics and optoelectronics. *Nature Photonics*. 2010;4:611–22. DOI: 10.1038/nphoton.2010.186
- [23] Chung K, Lee CH, Yi GC: Transferable GaN layers grown on ZnO-coated graphene layers for optoelectronic devices. *Science*. 2010;330:655–7. DOI: 10.1126/science.1195403
- [24] Geim AK: Graphene: status and prospects. *Science*. 2009;324:1530–4. DOI: 10.1126/science.1158877
- [25] Kim RH, Bae MH, Kim DG, Cheng H, Kim BH, Kim DH, Li M, Wu J, Du F, Kim HS, Kim S, Estrada D, Hong SW, Huang Y, Pop E, Rogers JA: Stretchable, transparent graphene interconnects for arrays of microscale inorganic light emitting diodes on rubber substrates. *Nano Letters*. 2011;11:3881–6. DOI: 10.1021/nl202000u
- [26] Lee CH, Kim YJ, Hong YJ, Jeon SR, Bae S, Hong BH, Yi GC: Flexible inorganic nanostructure light-emitting diodes fabricated on graphene films. *Advanced Materials*. 2011;23:4614–9. DOI: 10.1002/adma.201102407
- [27] Lee G-H, Yu Y-J, Cui X, Petrone N, Lee C-H, Choi MS, Lee D-Y, Lee C, Yoo WJ, Watanabe K, Taniguchi T, Nuckolls C, Kim P, Hone J: Flexible and transparent MoS₂ field-effect transistors on hexagonal boron nitride-graphene heterostructures. *ACS Nano*. 2013;7:7931–6. DOI: 10.1021/nn402954e
- [28] Novoselov KS, Jiang Z, Zhang Y, Morozov SV, Stormer HL, Zeitler U, Maan JC, Boebinger GS, Kim P, Geim AK: Room-temperature quantum Hall effect in Graphene. *Science*. 2007;315:1379. DOI: 10.1126/science.1137201
- [29] Chae SJ, Günes F, Kim KK, Kim ES, Han GH, Kim SM, Shin H-J, Yoon S-M, Choi J-Y, Park MH, Yang CW, Pribat D, Lee YH. Synthesis of large-area graphene layers on nickel film by chemical vapor deposition. *Advanced Materials*. 2009;21:2328–2333. DOI: 10.1002/adma.200803016
- [30] Reina A, Thiele S, Jia X, Bhaviripudi S, Dresselhaus MS, Schaefer JA, Kong J: Growth of large-area single- and Bi-layer graphene by controlled carbon precipitation on polycrystalline Ni surfaces. *Nano Research*. 2010;2:509–16. DOI: 10.1007/s12274-009-9059-y
- [31] Zhang Y, Gao T, Xie S, Dai B, Fu L, Gao Y, Chen Y, Liu M, Liu Z: Different growth behaviors of ambient pressure chemical vapor deposition graphene on Ni(111) and Ni

- films: a scanning tunneling microscopy study. *Nano Research*. 2012;5:402–11. DOI: 10.1007/s12274-012-0221-6
- [32] Yan Z, Lin J, Peng Z, Sun Z, Zhu Y, Li L, Xiang C, Samuel EL, Kittrell C, Tour JM: Toward the synthesis of wafer-scale single-crystal graphene on copper foils. *ACS Nano*. 2012;6:9110–7. DOI: 10.1021/nl303352k
- [33] Gao L, Guest JR, Guisinger NP: Epitaxial graphene on Cu(111). *Nano Letters*. 2010;10:3512–6. DOI: 10.1021/nl1016706
- [34] Geim AK, Novoselov KS: The rise of graphene. *Nature Materials*. 2007;6:183–91. DOI: 10.1038/nmat1849
- [35] Löher T, Tomm Y, Pettenkofer C, Jaegermann W: Van der Waals epitaxy of three-dimensional CdS on the two-dimensional layered substrate MoTe₂(0 0 1). *Applied Physics Letters*. 1994;65:555–7. DOI: 10.1063/1.112294
- [36] Alaskar Y, Arafin S, Wickramaratne D, Zurbuchen MA, He L, McKay J, Lin Q, Goorsky MS, Lake RK, Wang KL: Towards van der Waals epitaxial growth of GaAs on Si using a graphene buffer layer. *Advanced Functional Materials*. 24:6629–38. DOI: 10.1002/adfm.201400960
- [37] Löher T, Tomm Y, Klein A, Su D, Pettenkofer C, Jaegermann W: Highly oriented layers of the three-dimensional semiconductor CdTe on the two-dimensional layered semiconductors MoTe₂ and WSe₂. *Journal of Applied Physics*. 1996;80:5718–22. DOI: 10.1063/1.363624
- [38] Bae S, Kim H, Lee Y, Xu X, Park J-S, Zheng Y, Balakrishnan J, Lei T, Kim HR, Song YI, Kim Y-J, Kim KS, Özyilmaz B, Ahn J-H, Hong BH, Iijima S: Roll-to-roll production of 30-inch graphene films for transparent electrodes. *Nature Nanotechnology*. 2010;5:574–8. DOI: 10.1038/nnano.2010.132
- [39] Hawaldar R, Merino P, Correia MR, Bdikin I, Grácio J, Méndez J, Martín-Gago JA, Singh MK: Large-area high-throughput synthesis of monolayer graphene sheet by hot filament thermal chemical vapor deposition. *Scientific Reports*. 2012;2:682. DOI: 10.1038/srep00682
- [40] Alaskar Y, Arafin S, Lin Q, Wickramaratne D, McKay J, Norman AG, Zhang Z, Yao L, Ding F, Zou J, Goorsky MS, Lake RK, Zurbuchen MA, Wang KL: Theoretical and experimental study of highly textured GaAs on silicon using a graphene buffer layer. *Journal of Crystal Growth*. 2015;425:268–73. DOI: 10.1016/j.jcrysgro.2015.02.003
- [41] Hong YJ, Lee WH, Wu Y, Ruoff RS, Fukui T: Van der Waals epitaxy of InAs nanowires vertically aligned on single-layer graphene. *Nano Letters*. 2012;12:1431–6. DOI: 10.1021/nl204109t
- [42] Kim J, Bayram C, Park H, Cheng CW, Dimitrakopoulos C, Ott JA, Reuter KB, Bedell SW, Sadana DK: Principle of direct van der Waals epitaxy of single-crystalline films on epitaxial graphene. *Nature Communications*. 2014;5: 4836. DOI: 10.1038/ncomms5836

- [43] Chung K, In Park S, Baek H, Chung J-S, Yi G-C: High-quality GaN films grown on chemical vapor-deposited graphene films. *NPG Asia Materials*. 2012;4:e24. DOI: 10.1038/am.2012.45
- [44] Yoon J, Jo S, Chun IS, Jung I, Kim H-S, Meitl M, Menard E, Li X, Coleman JJ, Paik U, Rogers JA: GaAs photovoltaics and optoelectronics using releasable multilayer epitaxial assemblies. *Nature*. 2010;465:329–33. DOI: 10.1038/nature09054
- [45] Ueno K, Shimada T, Saiki K, Kama A: Heteroepitaxial growth of layered transition metal dichalcogenides on Sulfur terminated GaAs surface. *Applied Physics Letters*. 1990;56:327–9. DOI: 10.1063/1.102817
- [46] Lee WC, Kim K, Park J, Koo J, Jeong HY, Lee H, Weitz DA, Zettl A, Takeuchi S: Graphene-templated directional growth of an inorganic nanowire. *Nature Nanotechnology*. 2015;10:423–8. DOI: 10.1038/nnano.2015.36
- [47] Munshi AM, Dheeraj DL, Fauske VT, Kim DC, van Helvoort AT, Fimland BO, Weman H: Vertically aligned GaAs nanowires on graphite and few-layer graphene: generic model and epitaxial growth. *Nano Letters*. 2012;12:4570–6. DOI: 10.1021/nl3018115
- [48] Mohseni PK, Behnam A, Wood JD, English CD, Lyding JW, Pop E, Li X: In_xG_{1-x}As nanowire growth on graphene: van der Waals epitaxy induced phase segregation. *Nano Letters*. 2013;13:1153–61. DOI: 10.1021/nl304569d
- [49] Arafin S, Liu X, Mi Z: Review of recent progress of III-nitride nanowire lasers. *Journal of Nanophotonics*. 2013;7:074599. DOI: 10.1117/1.jnp.7.074599
- [50] Wang S, Zhang Y, Abidi N, Cabrales L: Wettability and surface free energy of graphene films. *Langmuir*. 2009;25:11078–81. DOI: 10.1021/la901402f
- [51] Al Balushi ZY, Miyagi T, Lin Y-C, Wang K, Calderin L, Bhimanapati G, Redwing JM, Robinson JA: The impact of graphene properties on GaN and AlN nucleation. *Surface Science*. 2015;634:81–8. DOI: 10.1016/0022-0248(86)90342-8
- [52] Liu X, Wang C-Z, Hupalo M, Lin H-Q, Ho K-M, Tringides M: Metals on graphene: interactions, growth morphology, and thermal stability. *Crystals*. 2013;3:79. DOI: 10.3390/cryst3010079
- [53] Zdyb A, Olchowik JM, Mucha M: Dependence of GaAs and Si surface energy on the misorientation angle of crystal planes. *Materials Science-Poland*. 2006;24:1109–14.
- [54] He X, Zhou W, Wang ZY, Zhang YN, Shi J, Wu RQ, Yarmoff JA: Surface termination of cleaved Bi₂Se₃ investigated by low energy ion scattering. *Physical Review Letters*. 2013;110:156101. DOI: 10.1103/PhysRevLett.110.156101
- [55] Nakada K, Ishii A. DFT calculation for adatom adsorption on graphene. In: Gong JR, editor. *Graphene Simulation Rijeka*. Croatia: InTech; 2011.
- [56] Seo TH, Park AH, Park S, Kim YH, Lee GH, Kim MJ, Jeong MS, Lee YH, Hahn Y-B, Suh E-K: Direct growth of GaN layer on carbon nanotube-graphene hybrid structure and

- its application for light emitting diodes. *Scientific Reports*. 2015;5:7747. DOI: 10.1038/srep07747
- [57] Bayram C, Vashaei Z, Razeghi M: Room temperature negative differential resistance characteristics of polar III-nitride resonant tunneling diodes. *Applied Physics Letters*. 2010;97:092104. DOI: 10.1063/1.3484280
- [58] Bayram C, Vashaei Z, Razeghi M: AlN/GaN double-barrier resonant tunneling diodes grown by metal-organic chemical vapor deposition. *Applied Physics Letters*. 2010;96:042103. DOI: 10.1063/1.3294633
- [59] Khoury M, Courville A, Poulet B, Teisseire M, Beraudo E, Rashid MJ, Frayssinet E, Damilano B, Semond F, Tottereau O, Vennéguès P: Imaging and counting threading dislocations in c-oriented epitaxial GaN layers. *Semiconductor Science and Technology*. 2013;28:035006. DOI: 10.1088/0268-1242/28/3/035006
- [60] Bayram C, Pau JL, McClintock R, Razeghi M: Delta-doping optimization for high quality p-type GaN. *Journal of Applied Physics*. 2008;104:083512. DOI: 10.1063/1.3000564
- [61] Engin A, Mustafa KO, Ali T, Suleyman O, Ekmel O: Buffer optimization for crack-free GaN epitaxial layers grown on Si(111) substrate by MOCVD. *Journal of Physics D: Applied Physics*. 2008;41:155317.
- [62] Reitmeier ZJ, Einfeldt S, Davis RF, Zhang X, Fang X, Mahajan S: Surface and defect microstructure of GaN and AlN layers grown on hydrogen-etched 6H-SiC(0001) substrates. *Acta Materialia*. 2010;58:2165–75. DOI: 10.1016/j.actamat.2009.12.002
- [63] Mohseni PK, Behnam A, Wood JD, Zhao X, Yu KJ, Wang NC, Rockett A, Rogers JA, Lyding JW, Pop E, Li X: Monolithic III-V nanowire solar cells on graphene via direct van der Waals epitaxy. *Advanced Materials*. 2014;26:3755–60. DOI: 10.1002/adma.201305909

Two-Dimensional Transition Metal Dichalcogenides for Electrocatalytic Energy Conversion Applications

Fengwang Li and Mianqi Xue

Additional information is available at the end of the chapter

<http://dx.doi.org/10.5772/63947>

Abstract

Electrocatalytic energy conversion using renewable power sources is one of the most promising ways for energy storage and energy utilization in the new century. Specific catalysts are needed to improve the electrocatalytic reactions. Two-dimensional transition metal dichalcogenides (2D TMDs) have attracted considerable interest as alternatives to noble metal catalysts due to their unique electronic structure and high catalytic activity. Over the past years, a great number of 2D TMD-based catalysts have been explored for various electrocatalytic reactions, such as the hydrogen evolution reaction (HER) as a half reaction of water splitting and CO₂ reduction reaction as part of artificial photosynthesis. This chapter provides an overview of recent progress on TMD-based electrocatalysts, including mechanism understanding of the advantages of 2D materials, especially 2D TMDs and the up-to-date synthesizing approaches of TMDs, and state-of-the-art applications of TMDs in electrocatalytic reactions, and finally outlines the current challenges and future opportunities.

Keywords: 2D materials, transition metal dichalcogenide, electrocatalysis, water splitting, hydrogen evolution reaction, CO₂ reduction reaction, artificial photosynthesis

1. Introduction

Owing to the rapid development of modern society, the enormous demand for energy has become one of the most important issues affecting human life since twentieth century. However, the excessive reliance on the combustion of nonrenewable fossil fuels, such as coal, petroleum, and natural gas, brings not only ecological and environmental problems but also harsh ongoing impacts on the global economy and society [1]. Hence, it has become one of the

crucial challenges faced with our society to develop reliable and “green” approaches for energy conversion and storage.

Electrocatalytic energy conversion utilizing renewable power sources (e.g. solar and wind energy) is regarded as one of the most efficient and cleanest energy conversion pathways [2–5]. Furthermore, the converted energy is easy to store and use as clean energy or chemical stock. Specifically, the involvement of the electrocatalytic hydrogen evolution reaction (HER) in the cathode and the oxygen evolution reaction (OER) in the anode can efficiently drive water splitting and finally convert the electrical energy into chemical form, that is, hydrogen energy [6–8]. When CO_2 is reduced in the cathode while OER happens in the anode, which is the scheme of so-called artificial photosynthesis, it converts the electrical energy into chemical forms stocked in CO or hydrocarbons [9–11]. Hence, in such context, it is urgently required in both academic and industrial fields to build our power-supply systems based on electrocatalysis, amongst which developing efficient electrocatalysts for the aforementioned reactions is the most fundamental but vital task in this endeavour.

Two-dimensional (2D) materials have been widely studied for their important physical and chemical properties over the last several decades [12]. Since the recent discovery of graphene [13], 2D materials have gained extensive attention since they exhibit novel and unique physical, chemical, mechanical, and electronic properties [3, 14–19]. In the abundant family of 2D materials, transition metal dichalcogenides (TMDs) have attracted significant interest and become the focus of fundamental research and technological applications due to their unique crystal structures, a wide range of chemical compositions, and a variety of material properties [5, 14, 20–24]. Recently, TMDs have emerged as one kind of efficient electrocatalysts for energy-related reactions, such as the HER and CO_2 reduction reaction [15, 21, 25–29].

2. Properties of 2D TMDs and advantages for electrocatalysis

2D TMDs are usually denoted as MX_2 , where M is a transition metal of groups 4–10 (e.g. Ti, V, Co, Ni, Nb, Mo, Hf, Ta, and W) and X is a chalcogen (S, Se, and Te). MX_2 constructs layered structures by the formation of X-M-X, three layers of atoms with the chalcogen atoms in two hexagonal planes separated by a plane of metal atoms, and the valence states of metal (M) and chalcogen (X) atoms are +4 and -2, respectively (**Figure 1a**) [30–32]. There are two combination modes of metal and chalcogen elements in MX_2 , trigonal prismatic or octahedral phases, which are referred to as monolayer 2H and 1T- MX_2 , respectively (**Figure 1b–d**). Transition metals in different groups have different numbers of *d*-electrons, which fill up the non-bonding *d* bands to different levels, resulting in varied electronic properties ranging from insulators such as HfS_2 , semiconductors such as MoS_2 and WS_2 , semimetals such as WTe_2 and TiSe_2 , to true metals such as NbS_2 and VSe_2 . A few bulk TMDs such as NbSe_2 and TaS_2 exhibit low-temperature phenomena including superconductivity, charge density wave (CDW), and Mott transition [14]. When these materials are exfoliated into mono- or few layers, their properties largely preserve and also present additional characteristics due to confinement effects [14, 15, 27, 33]. The mono- or few-layer TMDs have thickness at the atomic level or significantly lower than their edge lengths and thus appear like sheets (namely, nanosheets). The atomic-thin nature

endows them with many distinctive properties with respect to their bulk counterparts, such as high specific surface area owing to planar structures, abundant uncoordinated surface atoms, excellent solution dispersity, and mechanical flexibility. These features make the 2D TMDs ideal candidates (or component parts for hybrid structures) with improved electrocatalytic performance to substitute their parent materials.

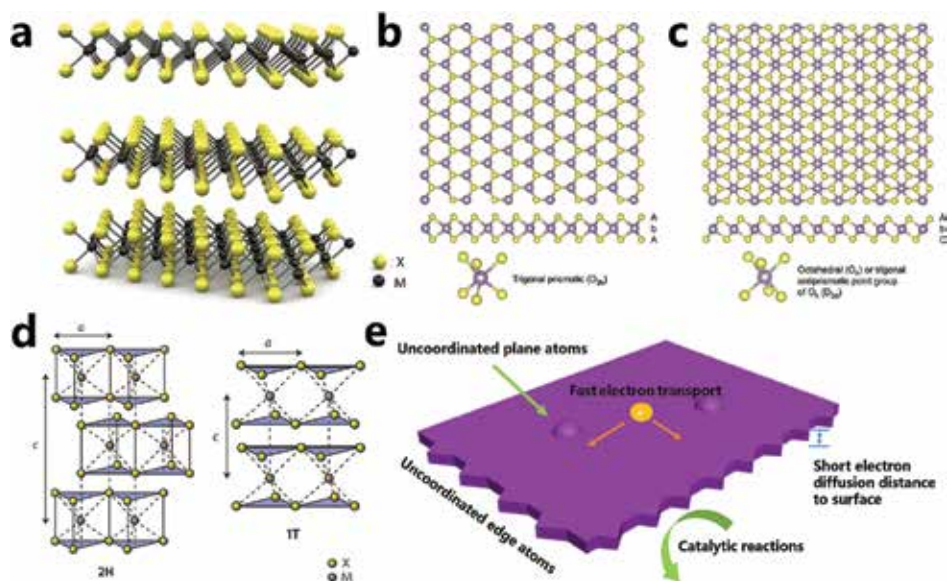


Figure 1. Structures of TMDs and schematic illustration for the advantages of TMDs as the electrocatalyst. (a) Structure of TMDs. Reproduced with permission from Radisavljevic et al. [32]; copyright 2011 Nature Publishing Group. Schematic representations of a typical TMD structure with trigonal prismatic (b) and octahedral (c) coordinations from *c*-axis (upper) and section view (middle). Reproduced with permission from Chhowalla et al. [14]; copyright 2013 Nature Publishing Group, (d) side view of the structure. Reproduced with permission from Wang et al. [33]; copyright 2012 Nature Publishing Group and (e) schematic illustration for the advantages of 2D TMDs as the electrocatalyst.

To advance the catalysis, especially electrocatalysis research, it is imperative to deepen the understanding on the underlying mechanisms involved in catalytic processes. As heterogeneous electrocatalysis essentially occurs at the interface of electrode (including catalyst) and bulk solution, the surface of catalysts should play a key role in determining species adsorption and electron transfer and, in turn, hold promise to tailoring reaction activity and selectivity in catalysis. In this regard, the 2D TMDs hold the advantages to catalyse the electrochemical reactions for the following reasons, except their unique intrinsic properties (**Figure 1e**).

(1) High surface areas. Since the electrocatalytic reactions occur on the surface of catalysts via electron transfer, species adsorption, and activation, it is the surface atom that mainly participates in the reactions. For this reason, boosting the surface-to-volume ratio would expose more atoms to the reaction species and thus help increase the probability of “active sites” to interact with reaction species. In comparison with conventional nanocatalysts, 2D materials possess significantly higher ratio of surface atom number to total atom number, thereby

promoting their catalytic activities. This ratio increases with the reduction in the number of atomic layers and hypothetically reaches its maximum value in monolayer.

(2) Abundant uncoordinated surface atoms. During a catalytic process, the reaction substrates are absorbed onto the surface atoms of the catalyst and then dissociated into highly reactive intermediates, which makes these surface atoms catalytically active sites. Certainly not all the surface atoms can efficiently participate in catalytic reactions. As a matter of fact, the adsorption and dissociation often take place on the coordinately unsaturated sites that are thermodynamically instable [16]. In the 2D materials, there are much more uncoordinatedly unsaturated atoms on the surface, which enhances their activities in catalysis. It is worth noting that the basal surfaces of catalysts might be catalytically inert in some certain reactions [14, 16]. Nevertheless, this feature does not diminish the advantage of 2D materials since catalytic activity can still arise from the active sites located along the edges of the nanosheets. For example, MoS₂ is a typical and efficient electrocatalyst for HER with higher activity at the edge compared to the basal part. The research indicates that atoms at the edges have lower coordination number than those on the surface, thereby providing reaction sites with higher catalytic activity [34, 35].

(3) Planar structure with atomic thickness. In general, the electrocatalytic performances of a catalyst are not only governed by the intrinsic nature and the number of active sites but also determined by the electron transfer between the active site and the supporting electrode [36]. From this point of view, the unique planar structure with atomic thickness of 2D materials is a decisive advantage for catalysis. The density of states should be significantly increased due to surface distortion of 2D materials, which favours the electron transport along the 2D conducting channels with high mobility as well as between its interface with other components or media, facilitating the electron diffusion between the catalytically active sites and the supporting electrode [37]. Furthermore, the unique planar structure of 2D materials also makes them ideal loading substrates for the assembly or growth of various novel hybrid catalysts. Other building blocks can be readily loaded on the flat surface or stacked layer by layer for various catalytic applications [38].

(4) Excellent solution dispersity. 2D materials often show excellent dispersity in certain solution whose type depends on their synthetic method. Thus far, exfoliation in aqueous solution is the most widespread method to produce 2D materials [39]. Most of the resulted materials are thus dispersible in water to facilitate further processing and applications towards green chemistry. In general, their superior dispersity to other counterparts is enabled by high surface area as well as large portion of uncoordinated surface atoms. The high specific surface area keeps nanosheets from precipitation, while electrostatic repulsion between the nanosheets further prevents their agglomeration.

(5) Highly tunable properties. One major difference between 2D TMDs and other 2D materials, such as graphene, is their high anisotropy and unique crystal structure. For this reason, the material properties of 2D TMDs can be effectively tuned in a wide range through different methodologies including reducing dimensions, intercalation, heterostructure, alloying, gating, pressure, lighting, and so forth [27, 40–44]. For example, through the intercalation of guest ions, the carrier densities of 2D TMDs can be tuned by multiple orders of magnitude,

which will affect the electron transfer rate in the electrocatalytic reactions [45]. 2D TMDs provide a great platform of tuning material properties towards desired activity and selectivity of a specific electrochemical reaction.

3. Preparation methods for 2D TMDs

2D TMDs provide excellent model systems to fundamentally establish structure-property relationship in electrocatalysis given their unique structural characteristics. Certainly the synthesis and fabrication of related materials are the central part of this research and both physical and chemical approaches have been utilized effectively for the synthesis of TMDs.

3.1. Exfoliation

Exfoliation is a top-down assembly method, in which physical and chemical driving forces are used to achieve separation of bulk materials. In the exfoliation of 2D materials, the precursors are usually their bulk counterparts. During the exfoliation, external or internal driving force is needed to weaken and eventually overcome the van der Waals force between adjacent layers. It can use mechanical force, such as friction or shear forces, or chemical force, in which the free energy or externally added electrochemical energy provides the driving force. Exfoliated sheets must typically be stabilized to prevent aggregation and re-stacking using surfactants, polymers, solvents, or liquid-liquid interfaces that trap and stabilize the exfoliated sheets [39, 46, 47].

It is the successful isolation of graphene from graphite using scotch tape that sparks the tremendous interest in exfoliating 2D TMD materials [13]. This mechanical exfoliation possesses the advantages of being highly reproductive and is quite suitable to fabricate single devices for research purposes and build devices based on all-layered materials [12, 48]. Nevertheless, mechanical exfoliation is not suitable for large-scale production due to the absence of layer number and lateral size control capability and it also suffers from low yield and contaminates monolayer surfaces with the adhesive polymer [32]. The limitations on throughput can be overcome by exfoliation in the liquid phases [46, 47, 49]. In general, direct sonication of a layered host is carried out in a solvent chosen to stabilize the exfoliated sheets and sometimes selected based on matching surface tension to solid surface energies. Although this method can partially exfoliate TMDs into few-layer materials, only a very low yield of monolayer TMDs can be produced.

In addition to the direct dry or liquid-phase exfoliation, a two-step process, ion intercalation followed by exfoliation, is able to produce TMDs with a higher yield. Lithium, sodium, or potassium ions are intercalated into the interlayer space and form ion-intercalated compounds, which can be further sonicated in water or organic solvents to form TMD dispersions [50]. Exfoliation of the bulk TMD crystals can also be achieved using organolithium compounds. For example, the *n*-BuLi reacts chemically with TMDs, forming Li-intercalated compounds [51]. The compounds are further exfoliated by the reaction of Li with water. A variety of TMD sheets, including MoS₂, TiS₂, TaS₂, and WS₂, can be produced by this method with the lateral size up to few microns (**Figure 2a**).

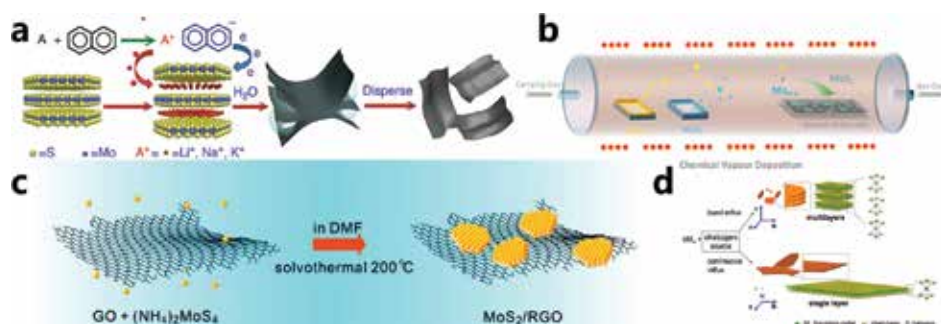
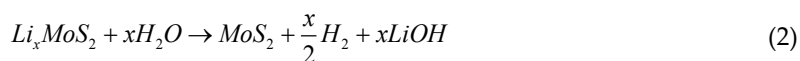


Figure 2. Preparation methods for TMDs. (a) Chemical exfoliation process of TMDs. Reproduced with permission from Zheng et al. [50]; copyright 2014 Nature Publishing Group, (b) CVD growth of TMDs. Reproduced with permission from Shi et al. [59]; copyright 2014 Royal Society of Chemistry, (c) hydrothermal growth of MoS₂ on reduced graphene oxide. Reproduced with permission from Li et al. [83]; copyright 2011 American Chemical Society, and (d) colloidal synthesis of TMDs. Reproduced with permission from Yoo et al. [85]; copyright 2014 American Chemical Society.

Electrochemical exfoliation has been used for several decades for exfoliation and restacking of layered materials to generate novel compounds [14]. It proceeds through the electrochemical insertion of an ion (such as Li⁺) into the host crystal. This destabilizes the crystal while inducing a phase change at the same time (Eq. (1)).



Placing the intercalated material in polar solvents forces hydrolysis of the lithiated species and formation of single-sheet colloidal suspensions (Eq. (2)) [52, 53]. The yield of this method is nearly 100% but requires long reaction times and careful exfoliation to prevent destruction. This method may be one of the most promising for large-scale fabrication of true monolayer materials [14, 52, 54, 55].

3.2. Chemical vapour deposition

Chemical vapour deposition (CVD) is an important and widely used technique for growing inorganic materials, which yields large, high-quality single crystals of oxide and chalcogenide materials with morphologies ranging from nanoribbons, plates, to monolayers [56–58]. In a typical CVD process, source powder(s) or molecular precursor in solution is heated. A carrier gas (e.g. argon, nitrogen, or forming gas) transports the vapour-phase precursors downstream to substrates that are placed in a region of appropriate temperature for nucleation of TMDs (Figure 2b). Optimization of substrate choice, molecular precursors, and reaction geometry can facilitate growth of monolayers [59]. Compared with chemical exfoliation, the CVD

method is more efficient in growing TMD monolayer films on substrates (SiO_2/Si [60] or Au [61]), with high quality and controllable thickness [46, 62].

Several CVD synthesis methods for TMDs have been studied, such as sulphurization of a transition metal or metal oxide thin film, thermal decomposition of thio-salts, and vapour-phase transport method [63–70]. Furthermore, Li and co-workers developed a growth method of TMDs via vapour-phase chemical reaction of transition metal oxide and chalcogen, which can control the thickness and crystallinity of TMDs [71, 72]. Specifically, metal oxide MoO_3 is used as transition metal source and it undergoes a two-step reaction. The suboxide MoO_{3-x} is firstly produced during the reaction, which further serves as an intermediate to react with chalcogen vapour (sulphur) and forms the monolayer TMDs with a triangular shape.

Further studies show that the formation of TMDs is controlled by the surface energy of substrate. The aromatic molecules can significantly enhance the wetting between precursors and the substrate surfaces and thus promote the nucleation and lateral growth of TMDs [73]. TMDs' single-crystal domain with lateral size up to several hundred micrometres can be produced by optimising the vapour-phase reaction conditions [74]. The direct vapour-phase reaction of transition metal oxide and sulphur/selenium has been widely adopted to produce TMDs including MoS_2 , WS_2 , MoSe_2 , and WSe_2 [62, 75–77].

3.3. Wet chemical approaches

Wet chemical approaches are bottom-up methods which offer a potentially powerful alternative to exfoliation and CVD. It can be used to synthesize TMDs with thicknesses ranging from the monolayer to hundreds of layers [78, 79]. Compared with CVD method, the reaction temperatures are much lower, and the produced materials are exceptional uniform and with low defect density. Thanks to diverse wet-chemical methods, the materials can be doped by adding other reagents during growth and one can also use ligand chemistry to cap the material's surface in order to modify or protect the surface [80–82]. Moreover, wet-chemical methods are often easily translated into larger-scale manufacturing processes, which may facilitate the commercialization of TMD materials. By selection of environmentally precursors and solvents, solution-based methods can be adapted to adhere to principles of green chemistry and manufacturing [80].

A traditional wet-chemical approach to chalcogenides involves hydrothermal or solvothermal growth (**Figure 2c**) [83]. Taking the synthesis of MoS_2 nanoflakes as an example, in a typical procedure, $(\text{NH}_4)_6\text{Mo}_7\text{O}_{24}\cdot 4\text{H}_2\text{O}$ and thiourea have been utilized as the precursors for the Mo and S elements in hydrothermal reactions [84]. After reaction in a Teflon-lined stainless steel autoclave, the low-quality MoS_2 flakes with abundant active sites are obtained.

Colloidal synthesis is a well-established technique for synthesizing TMDs [80]. In a typical process, similar to other colloidal synthetic routes, a cold solution of precursor chemicals is injected into a hot solvent or a one-pot route can also be adopted where precursors are mixed together and then heated (up to 320 °C). Recently, it was reported that monolayer TMDs such as TiS_2 , HfS_2 , and ZrS_2 could be synthesized by a novel colloidal referred to as “diluted chalcogen continuous influx” [85]. In this method, the delivery rate of a chalcogen source (such

as H_2S or CS_2) to a transition metal halide precursor in solution was controlled to be slow enough to favour the lateral (2D) growth over 3D growth (**Figure 2d**).

Although the wet-chemical approaches may unavoidably alter the lattice structure of thin TMDs and introduce extrinsic defects during exfoliation process, these defects may be helpful in electrocatalytic reactions [14, 16, 22].

4. Applications of 2D TMDs for electrocatalytic energy conversion

4.1. Hydrogen evolution reaction

H_2 is considered as one of the most promising energy carriers owing to its high energy density and environmentally benign character. Nevertheless, it is still a great challenge to produce H_2 efficiently [7, 9]. Amongst various H_2 production pathways, the electrocatalytic hydrogen evolution reaction is attracting tremendous attention due to its high energy-converting efficiency and the abundant raw material, namely, water. As is well known, hydrogen molecules can be generated from a process named water splitting, which can be divided into two independent half-reactions, HER to generate hydrogen in the cathode and OER to produce oxygen in the anode. However, the large electrolytic window of water means that appropriate electrocatalysts are required to lower the overpotential for water splitting.

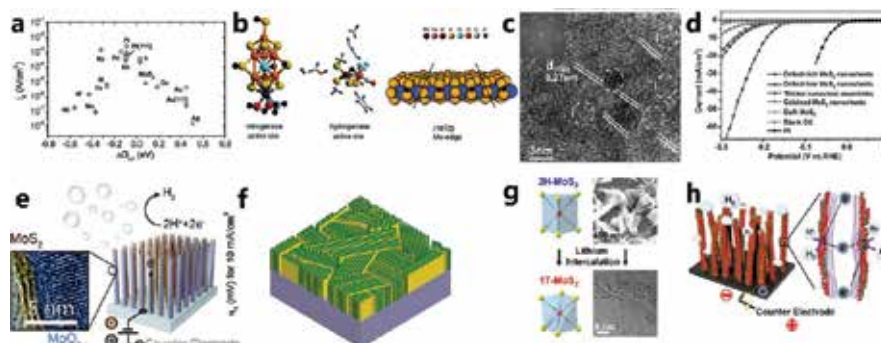


Figure 3. TMDs as electrocatalyst for HER. (a) Plot of exchange current density as a function of DFT-calculated Gibbs free energy of adsorbed atomic hydrogen for MoS_2 and pure metals. Reproduced with permission from Jaramillo et al. [34]; copyright 2007, American Association for the Advancement of Science, (b) nitrogenase (left) and hydrogenase (middle) inorganic compounds designed to mimic the edge sites of MoS_2 (right). Reproduced with permission from Hinnemann et al. [29]; copyright 2005 American Chemical Society, (c) HRTEM image and the Fourier transform pattern (inset) of the defect-rich MoS_2 ultrathin nanosheets, (d) polarization curves of various MoS_2 -based samples as indicated. Reproduced with permission from Xie et al. [87]; copyright 2013 Wiley, (e) schematics of MoO_3 - MoS_2 core-shell nanowires as catalysts for HER. Reproduced with permission from Chen et al. [90]; copyright 2011 American Chemical Society, (f) scheme for the vertically aligned MoS_2 layers. Reproduced with permission from Kong et al. [43]; copyright 2013 American Chemical Society, (g) exfoliation of 2H MoS_2 to 1T MoS_2 by lithium intercalation. Reproduced with permission from Lukowski et al. [91]; copyright 2013 American Chemical Society, and (h) scheme for the MoS_2 /NCNT forest hybrid catalyst. Reproduced with permission from Li et al. [94]; copyright 2014 American Chemical Society.

Pt is currently the most efficient electroactive and electrochemically stable catalyst for HER, but its high cost and rare existence limit its wide application. Hence, exploring other earth abundant materials with high catalytic activities has attracted intensive interest. The experimental explorations of TMDs as the electrocatalyst for HER were motivated by theoretical calculations on MoS₂ materials, which demonstrated that the hydrogen-binding energy of MoS₂ was close to that of metals such as Pt, Rh, Re, and Ir (**Figure 3a**) [29, 34, 86]. The density functional theory (DFT) calculations showed that metallic edges of trigonal prismatic (2H) MoS₂ clusters were highly active compared to the basal plane of the chalcogenide, where it remained inert from the electrochemical point of view [14]. The surface-active sites of MoS₂ was also probed by biomimicry of Mo(IV)-disulphide inorganic and organic (**Figure 3b**) [29, 35].

The activities of TMDs are usually limited by the proportion of active edge sites [16]. To tackle this problem, Lou and co-workers fabricated the defect-rich MoS₂ ultrathin nanosheets by adding excess thiourea in the precursors (**Figure 3c and d**) [87]. The excess thiourea played a key role in the formation of defect-rich MoS₂, which not only worked as a reductant to reduce VI Mo to IV Mo but also worked as a capping agent to stabilize the morphology of MoS₂ nanosheets. The resultant defect-rich MoS₂ showed outstanding electrocatalytic activity towards HER. It held a low overpotential of 120 mV, a large current density, and a small Tafel slope of 50 mV decade⁻¹. They attributed the superior performance to the additional active edge sites exposed on defect-rich MoS₂ ultrathin nanosheets. To increase the active surface of MoS₂, Kibsgaard et al. fabricated a 3D MoS₂ porous network [88]. Chen et al. synthesized vertically oriented MoO₃-MoS₂ core-shell nanowires, in which the MoS₂ shell contributes to the outstanding catalytic response as well as to protection against corrosion (**Figure 3e**) [89, 90]. Cui's group synthesized MoS₂ films with vertically aligned layers [43]. The structure predominantly exposes the edges on the film surface maximally (**Figure 3f**). The edge-terminated surface is obtained by overcoming the free energy barrier kinetically through rapid sulphurization.

Besides the active sites, the electric conductivity of MoS₂ is another crucial factor to affect its electrocatalytic activity. Jin and co-workers reported metallic 1T-MoS₂ nanosheets, which were prepared by chemical exfoliation via lithium intercalation to from semiconducting 2H-MoS₂ nanostructures (**Figure 3g**) [91]. This catalyst exhibited metallic conductivity and achieved a current density of 10 mA cm⁻² at an overpotential of -187 mV vs. RHE. Additionally, a small Tafel slope of 43 mV decade⁻¹ was reported for this catalyst. Xie's group studied the influence of active sites and conductivity of MoS₂ on the electrocatalytic activity and achieved the balance between them by controlling disorder engineering and oxygen incorporation in MoS₂ ultrathin nanosheets. This oxygen-doped MoS₂ with synergistically structural and electronic modulations achieved high-efficient HER activity [84].

In order to further improve the catalytic efficiency and stability of TMD-based electrocatalysts, enormous research efforts have been devoted to the incorporation of TMDs with other materials, such as noble metals and carbon materials (**Figure 3h**) [92–96]. Zhang and co-workers demonstrated the wet-chemical synthesis of noble metal nanostructures epitaxially grown on TMD nanosheets. The noble metal-TMD composites exhibit good electrocatalytic activity in hydrogen evolution reaction [97, 98].

4.2. CO₂ reduction reaction

Despite the tremendous efforts being made to implement renewable energy sources, there remains a need in the longer term to be able to sustainably generate liquid fuels for applications including aviation and mining [9, 11]. Electrochemical CO₂ reduction, recycling CO₂ back to fuels, and commodity chemicals utilizing renewable energy as a power source could potentially provide a solution to this problem [99]. However, CO₂ is very stable under environmental conditions and HER often prevails over CO₂ reduction in aqueous electrolytes under cathodic polarization [100, 101], making it essential to find a suitable catalyst to achieve cost-effective CO₂ reduction with high efficiency and selectivity. Metals and especially nanostructured metals derived from metal oxide have been widely studied as electrocatalysts for CO₂ reduction [100, 102–106]; however, these systems generally show low activities and/or selectivity for a solo product (such as CO, formate, methanol, methane, ethylene, and ethanol) or need nonaqueous solvents which may limit practical application.

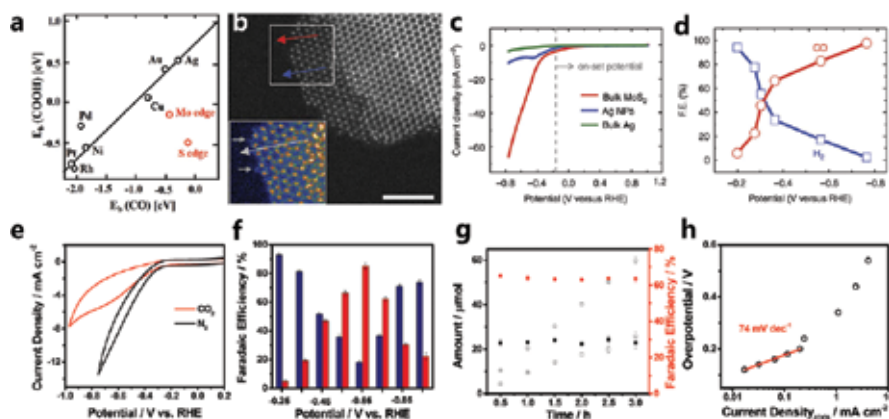


Figure 4. TMDs as electrocatalysts for electrochemical reduction of CO₂. (a) Binding energies $E_b(\text{COOH})$ vs. $E_b(\text{CO})$ for transition metals and Mo and S edges of MoS₂. Reproduced with permission from Shi et al. [108]; copyright 2014 Royal Society of Chemistry, (b) raw greyscale HAADF and false-colour low-angle annular dark-field (LAADF) image (inset) of MoS₂ edges (scale bar, 5 nm), (c) cyclic voltammetric (CV) curves for bulk MoS₂, Ag nanoparticles (Ag NPs), and bulk Ag in CO₂ environment. The electrolyte is a mixture of 96 mol% water and 4 mol% EMIM-BF₄, (d) CO and H₂ Faradaic efficiency (FE) at different applied potentials. Reproduced with permission from Asadi et al. [109]; copyright 2014 Nature Publishing Group, (e) CVs of rGO-PEI-MoS₂-modified GCE in N₂-saturated (black curve) and CO₂-saturated (red curve) 0.5 M aqueous NaHCO₃ solution. Scan rate was 50 mV s⁻¹, (f) Faradaic efficiency for CO (red bars) and H₂ (blue bars) as a function of potential, (g) amount and Faradaic efficiency of H₂ (circles) and CO (squares). Potentiostatic electrolysis at -0.4 V in CO₂-saturated 0.5 M aqueous NaHCO₃ solution and (h) Tafel plot of CO production partial current density vs. overpotential on rGO-PEI-MoS₂. Reproduced with permission from Li et al. [110]; copyright 2016 Royal Society of Chemistry.

Recently, Nørskov et al. demonstrated theoretically that MoS₂ or MoSe₂ could possibly be electrocatalysts for CO₂ reduction by DFT calculation [107, 108]. Their results indicate the edge site of MoS₂ or MoSe₂ is active for electrochemical CO₂ reduction due to the different scaling relationships of adsorption energies between key reaction intermediates (*CO and *COOH) on the edges of MoS₂ or MoSe₂ compared to transition metals (**Figure 4a**). Experimental results of MoS₂ as electrocatalyst for CO₂ reduction were firstly reported by Asadi et al. [109]

(Figure 4b–d). They uncovered that MoS₂ showed superior CO₂ reduction performance compared with the noble metals with a high current density and low overpotential (54 mV) in an ionic liquid. They also utilized DFT calculations to reveal the catalytic activity mainly arises from the molybdenum-terminated edges of MoS₂ due to their metallic character and a high *d*-electron density. The experimental result that vertically aligned MoS₂ showed an enhanced performance compared to bulk MoS₂ crystal supported their calculations.

Li and co-workers reported amorphous MoS₂ on a polyethylenimine-modified reduced graphene oxide substrate as an effective catalyst for electrocatalytic CO₂ reduction (Figure 4e–h) [110]. The catalyst is capable of producing CO at an overpotential as low as 140 mV and reaches a maximum Faradaic efficiency (FE) of 85.1% at an overpotential of 540 mV. Another interesting point is that at an overpotential of 290 mV with respect to the formation of CO, it catalyses the formation of syngas with high stability, which could be readily utilized in the current Fischer-Tropsch process and produce liquid fuels, such as ethanol and methanol. Their detailed mechanism investigation indicated that the efficiency and selectivity towards CO₂ reduction rather than hydrogen evolution at the optimal applied potential were attributed to the synergetic effect of MoS₂ and PEI: (1) the intrinsic properties of MoS₂ that it can selectively bind the intermediate during the CO₂ reduction reaction path is the principal factor contributing the CO₂ reduction and (2) PEI, an amine containing polymer with outstanding CO₂ adsorption capacity, can stabilize the intermediate and thus lower the energy barrier by hydrogen bond interaction.

5. Summary and outlook

Energy issue is one of the most urgent and critical topics in our modern society. Recently, there is increasing demand for cost-effective, efficient, and environmental-friendly energy conversion and storage devices to reduce the excessive reliance on nonrenewable fossil fuels. Due to the unique physicochemical properties of 2D TMDs, they have shown enormous potential for wide-ranging and diversified fundamental and technological applications, which include intensive research on electrocatalytic energy conversion applications, especially hydrogen evolution reaction and CO₂ reduction reaction. In these electrocatalytic reactions, the maximization of active edges and the conductivity are identified as the core issues for further development of TMD-based catalysts. A large number of synthetic strategies have been focused on maximizing the exposure of edge sites; phase structure tuning has also been as a potential tool for enhancing the electrical transport properties of TMDs.

Overall, the rich chemistry of TMDs builds an extensive platform for the study of fundamental and practical scientific phenomena in the development of real electrocatalysts for energy conversion applications. There is still much room to further improve the electrocatalytic performance of TMDs. Specifically, the fine tune of band structure and Fermi level could provide as powerful tools. Hence, a combination of theoretical, fundamental, and electrocatalysis-based applications should be explored in order to make a guidance to the developing directions. Furthermore, the mass-productive synthesis of high-quality TMDs should emerge as an urgent issue to adapt to the widely application of them in an industry level.

Author details

Fengwang Li¹ and Mianqi Xue^{2*}

*Address all correspondence to: xuemq@iphy.ac.cn

¹ School of Chemistry, Monash University, Melbourne, Australia

² Institute of Physics, Beijing National Laboratory for Condensed Matter Physics, Chinese Academy of Sciences, Beijing, China

References

- [1] Dresselhaus M, Thomas I. Alternative energy technologies. *Nature*. 2001;414:332–337.
- [2] Hong WT, Risch M, Stoerzinger KA, Grimaud A, Suntivich J, Shao-Horn Y. Toward the rational design of non-precious transition metal oxides for oxygen electrocatalysis. *Energy and Environmental Science*. 2015;8:1404–1427.
- [3] Bonaccorso F, Colombo L, Yu G, Stoller M, Tozzini V, Ferrari AC, et al. 2D materials. Graphene, related two-dimensional crystals, and hybrid systems for energy conversion and storage. *Science*. 2015;347:1246501.
- [4] Xie J, Xie Y. Transition metal nitrides for electrocatalytic energy conversion: opportunities and challenges. *Chemistry – A European Journal*. 2015;22:3588–3598.
- [5] Zhang G, Liu H, Qu J, Li J. Two-dimensional layered MoS₂: rational design, properties and electrochemical applications. *Energy and Environmental Science*. 2016;9:1190–1209. DOI: 10.1039/c5ee03761a.
- [6] Mallouk TE. Water electrolysis: divide and conquer. *Nature Chemistry*. 2013;5:362–363.
- [7] Turner JA. Sustainable hydrogen production. *Science*. 2004;305:972–974.
- [8] Norskov JK, Christensen CH. Toward efficient hydrogen production at surfaces. *Science*. 2006;312:1322–1323.
- [9] Gasteiger HA, Markovic NM. Just a dream- or future reality? *Science*. 2009;324:48–49.
- [10] House RL, Iha NYM, Coppo RL, Alibabaei L, Sherman BD, Kang P, et al. Artificial photosynthesis: where are we now? Where can we go? *Journal of Photochemistry and Photobiology C: Photochemistry Reviews*. 2015;25:32–45.
- [11] Lackner KS. A guide to CO₂ sequestration. *Science*. 2003;300:1677–1678.
- [12] Geim AK, Novoselov KS. The rise of graphene. *Nature Materials*. 2007;6:183–191.

- [13] Novoselov KS, Geim AK, Morozov S, Jiang D, Zhang Y, Dubonos Sa, et al. Electric field effect in atomically thin carbon films. *Science*. 2004;306:666–669.
- [14] Chhowalla M, Shin HS, Eda G, Li LJ, Loh KP, Zhang H. The chemistry of two-dimensional layered transition metal dichalcogenide nanosheets. *Nature Chemistry*. 2013;5:263–275.
- [15] Das S, Robinson JA, Dubey M, Terrones H, Terrones M. Beyond graphene: progress in novel two-dimensional materials and van der Waals solids. *Annual Review of Materials Research*. 2015;45:1–27.
- [16] Sun Y, Gao S, Lei F, Xie Y. Atomically-thin two-dimensional sheets for understanding active sites in catalysis. *Chemical Society Reviews*. 2015;44:623–636.
- [17] Wang Z, Zhu W, Qiu Y, Yi X, von dem Bussche A, Kane A, et al. Biological and environmental interactions of emerging two-dimensional nanomaterials. *Chemical Society Reviews*. 2016;45:1750–1780.
- [18] Zhang X, Xie Y. Recent advances in free-standing two-dimensional crystals with atomic thickness: design, assembly and transfer strategies. *Chemical Society Reviews*. 2013;42:8187–8199.
- [19] Luo B, Liu G, Wang L. Recent advances in 2D materials for photocatalysis. *Nanoscale*. 2016;8:6904–6920. DOI: 10.1039/c6nr00546b.
- [20] Lv R, Robinson JA, Schaak RE, Sun D, Sun Y, Mallouk TE, et al. Transition metal dichalcogenides and beyond: synthesis, properties, and applications of single- and few-layer nanosheets. *Accounts of Chemical Research*. 2015;48:56–64.
- [21] Gao MR, Xu YF, Jiang J, Yu SH. Nanostructured metal chalcogenides: synthesis, modification, and applications in energy conversion and storage devices. *Chemical Society Reviews*. 2013;42:2986–3017.
- [22] Wang H, Yuan H, Sae Hong S, Li Y, Cui Y. Physical and chemical tuning of two-dimensional transition metal dichalcogenides. *Chemical Society Reviews*. 2015;44:2664–2680.
- [23] Li H, Shi Y, Chiu M-H, Li L-J. Emerging energy applications of two-dimensional layered transition metal dichalcogenides. *Nano Energy*. 2015;18:293–305.
- [24] Wang H, Feng H, Li J. Graphene and graphene-like layered transition metal dichalcogenides in energy conversion and storage. *Small*. 2014;10:2165–2181.
- [25] Bang GS, Choi S-Y. Graphene and two-dimensional transition metal dichalcogenide materials for energy-related applications. In: Kyung C-M, editor. *Nano Devices and Circuit Techniques for Low-Energy Applications and Energy Harvesting*. KAIST Research Series. Netherlands: Springer; 2016. p. 253–291.

- [26] Zhang X, Liang J, Ding S. The application of nanostructure MoS₂ materials in energy storage and conversion. In: Wang MZ, editor. MoS₂. Lecture Notes in Nanoscale Science and Technology. Switzerland: Springer; 2014. p. 237–268.
- [27] Jariwala D, Sangwan VK, Lauhon LJ, Marks TJ, Hersam MC. Emerging device applications for semiconducting two-dimensional transition metal dichalcogenides. *ACS Nano*. 2014;8:1102–1120.
- [28] Bai S, Xiong Y. Recent advances in two-dimensional nanostructures for catalysis applications. *Science of Advanced Materials*. 2015;7:2168–2181.
- [29] Hinnemann B, Moses PG, Bonde J, Jørgensen KP, Nielsen JH, Horch S, et al. Biomimetic hydrogen evolution: MoS₂ nanoparticles as catalyst for hydrogen evolution. *Journal of the American Chemical Society*. 2005;127:5308–5309.
- [30] Huang X, Zeng Z, Zhang H. Metal dichalcogenide nanosheets: preparation, properties and applications. *Chemical Society Reviews*. 2013;42:1934–1946.
- [31] Sun Y, Gao S, Xie Y. Atomically-thick two-dimensional crystals: electronic structure regulation and energy device construction. *Chemical Society Reviews*. 2014;43:530–546.
- [32] Radisavljevic B, Radenovic A, Brivio J, Giacometti V, Kis A. Single-layer MoS₂ transistors. *Nature Nanotechnology*. 2011;6:147–150.
- [33] Wang QH, Kalantar-Zadeh K, Kis A, Coleman JN, Strano MS. Electronics and optoelectronics of two-dimensional transition metal dichalcogenides. *Nature Nanotechnology*. 2012;7:699–712.
- [34] Jaramillo TF, Jørgensen KP, Bonde J, Nielsen JH, Horch S, Chorkendorff I. Identification of active edge sites for electrochemical H₂ evolution from MoS₂ nanocatalysts. *Science*. 2007;317:100–102.
- [35] Karunadasa HI, Montalvo E, Sun Y, Majda M, Long JR, Chang CJ. A molecular MoS₂ edge site mimic for catalytic hydrogen generation. *Science*. 2012;335:698–702.
- [36] Lai J, Li S, Wu F, Saqib M, Luque R, Xu G. Unprecedented metal-free 3D porous carbonaceous electrodes for water splitting. *Energy and Environmental Science*. 2016;9:1210–1214. DOI: 10.1039/c5ee02996a.
- [37] Sun Y, Cheng H, Gao S, Sun Z, Liu Q, Liu Q, et al. Freestanding tin disulfide single-layers realizing efficient visible-light water splitting. *Angewandte Chemie International Edition*. 2012;51:8727–8731.
- [38] Huang X, Tan C, Yin Z, Zhang H. 25th anniversary article: hybrid nanostructures based on two-dimensional nanomaterials. *Advanced Materials*. 2014;26:2185–2204.
- [39] Nicolosi V, Chhowalla M, Kanatzidis MG, Strano MS, Coleman JN. Liquid exfoliation of layered materials. *Science*. 2013;340:1226419.

- [40] Fuhrer MS, Hone J. Measurement of mobility in dual-gated MoS₂ transistors. *Nature Nanotechnology*. 2013;8:146–147.
- [41] Koski KJ, Cui Y. The new skinny in two-dimensional nanomaterials. *ACS Nano*. 2013;7:3739–3743.
- [42] Lopez-Sanchez O, Lembke D, Kayci M, Radenovic A, Kis A. Ultrasensitive photodetectors based on monolayer MoS₂. *Nature Nanotechnology*. 2013;8:497–501.
- [43] Kong D, Wang H, Cha JJ, Pasta M, Koski KJ, Yao J, et al. Synthesis of MoS₂ and MoSe₂ films with vertically aligned layers. *Nano Letters*. 2013;13:1341–1347.
- [44] Yang Z, Liang H, Wang X, Ma X, Zhang T, Yang Y, et al. Atom-thin SnS_{2-x}Se_x with adjustable compositions by direct liquid exfoliation from single crystal. *ACS Nano*. 2016;10:755–762.
- [45] Dresselhaus MS. *Intercalation in Layered Materials*. Netherlands: Springer; 2013.
- [46] Coleman JN, Lotya M, O'Neill A, Bergin SD, King PJ, Khan U, et al. Two-dimensional nanosheets produced by liquid exfoliation of layered materials. *Science*. 2011;331:568–571.
- [47] Smith RJ, King PJ, Lotya M, Wirtz C, Khan U, De S, et al. Large-scale exfoliation of inorganic layered compounds in aqueous surfactant solutions. *Advanced Materials*. 2011;23:3944–3948.
- [48] Li H, Lu G, Wang Y, Yin Z, Cong C, He Q, et al. Mechanical exfoliation and characterization of single- and few-layer nanosheets of WSe₂, TaS₂, and TaSe₂. *Small*. 2013;9:1974–1981.
- [49] Paton KR, Varrla E, Backes C, Smith RJ, Khan U, O'Neill A, et al. Scalable production of large quantities of defect-free few-layer graphene by shear exfoliation in liquids. *Nature Materials*. 2014;13:624–630.
- [50] Zheng J, Zhang H, Dong S, Liu Y, Nai CT, Shin HS, et al. High yield exfoliation of two-dimensional chalcogenides using sodium naphthalenide. *Nature Communications*. 2014;5:2995.
- [51] Eda G, Yamaguchi H, Voiry D, Fujita T, Chen M, Chhowalla M. Photoluminescence from chemically exfoliated MoS₂. *Nano Letters*. 2011;11:5111–5116.
- [52] Zeng Z, Yin Z, Huang X, Li H, He Q, Lu G, et al. Single-layer semiconducting nanosheets: high-yield preparation and device fabrication. *Angewandte Chemie International Edition*. 2011;50:11093–11097.
- [53] Auerbach SM, Carrado KA, Dutta PK. *Handbook of Layered Materials*. Boca Raton: CRC Press; 2004.
- [54] Benavente E, Santa Ana M, Mendizábal F, González G. Intercalation chemistry of molybdenum disulfide. *Coordination Chemistry Reviews*. 2002;224:87–109.

- [55] Golub AS, Zubavichus YV, Slovokhotov YL, Novikov YN. Single-layer dispersions of transition metal dichalcogenides in the synthesis of intercalation compounds. *Russian Chemical Reviews*. 2003;72:123–141.
- [56] Miró P, Audiffred M, Heine T. An atlas of two-dimensional materials. *Chemical Society Reviews*. 2014;43:6537–6554.
- [57] Zhi C, Bando Y, Tang C, Kuwahara H, Golberg D. Large-scale fabrication of boron nitride nanosheets and their utilization in polymeric composites with improved thermal and mechanical properties. *Advanced Materials*. 2009;21:2889–2893.
- [58] Cai G, Jian J, Chen X, Lei M, Wang W. Regular hexagonal MoS₂ microflakes grown from MoO₃ precursor. *Applied Physics A*. 2007;89:783–788.
- [59] Shi Y, Li H, Li L-J. Recent advances in controlled synthesis of two-dimensional transition metal dichalcogenides via vapour deposition techniques. *Chemical Society Reviews*. 2015;44:2744–2756.
- [60] Ji Q, Zhang Y, Gao T, Zhang Y, Ma D, Liu M, et al. Epitaxial monolayer MoS₂ on mica with novel photoluminescence. *Nano Letters*. 2013;13:3870–3877.
- [61] Shi J, Ma D, Han G-F, Zhang Y, Ji Q, Gao T, et al. Controllable growth and transfer of monolayer MoS₂ on Au foils and its potential application in hydrogen evolution reaction. *ACS Nano*. 2014;8:10196–10204.
- [62] Najmaei S, Liu Z, Zhou W, Zou X, Shi G, Lei S, et al. Vapour phase growth and grain boundary structure of molybdenum disulphide atomic layers. *Nature Materials*. 2013;12:754–759.
- [63] Zhan Y, Liu Z, Najmaei S, Ajayan PM, Lou J. Large-area vapor-phase growth and characterization of MoS₂ atomic layers on a SiO₂ substrate. *Small*. 2012;8:966–971.
- [64] Lin Y-C, Zhang W, Huang J-K, Liu K-K, Lee Y-H, Liang C-T, et al. Wafer-scale MoS₂ thin layers prepared by MoO₃ sulfurization. *Nanoscale*. 2012;4:6637–6641.
- [65] Liu K-K, Zhang W, Lee Y-H, Lin Y-C, Chang M-T, Su C-Y, et al. Growth of large-area and highly crystalline MoS₂ thin layers on insulating substrates. *Nano Letters*. 2012;12:1538–1544.
- [66] Wu S, Huang C, Aivazian G, Ross JS, Cobden DH, Xu X. Vapor–solid growth of high optical quality MoS₂ monolayers with near-unity valley polarization. *ACS Nano*. 2013;7:2768–2772.
- [67] Ubaldini A, Jacimovic J, Ubrig N, Giannini E. Chloride-driven chemical vapor transport method for crystal growth of transition metal dichalcogenides. *Crystal Growth & Design*. 2013;13:4453–4459.
- [68] Ubaldini A, Giannini E. Improved chemical vapor transport growth of transition metal dichalcogenides. *Journal of Crystal Growth*. 2014;401:878–882.

- [69] Shaw JC, Zhou H, Chen Y, Weiss NO, Liu Y, Huang Y, et al. Chemical vapor deposition growth of monolayer MoSe₂ nanosheets. *Nano Research*. 2015;7:511–517.
- [70] Nayak PK, Lin F-C, Yeh C-H, Huang J-S, Chiu P-W. Robust room temperature valley polarization in monolayer and bilayer WS₂. *Nanoscale*. 2016;8:6035–6042.
- [71] Lee YH, Zhang XQ, Zhang W, Chang MT, Lin CT, Chang KD, et al. Synthesis of large-area MoS₂ atomic layers with chemical vapor deposition. *Advanced Materials*. 2012;24:2320–2325.
- [72] Lee Y-H, Yu L, Wang H, Fang W, Ling X, Shi Y, et al. Synthesis and transfer of single-layer transition metal disulfides on diverse surfaces. *Nano Letters*. 2013;13:1852–1857.
- [73] Ling X, Lee Y-H, Lin Y, Fang W, Yu L, Dresselhaus MS, et al. Role of the seeding promoter in MoS₂ growth by chemical vapor deposition. *Nano Letters*. 2014;14:464–472.
- [74] van der Zande AM, Huang PY, Chenet DA, Berkelbach TC, You Y, Lee G-H, et al. Grains and grain boundaries in highly crystalline monolayer molybdenum disulphide. *Nature Materials*. 2013;12:554–561.
- [75] Huang J-K, Pu J, Hsu C-L, Chiu M-H, Juang Z-Y, Chang Y-H, et al. Large-area synthesis of highly crystalline WSe₂ monolayers and device applications. *ACS Nano*. 2013;8:923–930.
- [76] Zhang Y, Zhang Y, Ji Q, Ju J, Yuan H, Shi J, et al. Controlled growth of high-quality monolayer WS₂ layers on sapphire and imaging its grain boundary. *ACS Nano*. 2013;7:8963–8971.
- [77] Chang Y-H, Zhang W, Zhu Y, Han Y, Pu J, Chang J-K, et al. Monolayer MoSe₂ grown by chemical vapor deposition for fast photodetection. *ACS Nano*. 2014;8:8582–8590.
- [78] Miró P, Han JH, Cheon J, Heine T. Hexagonal transition-metal chalcogenide nanoflakes with pronounced lateral quantum confinement. *Angewandte Chemie International Edition*. 2014;53:12624–12628.
- [79] Bianco E, Butler S, Jiang S, Restrepo OD, Windl W, Goldberger JE. Stability and exfoliation of germanane: a germanium graphane analogue. *ACS Nano*. 2013;7:4414–4421.
- [80] Han JH, Lee S, Cheon J. Synthesis and structural transformations of colloidal 2D layered metal chalcogenide nanocrystals. *Chemical Society Reviews*. 2013;42:2581–2591.
- [81] Kong D, Koski KJ, Cha JJ, Hong SS, Cui Y. Ambipolar field effect in Sb-doped Bi₂Se₃ nanoplates by solvothermal synthesis. *Nano Letters*. 2013;13:632–636.
- [82] Li J, Chen Z, Wang R-J, Proserpio DM. Low temperature route towards new materials: solvothermal synthesis of metal chalcogenides in ethylenediamine. *Coordination Chemistry Reviews*. 1999;190:707–735.

- [83] Li Y, Wang H, Xie L, Liang Y, Hong G, Dai H. MoS₂ nanoparticles grown on graphene: an advanced catalyst for the hydrogen evolution reaction. *Journal of the American Chemical Society*. 2011;133:7296–7299.
- [84] Xie J, Zhang J, Li S, Grote F, Zhang X, Zhang H, et al. Controllable disorder engineering in oxygen-incorporated MoS₂ ultrathin nanosheets for efficient hydrogen evolution. *Journal of the American Chemical Society*. 2013;135:17881–17888.
- [85] Yoo D, Kim M, Jeong S, Han J, Cheon J. Chemical synthetic strategy for single-layer transition-metal chalcogenides. *Journal of the American Chemical Society*. 2014;136:14670–14673.
- [86] Li T, Galli G. Electronic properties of MoS₂ nanoparticles. *The Journal of Physical Chemistry C*. 2007;111:16192–16196.
- [87] Xie J, Zhang H, Li S, Wang R, Sun X, Zhou M, et al. Defect-rich MoS₂ ultrathin nanosheets with additional active edge sites for enhanced electrocatalytic hydrogen evolution. *Advanced Materials*. 2013;25:5807–5813.
- [88] Kibsgaard J, Chen Z, Reinecke BN, Jaramillo TF. Engineering the surface structure of MoS₂ to preferentially expose active edge sites for electrocatalysis. *Nature Materials*. 2012;11:963–969.
- [89] Voiry D, Salehi M, Silva R, Fujita T, Chen M, Asefa T, et al. Conducting MoS₂ nanosheets as catalysts for hydrogen evolution reaction. *Nano Letters*. 2013;13:6222–6227.
- [90] Chen Z, Cummins D, Reinecke BN, Clark E, Sunkara MK, Jaramillo TF. Core-shell MoO₃-MoS₂ nanowires for hydrogen evolution: a functional design for electrocatalytic materials. *Nano Letters*. 2011;11:4168–4175.
- [91] Lukowski MA, Daniel AS, Meng F, Forticaux A, Li L, Jin S. Enhanced hydrogen evolution catalysis from chemically exfoliated metallic MoS₂ nanosheets. *Journal of the American Chemical Society*. 2013;135:10274–10277.
- [92] Hong X, Liu J, Zheng B, Huang X, Zhang X, Tan C, et al. A universal method for preparation of noble metal nanoparticle-decorated transition metal dichalcogenide nanobelts. *Advanced Materials*. 2014;26:6250–6254.
- [93] Zheng X, Xu J, Yan K, Wang H, Wang Z, Yang S. Space-confined growth of MoS₂ nanosheets within graphite: the layered hybrid of MoS₂ and graphene as an active catalyst for hydrogen evolution reaction. *Chemistry of Materials*. 2014;26:2344–2353.
- [94] Li DJ, Maiti UN, Lim J, Choi DS, Lee WJ, Oh Y, et al. Molybdenum sulfide/N-doped CNT forest hybrid catalysts for high-performance hydrogen evolution reaction. *Nano Letters*. 2014;14:1228–1233.
- [95] Liao L, Zhu J, Bian X, Zhu L, Scanlon MD, Girault HH, et al. MoS₂ formed on mesoporous graphene as a highly active catalyst for hydrogen evolution. *Advanced Functional Materials*. 2013;23:5326–5333.

- [96] Yu XY, Hu H, Wang Y, Chen H, Lou XWD. Ultrathin MoS₂ nanosheets supported on N-doped carbon nanoboxes with enhanced lithium storage and electrocatalytic properties. *Angewandte Chemie International Edition*. 2015;54:7395–7398.
- [97] Huang X, Zeng Z, Bao S, Wang M, Qi X, Fan Z, et al. Solution-phase epitaxial growth of noble metal nanostructures on dispersible single-layer molybdenum disulfide nanosheets. *Nature Communications*. 2013;4:1444.
- [98] Zeng Z, Tan C, Huang X, Bao S, Zhang H. Growth of noble metal nanoparticles on single-layer TiS₂ and TaS₂ nanosheets for hydrogen evolution reaction. *Energy and Environmental Science*. 2014;7:797–803.
- [99] Qiao J, Liu Y, Hong F, Zhang J. A review of catalysts for the electroreduction of carbon dioxide to produce low-carbon fuels. *Chemical Society Reviews*. 2014;43:631–675.
- [100] Hori Y. Electrochemical CO₂ reduction on metal electrodes. In: Vayenas CG, White RE, Gamboa-Aldeco ME, editors. *Modern Aspects of Electrochemistry*, vol. 42. New York: Springer; 2008. p. 89–189.
- [101] Schneider J, Jia H, Muckerman JT, Fujita E. Thermodynamics and kinetics of CO₂, CO, and H⁺ binding to the metal centre of CO₂ reduction catalysts. *Chemical Society Reviews*. 2012;41:2036–2051.
- [102] Chen Y, Kanan MW. Tin oxide dependence of the CO₂ reduction efficiency on tin electrodes and enhanced activity for tin/tin oxide thin-film catalysts. *Journal of the American Chemical Society*. 2012;134:1986–1989.
- [103] Costentin C, Robert M, Savéant J-M. Catalysis of the electrochemical reduction of carbon dioxide. *Chemical Society Reviews*. 2013;42:2423–2436.
- [104] Tripkovic V, Vanin M, Karamad M, Bjōrketun ME, Jacobsen KW, Thygesen KS, et al. Electrochemical CO₂ and CO reduction on metal-functionalized porphyrin-like graphene. *The Journal of Physical Chemistry C*. 2013;117:9187–9195.
- [105] Chen Y, Li CW, Kanan MW. Aqueous CO₂ reduction at very low overpotential on oxide-derived Au nanoparticles. *Journal of the American Chemical Society*. 2012;134:19969–19972.
- [106] Zhang S, Kang P, Meyer TJ. Nanostructured tin catalysts for selective electrochemical reduction of carbon dioxide to formate. *Journal of the American Chemical Society*. 2014;136:1734–1737.
- [107] Chan K, Tsai C, Hansen HA, Nørskov JK. Molybdenum sulfides and selenides as possible electrocatalysts for CO₂ reduction. *ChemCatChem*. 2014;6:1899–1905.
- [108] Shi C, Hansen HA, Lausche AC, Nørskov JK. Trends in electrochemical CO₂ reduction activity for open and close-packed metal surfaces. *Physical Chemistry Chemical Physics*. 2014;16:4720–4727.

- [109] Asadi M, Kumar B, Behranginia A, Rosen BA, Baskin A, Reprin N, et al. Robust carbon dioxide reduction on molybdenum disulphide edges. *Nature Communications*. 2014;5:4470.
- [110] Li F, Zhao S-F, Chen L, Khan A, MacFarlane DR, Zhang J. Polyethylenimine promoted electrocatalytic reduction of CO₂ to CO in aqueous medium by graphene-supported amorphous molybdenum sulphide. *Energy and Environmental Science*. 2016;9:216–223.

Defect Engineered 2D Materials for Energy Applications

Sai Sunil Kumar Mallineni, Sriparna Bhattacharya,
Fengjiao Liu, Pooja Puneet, Apparao Rao,
Anurag Srivastava and Ramakrishna Podila

Additional information is available at the end of the chapter

<http://dx.doi.org/10.5772/64605>

Abstract

Two-dimensional (2D) materials display unique properties that could be useful for many applications ranging from electronics and optoelectronics to catalysis and energy storage. Entropically necessary defects are inevitably present in 2D materials in the form of vacancies and grain boundaries. Additional defects, such as dopants, may be intentionally introduced to tune the electronic structure of 2D materials. While defects are often perceived as performance limiters, the presence of defects and dopants in 2D materials results in new electronic states to endow unique functionalities that are otherwise not possible in the bulk. In this chapter, we review defect-induced phenomena in 2D materials with some examples demonstrating the relevance of defects in electronic and energy applications. In particular, we present how the (i) N-dopant configuration in graphene changes the electron-phonon interactions, (ii) zigzag defects and edges in graphene increase the quantum capacitance to improve energy density of graphene-based supercapacitors, and (iii) charged grain boundaries in exfoliated Bi_2Te_3 preferentially scatter low-energy electrons and holes to enhance the thermoelectric performance.

Keywords: Engineering defects, 2D materials, Quantum capacitance, Energy storage

1. Introduction

Two-dimensional (2D) materials have intrigued physicists and material scientists for many decades due to an abundance of unusual physical phenomena that result from the confinement of charge, heat, and entropy flow to a plane [1]. For example, the ingenious harness of quantum mechanical phenomena, particular to lower dimensionality in graphene, has resulted

in intriguing observations such as the quantum Hall effect at room temperatures, quantized optical transmittance, nonlocal hot carrier transport, and Klein tunneling [2, 3]. Despite such fundamental breakthroughs, the potential of 2D materials has not yet completely manifested into practical devices due to material limitations [1, 4]. For instance, the lack of a band gap resulted in serious limitations for using graphene in electronics [4]. Defects in material science and engineering are often perceived as performance limiters, but in the case of 2D materials, defect engineering could provide a way to overcome many roadblocks and forge new frontiers. In this regard, others and we have shown that defects in 2D materials (e.g., dopants, vacancies) can provide an excellent handle to control material properties [5–8]. Specifically, we have shown that defects such as vacancies and N dopants in graphene could be used to control the electron–electron and electron–phonon scattering pathways [8]. These results provided critical breakthroughs for improving the quantum capacitance of graphene and doping graphene without compromising its intrinsic characteristics [6]. Defects also play a vital role in improving the properties of the so-called “beyond graphene” 2D materials. Previously, we used spark plasma sintering (SPS) to introduce charged grain boundaries (GB) in 2D Bi_2Te_3 for improving its thermoelectric (TE) figure of merit and compatibility factor [5]. Similarly, it has been demonstrated that defect engineering in 2D materials could improve many qualities ranging from electronic levels, conductivity, magnetism, and optics to structural mobility of dislocations and catalytic activities [9, 10]. As discussed in this chapter, defect engineering in 2D materials leads to the discovery of potentially exotic properties, which can enable unprecedented technological applications. In particular, we present how dopants and defects in (i) graphene could be used for optical and electrochemical energy storage applications and (ii) 2D Bi_2Te_3 could be controlled for enhancing its thermoelectric efficiency.

2. Nitrogen dopants for tuning the electronic and optical properties of graphene

Graphene is an ideal platform for many optoelectronic devices due to its distinctive combination of high electron mobility (μ), optical transparency, and gate/dopant-tunable carrier density [2]. However, to truly harness the potential of this combination and make graphene-based efficient optoelectronic devices a reality, optical and electronic properties of graphene must be tuned via substitutional doping [8]. While doping graphene with boron (B) or nitrogen (N) can tune the Fermi energy (E_F) and lead to *p*- or *n*-type graphene, it also compromises the inherently high electron mobility in doped graphene, which is useful for electronic applications [11–13]. Furthermore, the recombination rate of photogenerated carriers is also known to decrease with the presence of defects and dopants limiting applications of graphene in optoelectronics [8]. Indeed, the focus of many synthesis efforts in graphene has been to achieve large-area “defect-free” graphene for electronic applications because carrier-defect scattering limits the electron mobility—an important parameter for high-speed electronics [14–17]. Contrary to this conventional wisdom, we recently demonstrated that the defect configuration (in particular, N-dopant configuration in bilayer graphene lattice shown in **Figure 1a**) is more

important than the defect concentration for increasing carrier concentration without compromising photogenerated carrier lifetime [8].

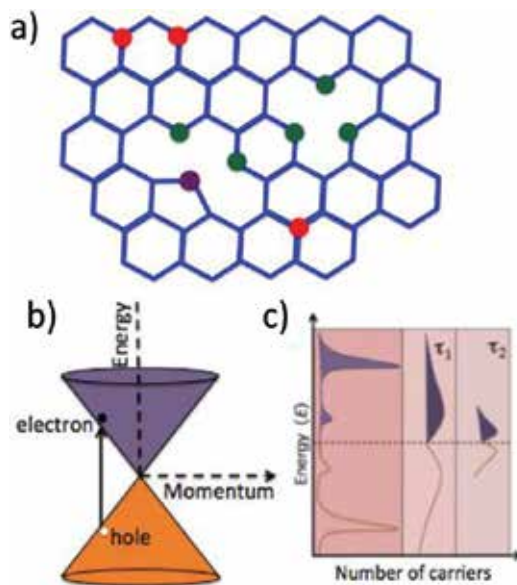


Figure 1. (a) Possible nitrogen dopant configurations in graphene lattice include pyridinic (green), pyrrolic (purple), and graphitic (red). While graphitic dopants (red) are purely substitutional, non-graphitic dopants (pyridinic and pyrrolic) result in additional defects such as vacancies or pentagons. (b) A schematic representation showing the linear energy dispersion for single-layer graphene and the arrow indicates excitation of electrons from the valence to the conduction band. (c) Under intense photoexcitation, the nonequilibrium carrier distribution (in the E-k space depicted by the energy dispersion shown in (b)) results in an initial rise in the transmitted intensity. The carriers (electron and hole distribution shown in blue and orange, respectively) equilibrate by carrier-carrier scattering on a timescale τ_1 . Subsequently, the carrier thermalization and decay occur through carrier-phonon scattering on a timescale τ_2 .

The electronic and optical properties of a single-layer graphene (SLG) can be described in terms of massless Dirac fermions with linear dispersion near the Fermi energy (**Figure 1b**). The semimetallic nature and electronic band structure of SLG allow for the photogeneration of electron-hole pairs at any wavelength in the visible-light spectrum [3]. This property is critical for many wide-bandwidth optoelectronic applications. As shown in **Figure 1b**, incident light excites electrons from the valence band (orange) into the conduction band (purple). Shortly after photoexcitation, incident photon-electron interactions create an out-of-equilibrium electron distribution (purple in **Figure 1c**), which initially relaxes on an ultrafast timescale ($\tau_1 \sim 100\text{--}300$ fs) to a hot Fermi-Dirac distribution and subsequently cools via phonon emission or defect scattering ($\tau_2 \sim 1\text{--}2$ ps) in graphene [8, 18]. In optoelectronic devices, when photoexcited electrons are scattered by phonons or defects, energy transferred to the lattice is dissipated as heat decreasing the net energy transported through charge carriers to drive a circuit. In the current scenario of graphene optoelectronic devices, a critical challenge is to increase the net charge carrier density and quench electron-defect relaxation pathways to extend photogenerated carrier lifetime.

The influence of defects on photogenerated carriers could be accounted by the inclusion of an extra term (A) in the expression for carrier scattering rate $\tau^{-1}(N) = A + BN + CN^2$, where A represents nonradiative recombination, usually due to defects or traps, B represents radiative recombination, N is the carrier density, and C represents Auger recombination. The photogenerated carriers are quickly cooled to ground state through scattering by defects (represented by A) in addition to the existing carrier-carrier and carrier-phonon scattering (term B) and Auger recombination (term C). In the context of optoelectronic applications, it is imperative to identify ideal dopant concentration and configuration in graphene for which A in the carrier scattering rate equation is minimized. As mentioned earlier, heteroatomic doping can tune E_F and alter density of states (DOS) and thereby modify its electronic and optical properties. For instance, N-doping in chemical vapor deposition (CVD) graphene resulted in a bandgap due to the suppression of electronic density of states near the Fermi level and a consequent reduction in μ [19, 20]. As mentioned earlier, it is well known that N atoms can be substitutionally doped in the graphene lattice either in the pyridinic, pyrrolic, or graphitic configurations (see **Figure 1a**). Our density functional theory (DFT) calculations previously showed that all the three dopant configurations (viz., pyridinic, pyrrolic, and graphitic) are stable structures with a positive energy (>9.5 eV) released during the formation with graphitic dopants exhibiting the highest stability (**Figure 2**) [8].

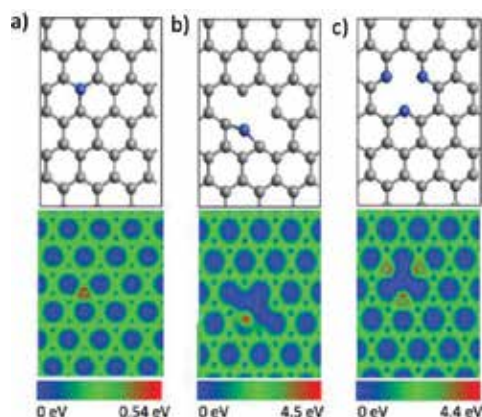


Figure 2. The lattice structure (top three panels) of graphitic (a), pyridinic (b), and pyrrolic (c) defects in graphene along with their electron density, obtained from our DFT calculations, shown in the bottom panels. The energy released on the formation of structure from free atoms for all the configurations was found to be positive (graphitic, 10.22 eV; pyridinic, 9.77 eV; and pyrrolic, 9.55 eV) confirming the stability of N-doped configurations.

2.1. CVD synthesis of N-graphene

Previously, we employed atmospheric pressure chemical vapor deposition (CVD) method for growing N-graphene [7]. This CVD set up consisted of a Cu foil loaded inside a 1 in. quartz tube at a temperature of 1,000 °C. Methane gas was used as the carbon source for graphene growth, while acetonitrile (AN) and benzylamine (BA) were used as precursors for N dopants in varying concentrations. The reaction was carried out under inert atmosphere by passing a

mixture of Ar and H₂ through the quartz tube reaction chamber. In particular, 450 sccm of Ar and 50 sccm of H₂ were used, and 2 sccm of methane was bubbled through the mixture of BA and AN. The volume percent of BA and AN varied in the ratio of 0:1, 1:1, and 3:1. Accordingly, the obtained samples were labeled S1, S2, and S3, respectively. Interestingly, we found that the N-dopant configuration (viz., graphitic, pyrrolic, and pyridinic) could be controlled using the ratio of BA to AN precursors.

2.2. The effects of N dopants in graphene: X-ray and Raman spectroscopy

We observed a strong correlation between the N-dopant configuration and the accompanying vibrational properties of N-doped CVD graphene: the N atoms bonded in the non-graphitic configurations (pyridinic and pyrrolic, observed using X-ray photoelectron spectroscopy or XPS) resulted in intense Raman disorder bands unlike the N atoms bonded in the graphitic configuration, even though the concentration of N dopants was higher in the latter case [7].

As shown in **Figure 3a**, we identified XPS peaks corresponding to graphitic, pyrrolic, and pyridinic configurations [21]. For pyridinic configuration, the N1s peak positions reported in the literature are usually in the range 398.1–399.3 eV. Similarly, pyrrolic configuration gives rise to peaks in the range 399.8–401.2 eV, while the peak around 400.5 eV (blue colored) is associated with the graphitic configuration. The orange-colored peak at ~401.5 and 406 eV may be attributed to different nitrogenated adsorbents [20, 21]. XPS results confirmed that the atomic percentages of nitrogen in S1, S2, and S3 were 0.2, 2.5, and 3.8 %, respectively [7]. It is important to note that S1 and S3 showed more non-graphitic N dopants compared to S2, which was purely graphitic doping. In order to further understand the effect of various nitrogen-doping configurations and concentrations on the electronic structure of graphene, we performed Raman spectroscopy of the samples S1, S2, and S3. The Raman spectrum of graphene displays four important bands [22, 23]: (i) the disorder or D band appears ~1350 cm⁻¹ due to the presence of defects such as edges, grain boundaries, or any other type of defects including dopants in the graphene lattice; (ii) in some studies, researchers have also reported the presence of D'-band ~1600–1625 cm⁻¹ in the Raman spectrum of highly disordered graphene [22]; (iii) the graphitic G band ~ 1585 cm⁻¹ arises due to doubly degenerate optical phonon modes at the Brillouin zone center. It is a first-order Raman scattering process, and (iv) the 2D band ~ 2700 cm⁻¹ is a consequence of second-order Raman scattering process involving intervalley scattering of in-plane transverse optical (*iTO*) phonons. Unlike the D band, which requires the presence of a defect to conserve the momentum of scattered electron along with an *iTO* phonon, 2D band does not require the presence of any defect due to the involvement of two *iTO* phonons and is always present in Raman spectra of both pristine and doped graphene [22]. The shape and width of the 2D band are sensitive to the number of layers in graphene. For example, 2D band in single-layer graphene (SLG) can be fit into a single Lorentzian peak, while for bilayer graphene, 2D band can be deconvoluted into four sub-peaks [23].

As seen in **Figure 3b**, the Raman spectra of pristine graphene samples did not exhibit strong D band in our studies. While samples S1 and S3, which contain non-graphitic doping configuration of nitrogen, showed strong D bands, the D band in sample S2 (graphitic) is similar to

that in pristine sample despite higher dopant concentration (~2.5 %). These results are consistent with our observations in the XPS spectra shown in **Figure 3a**. When nitrogen atoms enter the graphene lattice in non-graphitic configuration, vacancies are needed and result in armchair-type edges. Previous reports showed that armchair edges in graphene allow intervalley scattering of *iTO* phonons in the Brillouin zone unlike zigzag edges [22] and thus increase the intensity of the D band as in samples S1 and S3.

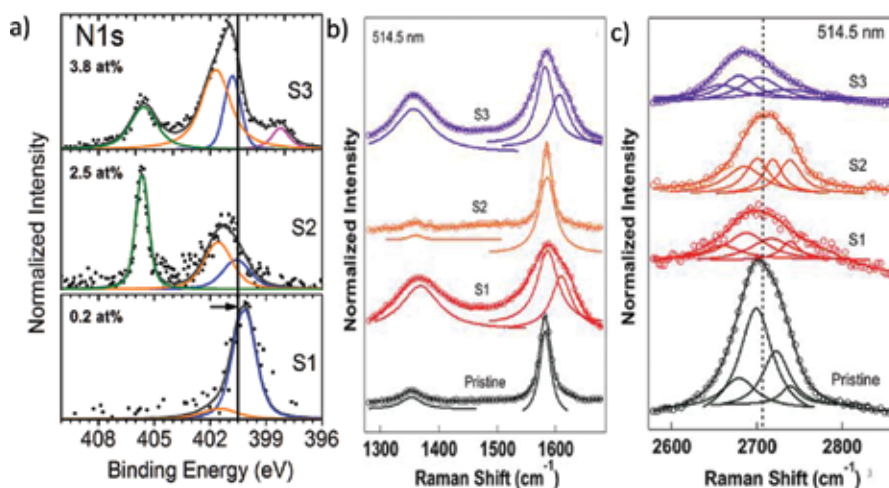


Figure 3. (a) XPS spectra for N1s line. The colored peaks represent the deconvolution of N1s peaks. The resolution of the spectrometer was 0.5 eV. The peak at 400.5 eV corresponds to graphitic configuration. Peaks at 398 and 400 eV correspond to non-graphitic. Raman spectra of pristine and N-graphene are shown in (b) and (c). As seen in (b), the D and D' bands increase in intensity for non-graphitic samples S1 and S3. The deconvolution of 2D band in (c) suggests that graphene samples are bilayer.

From the line-shape analysis of Raman 2D band (**Figure 3c**), we confirmed that our CVD-grown graphene samples are predominantly bilayers. As seen in **Figure 3c**, maximum downshift in 2D band (25 cm^{-1}) was observed for sample S3 with relatively large dopant percentage (~3.5 %). On the other hand, sample S2 (graphitic configuration) showed little downshift in 2D band compared to sample S1 in spite of having higher dopant concentration. 2D band in S1 showed a downshift of $\sim 10\text{--}15 \text{ cm}^{-1}$ even in the presence of low dopant concentrations (~0.2 %). These differences in the 2D band shift in the Raman spectra can also be attributed to the nature of the dopant environment. For example, in samples S1 and S3 that are non-graphitic in nature, due to lattice symmetry breaking, electronic structure of graphene is strongly perturbed leading to possible renormalization of electron and phonon energies. Such a renormalization in electron energies results in a concomitant downshift in phonon energies of 2D band [7].

2.3. Nonlinear optical studies of N-graphene

We further explored the influence of defects on the carrier scattering rate using pump-probe (PP) spectroscopy [8]. The differential transmittance ($\Delta T/T$) was obtained by taking the ratio of pump-induced change in the probe transmittance (ΔT) at a time t after the pump excitation

to the probe transmittance (T) in the absence of a pump (**Figure 4a**). The initial response is an incident pulse-width-limited rise in the transmitted signal immediately after the zero delay ($t = 0$), which eventually decays in an exponential manner. The best fit to the PP data was obtained with a bi-exponentially decaying function, $\Delta T/T = A_1 \exp(-t/\tau_1) + A_2 \exp(-t/\tau_2)$ with two distinct time scales: a fast component (τ_1) corresponding to the intraband carrier-carrier scattering and a slower component (τ_2) corresponding to carrier-phonon scattering (discussed before in **Figure 1b**). Both τ_1 and τ_2 values obtained from the best-fitted curves for the samples are tabulated in **Figure 4b**. As shown in **Figure 4b**, the carrier-carrier and carrier-phonon relaxation times do not decrease monotonically with increasing N content, akin to the Raman features described in **Figure 3**. Clearly, the dopants present in the non-graphitic configurations exhibit much faster relaxation times relative to dopants present in S2 with graphitic bonding or pristine graphene. Indeed, carriers in sample S1 decay much faster (within fs), despite lower N content, due to the presence of extended defects that lead to increased contribution from carrier-defect scattering. More importantly, N dopants in graphitic configuration do not affect the carrier recombination times even at >1 % doping, while pyrrolic/pyridinic configurations drastically decrease carrier lifetimes at concentrations as low as ~0.2 %.

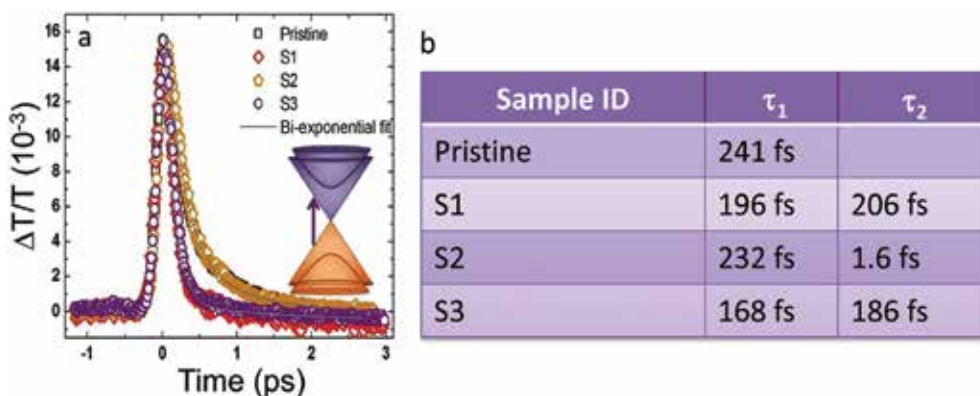


Figure 4. (a) Time-resolved differential transmission spectra of pristine and N-doped graphene samples S1, S2, and S3, respectively, obtained through pump-probe spectroscopy. The inset shows parabolic energy dispersion for bilayer graphene, where the arrow indicates excitation of electrons from valence to the conduction band. The solid lines represent bi-exponential fits based on the above equation. (b) Tabulated values of relaxation times τ_1 and τ_2 , corresponding to intraband carrier-carrier scattering and carrier-phonon scattering, respectively, obtained from the fits.

3. Defects in graphene for energy storage

The increasing global energy demands have spurred a rigorous search for new renewable energy sources. In recent times, fuel cells, photovoltaic devices/solar cells, and various other renewable energy sources have received much attention and are all promising candidates for clean energy production. However, today's batteries and capacitors, which are the main components for energy storage, cannot meet the world's demand for combined power and

energy densities [24–27]. As an example, the plot in **Figure 5** shows the general performance metrics for commercially available formats of charge/energy storage devices. This plot depicts *electrical capacitors* (on the top left hand side) with a fast response time and high-power-density *batteries and fuel cells* (on the bottom right hand side), which exhibit a large energy density due to the chemical/ionic basis of their reactions. The drawback of electrical capacitors is their inability to store large amounts of energy, while the batteries are incapable of fast charge/discharge cycles due to the slow nature of the ion diffusion processes. This gap between capacitors and battery performance has been a *major roadblock* in electrochemical energy storage. Electrochemical double-layer capacitors (EDLCs) or *supercapacitors* have been proposed to bridge the gap between these disparate devices by incorporating elements of both technologies [12, 28–33]. The charge is stored in the electric double layer, which forms at the electrode/electrolyte interfaces and leads to a double-layer capacitance (C_{dl}). The specific energy (E) of the EDLC may be expressed in terms of the total measured device capacitance (C_{meas}) and the operating voltage (V) as $E = (1/2)C_{meas}V^2$. Unlike traditional Li-ion batteries, EDLCs can be reliably used for hundreds of thousands of cycles since their charge storage mechanism does not involve ion motion and the consequent chemical irreversibility. Although the EDLCs are superior (say, to batteries) in terms of long-term cyclability, they suffer from poor energy density in that energy (or charge) is only stored at the surface/interface rather than within the bulk of the material.

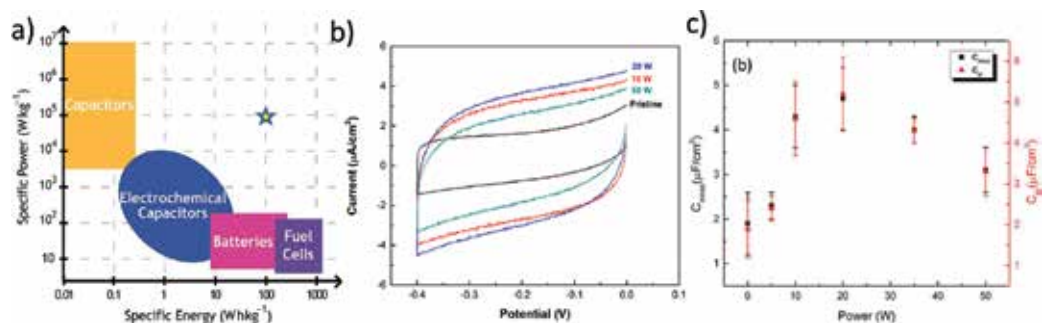


Figure 5. (a) Ragone plot showing specific power versus specific energy for common electrical energy storage devices. Supercapacitors are expected to bridge the gap between batteries and capacitors and impact nearly every area of electrical energy usage. For practical applications, the energy and power densities indicated by the star are needed. (b) Cyclic voltammetry (CV) characterization of plasma processed FLG samples (in 0.25 M TBAHFP dissolved in a 1 M acetonitrile). The area enclosed by the CV curves was used to parametrize the C_{meas} which increases with plasma power (indicated on the figure). (c) A close to threefold enhancement in the C_{meas} (left axis) and the contributions of the computed C_q (right axis), i.e., $1/C_{meas} = 1/C_{dl} + 1/C_q$ as a function of the plasma power.

Nanocarbons including carbon nanotubes and graphene have been widely used as an electrode in EDLCs due to their high surface area (~ 2000 m²/g), modest electrical conductivity, electrochemical stability, and open porosity [25, 27]. However, the performance of the carbon-based EDLCs (particularly, graphene) is fundamentally limited by the so-called quantum capacitance (C_q), which is defined as $C_q = e^2 \text{DOS}(E_F)$ with e being the charge of an electron [6]. An intrinsically small DOS (E_F) in graphene results in a small serial C_q which diminishes the total device

capacitance value ($1/C_{\text{meas}} = 1/C_{\text{dl}} + 1/C_{\text{q}}$) in EDLCs [6, 28]. Although graphene has high surface area and consequently high C_{dl} , the total EDLC energy is limited by small C_{q} . Defects can be advantageous for alleviating the limitation of C_{q} by increasing the DOS (discussed later in **Figures 5b** and **c**). In our previous work [6], we synthesized few-layer graphene (FLG) on Ni foil substrates through chemical vapor deposition and subsequently subjected to argon-based plasma processing to intentionally induce charged defects (see the inset in **Figure 6**). Argon was chosen because the constituent ionic species are limited to Ar^+ , implying relatively simple plasma chemistry.

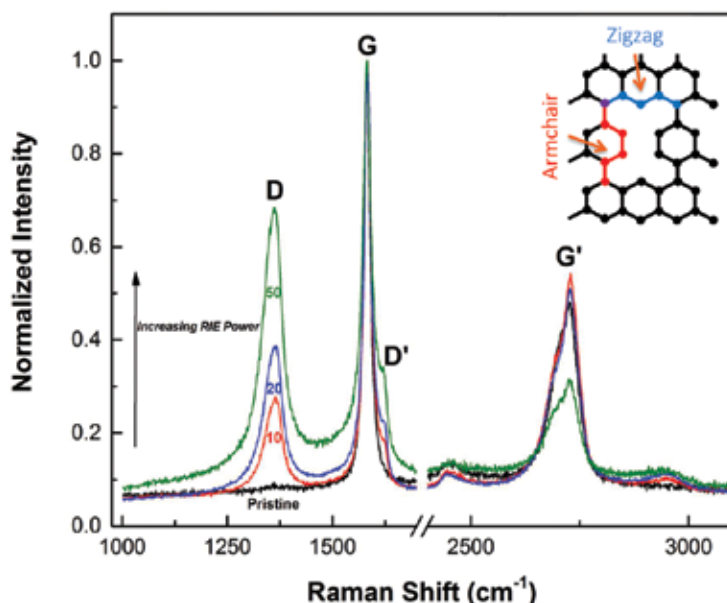


Figure 6. Enhanced plasma processing applied to the pristine sample results in a substantial intensity enhancement of the D- and D'-peaks as seen in the Raman spectra (normalized to the G-peak). An increase in power, say to 50 W, may result in irreversible changes due to graphene removal. The inset schematic shows the difference between armchair and zigzag defects (created using plasma processing) in the graphene lattice.

As shown in **Figure 6**, we found that the D band in the Raman spectrum of graphene increased with increasing power of plasma etching due to the introduction of new structural defects such as pores, which contain both armchair and zigzag edges. An important attribute of zigzag defects is that they may be electrically active and could contribute to an enhanced DOS much more than the armchair-type edge defects (which contribute less due to the two constituent carbon atoms belonging to different sublattices). We observed that the increase in plasma power resulted in a high device capacitance due to higher C_{q} arising from defect-induced DOS (E_{F}). Indeed, we used cyclic voltammetry to quantify the changes in C_{q} and C_{meas} (**Figure 5b**). The more than doubling of the C_{meas} from $1.9 \mu\text{F}/\text{cm}^2$ (for the pristine sample) to $4.7 \mu\text{F}/\text{cm}^2$ (for the sample subject to 20 W plasma) is remarkable and suggests a novel means of substantially enhancing capacitance through defects. However, at higher plasma power (>20 W), high

defect concentration results in poor electrical conductivity leading to a drop in C_{meas} suggesting the importance of defect concentration in determining 2D material properties.

Thus, as evidenced by our data in graphene, the presence of defects does not necessarily deteriorate the material performance. Though there is only one way for a given material to be defect-free, there are many possibilities for it to be imperfect. While defect configuration is important in determining the mobility through carrier scattering rate, controlling defect concentration is critical for electrochemical applications. Accordingly, future efforts must be focused on finding new approaches to identify and control the right defect configurations (e.g., N in graphitic configuration to increase carrier concentration without compromising carrier scattering rates or mobility) and concentrations, which could improve material properties instead of dismissing all defects as detrimental for carrier mobility.

4. Defects in 2D bulk materials for thermoelectric power generation

Thermoelectric (TE) materials have the potential to reduce global energy crisis and global warming effects by converting waste heat to electricity. As of 2005, the world energy usage was ~15 terawatts of energy, of which ~90 % was first converted to heat and the remainder ~10 % of energy was utilized [24]. In general, power plants and the transportation industry are the two main sources of heat energy losses that contribute to global warming. In recent years, prototype car models developed by automobile industries BMW and Ford have successfully transformed the waste heat from car exhausts to electricity using thermoelectric power generators, thus improving the fuel efficiency [24, 34].

A basic thermoelectric energy conversion module consists of n and p -type semiconducting materials, connected electrically in series and thermally in parallel [35]. The maximum thermoelectric efficiency is a product of the Carnot Efficiency and a term consisting of ZT or the thermoelectric figure of merit, which embodies interrelated material parameters, as given by $ZT = \alpha^2 \sigma T / k$, where α is Seebeck coefficient or thermopower, σ is the electrical conductivity, and $k (= k_E + k_L)$ is the total thermal conductivity comprised of electronic (k_E) and lattice contributions (k_L), respectively. The main challenge of improving the energy conversion efficiency and consequently the ZT of thermoelectric materials is the inherent *coupling* between the electrical conductivity and the Seebeck coefficient. In recent years, there has been significant scientific progress in the field of thermoelectrics with the use of nanostructured materials (e.g., superlattices, nanowires, and nanocomposites) that have simultaneously increased the power factor (the numerator of ZT) and reduced the thermal conductivity to achieve a high $ZT > 1$ [36].

4.1. Quantum confinement effects in 2D thermoelectric materials

In the early 1990s, Hicks et al. [37] predicted intriguing changes in transport properties upon lowering the dimensionality of existing bulk materials (e.g., from 3D to 2D) that were not observed in the corresponding bulk materials. A dramatic increase in the density of states (DOS) of low-dimensional materials was predicted that could increase the Seebeck coefficient

and potentially decouple the electronic transport properties. Moreover, the presence of numerous interfaces in low-dimensional materials also increased phonon scattering effects that reduced the lattice thermal conductivity, thus introducing opportunities to independently vary all the parameters constituting the ZT [38]. In the low-dimensional thermoelectric materials, dramatic changes in the density of states were observed in the PbTe-based thermoelectric materials owing to the quantum confinement effects that led to further *decoupling* of the TE transport properties and an enhancement of ZT [39].

Nevertheless, it is challenging to fabricate low-dimensional materials for commercial thermoelectric applications and devices, which must be a cost-effective and facile process. In addition, the nanostructured thermoelectric materials have to be thermodynamically stable to retain the desired 2D properties over time, to make the devices reliable and long lasting. To be able to make use of the advantages of low-dimensional materials as well as robustness of the bulk materials, bulk nanomaterials or nanocomposites have been used to enhance the thermoelectric performance of existing thermoelectric materials such as SiGe and PbTe [40, 41].

Controlling the multi-scale microstructures via defect engineering and consequently the length scales of the electrical and thermal transport is essential for enhancing TE performance. However, material properties (thermopower, electrical, and thermal conductivity) dictating the ultimate compatibility factor and ZT are inherently coupled at the nanoscale. Thus, any efforts to improve only one particular property (e.g., thermopower) using microstructure changes are often futile as they inadvertently deteriorate remaining properties (e.g., electrical conductivity). In this section, we describe how charged defects in 2D materials can introduce low-energy carrier filtering and selective charge carrier scattering (e.g., hole excessively scattered compared to electrons) to improve ZT and compatibility factor in Bi_2Te_3 .

4.2. Impact of charged grain boundaries in few-layered Bi_2Te_3

Discovered in the early 1950s by Goldsmid [42], Bi_2Te_3 is one of the most used and commercialized TE materials for room-temperature power generation and refrigeration applications [43]. The first TE refrigerator was designed using the p -type Bi_2Te_3 , which was estimated to have a figure of merit ~ 0.48 . In 2001, the thin-film superlattices were reported to exhibit enhanced $ZT \sim 2.4$ and ~ 1.4 at 300 K in the p -type $\text{Bi}_2\text{Te}_3/\text{Sb}_2\text{Te}_3$ and the n -type $\text{Bi}_2\text{Te}_3/\text{Bi}_2\text{Te}_{2.83}\text{Se}_{0.17}$, respectively [44]. While a high $ZT \sim 1.5$ was realized in the bulk p -type Bi_2Te_3 via nanostructuring techniques such as ball-milling [45], melt-spinning [46, 47], and hydrothermal synthesis [48], it was found that these methods were ineffective for the n -type Bi_2Te_3 . Like graphite, n -type Bi_2Te_3 is easily cleavable, and these traditional nanostructuring methods were too harsh and resulted in the deterioration of its basal plane (or *in-plane*) properties (**Figure 7a**).

Recently, Puneet et al. [5] utilized a novel technique of chemical exfoliation followed by spark plasma sintering (CE-SPS) in the n -type $\text{Bi}_2\text{Te}_{2.7}\text{Se}_{0.3}$ that significantly improved the TE compatibility factor and stabilized the ZT peak at higher temperatures (300–450 K) as compared to the commercial ingot. Based on the studies of emerging two-dimensional (2D) materials (e.g., graphene), it may be expected that the electronic, thermal, and optical properties of chemically exfoliated n -type Bi_2Te_3 should exhibit properties that are different from the

bulk. In the following paragraphs, we discuss the effect of the chemical exfoliation and spark plasma sintering of *n*-type Bi₂Te₃ as compared to the bulk commercial ingot.

The bulk bismuth telluride (Bi₂Te₃) exhibits a rhombohedral crystal structure belonging to the space group $R\bar{3}m(D5)$, which is more commonly represented by a hexagonal crystal structure as shown in **Figure 7a**. The hexagonal unit cell of Bi₂Te₃ is composed of three quintuples with lattice constants $a = 0.4384 \text{ \AA}$ and $c = 3.036 \text{ \AA}$, respectively. As shown in the figure, each quintuple consists of five atoms stacked in the order Te¹-Bi-Te²-Bi-Te¹ along the *c*-axis, which are bonded by ionic-covalent bonds. The Te¹-Te¹ layers between the two quintuples are held together by the weak van der Waals forces that make the Bi₂Te₃ easily cleavable. The *n*-type Bi₂Te₃ was obtained by partially doping Se at the Te¹ or Te² sites, which represent the Te atoms with two types of bonding.

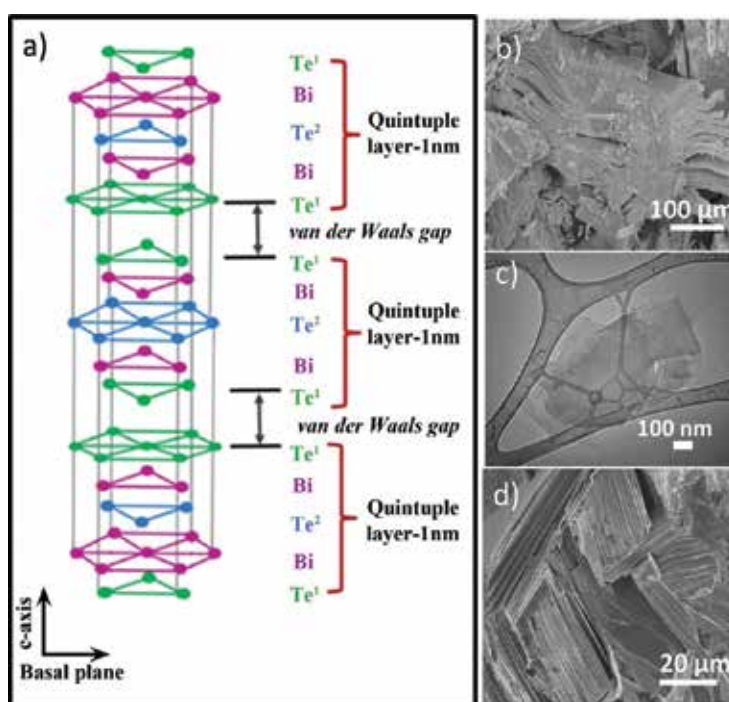


Figure 7. (a) A schematic representation showing Bi₂Te₃ rhombohedral crystal structure belonging to the space group $R\bar{3}m(D5)$. Upon chemical exfoliation, the crystal breaks at the van der Waals gap. (b) A scanning electron micrograph showing the layered structure of bulk Bi₂Te₃ ingot. (c) A transmission electron micrograph showing chemically exfoliated quasi-2D Bi₂Te₃, which is repacked using spark plasma sintering (d) to achieve better thermoelectric performance through charged grain boundaries.

The nanostructuring of the commercial *n*-type Bi₂Te₃ ingot (see **Figure 7b**, purchased from the Marlow Industries, USA) was achieved by the chemical exfoliation method, using *N*-methyl-2-pyrrolidone (NMP) solution which was ultrasonicated using a tip sonicator (Branson 250) for 3, 5, 8, or 13 h, respectively. After centrifuging the solution and vacuum filtering the supernatant through a 0.45 mm nylon filter paper, the filtered powder was washed several times using

deionized water to remove any residual NMP. The exfoliated nanolayers (see **Figure 7c**) were ~50 nm in thickness, which were then compacted using the spark plasma sintering (SPS, Dr. Sinter LabH-515S) technique at a holding temperature of 500 °C and an applied pressure of 30 MPa for 5 min under a dynamic vacuum. For the SPS process, the samples were loaded into graphite dies, and the pressure was applied using graphite rods. The resulting SPS-processed pellets were 12.5 mm in diameter and 2–3 mm in thickness, yielding samples with 98–99 % of the theoretical density (see **Figure 7c**).

The rapid densification technique by SPS has distinct advantages over other types of sintering techniques, such as the hot pressing. The SPS process is capable of sintering material powders within a very short time, in the order of minutes [49, 50]. As a result, it is possible to retain the metastable micro-/nanostructures of materials by limiting their grain growth and excessive diffusion during the sintering process. Furthermore, unlike other sintering techniques like hot pressing which uses furnace heating, only the graphite cylinder, rods, and sample are heated by the joule heating produced by pulsed dc in the SPS, which leads to even shorter processing times.

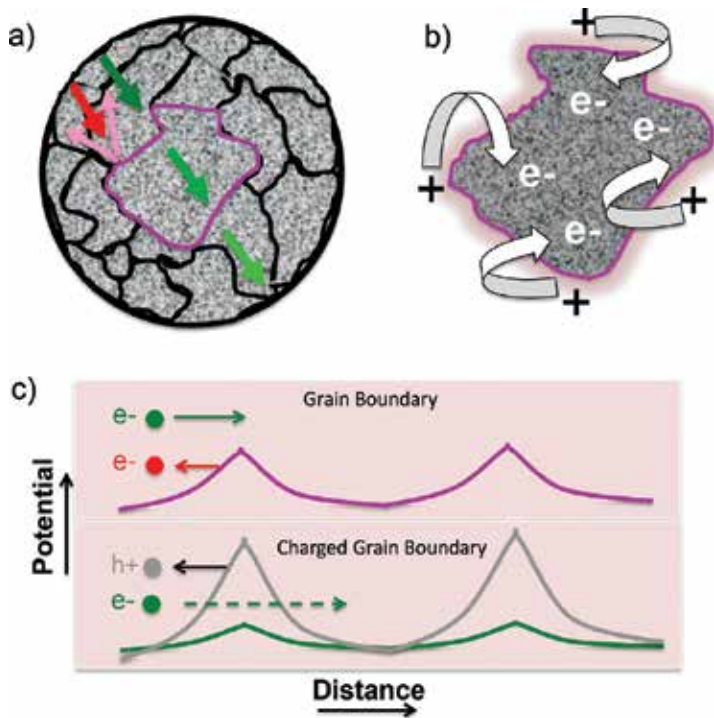


Figure 8. (a) Charged defects near the grain boundaries (GB) can induce excess majority carriers (b) and preferentially scatter holes over electrons and low kinetic energy carriers (red arrow in panels a and c) due to engineered charged GB potential barriers shown in (c).

Contrary to the general understanding that defects in a crystal lattice are detrimental to the transport properties of materials, the defects in 2D materials are extremely useful and could

be manipulated to generate controlled defects for novel and innovative applications. As observed in the few-layered bulk Bi_2Te_3 , the localized positive charges in the grain boundaries introduced extra electrons in the material, thereby increasing the carrier concentration n (see **Figure 3a** in Ref. [5]). This increase in n was attributed to the injection of donor-like defects (**Figure 8a** and **b**), arising from positively charged anti-sites/Te vacancies on the exfoliated grain boundaries, due to chemical/mechanical exfoliation [51]. Moreover, these positively charged or interfacial charged *defects* acted as a potential barrier (see **Figure 8c**) to selectively filter out low-energy holes (or minority carriers) as shown schematically by Puneet et al. (see **Figure 3** in Ref. [5]). These charged *defects* in the few-layered n -type Bi_2Te_3 thus shifted the onset of the bipolar (or two carrier) effects and consequently the maximum ZT value to higher temperatures, thus optimizing the ZT over a broader range of temperature. In addition, the thermoelectric compatibility factor of the few-layered n -type Bi_2Te_3 was significantly improved, which determined the ability of these materials to be segmented to other thermoelectric materials such as PbTe at higher temperatures, for operation over a broader range of temperature.

In summary, the CE-SPS processing of 2D Bi_2Te_3 leads to preferential scattering of electrons at charged grain boundaries and optimizes the band filling, thereby increasing the electrical conductivity despite the presence of numerous grain boundaries, and mitigates the bipolar effect via band occupancy optimization leading to an upshift in ZT peak (by ~ 100 K) and stabilization of the ZT peak over a broad temperature range of ~ 150 K. These changes in electrical and thermal transport led in turn to a more device-design friendly compatibility factor.

5. Conclusions

As exemplified by graphene and Bi_2Te_3 , the presence of defects and dopants imparts the host material with new micro/quantum states or energy configurations that can strongly influence optical, electronic, and thermal properties. In addition to the above properties, S and F dopants are being explored to make graphene magnetic [10, 52–55], while N dopants are expected to provide much higher enhancements in quantum capacitance without compromising electrical conductivity [28]. Similar to Bi_2Te_3 , defects in other layered systems such as SnSe and TaSe₂ could be engineered to achieve better thermoelectric performance [56–62]. Although this chapter presented only some examples of defects in 2D materials, the same concepts also hold true for other 2D materials such as MoS₂, WS₂, and BN. Indeed, some properties (e.g., luminescence and catalytic activity) of these materials can be tuned using defects [63–68]. As the design and development of new 2D materials are costly, complex, and limited due to the relatively poor air stability of many materials (e.g., silicene and phosphorene), the realization of desired properties and functionalities through control of defects (e.g., vacancies, dopants) in 2D materials is necessary. Though there is only one way for a given material to be defect-free, there are many possibilities for materials to be imperfect. The global scientific endeavors on understanding defects, such as the efforts presented in this chapter, provide a glimpse of the enormous potential of defects warranting further interdisciplinary research efforts.

Author details

Sai Sunil Kumar Mallineni¹, Sriparna Bhattacharya¹, Fengjiao Liu¹, Pooja Puneet¹, Apparao Rao^{1,2}, Anurag Srivastava³ and Ramakrishna Podila^{1,2,3,4*}

*Address all correspondence to: rpodila@g.clemson.edu

1 Department of Physics and Astronomy, Clemson Nanomaterials Center, Clemson University, Clemson, SC, USA

2 Center for Optical Materials Science and Engineering Technologies, Clemson University, Clemson, SC, USA

3 ABV-Indian Institute of Information Technology and Management, Gwalior, MP, India

4 Laboratory of Nano-bio Physics, Clemson University, Clemson, SC, USA

References

- [1] Butler SZ, Hollen SM, Cao L, Cui Y, Gupta JA, Gutiérrez HR, et al. Progress, challenges, and opportunities in two-dimensional materials beyond graphene. *ACS Nano*. 2013; 7:2898–926.
- [2] Geim AK, Novoselov KS. The rise of graphene. *Nat Mater* [Internet]. 2007;6(3):183–91. Available from: <http://www.nature.com/doi/10.1038/nmat1849>
- [3] Bonaccorso F, Sun Z, Hasan T, Ferrari AC. Graphene photonics and optoelectronics. *Nat Photonics* [Internet]; 2010;4(9):611–22. Available from: <http://arxiv.org/abs/1006.4854>
- [4] Geim a K, Grigorieva I.V. Van der Waals heterostructures. *Nature* [Internet]; 2013;499(7459):419–25. Available from: <http://www.ncbi.nlm.nih.gov/pubmed/23887427>
- [5] Puneet P, Podila R, Karakaya M, Zhu S, He J, Tritt TM, et al. Preferential scattering by interfacial charged defects for enhanced thermoelectric performance in few-layered n-type Bi₂Te₃. *Sci Rep* [Internet]. 2013;3:3212. Available from: <http://www.pubmedcentral.nih.gov/articlerender.fcgi?artid=3827612&tool=pmcentrez&rendertype=abstract>
- [6] Narayanan R, Yamada H, Karakaya M, Podila R, Rao AM, Bandaru PR. Modulation of the electrostatic and quantum capacitances of few layered graphenes through plasma processing. *Nano Lett.*; 2015;15(5):3067–72.
- [7] Podila R, Chacón-Torres J, Spear JT, Pichler T, Ayala P, Rao A.M. Spectroscopic investigation of nitrogen doped graphene. *Appl Phys Lett* [Internet]. 2012;101(12):

123108. Available from: <http://link.aip.org/link/APPLAB/v101/i12/p123108/s1&Agg=doi>
- [8] Anand B, Karakaya M, Prakash G, Sankara Sai SS, Philip R, Ayala P, et al. Dopant-configuration controlled carrier scattering in graphene. *RSC Adv* [Internet]; 2015;5(73): 59556–63. Available from: <http://xlink.rsc.org/?DOI=C5RA05338B>
- [9] Araujo PT, Terrones M, Dresselhaus MS. Defects and impurities in graphene-like materials. *Mater. Today*. 2012;15:98–109.
- [10] Zou X, Yakobson BI. An open canvas—2D materials with defects, disorder, and functionality. *Acc Chem Res*. 2015;48(1):73–80.
- [11] Rao CNR, Gopalakrishnan K, Govindaraj A. Synthesis, properties and applications of graphene doped with boron, nitrogen and other elements. *Nano Today*. 2014;9: 324–43.
- [12] Han J, Zhang LL, Lee S, Oh J, Lee KS, Potts JR, et al. Generation of B-doped graphene nanoplatelets using a solution process and their supercapacitor applications. *ACS Nano*. 2013;7(1):19–26.
- [13] Wei D, Liu Y, Wang Y, Zhang H, Huang L, Yu G. Synthesis of n-doped graphene by chemical vapor deposition and its electrical properties. *Nano Lett*. 2009;9(5):1752–8.
- [14] Park KH, Lee D, Kim J, Song J, Lee YM, Kim HT, et al. Defect-free, size-tunable graphene for high-performance lithium ion battery. *Nano Lett*. 2014;14(8):4306–13.
- [15] Wang M, Jang SK, Jang WJ, Kim M, Park SY, Kim SW, et al. A platform for large-scale graphene electronics - CVD growth of single-layer graphene on CVD-grown hexagonal boron nitride. *Adv Mater*. 2013;25(19):2746–52.
- [16] Paton KR, Varrla E, Backes C, Smith RJ, Khan U, O'Neill A, et al. Scalable production of large quantities of defect-free few-layer graphene by shear exfoliation in liquids. *Nat Mater* [Internet]. 2014;13(6):624–30. Available from: <http://www.ncbi.nlm.nih.gov/pubmed/24747780>
- [17] Coleman JN. Liquid exfoliation of defect-free graphene. *Acc Chem Res*. 2013;46(1):14–22.
- [18] Lee C, Schibli T. Ultra-short optical pulse generation with single-layer graphene. *J Nonlinear Opt Phys Mater* [Internet]. 2010;6. Available from: <http://arxiv.org/abs/1010.0990> \n<http://www.worldscientific.com/doi/pdf/10.1142/S021886351000573X>
- [19] Lherbier A, Blase X, Niquet YM, Triozon F, Roche S. Charge transport in chemically doped 2D graphene. *Phys Rev Lett*. 2008;101(3).
- [20] Wang H, Maiyalagan T, Wang X. Review on recent progress in nitrogen-doped graphene: synthesis, characterization, and its potential applications. *ACS Catal*. 2012;2:781–94.

- [21] Susi T, Pichler T, Ayala P. X-ray photoelectron spectroscopy of graphitic carbon nanomaterials doped with heteroatoms. *Beilstein J Nanotechnol.* 2015;6:177–92.
- [22] Malard LM, Pimenta MA, Dresselhaus G, Dresselhaus MS. Raman spectroscopy in graphene. *Phys Rep.* 2009;473:51–87.
- [23] Ferrari AC, Meyer JC, Scardaci V, Casiraghi C, Lazzeri M, Mauri F, et al. Raman spectrum of graphene and graphene layers. *Phys Rev Lett.* 2006;97(18).
- [24] Cullen JM, Allwood JM. The efficient use of energy: Tracing the global flow of energy from fuel to service. *Energy Policy.* 2010;38(1):75–81.
- [25] Liu C, Li F, Ma L-P, Cheng H-M. Advanced materials for energy storage. *Adv Mater.* 2010;22(8):E28–62.
- [26] Gogotsi Y. What nano can do for energy storage. *ACS Nano.* 2014;8:5369–71.
- [27] Brownson DAC, Kampouris DK, Banks CE. An overview of graphene in energy production and storage applications. *J Power Sources [Internet]* . 2011;196(11):4873–85. Available from: <http://www.sciencedirect.com/science/article/pii/S0378775311003764>
- [28] Karakaya M, Zhu J, Raghavendra AJ, Podila R, Parler SG, Kaplan JP, et al. Roll-to-roll production of spray coated N-doped carbon nanotube electrodes for supercapacitors. *Appl Phys Lett [Internet]*. 2014;105(26):263103. Available from: <http://scitation.aip.org/content/aip/journal/apl/105/26/10.1063/1.4905153>
- [29] Zhou R, Meng C, Zhu F, Li Q, Liu C, Fan S, et al. High-performance supercapacitors using a nanoporous current collector made from super-aligned carbon nanotubes. *Nanotechnology.* 2010;21(34):345701.
- [30] Chen X, Lin H, Chen P, Guan G, Deng J, Peng H. Smart, stretchable supercapacitors. *Adv Mater.* 2014;26(26):4444–9.
- [31] Kim B, Chung H, Kim W. High-performance supercapacitors based on vertically aligned carbon nanotubes and nonaqueous electrolytes. *Nanotechnology.* 2012;23:155401.
- [32] Chen T, Peng H, Durstock M, Dai L. High-performance transparent and stretchable all-solid supercapacitors based on highly aligned carbon nanotube sheets. *Sci Rep [Internet]*. 2014;4:3612. Available from: <http://www.pubmedcentral.nih.gov/articlerender.fcgi?artid=3885879&tool=pmcentrez&rendertype=abstract>
- [33] Arcila-Velez MR, Zhu J, Childress A, Karakaya M, Podila R, Rao AM, et al. Roll-to-roll synthesis of vertically aligned carbon nanotube electrodes for electrical double layer capacitors. *Nano Energy [Internet]*. 2014;8:9–16. Available from: <http://dx.doi.org/10.1016/j.nanoen.2014.05.004>
- [34] Karpe S. Thermoelectric power generation using waste heat of automobile. *International Journal of Current Engineering and Technology.* 2016;4(4):144–8.

- [35] Tritt TM. Thermoelectrics run hot and cold. *Science* (80-) [Internet]. 1996;272(5266):1276–7. Available from: <http://www.sciencemag.org/content/272/5266/1276> \n<http://www.sciencemag.org/content/272/5266/1276.full.pdf> \n<http://www.sciencemag.org/content/272/5266/1276.summary?sid=4cff17c5-fc80-4d5d-9567-95557e8c2b64>
- [36] Minnich AJ, Dresselhaus MS, Ren ZF, Chen G. Bulk nanostructured thermoelectric materials: current research and future prospects. *Energy Environ Sci* [Internet]. 2009;2(5):466. Available from: <http://xlink.rsc.org/?DOI=b822664b>
- [37] Hicks LD, Harman TC, Sun X, Dresselhaus MS. Experimental study of the effect of quantum-well structures on the thermoelectric figure of merit. *Phys Rev B* [Internet]. 1996;53(16):R10493–6. Available from: <http://link.aps.org/doi/10.1103/PhysRevB.53.R10493> \nhttp://prb.aps.org/abstract/PRB/v53/i16/pR10493_1 \nhttp://prb.aps.org/pdf/PRB/v53/i16/pR10493_1
- [38] Dresselhaus MS, Chen G, Tang MY, Yang R, Lee H, Wang D, et al. New directions for low-dimensional thermoelectric materials. *Adv Mater*. 2007;19(8):1043–53.
- [39] Hicks LD, Dresselhaus MS. Effect of quantum-well structures on the thermoelectric figure of merit. *Phys Rev B*. 1993;47:12727–31. [Internet]. Available from: <http://link.aps.org/doi/10.1103/PhysRevB.47.12727>
- [40] Hsu KF, Loo S, Guo F, Chen W, Dyck JS, Uher C, et al. Cubic AgPb(m)SbTe(2+m): bulk thermoelectric materials with high figure of merit. *Science*. 2004;303(5659):818–21.
- [41] Wang XW, Lee H, Lan YC, Zhu GH, Joshi G, Wang DZ, et al. Enhanced thermoelectric figure of merit in nanostructured n-type silicon germanium bulk alloy. *Appl Phys Lett* [Internet]. 2008;93(19):193121. Available from: <http://scitation.aip.org/content/aip/journal/apl/93/19/10.1063/1.3027060>
- [42] Goldsmid HJ. Thermoelectric refrigeration. *Proc Intersoc Energy Convers Eng Conf*. 1964;1:iv, 106.
- [43] Goldsmid HJ, Douglas RW. The use of semiconductors in thermoelectric refrigeration. *Br J Appl Phys*. 2002;5(12):458–458.
- [44] Venkatasubramanian R, Siivola E, Colpitts T, O'Quinn B. Thin-film thermoelectric devices with high room-temperature figures of merit. *Nature* [Internet]. 2001;413(6856):597–602. Available from: <http://www.ncbi.nlm.nih.gov/pubmed/11595940>
- [45] Poudel B, Hao Q, Ma Y, Lan Y, Minnich A, Yu B, et al. High-thermoelectric performance of nanostructured bismuth antimony telluride bulk alloys. *Science*. 2008;320(5876):634–8.
- [46] Li J-F, Liu W-S, Zhao L-D, Zhou M. High-performance nanostructured thermoelectric materials. *NPG Asia Mater*. 2010;2(4):152–8.
- [47] Xie W, Tang X, Yan Y, Zhang Q, Tritt TM. High thermoelectric performance BiSbTe alloy with unique low-dimensional structure. *J Appl Phys*. 2009;105(11).

- [48] Ji X, He J, Su Z, Gothard N, Tritt TM. Improved thermoelectric performance in polycrystalline p-type Bi_2Te_3 via an alkali metal salt hydrothermal nanocoating treatment approach. *J Appl Phys* [Internet]. 2008;104(3):034907. Available from: <http://scitation.aip.org/content/aip/journal/jap/104/3/10.1063/1.2963706>
- [49] Yang K, He J, Su Z, Reppert JB, Skove MJ, Tritt TM, et al. Inter-tube bonding, graphene formation and anisotropic transport properties in spark plasma sintered multi-wall carbon nanotube arrays. *Carbon N Y* [Internet]. 2010;48(3):756–62. Available from: <http://dx.doi.org/10.1016/j.carbon.2009.10.022>
- [50] Puneet P, Podila R, Zhu S, Skove MJ, Tritt TM, He J, et al. Enhancement of thermoelectric performance of ball-milled bismuth due to spark-plasma-sintering-induced interface modifications. *Adv Mater*. 2013;25(7):1033–7.
- [51] Teweldebrhan D, Goyal V, Balandin AA. Exfoliation and characterization of bismuth telluride atomic quintuples and quasi-two-dimensional crystals. *Nano Lett*. 2010;10(4):1209–18.
- [52] Yazyev O.V., Helm L. Defect-induced magnetism in graphene. *Phys Rev B: Condens Matter Mater Phys*. 2007;75(12).
- [53] Yazyev O.V. Magnetism in disordered graphene and irradiated graphite. *Phys Rev Lett*. 2008;101(3).
- [54] Sepioni M, Nair RR, Rablen S, Narayanan J, Tuna F, Winpenny R, et al. Limits on intrinsic magnetism in graphene. *Phys Rev Lett*. 2010;105(20).
- [55] Zhu J, Park H, Podila R, Wadehra A, Ayala P, Oliveira L, et al. Magnetic properties of sulfur-doped graphene. *J Magn Magn Mater*. 2016;401:70–6.
- [56] Bovet M, Popović D, Clerc F, Koitzsch C, Probst U, Bucher E, et al. Pseudogapped Fermi surfaces of 1T-TaS₂ and 1T-TaSe₂: a charge density wave effect. *Phys Rev B*. 2004;69(12):1–9.
- [57] Demsar J, Forró L, Berger H, Mihailovic D. Femtosecond snapshots of gap-forming charge-density-wave correlations in quasi-two-dimensional dichalcogenides 1T-TaS₂ and 2H-TaSe₂. *Phys Rev B* [Internet] . 2002;66(4):041101. Available from: <http://arxiv.org/abs/cond-mat/0203590> \n<http://link.aps.org/doi/10.1103/PhysRevB.66.041101>
- [58] Neal AT, Du Y, Liu H, Ye PD. Two-dimensional TaSe₂ metallic crystals: spin-orbit scattering length and breakdown current density. *ACS Nano*. 2014;8(9):9137–42.
- [59] Yan Z, Jiang C, Pope TR, Tsang CF, Stickney JL, Goli P, et al. Phonon and thermal properties of exfoliated TaSe₂ thin films. *J Appl Phys*. 2013;114(20).
- [60] Snyder GJ, Toberer ES. Complex thermoelectric materials. *Nat Mater*. 2008;7(2):105–14.

- [61] Wang FQ, Zhang S, Yu J, Wang Q. Thermoelectric properties of single-layered SnSe sheet. *Nanoscale* [Internet]. 2015;7(38):15962–70. Available from: <http://www.ncbi.nlm.nih.gov/pubmed/26367369>
- [62] Zhao L-D, Lo S-H, Zhang Y, Sun H, Tan G, Uher C, et al. Ultralow thermal conductivity and high thermoelectric figure of merit in SnSe crystals. *Nature* [Internet]. 2014;508(7496):373–7. Available from: <http://www.ncbi.nlm.nih.gov/pubmed/24740068>
- [63] Kim CJ, Brown L, Graham MW, Hovden R, Havener RW, McEuen PL, et al. Stacking order dependent second harmonic generation and topological defects in h-BN bilayers. *Nano Lett.* 2013;13(11):5660–5.
- [64] Pierret A, Loayza J, Berini B, Betz A, Plaçais B, Ducastelle F, et al. Excitonic recombinations in h-BN: from bulk to exfoliated layers. *Phys Rev B: Condens Matter Mater Phys.* 2014;89(3).
- [65] Yuan S, Roldan R, Katsnelson MI, Guinea F. Effect of point defects on the optical and transport properties of MoS₂ and WS₂. *Phys Rev B: Condens Matter Mater Phys.* 2014;90(4).
- [66] Chen Z, Forman AJ, Jaramillo TF. Bridging the gap between bulk and nanostructured photoelectrodes: the impact of surface states on the electrocatalytic and photoelectrochemical properties of MoS₂. *J Phys Chem C.* 2013;117(19):9713–22.
- [67] Mouri S, Miyauchi Y, Matsuda K. Tunable photoluminescence of monolayer MoS₂ via chemical doping. *Nano Lett.* 2013;13(12):5944–8.
- [68] Nan H, Wang Z, Wang W, Liang Z, Lu Y, Chen Q, et al. Strong photoluminescence enhancement of MoS₂ through defect engineering and oxygen bonding. *ACS Nano.* 2014;8(6):5738–45.

Graphene against Other Two-Dimensional Materials: A Comparative Study on the Basis of Electronic Applications

Rafael Vargas-Bernal

Additional information is available at the end of the chapter

<http://dx.doi.org/10.5772/63916>

Abstract

The evolution of the electronics industry since almost 75 years ago has depended on the novel materials and devices that continuously are introduced. In first decades of this century, 2D materials are impelling this development through materials such as graphene, graphane, graphone, graphyne, graphdiyne, silicene, silicane, germanene, germanane, stanene, phosphorene, arsenene, antimonene, borophene, hexagonal boron nitride (*h*BN), transition metal dichalcogenides (TMDs), and MXenes. In this work, the main strategies to modify electrical properties of 2D materials are studied for obtaining dielectric, semiconducting, or semimetallic properties. The effects of doping, chemical modification, electrical field, or compressive and/or tensile strains are considered. In addition, the light-matter interaction to develop optoelectronic applications is analyzed. In next three decades, a lot of scientific research will be realized to completely exploit the use of 2D materials either as single monolayers or as stacked multilayers in several fields of knowledge with a special emphasis on the benefit to the electronic industry and ultimately our society.

Keywords: Graphene, 2D materials, electronic devices, electrical properties, nanoelectronics, flexible electronics

1. Introduction

The more novel electronic devices that will be produced in the current century will be made a reality, thanks to the emerging two-dimensional (2D) nanomaterials based on carbon (C), silicon (Si), germanium (Ge), tin (Sn), phosphorus (P), arsenic (As), antimony (Sb), boron (B), and their

combinations. Until now, many papers presenting reviews related to 2D materials have been presented [1–5]; however, a direct comparison of these materials for electronic applications is necessary. This study will allow us to know the advantages and disadvantages of 2D materials for electronic applications. A clear trend related to the choice of these materials for determined applications must be established. In this context, a comparison of the physical properties of these materials is used to exploit them from several technical points of view. Moreover, the possible synergy between 2D materials is presented as a strategic way to exploit these materials completely in more complex applications such as the development of hybrid or multifunctional materials.

Several 2D materials, such as carbon-based 2D materials, silicate clays, transition metal dichalcogenides (TMDs), and transition metal oxides (TMOs), have been used in electronic devices. Particularly, materials such as graphene, molybdenum disulfide (MoS_2), tungsten disulfide (WS_2), molybdenum trioxide (MoO_3), and silicon carbide (SiC) provide enhanced physical and chemical functionality making use of uniform shapes, high surface-to-volume ratios, and surface charge [1–5]. While dichalcogenides and buckled nanomaterials have sizeable band gaps, graphene has zero band gap and they also become semiconducting or metallic materials. These materials are very sensitive to the number of layers, ranging from indirect band-gap semiconductor in the bulk phase to direct band-gap semiconductor in monolayers. 2D materials are leading to ubiquitous flexible and transparent electronic systems for applications in integrated circuits, solar cells, and storage energy [2, 4]. Comparison of the performance in electrical and optical properties of 2D materials is presented here.

A few decades ago, the potential of the electronics industry depended entirely on silicon. New materials such as carbon allotropes of the groups III, IV and V are being introduced to increase efficiency, specific capacity, and speed of information processing. Actually, in electronics, 2D materials are used in the manufacture of supercapacitors, batteries, field-effect transistors (FETs), solar cells, light-emitting diodes, transparent electrodes, coatings for electrostatic dissipation, and/or electromagnetic interference shielding, etc. The potential of the 2D materials has not been fully discovered yet; however, new potential applications are being invented and others are emerging from the laboratory, which are beneficial for the development of materials science and engineering. The use of 2D materials in the electronic industry will be extended in the design of new electronic devices being applied either individually or as a component within a composite, hybrid, or functional material. This chapter has been divided as follows: Section 2 introduces basic concepts about 2D materials. Graphene and its derivatives are studied in Section 3. Section 4 analyses different allotropes based on chemical elements with the exception of carbon. 2D materials such as hexagonal boron nitride ($h\text{BN}$), TMDs, and MXenes are discussed in Section 5. In Section 6, optoelectronic applications are presented. Finally, conclusions about the work are given in Section 7.

2. Basic concept about 2D materials

2D materials, also known as 2D topological materials or single-layer materials, can be defined as crystalline materials with a single layer of atoms or chemical compounds. These materials

are substances with a thickness of a few nanometres or less (one or two atoms thick). The extraordinary properties of these 2D materials have opened new opportunities for scientists and engineers to increase the research activities in this novel engineering materials field [4]. Electronic transport is realized in the 2D plane of the material, where electrons move freely [2]. In addition, electrons have restricted motion in the third direction, due to which this phenomenon is governed by quantum mechanics. They can be constituted by 2D allotropes of diverse chemical elements or compounds. Actually, graphene is the most researched 2D material till now. In addition, they can be classified as elemental, compounds, or van der Waals heterostructures. The elemental 2D materials use the *-ene* suffix in their names, for example, graphene, germanene, borophene, silicene, stanene, and phosphorene. Compounds consist of two or more covalently bonded elements and carry the *-ane* or *-ide* suffixes in their names, for example, graphane, hexagonal boron nitride (*hBN*), germanane, chalcogenide, Molybdenum disulfide (MoS_2), and tungsten diselenide (WSe_2). Van der Waals heterostructures are constituted of layered combinations of different 2D materials and as examples they are presented as MXenes (few atoms thick layers of transition metal carbide or carbonitrides) or organic compounds, such as $\text{Ni}_3(\text{HITP})_2$, where HITP is 2, 3, 6, 7, 10, 11-hexaaminotriphenylene.

The first 2D material discovered was graphene in 2004, which was isolated from graphite. Since 2010, graphene is not alone. Since this success a large amount of research has been realized to isolate other 2D materials due to their remarkable chemical, electronic, optical, and mechanical properties. 2D materials possess exceptional properties, since they are strong, lightweight, flexible, and good conductors of heat and electricity. 2D materials exhibit diverse electronic properties, ranging from insulating, semiconducting to semimetallic properties [3]. Some 2D materials are nearly optically transparent. Such properties proceed from the variations in structure (tunable architectures) as a consequence of changing metal centres [6]. Despite great advances achieved until now, none of these materials has been used for large-scale commercial applications with the possible exception of graphene. Their main areas of applications are electronics and optoelectronics, sensors, biological engineering, filtration (water purification), lightweight/strong composite materials, photovoltaic systems (electrodes), medicine, quantum dots, thermal management, ethanol distillation, and energy storage [3, 7].

Optical and electronic properties of the 2D materials are completely different from those of the bulk materials due to confinement of electrons and absence of interlayer interactions, which play an important role in the band structure presented in these materials [6]. On the other hand, mechanical and chemical properties are obtained thanks to geometric effects (chirality, dilution, defects, etc.) and to the high surface-volume ratio (it trends to infinity in the thinnest materials) [8]. Graphene and TMDs are building blocks for optoelectronic applications in areas such as ultrafast and ultrasensitive detection of light in the ultraviolet, visible, infrared and terahertz frequency ranges [3, 7].

Three different strategies have been developed to achieve a finite band gap in 2D materials: (1) chemical modification, (2) deposition on substrates, and (3) application of 2D chemical compounds [1–5]. Each of the above strategies has a direct influence on the properties and applications of each of the different types of 2D materials that have been discovered. Section 3 studies graphene-based materials; the 2D allotropes of groups III, IV, and V, with the

exception of the carbon (C), are analyzed in Section 4; the *h*BN, 2D TMDs, and MXenes are discussed in Section 5, and finally, the optoelectronic applications are analyzed in Section 6.

3. Graphene and its derivatives

Graphene is a stable 2D material based on carbon (C). It has been very successful, since it is composed of van der Waals type layers which are one or few atoms thick [1]. It has attracted designers due to its exceptional electronic properties. In addition, graphene is one million times thinner than paper, transparent, and the strongest material in the world. Gapless graphene strongly interacts with light from terahertz to ultraviolet (mainly, photodetectors) range [3]. Graphene has a very high carrier mobility (15,000 cm²/Vs for graphene on SiO₂ substrate and 200,000 cm²/Vs for suspended graphene) and low losses through the Joule effect. Unfortunately, graphene has zero band gap, which disqualifies it due to its low on/off ratio required by FETs for applications in digital circuits.

For example, graphene has been chemically modified into different versions such as graphane [9], graphone [10], graphyne [10], graphdiyne [10], fluorographene [11], or graphXene [12]. Graphyne is better than graphene in directional electronic properties and charge carriers. Graphone (partially hydrogenated) and graphane (100% hydrogenation of graphene with stoichiometry CH) have applications in nanoelectronics and spintronics due to the presence of band gap and magnetic properties [1]. Graphone with hydrogen coverage of 8% reaches a band gap of ~1.0 eV due to the rehybridization from sp² to sp³, and other authors have reported a band gap of 1.25 eV for different coverage [13]. Therefore, the size of the band gap depends exclusively on the H/C ratio, where band gaps of up to 1 eV are obtainable. Graphane achieves a band gap of 3.5 eV (insulating behaviour), although theoretically it achieves a value of 4.5 eV [13–14]. The presence of configuration changes from sp² to sp³ configuration, should lead to a band gap of 3.12 eV. Unfortunately, graphane has an optical band gap different from the electronic band gap, which is not expected for direct band gap materials. FETs based on graphane and/or graphone present large I_{on} and I_{on}/I_{off} ratios [2], reduced band-to-band tunnelling, without disadvantages such as lithography and patterning requirements for conventional circuit integration [9]. Graphyne (allotrope of graphene with one atom thick planar sheet of sp and sp² bonded carbon atoms arranged in a crystal lattice) and graphdiyne (allotrope of graphene containing two acetylenic linkages in each unit cell rather the one linkage as in graphyne), thanks to their crystalline structures, present tunable band gap giving place to semiconducting materials [10]. The band gap is increased with the reduction in the ribbon width and the number of sheets involved. Graphyne ribbons have band gaps in the semiconducting range from 0.59 to 1.25 eV. A tensile strain of 0.15 increases the band gap in 1 eV, while a compressive strain of 0.1 reduces the band gap in 0.3 eV. For strain-free graphdiyne, its band gap is 0.47 eV, while with strain it varies from 0.28 to 0.71 eV. Graphdiyne with low doping levels of boron nitride (BN) increases its band gap by 1 eV, and the trend is linear with the increasing dopant concentration [15]. When BN replaces all carbon atoms, a new material is formed, which is called BNdiyne with band gap of 4.39 eV (achieving an insulating behaviour) [10]. Fluorographene (FG), which results due to the exposure of graphene to atomic F,

has an excellent behaviour as an insulator and possesses a high thermal and chemical stability [11]. It presents an optical band gap of 3.0 eV and an electrical band gap of ~ 3.5 eV (electrical insulator). Graphene can be made to interact with Group IA and Group VIIA elements to form materials called graphXenes [12]. These materials present a range of band gap between 0 and 6.4 eV. Therefore, metallic, semiconducting, and insulating behaviours are presented, and it is obtained through a mixture of sp^2/sp^3 systems. Combinations, such as $C_2HCl_{0.5}F_{0.5}$ and C_2HCl , show semiconducting behaviour, while combinations C_2HF and C_2F_2 show insulating behaviour [12].

4. 2D allotropes of Si, Ge, Sn, P, As, Sb, and B

Elemental monolayers of the Group III (B), IV (Si, Ge), and V (P, As, Sb) are emerging as promising 2D materials with electronic applications. These materials are denominated as borenene, silicene, silicane, germanene, germanane, phosphorene, arsenene, and antimonene. A brief summary of the applications in the electronics area of the different 2D allotropes of groups III, IV and V, excluding carbon, is presented below.

Silicene is a crystalline 2D allotrope of silicon, with a hexagonal honeycomb structure similar to that of graphene [16]. Silicene has a buckled honeycomb atomic arrangement of sp^3/sp^2 -like hybridized Si atoms, which produces a non-trivial electronic structure and a spin-orbit coupling of 1.55 meV (under pressure it is increased to 2.9 meV), whose value is much larger than that of graphene (10^{-2} meV). In addition, silicene is more easily integrated into current Si-based electronics compared to graphene. The use of inert substrates such as *h*BN monolayer and SiC (0001) has silicene-substrate interaction energies range in 0.067–0.089 eV per Si atom, belonging to typical van der Waals interaction [17]. The characteristic Dirac cone is preserved for silicene deposited on substrates as *h*BN monolayer or hydrogenated Si-terminated SiC (0001) surface. On the other hand, silicene presents a metallic behaviour, when it is deposited on a hydrogenated C-terminated SiC (0001) surface. Therefore, silicene presents different electronic properties in accordance with the substrate where it is deposited, which allow to tune a different band gap via the substrate [17]. The presence of Stone-Wales (SW) defects in silicene can be effectively recovered by thermal annealing. The existence of single and double vacancies (SVs and DVs) in silicene induces small band gaps, and SV defects may transform semimetallic silicene into metallic silicene. Dramatic changes in the electronic properties of the silicene are produced by the presence of Si adatoms, for example, a semimetal behaviour is changed into magnetic semiconductor behaviour [18]. Its thin films provide novel electronic properties suitable for semiconductor device applications at room temperature. It has no band gap, but it can be used in the channel of high-performance FETs when a vertical electric field is applied [19]. Moreover, it has been predicted that silicene will exhibit a quantum spin Hall effect (QSHE) under an accessible temperature regime [20]. This effect is adequate to applications where it is desired that electrical conductance cannot be destroyed by magnetic fields applied to the sample. The physicochemical properties of the silicene will allow the design of novel devices in future electronic industry. Its applications are completely similar to those of graphene. Silicene presents excitonic resonance ($\pi \rightarrow \pi^*$ excitation) at 1.23 eV due to its quasi-particle excitation and optical absorption spectrum [21]. It is thermodynamically more stable

than graphene. It can be used for digital electronic applications, photonic and spintronic (magnetic semiconductor) devices, and lithium ion battery electrodes [22].

Germanene is a material made up of a single layer of germanium atoms, which is deposited under high vacuum and high temperature on a substrate such as gold (111) [23]. Its high-quality thin films provide novel electronic properties suitable for semiconductor device applications. It has no band gap, but it can be used in the channel of high-performance FETs when a vertical electric field is applied [19]. Germanene presents excitonic resonance ($\pi \rightarrow \pi^*$ excitation) at 1.10 eV due to its quasi-particle excitation and optical absorption spectrum [21]. The first bright exciton in germanene is located at 1.45 eV with a binding energy of 0.92 V. It is thermodynamically more stable than graphene. It has no band gap, but attaching a hydrogen atom to each germanium atom creates one band gap that can be exploited in diverse electronic applications [24].

Silicane is the hydride of silicene, that is, it is a crystalline single layer composed of silicene with one hydrogen atom bonded in each atom of Silicon. It is a semiconductor with indirect band gap [25]. Hydrogenation produces an indirect band gap in silicene called silicane, in the range of 2 to 4 eV, due to the rehybridization from sp^2 to sp^3 . Its applications may include polariton lasers and optical switches for the observation of excitonic effects at high temperature and in the visible optical range [26]. The first bright exciton in silicane is located at 3.00 eV with a binding energy of 1.07 V. It presents strongly bound excitons with considerable binding energies [21].

Germanane is a crystalline single layer composed of germanium with one hydrogen atom bonded in the z -direction for each atom, that is, with a similar structure to graphene. It is a semiconductor with indirect band gap [25]. Hydrogenation opens a direct band gap in germanene called germanane, in the range of 1.5–3 eV, due to the rehybridization from sp^2 to sp^3 . This material is potentially interesting for optoelectronic applications in the blue/violet spectral range such as light-emitting diodes due to the value of its direct band gap [24]. Its optical band gap is smaller than that of graphene to detect lower photon energies [26]. It presents strongly bound excitons with considerable binding energies [21].

Stanene is a crystalline allotrope of tin arranged in a single layer of atoms as graphene, whose behaviour is of a topological insulator with the capacity of displaying dissipationless currents at its edges near room temperature. It has an inverted band gap which can be tuned by compressive strain [27]. When magnetic doping and electrical gating are applied in stanene deposited on InSb substrate, then properties such as quantum anomalous Hall effect, Chern half metallicity, and topological superconductivity can be implemented. The spin-orbit interaction opens a 70 meV energy band gap in the k point of first Brillouin zone, but by applying strain the energy band gap in the band structure is closed [28]. It has a behaviour of topological insulator and phonon-mediated superconductor (doping with calcium and/or lithium) at a very low transition temperature ($T_c \sim 1.3$ K) [29]. 2D stanene with hydrogenation (Stanane) has a band gap that can be modulated by electric field and strain, and also, it has room-temperature ferromagnetic behaviour. These qualities are dependent on the arrangement of hydrogen atoms in the stanene [30].

Phosphorene is the 2D crystalline allotrope of phosphorus consisting of a single layer of atoms as graphene, which possesses a non-zero band gap (~ 0.1 eV) while displaying high electron mobility. These qualities make it a better electronic material than graphene [31]. Zigzag phosphorene nanoribbons have metallic behaviour regardless of the ribbon width, whereas armchair phosphorene has semiconducting behaviour with indirect band gap which decreases with increasing ribbon width [32]. A compressive (or tensile) strain can reduce (or enlarge) the band gap of phosphorene, while in-plane electric field can reduce the band gap of phosphorene. Phosphorene is a *p*-type semiconducting material with a band gap value of 0.31–0.36 eV, carrier mobility of 286 cm²/Vs, and presents photoluminescence in the visible optical range [33]. Besides, phosphorene has a high specific capacity, superb stability, and high electrical conductivity [34]. These capacities allow its use in FETs, batteries, radio receivers, and gas sensors.

Arsenene is a 2D crystalline allotrope of arsenic consisting of a single layer of atoms as the graphene, which can absorb light atoms to develop an effective method to functionalize it with B, C, N, and/or F to induce magnetism or N and/or F to induce *n*-type doping [35]. Its electronic band structure is dependent on edge shapes; armchair nanoribbons have large indirect band gap (due to stronger quantum confinement), while zigzag nanoribbons have small direct band gap [36]. In addition, arsenene has small carrier mobilities in the orders of magnitude of 0.5–1.2 $\times 10^3$ cm²/Vs for potential applications in nanoelectronics and nanodevices. A tensile strain (6%) applied to the monolayers provides an indirect-direct band gap transition (whose value is reduced with the strain), which allows these materials to be applied in light-emitting diodes and solar cells [37]. Under compressive strains, the band gap of monolayer and bilayer arsenenes initially increases and then rapidly decreases [38].

Antimonene is a 2D crystalline of antimony consisting of a single layer of atoms as the graphene, which has two stable and semiconducting allotropes (α and β), and with indirect band gap. α -Sb has a puckered structure with two atomic sub-layers, and β -Sb has a buckled hexagonal lattice. A moderate tensile strain applied to the monolayers provides an indirect-direct band gap transition, which allows these materials to be applied in optoelectronics [39]. In addition, antimonene can be tuned as a topological insulator to achieve QSHE at high temperatures using large tensile strain up to 18% and a band gap of 270 meV and whose characteristics meet the requirements of future electronic devices with low power consumption [40]. It has the same behaviour as that of arsenene with respect to the electronic band structure.

Borophene is a crystalline allotrope of boron consisting of icosahedral B₁₂ units fused as supericosahedra arranged in a 2D sheet with a hexagonal hole in the middle on silver surfaces under ultrahigh vacuum conditions [41]. Boron is non-metallic by nature as a bulk material, but it shows metallic and semiconducting behaviour at the nanoscale and has atomic thickness. Thanks to the hexagonal holes, various chemical modifications are possible to tune the electronic, optical, and chemical properties of borophenes [42]. It has a higher tensile strength than any other known material. The stability of these sheets is enhanced by vacancies or out-of-plane distortions. Borophene has a highly anisotropic metallic behaviour, where electrical conductivity is confined along the chains [41]. It is maintained as a promising material for applications ranging from electronics (sensors and electronic devices), photovoltaics (electro-

des), and energy storage (batteries); however, a lot of work is still required to determine its practical applications.

5. Compounds: *h*BN, TMDs, and MXenes

*h*BN is an interesting 2D material with a band gap of around 6 eV, which makes it an excellent dielectric, and it can be incorporated into different heterostructures for the electrostatic gating (protective cover, substrate, gate dielectric, or tunnel barrier) of other 2D materials due to that it does not require a lattice matching to generate van der Waals structures (electronic bands near the Fermi level (E_f) have graphene-like linear dispersion) [3]. It forms a 2D-crystalline structure composed of alternating atoms of boron and nitrogen, with lattice spacing similar to that of graphene [43]. It is commonly used in FETs as ideal substrate and gate dielectric. The doping level can also be varied by applying an external electric field, and it decreases with increasing *h*BN layer thickness and approaches zero for thick layers. It can be partially oxidized (PO-*h*BN) to decrease its optical transmission (>60%) and band gap (from 3.97 to 5.46 eV) [44].

Transition metal chalcogenides (TMCs) are thin-layered semiconducting structures of the type MX_2 , where M is a transition metal atom (Mo, W, etc.) and X is a chalcogen atom (S, Se, or Te) [45]. One layer of M atoms is sandwiched between two layers of X atoms. TMCs are commonly restricted to chemical elements of the groups IV (Ti, Zr, Hf and so on), group V (for example V, Nb or Ta), or group VI (Mo, W and so on), and X is a chalcogen (S, Se or Te) [46]. These materials have layered structures of the form chalcogen-metal-chalcogen ($X-M-X$), with the chalcogen atoms in two hexagonal planes separated by a plane of metal atoms. The overall symmetry of TMDs is hexagonal or rhombohedral, and the metal atoms have octahedral or trigonal prismatic coordination [46]. MoS_2 is one of the most typical TMDs; it has a direct band gap of 1.8 eV in monolayer, which can be tuned in different ways [47]. A MoS_2 monolayer has a thickness of 6.5 Å, and it has been used in chemical and gas sensors [48]. MoS_2 -based sensors have been implemented to detect NH_3 down of 400 ppb [49]. Besides, MoS_2 has applications in fields such as flexible electronics, energy storage and harvesting as well as electrochemical catalysis [47].

Chemical formula	Chemical formula	Chemical formula	Chemical formula	Chemical formula	Chemical formula
C (graphene)	NbS_2	WTe_2	VBr_2	VS_2	CrS_2
FeSe	$NbSe_2$	$CoTe_2$	VI_2	VSe_2	$CrSe_2$
LiFeAs	$NbTe_2$	$RhTe_2$	PFeLi	VTe_2	$CrTe_2$
YSe_2	TaS_2-AB	$IrTe_2$	IYGa	Ni_2Te_2Sb	$ZnIn_2S_4$
$TiSe_2$	TaS_2-AA	$NiTe_2$	PTe_2Ti_2	Cu_2S	$Zn_2In_2S_5$
$TiTe_2$	$TaSe_2-AB$	$SiTe_2$	FeS	VCl_2	SbSiNi
$ZrTe_2$	$TaSe_2-AA$	$AlCl_2$	FeTe	$HfTe_2$	Ag_2ReCl_6
	$TaTe_2$				

Table 1. 2D materials with metallic behaviour, that is, band gap = 0.0 eV [50].

In order to compare the electrical properties of different 2D materials, three tables were created for ordering these materials in three groups, as follows: (a) 2D materials with metallic behaviour (**Table 1**), (b) 2D materials with semiconducting behaviour (**Table 2**), and (c) 2D materials with electrical insulator behaviour (**Table 3**).

Chemical formula	Band gap (eV)	Chemical formula	Band gap (eV)	Chemical formula	Band gap (eV)
Bi ₂ Se ₃	0.9	MoS ₂	1.6	PdS ₂	1.1
Bi ₂ Te ₃	0.9	MoSe ₂	1.4	PdSe ₂	1.3
TiS ₂	0.02	MoTe ₂	1.15	PdTe ₂	0.2
ZrS ₂	1.1	WS ₂	1.8	PtS ₂	1.8
ZrSe ₂	0.4	WSe ₂	1.5	PtSe ₂	1.4
HfS ₂	1.3	TcS ₂	1.2	PtTe ₂	0.8
HfSe ₂	0.6	ReS ₂	1.4	SnS ₂	1.6
PbIF	2.3	ReSe ₂	1.3	SnSe ₂	0.8
HgI ₂	1.8	P ₂ AgSe ₆ Bi	1.4	GaS	2.4
ZrClN	1.9	P ₂ CuSe ₆ Bi	0.8	GaSe	1.8
Bi ₁₄ Te ₁₃ S ₈	0.9	CdI ₂	2.5	BiIO	1.5
PbO	2.5	PbBi ₂ Te ₄	1.0	FeBr ₃	0.5
Sb ₂ Ge ₂ Te ₅	0.2	PbSb ₂ Te ₄	0.8	ScP ₂ AgSe ₆	1.8
MgPSe ₃	2.1	CrSiTe ₃	0.6	FePSe ₃	0.05

Table 2. 2D materials with semiconducting behaviour ($0 < E_g < 3$ eV) [50].

Chemical formula	Band gap (eV)	Chemical formula	Band gap (eV)	Chemical formula	Band gap (eV)
BN	4.7	BaIF	4.3	KC ₆ FeO ₃ N ₃	4.5
YI ₃	3.1	SrIF	4.5	MgBr ₂	4.8
				MgI ₂	3.6

Table 3. 2D materials with insulating dielectric behaviour ($E_g > 3.0$ eV) [50].

TMCs can be formed with multiple layers bound to each other by van der Waals forces. 2D TMDs are exciting materials for future applications in nanoelectronics, nanophotonics, and sensing [49]. TMDs monolayers such as MoS₂, MoSe₂, MoTe₂, WS₂, and WSe₂ have a direct band gap and can be used in electronics as FETs and in optoelectronics as emitters (light-emitting diodes) and optical detectors (photodetectors) [3]. Molybdenum and tungsten dichalcogenides are a family of compounds that is structurally and chemically well defined. WS₂ is a layered material consisting of stacked S-W-S slabs with a binding energy in *c*-direction of 0.14 eV.

WS₂ has optical band gap energy of 1.46 eV; its electrical conductivity is in the order of 10⁻³ S/cm and has *n*-type conductivity [51]. Also, this material can be used in heterogeneous catalysis and electrochemical hydrogen storage. MoS₂, MoSe₂, WS₂, and WSe₂ are promising semiconducting materials for solar energy conversion, since they work as absorber materials due to the weak connection by intermolecular van der Waals forces among monolayers.

The TMD monolayer crystalline structure has no inversion centre, which allows a new degree of freedom of charge carriers called the *k*-valley index giving place to the new field of physics called valleytronics (technology that controls the valley degree of freedom of certain semiconductors, that is, a local maximum/minimum on the valence/conduction band, that present multiple valleys inside the first Brillouin zone) [48]. WSe₂-MoSe₂ heterostructures can be optically polarized to produce valley-specific interlayer excitons with lifetimes of 40 ns, which can be exploited in optoelectronic applications [52]. In addition, spin-orbit coupling among TMDC monolayers allows control of the electron spin through of the tuning the applied photonic energy, due to that a spin splitting in the meV range is presented in conduction and valence bands. TMDs can be combined with other 2D materials such as graphene and *h*BN to generate a new class of van der Waals heterostructure devices. TMDs can behave as electrical conductor, semimetal, semiconductor, and dielectric material, [50, 53–54], as well as, superconductor [55–56]. In the case of semiconductors, they have direct and indirect band gaps with values ranging from ultraviolet range to infrared range through the visible range. TMD monolayers are structurally stable; these have band gaps and show electron mobilities with comparable values to those of silicon. Therefore, they can be used to fabricate FETs [46].

Stacking of 2D materials on top of each other in a controlled fashion can create heterostructures with tailored physical properties that offers another promising approach to design and fabricate novel electronic devices [5]. In addition, either the in-plane heterojunction or the vertical stacking heterostructures can be realized by delicately tuning the composition and stacking sequences among 2D materials [5]. The development of FETs based on MoS₂ increased the scientific interest in the research of TMCs monolayers for novel ultrathin and flexible devices applied in electronics and optoelectronics [54]. Tunnel field-effect transistors (TFETs) based on vertical stacking of 2D materials can be used to build *p-n* junctions of TMC monolayers to design low-power logic devices [57]—VIB-MeX₂ (Me = W, Mo; X = Te, Se) monolayers as the *n*-type source and IVB-MeX₂ (Me = Zr, Hf; X = S, Se) as the *p*-type drain [57]. The two groups of semiconductors have distinct band edge characters, which will generate intervalley scattering during the electron tunnelling process. Strain is highlighted as an effective way to modify the band edge properties of these 2D TMDs [57]. Graphene (contact electrodes and circuit interconnections)/MoS₂ (transistor channel) heterostructures offer a technological alternative to design FETs with metallic drains and sources for practical flexible transparent electronics [58]. Graphene/MoS₂ heterostructure opens a 1 meV band gap in MoS₂-supported graphene, and the band gap is tunable under different interlayer distances [59]. Moreover, this heterostructure displays an enhanced light response, which allows even photocatalytic applications. 2D heterostructures play a pivotal role in electrochemical energy storage, sensing, hydrogen generation by photochemical water splitting, and electronic device applications such as FETs [60]. Particularly, in the field of energy conversion and storage, these hybrids will be

useful as anodes in lithium ion batteries and supercapacitors [60]. MoS₂ and WSe₂ have potential applications in electronics because they present high I_{on}/I_{off} current ratios and unique electro-optical properties [61]. Lateral WSe₂-MoS₂ heterojunction is a key component for building monolayer *p-n* rectifying diodes, light-emitting diodes, photovoltaic devices, and bipolar junction transistors [61].

2D TMDs under out-of-plane pressure decrease their band gap with increasing pressure and it can be closed too, which implies a semiconductor-metal transition [62]. The critical pressure for the semiconductor-metal transition is larger for the thinner nanoribbons, and the band gap closes faster for the Mo-containing nanoribbons than the W-containing ones. In addition, the physical mechanism of the band gap variation relates to the charge accumulation and delocalization in the interlayer region [62].

Layered TMDs are susceptible to electronic instability because its charge density wave (CDW) phases are diverse and commensurate, which leads to a strong electron-phonon and electron-electron interactions due to the Mott insulating phase presented [55]. Therefore, it is necessary find an adequate ordering of atoms to produce star-of-David clusters that allow boost superconductivity in a layered chalcogenide such as 1T-TaS_{2-x}Se_x to achieve different electronic degrees of freedom leading to tunable band gaps. Because the Ta 5*d* orbital allows superconductivity and Se 4*p* orbital leads to metallic phase, an unusual Se/S ordering creates superconductivity stable states [55]. Superconductivity can be induced through electrostatic gating using ionic liquid in materials such as MoSe₂, while electrochemical gating can be induced using KClO₄/polyethylene glycol (PEG) using a crossover from surface doping to bulk doping in materials such as MoTe₂ and WS₂ [56]. Moreover, the discovery of superconductors based on Mo and W allow to affirm that superconductivity is a common property for semiconducting TMDs. In bulk materials, the Zeeman effect is detrimental to superconductivity, however, in nanomaterials such as MoS₂ monolayers, it allows the development of ionic-gated transistors capable of realizing magnetotransport at coupling the spin-orbit with the spins of Cooper pairs in a direction orthogonal to the magnetic field [63]. This discovery leads to the Ising superconductor with a critical magnetic field B_{c2} far beyond the Pauli paramagnetic limit, consistent with Zeeman-protected superconductivity [63].

In 2D TMDs with 1T-MX₂ structure, where $M = (W \text{ or } Mo)$ and $X = (Te, Se, \text{ or } S)$, it is possible that a structural distortion causes an intrinsic band inversion between chalcogenide-*p* and metal-*d* bands [64]. Moreover, spin-orbit coupling opens a band gap that is tunable by vertical electrical fields and/or strains. It is feasible to develop a topological FET made of van der Waals heterostructures of 1T-MX₂ and 2D dielectric layers that can be switched off by electric field through a topological phase transition instead of carrier depletion [64].

MXenes can be defined as layered transition metal carbides and carbonitrides with general formula of $M_{n+1}AX_n$ (e.g., Ti₂AlC, Ti₃AlC₂, Ta₄AlC₃), where M stands for early transition metal, A is mainly a group IIA or IVA (i.e., groups 13 or 14) element, X stands for carbon and/or nitrogen with $n = 1, 2 \text{ or } 3$ [65]. MXenes have high electric conductivity (1500 S/cm, due to the metallic conductivity of transition metal carbides) combined with hydrophilic surfaces (due to their hydroxyl or oxygen terminated surfaces) [66], that is, they behave as conductive clays.

These materials show to be promising in energy storage applications such as Li-ion batteries and supercapacitors [65–66].

6. Optoelectronic applications

2D materials have interesting properties for photonics and optoelectronics compared with other materials. 2D materials enables charge carrier generation by light absorption over a very wide energy spectrum including the ultraviolet, visible, short-wave infrared (SWIR), near-infrared (NIR), mid-infrared (MIR), far-infrared (FIR), and terahertz (THz) spectral regimes [7]. Moreover, 2D materials have ultrafast carrier dynamics, wavelength-independent absorption, tunable optical properties via electrostatic doping, low dissipation rates and high mobility, and ability to confine electromagnetic energy in small volumes [3]. Electrons in 2D crystals possess a valley degree of freedom (DOF) in addition to charge and spin [67]. 2D materials exhibit an anomalous Hall effect whose sign depends on the valley index effect (VHE). It implies that circularly polarized light excites electrons into a specific valley in the structure band, causing a finite anomalous Hall voltage whose sign is controlled by the helicity of the light [67]. The electronic structure changes at the edges of the 2D crystalline structure of MoS₂ resulting in strong resonant nonlinear optical susceptibilities due to the translational symmetry breaking [68]. Graphene layers are used as electrodes with tunable work function, while TMDs are applied as photoactive material due to the strong light-matter interaction and photon absorption. TMDs exhibit transparency, mechanical flexibility, and easy processing [7]. Also, they have the ability to tune the optical band gap by varying the number of monolayers to allow the detection and emission of light (electroluminescence) at different wavelengths. 2D materials present the photovoltaic effect, the photo-thermoelectric effect, the bolometric effect, the photogating effect and the plasma-wave-assisted mechanism [3, 69]. Applications such as transparent electrodes in displays, photovoltaic modules, photodetectors, optical modulators, plasmonic devices, and ultrafast lasers have been developed [7]. 2D TMDs exploit their primary figure of merit and low room-temperature photoluminescence quantum yield (QY) for applications such as light-emitting diodes, lasers, and solar cells based on MoS₂ [70].

7. Conclusions

2D materials represent the set of materials more prominent that will be exploited for electronic industry in the following three decades. The most representative 2D materials are graphene, graphane, graphone, graphyne, graphdiyne, silicene, silicane, germanene, germanane, stanene, phosphorene, arsenene, antimonene, borophene, *h*BN, TMDs, and MXenes. The main strategy to change electrical properties of 2D materials containing single- and multilayer nanoribbons consists in modifying its structure band leading to dielectric, semiconducting, or semimetallic behaviours. Their electrical properties can be modified either by doping (addition of chemical elements), chemical modification (for example, hydrogenation for changing the sp² orbitals into a sp or sp³ type), electrical field, or by means of strains (compressive and/or

tensile type). The emerging fields called valleytronics and spintronics will be possible thanks to 2D materials. They are an exceptional family of materials that will enhance the light-matter interaction to develop light emission, detection, modulation, and manipulation applications. The prospects for commercializing of 2D materials will be dependent not only on their performance, distinct advantages and capabilities but also on the ability of the researchers to achieve a production to large scale at low cost and their integration to the existing photonic and electronic platforms.

Acknowledgements

The author acknowledges funding from the CONACYT (contract no. 152524, basic science), Tecnológico Nacional de México (contract no. 284.15-PD), and Instituto Tecnológico Superior de Irapuato (ITESI).

Author details

Rafael Vargas-Bernal

Address all correspondence to: ravargas@itesi.edu.mx

Materials Engineering Department, Instituto Tecnológico Superior de Irapuato, Irapuato, Guanajuato, México

References

- [1] Butler S.Z., Hollen S.M., Cao L., Cui Y., Gupta J.A., Gutiérrez H.R., Heinz T.F., Hong S.S., Huang J., Ismach A.F., Johnston-Halperin E., Kuno M., Plashnitsa V.V., Robinson R.D., Ruoff R.S., Salahuddin S., Shan J., Shi L., Spencer M.G., Terrones M., Windl W., Goldberg J.E. Progress, Challenges, and Opportunities in Two-Dimensional Materials Beyond Graphene. *ACS Nano*. 2013; 7(4): 2898–2926. DOI: 10.1021/nn400280c
- [2] Fiori G., Bonaccorso F., Iannaccone G., Palacios T., Neumaier D., Seabaugh A., Banerjee S.K., Colombo L. Electronics Based on Two-Dimensional Materials. *Nature Nanotechnology*. 2014; 9(10): 768–779. DOI: 10.1038/nnano.2014.207
- [3] Xia F., Wang H., Xiao D., Dubey M., Ramasubramaniam A. Two-Dimensional Material Nanophotonics. *Nature Photonics*. 2014; 8(12): 899–907. DOI: 10.1038/nphoton.2010.271
- [4] Gupta A., Sakthivel T., Seal S. Recent Development in 2D Materials Beyond Graphene. *Progress in Materials Science*. 2015; 73: 44–126. DOI: 10.1016/j.pmatsci.2015.02.002

- [5] Niu T., Li A. From Two-Dimensional Materials to Heterostructures. *Progress in Surface Science*. 2015; 90: 21–45. DOI: 10.1016/j.progsurf.2014.11.001
- [6] Mas-Ballesté R., Gómez-Navarro C., Gómez-Herrero J., Zamora F. 2D Materials: To Graphene and Beyond. *Nanoscale*. 2011; 3(1): 20–30. DOI: 10.1039/c0nr00323a
- [7] Koppens F.H.L., Mueller T., Avouris P., Ferrari A.C., Vitiello M.S., Polini M. Photodetectors Based on Graphene, Other Two-Dimensional Materials and Hybrid Systems. *Nature Nanotechnology*. 2014; 9(10): 780–793. DOI: 10.1038/nnano.2014.215
- [8] Yazyev O.V., Chen Y.P. Polycrystalline Graphene and Other Two-Dimensional Materials. *Nature Nanotechnology*. 2014; 9(10): 755–767. DOI: 10.1038/nnano.2014.166
- [9] Fiori G., Lebègue S., Betti A., Michetti P., Klintonberg M., Eriksson O., Iannaccone G. Simulation of Hydrogenated Graphene Field-Effect Transistors Through a Multiscale Approach. *Physical Review B*. 2010; 82(15): 153404. DOI: 10.1103/PhysRevB.82.153404
- [10] Peng Q., Dearden A.K., Crean J., Han L., Liu S., Wen X., De S. New Materials Graphyne, Graphdiyne, Graphone, and Graphane: Review of Properties, Synthesis, and Application in Nanotechnology. *Nanotechnology, Science and Applications*. 2014; 7: 1–29. DOI: 10.2147/NSA.S40324
- [11] Nair R.R., Ren W., Jalil R., Riaz I., Kravets V.G., Britnell L., Blake P., Schedin F., Mayorov A.S., Yuan S., Katnelson M.I., Cheng H.-M., Strupinski W., Bulusheva L.G., Okotrub A.V., Grigoreva I.V., Grigorenko A.N., Novoselov K.S., Geim A.K. Fluorographene: A Two-Dimensional Counterpart of Teflon. *Small*. 2010; 6(24): 2877–2884. DOI: 10.1002/sml.201001555
- [12] Klintonberg M., Lebègue S., Katsnelson M.I., Eriksson O. Theoretical Analysis of the Chemical Bonding and Electronic Structure of Graphene Interacting with Group IA and Group VIIA Elements. *Physical Review B*. 2010; 81(8): 085433. DOI: 10.1103/PhysRevB.81.085433
- [13] Haberer D., Vyalikh D.V., Taioli S., Dora B., Farjam M., Fink J., Marchenko D., Pichler T., Ziegler K., Simonucci S., Dresselhaus M.S., Knupfer M., Büchner B., Grüneis A. Tunable Band Gap in Hydrogenated Quasi-Free-Standing Graphene. *Nano Letters*. 2010; 10(9): 3360–3366. DOI: 10.1021/nl101066m
- [14] Ray S.C., Soin N., Makgato T., Chuang C.H., Pong W.F., Roy S.S., Ghosh S.K., Strydom A.M., McLaughlin J.A. Graphene Supported Graphone/Graphane Bilayer Nanostructure Material for Spintronics. *Scientific Reports*. 2014; 4: 3862. DOI: 10.1038/srep03862
- [15] Majidi R., Karami A.R. Electronic Properties of BN-Doped Bilayer Graphene and Graphyne in the Presence of Electric Field. *Molecular Physics*. 2013; 111(21): 3194–3199. DOI: 10.1080/00268976.2013.775514
- [16] Vogt P., De Padova P., Quaresima C., Avila J., Frantzeskakis E., Asensio M.C., Resta A., Ealet B., Lay G.L. Silicene: Compelling Experimental Evidence for Graphenelike

- Two-Dimensional Silicon. *Physical Review Letters*. 2012; 108(15): 155501. DOI: 10.1103/PhyRevLett.108.155501
- [17] Liu H., Gao J., Zhao J. Silicene on Substrates: A Way to Preserve or Tune Its Electronic Properties. *The Journal of Physical Chemistry C*. 2013; 117(20): 10353–10359. DOI: 10.1021/jp311836m
- [18] Gao J., Zhang J., Liu H., Zhang Q., Zhao J. Structures, Mobilities, Electronic and Magnetic Properties of Point Defects in Silicene. *Nanoscale*. 2013; 5(20): 9785–9792. DOI: 10.1039/c3nr02826g
- [19] Ni Z., Liu Q., Tang K., Zheng J., Zhou J., Qin R., Gao Z., Yu D., Lu J. Tunable Bandgap in Silicene and Germanene. *Nano Letters*. 2012; 12(1): 113–118. DOI: 10.1021/nl203065e
- [20] Liu C.-C., Feng W., Yao Y. Quantum Spin Hall Effect in Silicene and Two-Dimensional Germanium. *Physical Review Letters*. 2011; 107(7): 076802. DOI: 10.1103/PhysRevLett.107.076802
- [21] Wei W., Dai Y., Huang B., Jacob T. Many-Body Effects in Silicene, Silicane, Germanene and Germanane. *Physical Chemistry Chemical Physics*. 2013; 15(22): 8789–8794. DOI: 10.1039/c3cp51078f
- [22] Spencer M.J.S., Morishita T., (Ed.). *Silicene: Structure, Properties and Applications*. Switzerland: Springer; 2016. 283 p. DOI: 10.1007/978-3-319-28344-9
- [23] Dávila M.E., Xian L., Cahangirov S., Rubio A., Lay G.L. Germanene: A Novel Two-Dimensional Germanium Allotrope Akin to Graphene and Silicene. *New Journal of Physics*. 2014; 16(9): 095002. DOI: 10.1088/1367-2630/16/9/095002
- [24] Houssa M., Scalise E., Sankaran K., Pourtois G., Afanas'ev, Stesmans A. Electronic Properties of Hydrogenated Silicene and Germanene. *Applied Physics Letters*. 2011; 98(22): 223107. DOI: 10.1063/1.3595682
- [25] Voon L.C.L.Y., Sandberg E., Aga R.S., Farajian A.A. Hydrogen Compounds of Group-IV Nanosheets. *Applied Physics Letters*. 2010; 97(16): 163114. DOI: 10.1063/1.3495786
- [26] Pulci O., Gori P., Marsili M., Garbuio V., Del Sole R., Bechstedt F. Strong Excitons in Novel Two-Dimensional Crystals: Silicane and Germanene. *European Physics Letters*. 2012; 98(5): 37004. DOI: 10.1209/0295-5075/98/37004
- [27] Tang P., Chen P., Cao W., Huang H., Cahangirov S., Xian L., Xu Y., Zhang S.-C., Duan W., Rubio A. Stable Two-Dimensional Dumbbell Stanene: A Quantum Spin Hall Insulator. *Physical Review B*. 2014; 90(12): 121408(R)
- [28] Modarresi M., Kakoei A., Mogulkoc Y., Roknabadi M.R. Effect of External Strain on Electronic Structure of Stanene. *Computational Materials Science*. 2015; 101: 164–167. DOI: 10.1016/j.commatsci.2015.01.039

- [29] Shaidu Y., Akin-Ojo O. First Principles Predictions of Superconductivity in Doped Stanene. *Computational Materials Science*. 2016; 118: 11–15. DOI: 10.1016/j.commatsci.2016.02.029
- [30] Li S.-S., Zhang C.-W. Tunable Electronic Structures and Magnetic Properties in Two-Dimensional Stanene with Hydrogenation. *Materials Chemistry and Physics*. 2016; 173: 246–254. DOI: 10.1016/j.matchphys.2016.02.010
- [31] Li L., Yu Y., Ye G.J., Ge Q., Ou X., Wu H., Feng D., Chen X.H., Zhang Y. Black Phosphorus Field-Effect Transistors. *Nature Nanotechnology*. 2014; 9(5): 372–377. DOI: 10.1038/nnano.2014.35
- [32] Guo H., Lu N., Dai J., Wu X., Zeng X.C. Phosphorene Nanoribbons, Phosphorus Nanotubes, and van der Waals Multilayers. *The Journal of Physical Chemistry C*. 2014; 118(25): 14051–14059. DOI: 10.1021/jp505257g
- [33] Liu H., Neal A.T., Zhu Z., Luo Z., Xu X., Tománek D., Ye P.D. Phosphorene: An Unexplored 2D Semiconductor with a High Hole Mobility. *ACS Nano*. 2014; 8(4): 4033–4041. DOI: 10.1021/nn501226z
- [34] Bagheri S., Mansouri N., Aghaie E. Phosphorene: A New Competitor for Graphene. *International Journal of Hydrogen Energy*. 2016; 41: 4085–4095. DOI: 10.1016/j.ijhydene.2016.01.034
- [35] Li Y., Xia C., Wang T., Tan X., Zhao X., Wei S. Light Adatoms Influences on Electronic Structures of the Two-Dimensional Arsenene Nanosheets. *Solid State Communications*. 2016; 230: 6–10. DOI: 10.1016/j.ssc.2016.01.005
- [36] Wang Y., Ding Y. Electronic Structure and Carrier Mobilities of Arsenene and Antimonene Nanoribbons: A First-Principle Study. *Nanoscale Research Letters*. 2015; 10: 254. DOI: 10.1186/s11671-015-0955-7
- [37] Kamal C., Ezawa M. Arsenene: Two-Dimensional Buckled and Puckered Honeycomb Arsenic Systems. *Physical Review B*. 2015; 91(8): 085423. DOI: 10.1103/PhysRevB.91.085423
- [38] Cao H., Yu Z., Lu P. Electronic Properties of Monolayer and Bilayer Arsenene Under In-Plane Biaxial Strains. *Superlattices and Microstructures*. 2015; 86: 501–507. DOI: 10.1016/j.spmi.2015.08.006
- [39] Wang G., Pandey R., Karna S.P. Atomically Thin Group V Elemental Films: Theoretical Investigations of Antimonene Allotropes. *ACS Applied Materials & Interfaces*. 2015; 7(21): 11490–11496. DOI: 10.1021/acsami.5b02441
- [40] Zhao M., Zhang X., Li L. Strain-Driven Band Inversion and Topological Aspects in Antimonene. *Scientific Reports*. 2015; 5: 16108. DOI: 10.1038/srep16108
- [41] Mannix A.J., Zhou X.-F., Kiraly B., Wood J.D., Alducin D., Myers B.D., Liu X., Fisher B.L., Santiago U., Guest J.R., Yacaman M.J., Ponce A., Oganov A.R., Hersam M.C,

- Guisinger N.P. Synthesis of Borophenes: Anisotropic, Two-Dimensional Boron Polymorphs. *Science*. 2015; 350(6267): 1513–1516. DOI: 10.1126/science.aad1080
- [42] Piazza Z.A., Hu H.-S., Li W.L., Zhao Y.-F., Li J., Wang L.-S. Planar Hexagonal B₃₆ as a Potential Basis for Extended Single-Atom Layer Boron Sheets. *Nature Communications*. 2014; 5(1): 3113. DOI: 10.1038/ncomms4113
- [43] Qian X., Wang Y., Li W., Lu J., Li J. Modelling of Stacked 2D Materials and Devices. *2D Materials*. 2015; 2(3): 032003. DOI: 10.1088/2053-1583/2/3/032003
- [44] Nayak A.P., Dolocan A., Lee J., Chang H.-Y., Pandhi T., Holt M., Tao L., Akinwande D. Inversion of the Electrical and Optical Properties of Partially Oxidized Hexagonal Boron Nitride. *Nano: Brief Reports and Reviews*. 2014; 9(1): 145002. DOI: 10.1142/S1793292014500027
- [45] Lassner E. & Schubert W.-D. *Tungsten: Properties, Chemistry, Technology of the Element, Alloys, and Chemical Compounds*. New York, NY: Kluwer Academic Publishers; 1999. 456 p.
- [46] Wang Q.H., Kalantar-Zadeh K., Kis A., Coleman J.N., Strano M.S. Electronics and Optoelectronics of Two-Dimensional Transition Metal Dichalcogenides. *Nature Nanotechnology*. 2012; 7(11): 699–712. DOI: 10.1038/nano.2012.193
- [47] Li X., Zhu H. Two-Dimensional MoS₂: Properties, Preparation, and Applications. *Journal of Materiomics*. 2015; 1(1): 33–44. DOI: 10.1016/j.jmat.2015.03.003
- [48] Yazyev O.V., Kis A. MoS₂ and Semiconductors in the Flatland. *Materials Today*. 2015; 18(1): 20–30. DOI: 10.1016/j.mattod.2014.07.005
- [49] Gatensby R., McEvoy N., Lee K., Hallam T., Berner N.C., Rezvani E., Winters S., O'Brien M., Duesberg G.S. Controlled Synthesis of Transition Metal Dichalcogenide Thin Films for Electronic Applications. *Applied Surface Science*. 2014; 297: 139–146. DOI: 10.1016/j.apsusc.2014.01.103
- [50] Lebègue S., Björkman T., Klintonberg, M., Nieminen R.M., Eriksson O. Two-Dimensional Materials from Data Filtering and *Ab Initio* Calculations. *Physical Review X*. 2013; 3(3): 031002. DOI: 10.1103/PhysRevX.3.031002
- [51] Chate P.A., Sathe D.J., Hankare P.P. Electrical, Optical and Morphological Properties of Chemically Deposited Nanostructured Tungsten Disulfide Thin Films. *Applied Nanoscience*. 2013; 3(1): 19–23. DOI: 10.1007/s13204-012-0073-0
- [52] Rivera P., Seyler K.L., Yu H., Schaibley J.R., Yan J., Mandrus D.G., Yao, W., Xu X. Valley-Polarized Exciton Dynamics in a 2D Semiconductor Heterostructure. *Science*. 2016; 351(6274): 688–691. DOI: 10.1126/science.aac7820
- [53] Huang X., Zeng Z., Zhang H. Metal Dichalcogenide Nanosheets: Preparation, Properties and Applications. *Chemical Society Reviews*. 2013; 42(5): 1934–1946. DOI: 10.1039/c2cs35387c

- [54] Miró P., Audiffred M., Heine T. An Atlas of Two-Dimensional Materials. *Chemical Society Reviews*. 2014; 43(18): 6537–6554. DOI: 10.1039/c4cs00102h
- [55] Ang R., Wang Z.C., Chen C.L., Tang J., Liu Y., Lu W.J., Sun Y.P., Mori T., Ikuhara Y. Atomistic Origin of an Ordered Superstructure Induced Superconductivity in Layered Chalcogenides. *Nature Communications*. 2015; 6: 6091. DOI: 10.1038/ncomms7091
- [56] Shi W., Ye J., Zhang Y., Suzuki R., Yoshida M., Miyazaki J., Inoue N., Saito Y., Iwasa Y. Superconductivity Series in Transition Metal Chalcogenides by Ionic Gating. *Scientific Reports*. 2015; 5: 12534. DOI: 10.1038/srep12534
- [57] Gong C., Zhang H., Wang W., Colombo L., Wallace R.M., Cho K. Band Alignment of Two-Dimensional Transition Metal Dichalcogenides: Application in Tunnel Field Effect Transistors. *Applied Physics Letters*. 2013; 103(5): 053513. DOI: 10.1063/1.4817409
- [58] Yu L., Lee Y.-H., Ling X., Santos E.J.G., Shin Y.C., Lin Y., Dubey M., Kaxiras E., Kong J., Wang H., Palacios T. Graphene/MoS₂ Hybrid Technology for Large-Scale Two-Dimensional Electronics. *Nano Letters*. 2014; 14(6): 3055–3063. DOI:10.1021/nl404795
- [59] Yan Z., Xiong X., Chen Y., Ou-Yang F.P. Heterostructural Bilayers of Graphene and Molybdenum Disulfide: Configuration Types, Band Opening and Enhanced Light Response. *Superlattices and Microstructures*. 2014; 68: 56–65. DOI: 10.1016/j.spmi.2014.01.013
- [60] Kumar N.A., Dar M.A., Gul R., Baek J.-B. Graphene and Molybdenum Disulfide Hybrids: Synthesis and Applications. *Materials Today*. 2015; 18(5): 286–298. DOI: 10.1016/j.mattod.2015.01.016
- [61] Li M.-Y., Shi Y., Cheng C.-C., Lu L.-S., Lin Y.-C., Tang H.-L., Tsai M.-L., Chu C.-W., Wei K.-H., He J.-H., Chang W.-H., Suenaga K., Li L.-J. Epitaxial Growth of a Monolayer WSe₂-MoS₂ Lateral *p-n* Junction with an Atomically Sharp Interface. *Science*. 2015; 349(6247): 524–528. DOI: 10.1126/science.aab4097
- [62] Su X., Zhang R., Guo C., Zheng J., Ren Z. Band Engineering of Dichalcogenide MX₂ Nanosheets (M = Mo, W and X = S, Se) by Out-of-Plane Pressure. *Physics Letters A*. 2014; 378(9): 745–749. DOI: 10.1016/j.physleta.2013.12.044
- [63] Lu J.M., Zheliuk O., Leermakers I., Yuan N.F.Q., Zeitler U., Law K.T., Ye J.T. Evidence for Two-Dimensional Ising Superconductivity in Gated MoS₂. *Science*. 2015; 350(6266): 1353–1357. DOI: 10.1126/science.aab2277
- [64] Qian X., Liu, J., Fu L., Li J. Quantum Spin Hall Effect in Two-Dimensional Transition Metal Dichalcogenides. *Science*. 2014; 346(6215): 1344–1347. DOI: 10.1126/science.1256815
- [65] Naguib M., Mochalin V.N., Barsoum M.W., Gogotsi Y. 25th Anniversary Article: MXenes: A New Family of Two-Dimensional Materials. *Advanced Materials*. 2014; 26(7): 992–1005. DOI: 10.1002/adma.201304138

- [66] Naguib M., Kurtoglu M., Presser V., Lu J., Niu J., Heon M., Hultman L., Gogotsi Y., Barsoum M.W. Two-Dimensional Nanocrystals Produced by Exfoliation of Ti_3AlC_2 . *Advanced Materials*, 2011; 23(37): 4248–4253. DOI: 10.1002/adma.201102306
- [67] Mak K.F., McGill K.L., Park J., McEuen P.L. The Valley Hall Effect in MoS_2 Transistors. *Science*. 2014; 344(6191): 1489–1492. DOI: 10.1126/science.1250140
- [68] Yin X., Ye Z., Chenet D.A., Ye Y., O'Brien K., Hone J.C., Zhang X. Edge Nonlinear Optics on a MoS_2 Atomic Monolayer. *Science*. 2014; 344(6183): 488–490. DOI: 10.1126/science.1250564
- [69] Ferrari A.C., Bonaccorso F., Fal'ko V., Novoselov K.S., Roche S., Bøggild P., Borini S., Koppens F.H.L., Palermo V., Pugno N., Garrido J.A., Sordan R., Bianco A., Ballerini L., Prato M., Lidorikis E., Kivioja J., Marinelli C., Ryhänen T., Morpurgo A., Coleman J.N., Nicolasi V., Colombo L., Fert A., Garcia-Hernandez M., Bachtold A., Schneider G.F., Guinea F., Dekker C., Barbone M., Sun Z., Galiotis C., Grigorenko A.N., Konstantatos G., Kis A., Katnelson M., Vandersypen L., Loiseau A., Morandi V., Neumaier D., Treossi E., Pellegrini V., Polini M., Tredicucci A., Williams G.M., Hong B.H., Ahn J.-H., Kim J.M., Zirath H., van Wees B.J., van der Zant H., Occhipinti L., Di Matteo A., Kinloch I.A., Seyller T., Quesnel E., Feng X., Teo K., Rupasinghe N., Hakonen P., Neil S.R.T., Tannock Q., Löfwander T., Kinaret J. Science and Technology Roadmap for Graphene, Related Two-Dimensional Crystals, and Hybrid Systems. *Nanoscale*. 2015; 7(11): 4598–4810. DOI: 10.1039/c4nr01600a
- [70] Amani M., Lien D.-H., Kiriya D., Xiao J., Azcatl A., Noh J., Madhupathy S.R., Addou R., Kc S., Dubey M., Cho K., Wallace R.M., Lee, S.-C., He J.H., Ager III J.W., Zhang, X., Yablonovitch E., Javey A. Near-Unity Photoluminescence Quantum Yield in MoS_2 . *Science*. 2015; 350(6264): 1065–1068. DOI: 10.1126/science.aad2114.

Application of 2D Materials to Ultrashort Laser Pulse Generation

Grzegorz Sobon

Additional information is available at the end of the chapter

<http://dx.doi.org/10.5772/63336>

Abstract

In recent years, novel two-dimensional (2D) materials have revolutionized the field of ultrafast laser technology. They have emerged as efficient, cost-effective, and universal saturable absorbers for the so-called ultrafast lasers, which emit ultrashort optical pulses (on the timescale of femtoseconds). Thanks to their unique optical properties, such as broadband absorption, short recovery time, low saturation fluence, and high modulation depth, they might be used as saturable absorbers for different lasers (solid state, fiber, semiconductor) operating at different wavelengths (ranging from 500 to 2500 nm). Such lasers may find various applications in different areas of industry, medical procedures, precise metrology, gas sensing, laser spectroscopy, etc. This chapter discusses the recent achievements in the area of ultrafast fiber lasers utilizing 2D materials: graphene, topological insulators (Bi_2Te_3 , Bi_2Se_3 , Sb_2Te_3), transition metal dichalcogenides (MoS_2 , WS_2 , etc.), and black phosphorus. The optical properties of those materials will be described. Their usability in ultrafast photonics will be discussed.

Keywords: 2D materials, mode-locked lasers, ultrafast lasers, graphene, saturable absorbers

1. Introduction

Atomically thin layered materials, usually referred to as 2D materials or low-dimensional materials, are often characterized by unique and unexpected electronic and optical properties. The most popular example of a 2D material is graphene, which is composed of a single layer of carbon atoms, forming a 2D honeycomb lattice. Graphene is a fundamental building block of three-dimensional (3D) graphite. The growing interest in novel two-dimensional materials started in 2004 after the discovery of unique electrical properties of graphene [1]. After that

success, the scientists around the world extensively investigate other thin layered materials, such as topological insulators (TIs), transition metal dichalcogenides (TMDCs), black phosphorus (BP), and many others.

The popularity of 2D materials among researchers is mainly driven by their unique electrical properties and their potential applications in new-generation electronic devices. However, those materials are also characterized by multiple unique optical properties, such as broadband and almost wavelength-independent absorption or optical bistability (saturable absorption with ultrashort recovery time and high modulation depth). Those properties make 2D materials useful in laser technology, e.g., as saturable absorbers for lasers emitting ultrashort optical pulses. The so-called mode-locked lasers, emitting ultrashort pulses in the infrared range, are currently on demand of many industrial, military, and medical applications. They might be used in many various fields, e.g., in medicine and surgery [2], materials processing [3], laser spectroscopy [4, 5], and fundamental science (generation of terahertz waves [6], multiphoton systems for optical imaging [7], or supercontinuum generation [8]). Ultrafast lasers are also main building blocks of optical frequency combs, which are currently used in, e.g., spectrograph calibration enabling detection of extrasolar planets [9] or optical-atomic clocks [10]. The research on novel 2D materials strongly contributes to the development of novel laser sources, enabling generation of shorter pulses and broader bandwidths at new wavelength regions, previously uncovered by any other coherent light source. This chapter explains the fundamentals of ultrashort pulse generation and reviews and summarizes the most important recent achievements in the field of ultrafast lasers incorporating 2D materials.

2. Saturable absorbers

2.1. Saturable absorption effect

Saturable absorption (SA) is a nonparametric nonlinear optical process, which occurs in many materials under excitation with high-power light beam. In general, the optical transmittance of a saturable absorber is power dependent in a way that it introduces larger losses for low-intensity light. After illumination with high-intensity light, the absorption saturates and the SA becomes more transparent. A saturable absorber is characterized by three main parameters: its modulation depth (α_0), saturation intensity or saturation fluence (I_{sat}/F_{sat}), and nonsaturable losses (α_{NS}). All those parameters are bound with a simple formula, which describes the power-dependent absorption $\alpha(I)$ of a two-level saturable absorber [11]:

$$\alpha(I) = \frac{\alpha_0}{1 + \frac{I}{I_{sat}}} + \alpha_{NS} \quad (1)$$

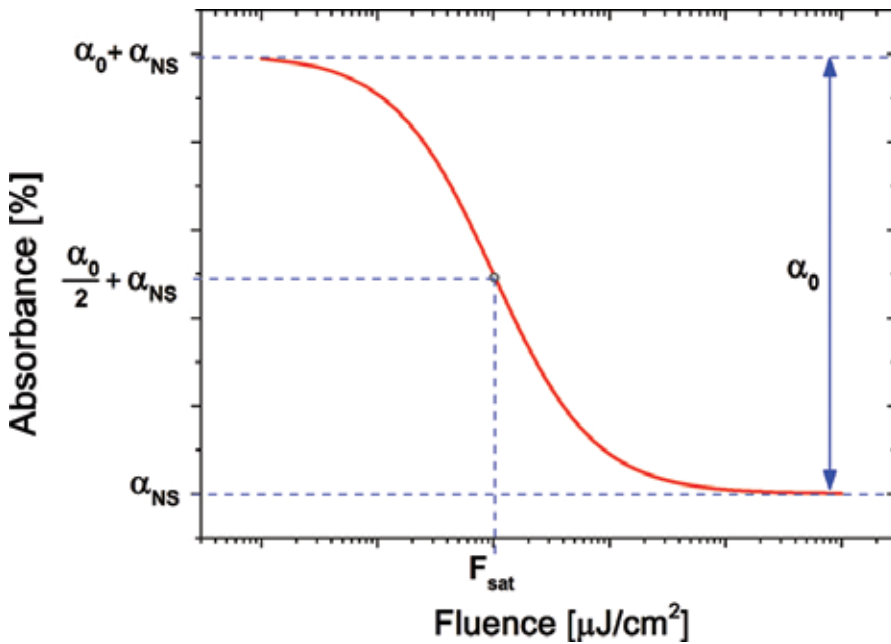


Figure 1. Theoretical saturable absorption curve calculated from formula (1) with indicated three main parameters of a saturable absorber.

The modulation depth can be understood as the contrast ratio between the “on” and “off” states of the SA, i.e., the difference between the minimum and maximum transmission. The nonsaturable loss is a constant linear loss level, which cannot be saturated. The saturation fluence (or saturation intensity) is usually defined as the incident fluence (or intensity) needed to achieve half of the modulation depth. A typical saturable absorption curve calculated with the use of formula (1) is plotted in **Figure 1** together with indicated parameters (note that the X-axis is in the logarithmic scale). Alternatively, the Y-axis might be scaled in the transmittance value.

2.2. Mode locking of lasers using saturable absorbers

Thanks to its “bistable” nature, a saturable absorber might act as a very fast optical switch when inserted into a laser cavity. A simplified schematic of a laser resonator incorporating a saturable absorber is depicted in **Figure 2(a)**. After turning on the laser (i.e., pumping the gain medium), the saturable absorber is in its “off” state, introducing quite high losses, which predominate the laser gain (see **Figure 2(b)**). After a short period of time (e.g., few hundreds of cavity roundtrips), an optical pulse will spontaneously arise from the continuous wave (CW) noise. If the intensity of the pulse will be high enough, it will pass through the SA with smaller losses than the CW noise. In consequence, a short pulse might be emitted from such laser [12]. An ultrashort pulse is always an effect of constructive interference between a certain number of longitudinal modes in the cavity. In order to achieve this interference, the consequent modes need to have fixed phase relationship with each other. In other words, the phase of the modes

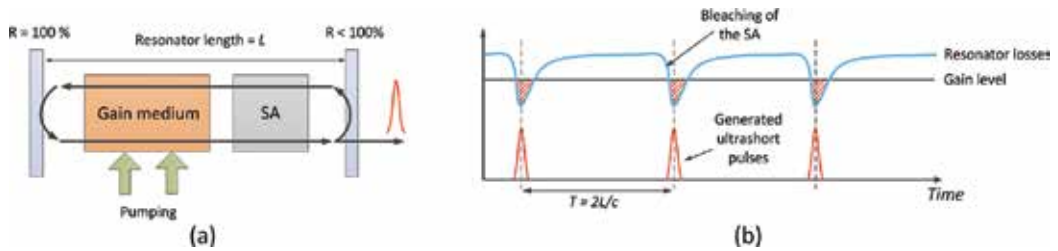


Figure 2. Illustration of a laser cavity with inserted saturable absorber (a) and pulse train formed in the cavity as a result of resonator loss modulation (b).

needs to be locked (“mode locking”). If the modes would oscillate randomly (without phase coherence), the output radiation would be multimode, continuous wave (CW). When the phases of the modes are locked, the laser will generate optical pulses according to the rule: more synchronized modes—shorter pulses.

There are several types of saturable absorbers currently used in laser technology. They can be generally classified into two categories: artificial and real SAs (see **Figure 3**). The term “artificial SA” refers to a mode-locking technique, where a nonlinear optical effect (which is power dependent) acts as a saturable absorber. Among those techniques, the most important include nonlinear polarization rotation (NPR), nonlinear loop mirrors (NOLM) or nonlinear amplifying loop mirror (NALM), and Kerr-lens mode locking (KLM).

Among real saturable absorbers we can distinguish two groups: semiconductors (so-called semiconductor saturable absorber mirrors, SESAMs) and nanomaterials. The SESAMs are currently one of the most widely used saturable absorbers in solid-state and fiber lasers, also in commercially available industrial systems. They are based on a well-established technology developed for more than 20 years [13]. However, SESAMs have some limitations. The technology is based on semiconductors (e.g., InGaAs/GaAs quantum wells), which are characterized by an energy band gap. Consequently, this results in a limited wavelength operation range. Thus, each SESAM needs to be designed strictly for a specific laser (operating at a certain wavelength). Fabrication of the SESAM also involves expensive and complicated molecular beam epitaxy (MBE) technology [14]. All those limitations have driven the laser community to seek for alternative, new saturable absorber materials. The field of nanomaterial-based SAs emerged in recent years to one of the most important branches of ultrafast laser technology. This new era started in 2003 as Set et al. [15] demonstrated the first CNT mode-locked fiber laser. Few years later, in 2009, the first lasers utilizing graphene were reported [16, 17]. Starting from this date, the number of papers and reports on fiber lasers mode-locked with graphene and other 2D materials: topological insulators, transition metal dichalcogenides, and recently black phosphorus, grow rapidly.

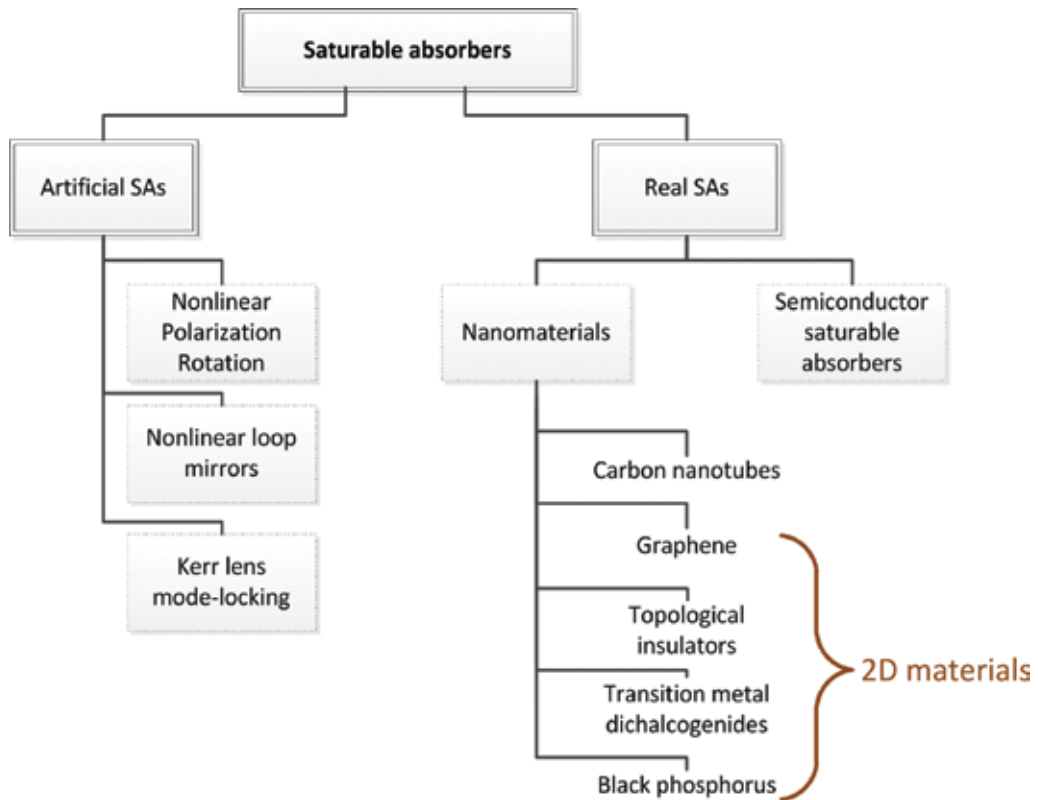


Figure 3. Types of saturable absorbers for ultrafast lasers.

There are several techniques of fabricating saturable absorber devices using 2D materials and make them suitable for use in a mode-locked laser, which might be either a solid-state or a fiber-based laser. The most popular approaches are illustrated in **Figure 4**.

The material might be deposited on a glass plate (plano window or a wedge) and inserted into the cavity as a free-space transmission saturable absorber (**Figure 4a**). This approach is most suitable for solid-state lasers [18–20]. For example, in the work of Ugolotti et al., a graphene monolayer grown via chemical vapor deposition (CVD) was transferred from a copper substrate on to a 1 mm thick quartz plate, with the use of poly(methylmethacrylate) (PMMA) polymer. Such SA exhibited 0.75% of modulation depth at 1 μm wavelength and supported mode locking with around 32 μm spot size on the graphene surface. Glass windows with deposited SA material might also be used in fiber lasers (e.g., with graphene [21]), but this approach seems not to be as efficient as the other methods. The world's first TI-based fiber laser used a Bi_2Te_3 layer deposited on a quartz plate and inserted into the cavity between two collimators [22].

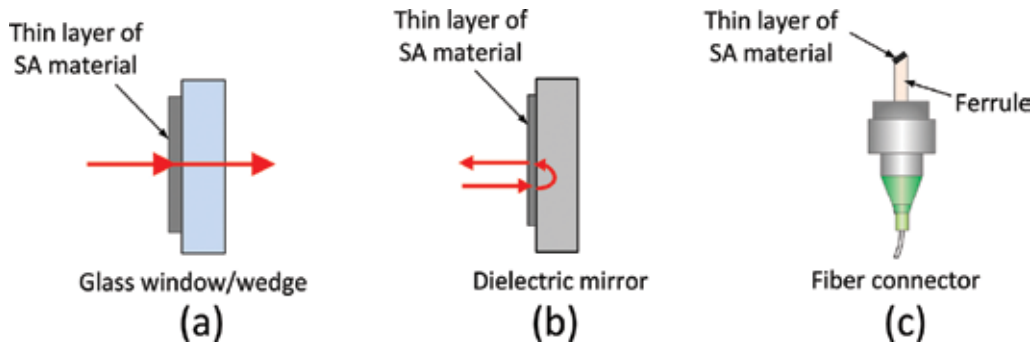


Figure 4. Common techniques of depositing SA material on optical substrates: on glass plates (a), mirrors (b), and fiber connectors (c).

The SA material might also be deposited on a mirror (**Figure 4b**) and inserted into a linear laser cavity (both fiber based or free space). In the case of a fiber ring-shaped resonator, one can use a circulator to couple the mirror with the cavity. This approach was used, e.g., by Xu et al. [23, 24] for the generation of femtosecond pulses from Er-doped fiber lasers. Graphene-coated mirrors might also serve as saturable absorbers in linear laser cavities as demonstrated by Cunning et al. [25]. However, usually graphene-coated mirrors serve as saturable absorbers for solid-state lasers [26–29]. The most impressive results were obtained by Ma et al. [29]. The SA was based on high-quality, CVD-grown monolayer graphene transferred onto a highly reflecting dielectric mirror. The spot size on the SA was about 60 μm . The laser was capable of generating 30 fs pulses at 50 nm bandwidth centered at 1070 nm [29].

The probably most popular and common technique of fabricating saturable absorbers with 2D materials is based on fiber connectors (as shown in **Figure 4c**). This approach was already demonstrated with graphene [30, 31], TIs [32, 33], TMDCs [34, 35], and BP [36, 37]. It is a very convenient method since it is alignment free and very robust. It allows to keep the cavity fully fiberized, which is very advantageous—the lasers are more compact, stable, and invulnerable to external disturbances.

The newest technique of SA fabrication is based on the evanescent field interaction effect. For this purpose, tapered fibers (microfibers) or side-polished (D-shaped) fibers might be used (**Figure 5**). The saturable absorption is based on the interaction between the evanescent field propagating in the cladding of the fiber and the deposited material. Such saturable absorbers were first used in combination with carbon nanotubes [38]. In 2010, Song et al. [39] demonstrated the usage of a graphene-coated D-shaped fiber as a saturable absorber. The laser was capable of generating pulses at 1561 nm with 2 nm of full width at half maximum (FWHM) bandwidth. Afterward, the deposition of TIs and TMDCs on such fibers was demonstrated [40, 41]. The alternative approach, using tapered fibers, is also commonly used and was demonstrated by several authors [42–46].

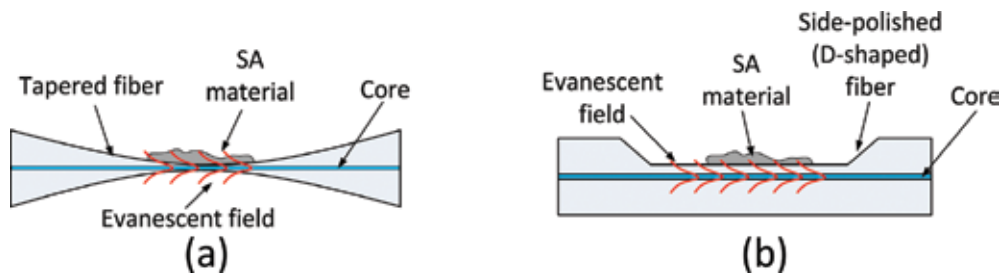


Figure 5. Saturable absorbers with evanescent field interaction: a fiber taper (a) and side-polished (D-shaped) fiber (b).

The performance of fiber lasers with evanescent field interaction is indisputable: 70 fs pulses were generated with a TI deposited on a tapered fiber [47], whereas Sb_2Te_2 deposited on a side-polished fiber allowed to achieve 128 fs pulses [48]. However, both techniques have some serious drawbacks. A saturable absorber based on a D-shaped fiber, due to its asymmetry, is always characterized by a polarization-dependent loss (PDL), which mostly depends on the material type (its refractive index), interaction length, and the distance between the polished region and the fiber core. In some reports, the PDL was kept at quite low levels (e.g., 1 dB in [49] with 6 μm distance between the material and the core), but sometimes it exceeds several dB [50]. In this situation, it is difficult to distinguish whether the mode locking originates from nonlinear polarization rotation or from the saturable absorption in the 2D material. In 2015, Bogusławski et al. [51] performed an experiment, which has unambiguously proven that mode locking in such oscillators is a combination of both effects. The study revealed that the hybrid mode-locking mechanism (combined NPR with saturable absorption of Sb_2Te_3 topological insulator) allows to achieve the best performance (in terms of bandwidth and pulse duration), when compared with a truly NPR or a TI-SA mode-locked laser. In the case of taper-based SAs, it is worth mentioning that in order to achieve sufficient interaction the fiber diameter needs to be reduced to less than 7 μm [42–45], which makes the taper quite long (from 5 to 18 cm waist length [44, 52]), and obviously much more fragile than a normal optical fiber. On the other hand, many authors who investigated evanescent field interaction claim higher optical power-induced damage threshold for such SA in comparison to connector end-face deposition due to better thermal management [39].

2.3. Nonlinear absorption measurements

The three basic nonlinear parameters of a saturable absorber (modulation depth, saturation fluence, and nonsaturable loss) might be measured in the so-called power-dependent transmission setup, which is depicted in **Figure 6**.

As a pumping source, an amplified pulsed laser (e.g., femtosecond or picosecond) is used in order to provide intensity high enough to saturate the saturable absorber. The beam from the laser is divided into two parts. The first beam acts as a reference channel and is directed to the power meter, whereas the second beam is focused by a lens and directed to the saturable absorber (e.g., 2D material deposited on a quartz plate). The sample is scanned along the waist of the beam (in the z -axis) in order to change the field intensity on the surface of the material.

The power in both arms is measured by a dual-channel power meter and afterward compared in order to calculate the saturable absorption curve.

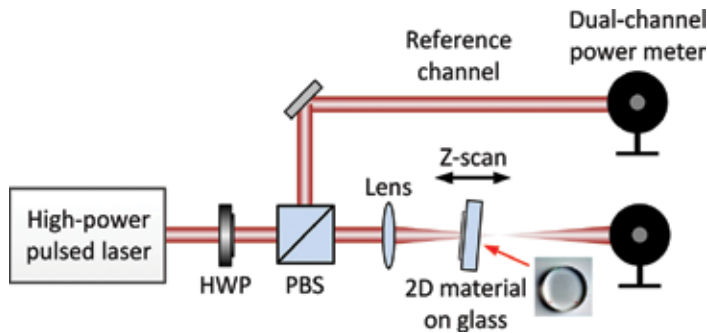


Figure 6. Power-dependent transmission measurement of a saturable absorber in free-space configuration.

In the case of fiber-based saturable absorbers (e.g., 2D material deposited on connectors or tapered fibers/D-shaped fibers), a modified version of the setup needs to be used. The schematic of an all-fiber power-dependent transmission experiment is depicted in **Figure 7**. Here, the power incident on the sample might tune with the use of a variable optical attenuator (VOA). The beam from the pump laser is also divided into two parts, but this time using a fiber coupler with defined coupling ratio, e.g., 50%/50%. Again, after passing through the absorber, the power is measured and compared with the reference channel.

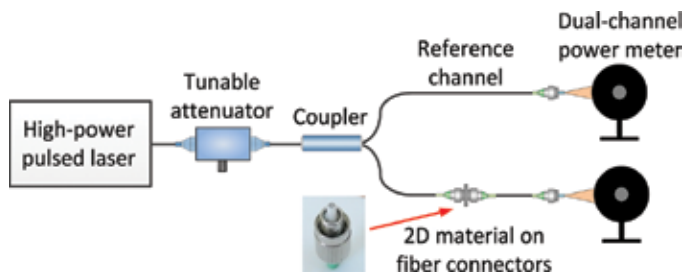


Figure 7. Power-dependent transmission measurement of a saturable absorber in all-fiber configuration.

3. Mode locking of lasers using graphene

3.1. Graphene

Graphene, one of the allotropes of carbon, is commonly described as a “wonderful material”, thanks to its unique electronic properties and a great number of possible applications. Besides the application in pulsed lasers, graphene was successfully used in many optoelectronic devices, such as photodetectors [53], modulators [54], polarizers [55], sensors [56], and solar

cells [57]. The lack of the band gap in pristine graphene [58] might generally be unwanted in some electronic applications, but makes it extremely useful in photonics. Thanks to this unique property, graphene is characterized by a constant absorption coefficient in a wide spectral range. In consequence, it might act as a saturable absorber in lasers operating at different wavelengths. The historically first lasers mode-locked with graphene were developed in 2009 independently by the groups from Singapore and United Kingdom [16, 17]. Shortly after those reports, a number of papers appeared, demonstrating novel concepts of ultrafast lasers utilizing various forms of graphene. In this section, the unique optical properties of graphene will be discussed. The recent experimental results reported in the literature are described and compared.

3.2. Saturable absorption of graphene

The process of saturable absorption in a graphene was extensively studied by researchers in the recent years [59–61]. The process is schematically explained in **Figure 8**. A single graphene layer absorbs approximately a 2.3% fraction of the incident light [62]. The illumination causes excitation of the electrons from the valence band to the conduction band. After a very short relaxation time, these electrons cool down to a Fermi–Dirac distribution (step 2). After further illumination with high intensity light, the energy states in both bands fill, which blocks further absorption (Pauli blocking), and the saturable absorber bleaches [16, 61]. Graphene is characterized by a fast 70 – 150 fs relaxation transient, followed by a slower relaxation process in the 0.5 – 2.0 ps range, which was confirmed by pump-probe measurements [59, 60].

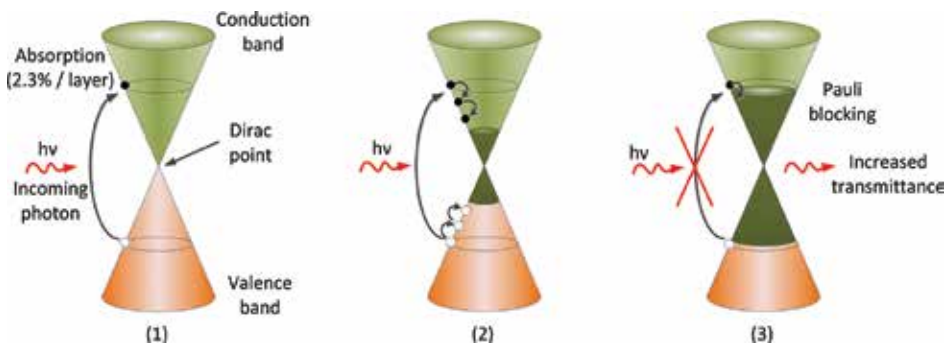


Figure 8. Saturable absorption in graphene [16, 59–61]. Light absorption and excitation of carriers (1), electrons cool down to a Fermi–Dirac distribution (2), and Pauli blocking (3).

As mentioned previously, a single layer of graphene absorbs approximately 2.3% of incident low intensity light. This absorption coefficient remains constant over a broad bandwidth, ranging from the visible to the mid-infrared [63]. However, the saturable absorption (i.e., the modulation depth) is slightly wavelength dependent. **Table 1** summarizes the experimentally obtained values of modulation depth, nonsaturable loss, and saturation fluence of monolayer graphene measured at four different wavelengths. It can be seen that the modulation depth is

the highest at shortest wavelength (800 nm) and drops quite rapidly with increased pump wavelength (0.5% at 1500 nm).

λ [nm]	ΔT [%]	α_{NS} [%]	F_{sat} [$\mu\text{J}/\text{cm}^2$]	Ref.
800	1.8	< 0.9	66.5	[20]
1040	0.75	1.59	50	[18]
1250	0.54	1.61	14.5	[64]
1500	0.5	1.9	14	[19]

Table 1. Summary of the experimentally obtained modulation depth value of monolayer graphene at different wavelengths.

An exemplary measurement of the nonlinear transmission through a CVD-grown monolayer of graphene deposited on a glass window is plotted in **Figure 9**. The curve was obtained using an experimental setup as depicted in **Figure 6**, with a 80-fs fiber laser operating at 1560 nm as an excitation source.

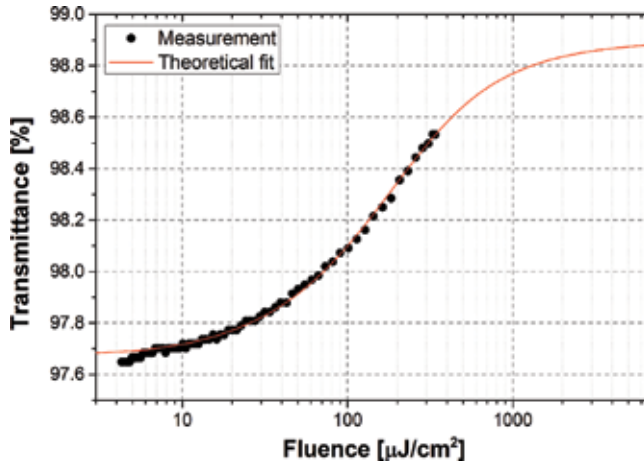


Figure 9. Measurement of saturable absorption in monolayer graphene.

Since graphene is considered as a fast saturable absorber (which is determined by its short relaxation time), its nonlinear transmission is described by different, more complex formula than the presented previously (Eq. (1)), valid for fast SAs [65, 66]:

$$T(F) = \frac{\Delta T}{\sqrt{\frac{F}{F_{sat}} + \left(\frac{F}{F_{sat}}\right)^2}} \operatorname{atanh}\left(\sqrt{\frac{F}{F_{sat} + F}}\right) + (1 - \alpha_{NS}) \quad (2)$$

where ΔT denotes the modulation depth. The theoretical fit (solid red line in **Figure 9**) was calculated using the following parameters: $F_{\text{sat}} = 105 \mu\text{J}/\text{cm}^2$, $\alpha_{\text{NS}} = 1.1\%$, and $\Delta T = 1.24\%$. The theoretical curve fits very well the experimental data; however, it can be seen that the sample was not fully saturated due to insufficient pump power.

3.3. Controlling the modulation depth of graphene-based saturable absorbers

As shown in the previous section, the modulation depth of a single graphene layer at the two most popular fiber laser wavelengths (1 and 1.55 μm) is quite small, at the level of 1%. Typically, in the case of fiber lasers, such modulation depth is insufficient to initiate stable mode locking and generate ultrashort optical pulses. It is therefore necessary to increase the modulation depth of a graphene-based saturable absorber. This might be done by scaling the number of graphene layers in the SA device. What is also important, the modulation depth is a critical parameter which determines the behavior of a laser. The influence of the modulation depth of the saturable absorber on the performance of mode-locked lasers was already extensively investigated numerically and experimentally. As an example, the study of Sobon et al. [67] has revealed that large numbers of graphene layers are required to achieve optimal performance for subpicosecond mode-locked operation of an Er- and Tm-doped laser. Unfortunately, increasing the number of layers does not only change the modulation depth, but causes also an increase of nonsaturable losses, which are usually unwanted in fiber lasers.

The optical transmittance of multilayer graphene was investigated by Zhu et al. They have derived a simplified formula, which describes the transmittance as a function of number of layers [68]:

$$T(N) = \left(1 + \frac{1.13 \cdot \pi \alpha N}{2} \right)^{-2} \quad (3)$$

where N denotes the number of layers and α is the fine-structure constant revealed by Nair et al. [62] ($\approx 1/137$). However, this formula is valid only for multilayer graphene with defined stacking sequence (e.g., ABA or ABC). Such ordered structure might be achieved, e.g., in a CVD growth process on nickel (Ni) substrate [68]. This formula takes into account the interactions between the adjacent layers, which are present only when the graphene layers are properly stacked.

In the case of undetermined stacking, when, e.g., the graphene layers were grown separately and afterward stacked together, and there are no inter-layer interactions, a different formula needs to be used to calculate the transmittance:

$$T(N) = (1 - \pi \alpha)^N \quad (4)$$

The passage of a laser beam through such a multilayer graphene stack is illustrated in **Figure 10**. The transmittance vs. number of layers curve calculated using both formulas is plotted in **Figure 11**, together with experimental data obtained in [67].

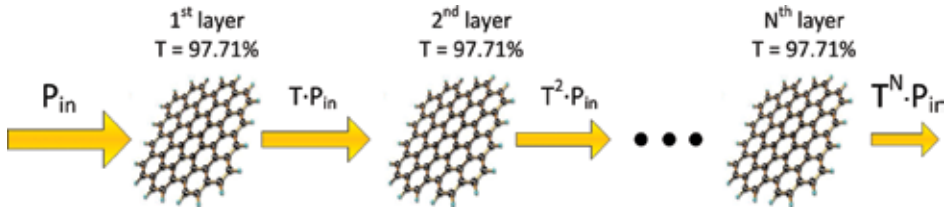


Figure 10. Light absorption in multilayer graphene without any interaction between the layers.

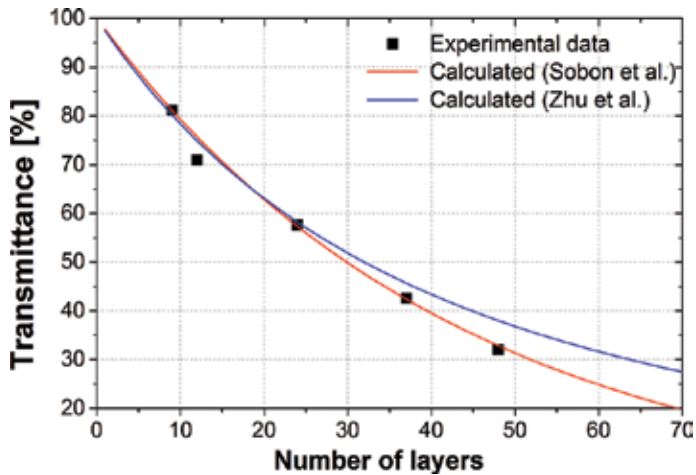


Figure 11. Optical transmittance of multilayer graphene: calculated from formula (1) (red line, no interaction between layers), calculated from formula (2) (blue line, including layer interactions), and measured using multilayer graphene (dotted line) [67].

As mentioned before, the modulation depth of graphene strongly depends on the number of layers. This allows to fabricate a proper saturable absorber to fulfill the requirements of a designed mode-locked laser. For example, dispersion-managed lasers (e.g., dissipative soliton lasers or stretched-pulse lasers) require much higher modulation depths than soliton lasers [69]. **Figure 12** shows the examples of nonlinear transmission curves of saturable absorbers containing 9, 12, 24, and 37 graphene layers [67]. It can be easily seen that the modulation depth increases with the growing number of layers. It starts from 3% for 9 layers, up to 7.5% for 37 layers.

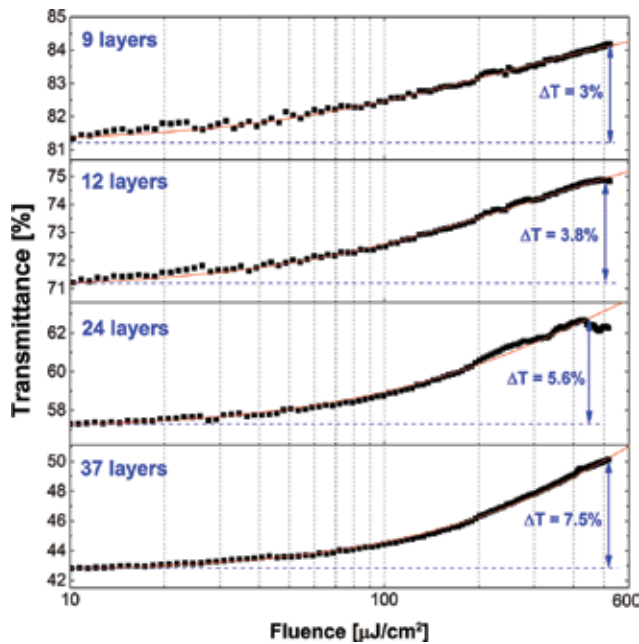


Figure 12. Nonlinear transmission curves of saturable absorbers containing 9, 12, 24, and 37 graphene layers.

3.4. Pulsed fiber lasers with graphene

The broadband saturable absorption of graphene makes this material an universal SA for different types of lasers. It has been already shown that the same graphene SA can provide mode locking in Yb-, Er-, and Tm-doped lasers [70], or can also synchronize and phase-lock two lasers simultaneously [71, 72].

Figure 13 shows the examples of three fiber lasers: Yb- (a), Er- (b) and Tm-doped (c) mode-locked with multilayer graphene composite. In the figure, each laser setup is depicted with its corresponding optical spectrum (e–g). All lasers were based on fully fiberized ring resonators and they utilized CVD-grown multilayer graphene immersed in a PMMA polymer support [73]. The Yb-doped oscillator consists of a segment of active fiber, an isolator, an output coupler (with 40/60% coupling ratio), a band-pass filter (BPF) with 2 nm FWHM, a polarization controller (PC), a 976 nm/1064 nm wavelength division multiplexer (WDM) and the saturable absorber. The laser was pumped by a 976 nm laser diode. Due to the normal dispersion of all fibers used in the cavity, a BPF is necessary to obtain dissipative soliton operation [74]. With the use of 48 layers of graphene in the SA, the laser generated pulses centered at 1059 nm and around 1.5 nm bandwidth and 17.1 MHz repetition frequency.

The Er-doped fiber laser shown in Figure 13(b) was realized in a simplified configuration, with the use of a hybrid component comprising an 10% output coupler (OC), a WDM and an isolator (ISO) in one integrated device. All fibers and components were polarization maintaining (PM), so there was no need to use a PC to initiate the mode locking. The optical spectrum generated

with the use of 32 layers of graphene is depicted in **Figure 13(e)**. It is centered at 1561 nm and has an FWHM of 20 nm, whereas the repetition rate was 100 MHz. The Tm-doped fiber laser was designed analogously to the Er-doped laser, but in this case the cavity was not all-PM, so the laser needs polarization alignment to initiate the mode locking. The oscillator is pumped at 1566 nm wavelength using a laser diode, beforehand amplified in an Erbium-doped fiber amplifier (EDFA). In this case, 12 layers of graphene were sufficient to support stable mode locking at 1968 nm with 10 nm of bandwidth (**Figure 13f**) and 100.25 MHz repetition frequency.

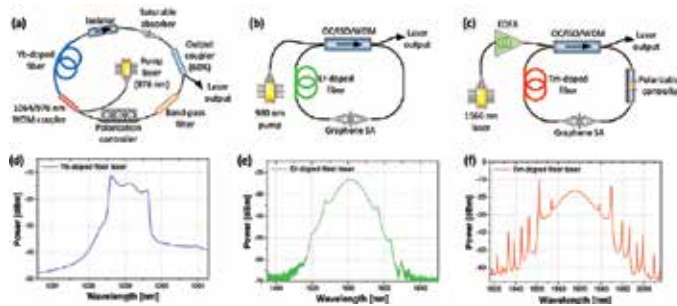


Figure 13. Fiber lasers operating at 1 μm (a), 1.55 μm (b), and 1.97 μm (c), and the corresponding optical spectra generated by those lasers (d, e, f).

3.5. Graphene-based ultrafast lasers – literature examples

3.5.1. Solid-state lasers

Efficient mode locking of solid-state lasers (SSLs) with the use of real saturable absorbers is quite challenging. The gain of an active medium (bulk crystal) is not as large as in fiber lasers, and in addition, the free-space resonator needs to be carefully aligned. Also the losses introduced by the SA should be possibly small. This is why most of the graphene-based SSLs utilize monolayer or bi-layer graphene. Up till now, mode locking of SSLs ranging from 532 to 2500 nm has been demonstrated [75, 76].

As an example, Baek et al. [20] demonstrated a Ti:Sapphire laser mode-locked with monolayer graphene. The laser generated 63 fs pulses at 800 nm central wavelength. There were also several reports on lasers operating around 1 μm wavelength [27–29]. The most prominent result was obtained by Ma et al. [29]. The authors have demonstrated stable 30 fs pulses centered at 1068 nm from diode pumped Yb:CaYAlO₄ laser by using high-quality CVD monolayer graphene as saturable absorber. These are the shortest pulses ever reported from graphene mode-locked lasers.

Broadband saturable absorption of graphene enables to achieve ultrashort pulse generation also in the mid infrared region. For example, Ma et al. [77] demonstrated a SSL based on a Tm-doped calcium lithium niobium gallium garnet (Tm:CLNGG) crystal, generating 729 fs pulses

at 2018 nm. The SA was formed by transferring CVD-grown, high-quality, and large-area graphene on a highly reflective plane mirror. Later, Cizmeciyan et al. [76] further extended the spectral coverage of graphene-based lasers by using a Cr:ZnSe crystal. High-quality monolayer graphene transferred on a CaF₂ windows enabled generation of 232 fs pulses at 2500 nm wavelength.

3.5.2. Ytterbium-doped fiber lasers

Mode locking of Yb-doped fiber lasers using real saturable absorbers might be challenging, mostly due to the fact that such oscillators are operated in the all-normal dispersion regime. The dispersion of standard single-mode fibers is normal for wavelengths shorter than ~1300 nm. Thus, a typical Yb-doped laser built from standard components will be characterized by a positive net group delay dispersion (GDD). This implies dissipative soliton operation of such laser. In order to generate a dissipative soliton, several conditions must be fulfilled [78]. The saturable absorber needs to have sufficient modulation depth in order to imitate and maintain the mode locking. In the case of graphene, it implies the usage of multilayer composites. Moreover, dissipative solitons are characterized by a quite large pulse energy, significantly larger than those achieved in conventional soliton lasers (e.g., Er- or Tm-doped). Optical damage of the SA might be a serious issue which precludes mode locking in Yb-doped fiber lasers.

Up to date, there were only few graphene-based, dissipative soliton Yb-doped fiber lasers reported [70, 79–82]. In all cases, the generated optical spectra were narrower than 2 nm. The broadest spectrum of 1.3 nm was achieved by Zhao et al. [79]. The obtained pulse duration was 580 ps. Such long pulse durations originates from the giant chirp, which is a consequence of the large normal dispersion of the cavity. Usually, dissipative soliton pulses from all-normal dispersion (ANDi) lasers are compressible almost to the transform-limited value [83, 84]. Nevertheless, the performance of the graphene-based YDFLs is far worse than of YDFLs utilizing other mode-locking techniques, such as NOLM/NALM, SESAM, or NPR, where broadband spectra with large pulse energies are achieved [85–87].

3.5.3. Erbium-doped fiber lasers

Erbium-doped fiber lasers are obviously the most popular constructions among all fiber lasers, thanks to the wide availability of cost-effective components for the telecom industry (couplers, isolators, multiplexers, photodiodes, etc.). The dispersion of standard optical fibers is anomalous at 1.55 μm, which implies soliton-type operation of a typical laser (without any dispersion compensation). Such lasers are quite easy to build in all-fiber configuration, without the necessity of using any free-space bulk components.

The first reported graphene-based fiber lasers back in 2009 were Er-doped fiber lasers [16, 17]. Shortly after those reports, a number of papers appeared, demonstrating novel concepts and ultrafast laser setups utilizing various forms of graphene. The shortest ever reported pulse generated from an Er-doped graphene-based fiber laser was 88 fs reported by Sotor et al. [88] in 2015. For a quite long time (over 4 years) the “world record” was held by Popa et al. (174

fs) [63]. In 2014, Tarka et al. [89] reported generation of 168 fs pulses. Both lasers (from [89] and [63]) were characterized by similar cavity design and similar saturable absorber (graphene obtained via LPE), with quite low modulation depth (2.6 and 2.0%). In both cases the pulse duration was also comparable (168 and 174 fs). The significant improvement in terms of pulse duration was possible not only by proper dispersion management, but mainly by increasing of the SA modulation depth to 11% [88]. The parameters of the three lasers with shortest reported pulses are summarized in **Table 2**.

Author/Group	Pulse duration	FWHM bandwidth	Cavity net dispersion	Saturable absorber type	SA mod. depth	Ref.
1J. Sotor et al. / Wroclaw Univ. of Technology	88 fs	48 nm	Balanced (~-0.0015 ps ²)	Multilayer CVD-graphene/PMMA	11%	[88]
2J. Tarka et al. / Wroclaw Univ. of Technology	168 fs	15.2 nm	Anomalous	LPE graphene in chitosan	2.6%	[89]
3D. Popa et al. / Cambridge Univ.	174 fs	15.6 nm	Balanced (~-0.05 ps ²)	LPE graphene in Polivinyll alcohol (PVA)	2%	[63]

Table 2. Summarized parameters of three graphene-based lasers emitting the shortest pulses.

3.5.4. Thulium-doped fiber lasers

Thulium-doped fiber lasers operating in the 1.9–2.0 μm are currently considered as one of the most important branches of laser technology [90, 91]. The number of applications of such lasers rapidly grows.

Pulsed Tm-doped fiber lasers are suitable for use in many surgical and dermatological procedures. Due to strong absorption of the 1.9–2.0 μm radiation in water, heating of only small areas of human tissues is achieved. The light penetration into the tissue is at the level of microns, which allows precise cutting. In addition, bleeding is suppressed by coagulation [92].

The second application, where Tm-doped fiber lasers might be used is laser spectroscopy, e.g., remote detection of air pollutants. The 1.9–2.0 μm spectral region contains multiple absorption lines of several molecules, especially two harmful greenhouse gases: carbon dioxide (CO_2) and nitrous oxide (N_2O). Carbon dioxide is the primary greenhouse gas that is contributing to recent climate change. It is absorbed and emitted naturally as part of the carbon cycle (e.g., animal and plant respiration, volcanic eruptions, ocean-atmosphere exchange), but also human activities strongly contribute to the global emission of CO_2 (e.g., burning of fossil fuels) [93]. Nitrous oxide is also a major greenhouse gas and air pollutant. The N_2O molecules stay in the atmosphere for an average of 120 years before being removed by a sink or destroyed through chemical reactions. Globally, about 40% of total N_2O emissions come from human activities [94]. Nitrous oxide is emitted from agriculture (when nitrogen is added to the soil

through the use of synthetic fertilizers), transportation (from burning of fuel), and industry activities (e.g., production of synthetic materials). It is predicted that N_2O emissions are going to increase by 5% between 2005 and 2020, driven largely by increases in emissions from agricultural activities [93–95].

Up to date there were only few reports on graphene-based Tm-doped fiber lasers. The first mode-locked TDFL was reported by Zhang et al. [96] in 2012. The authors have achieved 3.6 ps pulses at 1.94 μm . The laser was using chemically exfoliated graphene (via LPE method) dispersed in PVA host. Later, Wang et al. [97] demonstrated a TDFL emitting 2.1 ps pulses, based also on graphene exfoliated by ultrasonic method (dispersed in dimethylformamide). In 2013, Sobon et al. [98] reported an all-fiber Tm-doped laser which generated 1.2 ps pulses at 1884 nm, using a CVD-graphene/PMMA composite. Improvements in the graphene technology and careful cavity optimization allowed the same authors to further shorten the pulse almost twice (654 fs at 1940 nm [73]). An interesting concept of a Tm/Ho-doped fiber laser was presented by Jung et al. [49]. The oscillator was mode-locked by a side-polished (D-shaped) fiber with deposited graphene oxide. Unfortunately, the pulse duration directly from the oscillator was unknown, due to insufficient output power to perform an autocorrelation measurement [49]. Later, the first polarization maintaining laser was demonstrated. The oscillator was capable of generating 603 fs pulses at 1876 nm [99]. The same group also reported chirped pulse amplification (CPA) of a Tm-doped oscillator in a fully fiberized design, achieving 260 fs pulses with more than 1 nJ energy at 1970 nm [100].

4. Other low-dimensional materials as saturable absorbers

4.1. Topological insulators

Among all the identified topological insulators, three have found very much attention by the photonics community: bismuth telluride (Bi_2Te_3), bismuth selenide (Bi_2Se_3) and antimony telluride (Sb_2Te_3). Carrier recombination mechanism in those materials was already investigated using time-resolved and angle-resolved photoelectron spectroscopy (tr-ARPES) [101–104], confirming the presence of surface metallic states.

The first mode-locked fiber laser incorporating a TI-based saturable absorber was proposed by Zhao et al. [22]. The oscillator emitted 1.21 ps pulses at 1558 nm with the use of Bi_2Te_3 TI. Further studies on the third-order nonlinear properties of Bi_2Te_3 performed by the same group revealed that the material might exhibit modulation depth up to 61.2% and possesses a very high third-order nonlinear refractive index, at the level of $10^{-14} \text{ m}^2/\text{W}$ [105]. The most prominent and important research results on TI-based lasers include: the first demonstration of a Bi_2Se_3 -based fiber laser [106], the first demonstration of harmonic mode locking with Bi_2Te_3 [107], first demonstration of the usage of Sb_2Te_3 topological insulator for mode locking [32], harmonic mode locking with Sb_2Te_3 [108], or development of TI-polymer composites [33]. The shortest pulse generated with a TI-based saturable absorber was reported in 2016 by Liu et al. [47]. The oscillator incorporated Sb_2Te_3 TI deposited on a tapered fiber and delivered 70 fs pulses at 1542 nm wavelength, whose 3 dB spectral width is 63 nm with a repetition rate of 95.4 MHz.

However, the mode locking was not truly SA based—the cavity contained an additional polarizer and wave-plates. Thus, the mode locking was a result of a hybrid combination of saturable absorption and NPR. The shortest pulses achieved directly from an oscillator mode-locked only by a TI-based SA were 128 fs [48].

4.2. Transition metal dichalcogenides

Transition metal dichalcogenides are in general characterized by the chemical formula MX_2 , where M is a transition metal, e.g., molybdenum (Mo) or tungsten (W), and X is a group VI element: sulfur (S), selenium (Se), or tellurium (Te). Those materials were already investigated in the late 1960s of the twentieth century [109]. The general interest in TMDCs was renewed after the great success of graphene. Materials as such as MoS_2 , MoSe_2 , WS_2 , WTe_2 , MoTe_2 , and WSe_2 are currently extensively investigated, since they allow applications as transistors, photodetectors, and optoelectronic devices [110]. In contrast to graphene, TMDCs are characterized by a band gap, which varies significantly with the material thickness [111].

The first TMDC material used as SA in lasers was molybdenum disulfide. The saturable absorption effect in MoS_2 nanosheets was already investigated in 2013 [112]. Less than one year after this discovery, Zhang et al. [34] demonstrated the first laser mode-locked with the use of MoS_2 . The Yb-doped fiber laser generated stable pulses centered at 1054.3 nm, with a 3-dB spectral bandwidth of 2.7 nm and duration of 800 ps. Later, the same group has demonstrated ultrashort pulse generation from an Er-doped fiber laser mode-locked with MoS_2 -based saturable absorber [35]. The laser generated 710 fs pulses centered at 1569.5 nm wavelength with a repetition rate of 12.09 MHz. Wavelength-tunable operation of a MoS_2 -based fiber laser in a very broad spectral range was reported by Zhang et al. [113]. The demonstrated laser utilized a PVA- MoS_2 saturable absorber and enabled continuous tuning from 1535 to 1565 nm. Molybdenum disulfide can be also used in combination with tapered fibers. For example, Du et al. [46] demonstrated an Yb-doped fiber laser which generated dissipative solitons at 1042.6 nm with pulse duration of 656 ps and a repetition rate of 6.74 MHz. Also a harmonically mode-locked Er-doped laser incorporating a microfiber-based MoS_2 SA was reported [114]. Very recently, Wu et al. [115] demonstrated a reflective MoS_2 saturable absorber for a short-cavity Er-doped fiber laser. They have achieved 606 fs pulses at 1556.3 nm with 463 MHz repetition rate.

The saturable absorption effect was also confirmed for other TMDCs [116], but up to date, probably not all of them were used as mode-lockers in lasers. Recently WS_2 has found attention of the ultrafast laser community. Lasers operating at 1.03 μm [117], 1.55 μm [118, 119], and 1.94 μm [41] were already reported with pulse durations down to 595 fs [119].

4.3. Black phosphorus

Similarly to TMDCs, black phosphorus is a material which was once on interest of the physics community (in the 1980s and 1990s of the twentieth century [120, 121]), and was “rediscovered” in the recent years after the great success of other 2D materials.

It has a graphene-like layered structure, in which the layers are bound with van der Waals forces [122, 123]. Mechanical exfoliation of black phosphorus leads to obtaining a single-layer 2D material called phosphorene [121–124] (analogously to “graphene”). Similarly to TMDCs, the energy band gap of BP scales with the number of layers. It might be tuned from approx. 1.5 eV for monolayer phosphorene up to ~ 0.3 eV for bulk black phosphorus [125]. Up till now, the broadband nonlinear optical response of BP has been confirmed at wavelengths ranging from 400 to 1930 nm [126, 127].

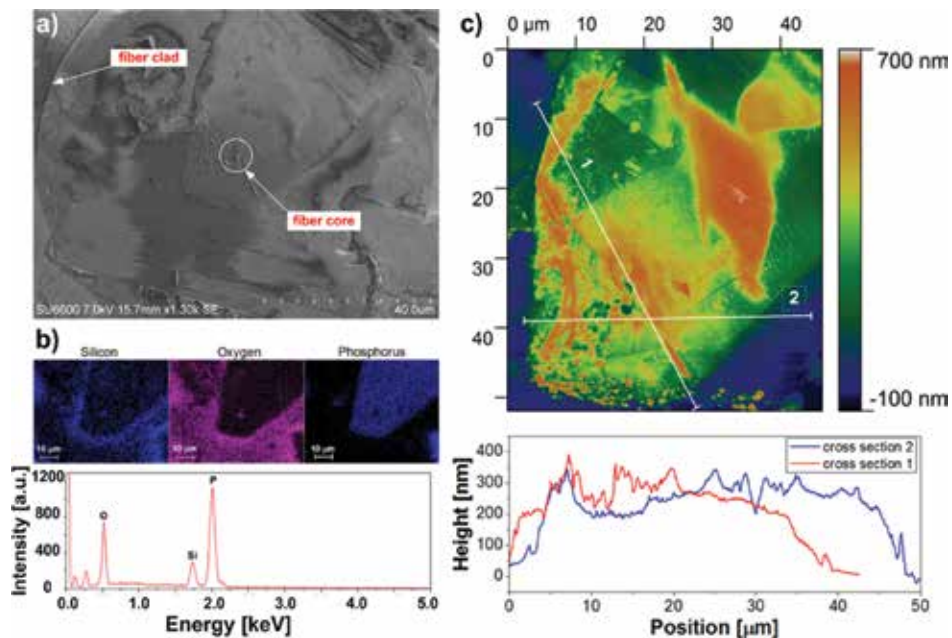


Figure 14. Characterization of the mechanically exfoliated BP layers transferred onto an optical fiber: (a) SEM image with marked fiber clad and core, (b) EDX spectroscopy data, (c) AFM image of the core area, and (d) cross section through the fiber core area indicating approx. 200–300 nm height of the BP flake on the core.

The first report on the usage of BP as a saturable absorber in a laser was posted on arXiv in 2015 [128]. Mode locking at both 1.55 and 1.9 μm wavelengths was reported. In both lasers, the BP layers were exfoliated mechanically from bulk material using an adhesive tape. Afterward, a ~ 300 nm thick layer was transferred onto a fiber connector, and connected with another one, just like shown in **Figure 14**. A scanning electron microscope (SEM) image of the fiber tip (with marked core and cladding of the fiber) with deposited BP layer is shown in **Figure 14(a)** [36]. The composition of the transferred layer onto the fiber core area was confirmed by energy-dispersive X-ray spectroscopy (EDX). The analysis of the spectroscopy data is shown in the inset of **Figure 14**. It confirms that the transferred material is black phosphorus (the Si and O peaks originate from the optical fiber). The atomic force microscope (AFM) measurement confirmed the average thickness of the layer at the level of 250–300 nm (**Figure 14b**).

The performance of the Tm-doped fiber laser mode-locked with the described BP-based saturable absorber is depicted in **Figure 15**. The laser generated soliton-shaped optical spectra centered at 1910 nm with 5.8 nm of FWHM bandwidth (a), which corresponded to a 739 fs pulse (b). It is worth mentioning that the authors claimed a high damage threshold of the BP layers. The laser was pumped with relatively high power (up to 400 mW) and the SA was not damaged or degraded during any of the performed experiments [37].

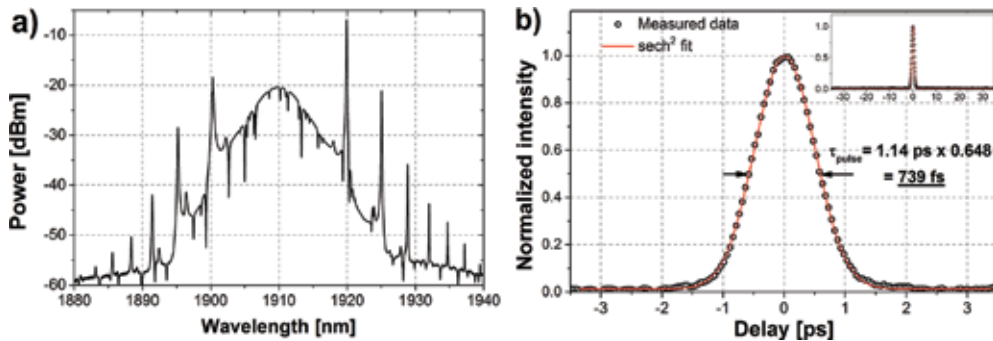


Figure 15. Optical spectrum generated by the BP mode-locked Tm-doped laser (a) and the autocorrelation trace of the emitted 739 fs pulse (b).

Black phosphorus in form of nanopallettes (NPs) was also used in combination with microfibers for evanescent field interaction. In their work, Yu et al. [129] reported that the SA had a modulation depth of 9.8% measured at 1.93 μm . A stable mode-locking operation at 1898 nm was achieved with a pulse width of 1.58 ps and a fundamental repetition rate of 19.2 MHz.

Similarly to graphene, BP is also suitable for operation in the midinfrared. In 2016, Wang et al. [130] demonstrated the first Cr:ZnSe laser incorporating BP as saturable absorber. However, the laser was not mode-locked but Q-switched. Generation of 189 ns pulses with average output power of 36 mW was obtained at 2.4 μm wavelength.

5. Summary and outlook

In summary, the recent most important advances in the field of ultrashort-pulsed lasers utilizing two-dimensional materials have been presented. A group of 2D materials, such as graphene, topological insulators, and transition metal dichalcogenides, have unambiguously revolutionized the field of mode-locked fiber-based and solid-state lasers. The discovery of unique optical properties of graphene has initiated an extremely fast progress in the science of two-dimensional nanomaterials, which strongly contributed to the development of novel ultrafast laser sources. It is evident that the interest in 2D material-based photonics will not slow down in the next years.

Acknowledgements

The author acknowledges the help and support from the members of the Laser & Fiber Electronics Group, especially Jaroslaw Sotor, Jakub Boguslawski, Maciej Kowalczyk, Jan Tarka, Karol Krzempek, and Krzysztof M. Abramski. The author also like to kindly thank the collaborators from the Institute of Electronic Materials Technology (Warsaw, Poland) for their excellent work on graphene fabrication and characterization. The research presented in this chapter was supported by the National Science Centre (NCN, Poland) under grants no. DEC-2013/11/D/ST7/03138 and DEC-2014/13/B/ST7/01699, and by the statutory funds of the Chair of EM Field Theory, Electronic Circuits and Optoelectronics (grant no. S50044).

Author details

Grzegorz Sobon

Address all correspondence to: grzegorz.sobon@pwr.edu.pl

Laser and Fiber Electronics Group, Faculty of Electronics, Wrocław University of Technology, Wrocław, Poland

References

- [1] Novoselov KS, Geim AK, Morozov SV, Jiang D, Zhang Y, Dubonos SV et al. Electric field effect in atomically thin carbon films. *Science*. 2004;306:666–669.
- [2] Mamalis N. Femtosecond laser. The future of cataract surgery? *J. Cataract Refract Surg*. 2011;37:1177–1178.
- [3] Gattass RR, Mazur E. Femtosecond laser micromachining in transparent materials. *Nat Photonics*. 2008;2:219–225.
- [4] Ehlers P, Silander I, Wang J, Foltynowicz A, Axner O. Fiber-laser-based noise-immune cavity-enhanced optical heterodyne molecular spectrometry incorporating an optical circulator. *Opt Lett*. 2014;39:279–282.
- [5] Kowzan G, Lee KF, Paradowska M, Borkowski M, Ablewski P, Wójtewicz S et al. Self-referenced, accurate and sensitive optical frequency comb spectroscopy with a virtually imaged phased array spectrometer. *Opt Lett*. 2016;41:974–977.
- [6] Stehr D, Morris CM, Schmidt C, Sherwin MS. High-performance fiber-laser-based terahertz spectrometer. *Opt Lett*. 2010;35:3799–3801.

- [7] Tang S, Liu J, Krasieva TB, Chen Z, Tromberg BJ. Developing compact multiphoton systems using femtosecond fiber lasers. *J Biomed Opt.* 2009;14:030508.
- [8] Buczynski R, Bookey HT, Pysz D, Stepien R, Kujawa I, McCarthy JE et al. Supercontinuum generation up to 2.5 μm in photonic crystal fiber made of lead-bismuth-galate glass. *Laser Phys Lett.* 2010;7:666–672.
- [9] Wilken T, Lo Curto G, Probst RA, Steinmetz T, Manescau A, Pasquini L et al. A spectrograph for exoplanet observations calibrated at the centimetre-per-second level. *Nature.* 2012;485:611–614.
- [10] Ludlow AD, Boyd MM, Ye J, Peik E, Schmidt PO. Optical atomic clocks. *Rev Mod Phys.* 2015;87:637–701.
- [11] Boyd RW. *Nonlinear Optics.* San Jose: Academic Press; 2003.
- [12] Kärtner FX, Aus der Au J, Keller U. Mode-locking with slow and fast saturable absorbers – what’s the difference?. *IEEE J Sel Top Quant.* 1998;4:159–168.
- [13] Keller U, Weingarten KJ, Kärtner FX, Kopf D, Braun B, Jung ID et al. Semiconductor saturable absorber mirrors (SESAMs) for femtosecond to nanosecond pulse generation in solid-state lasers. *IEEE J Sel Top Quant Electron.* 1996;2:435–453.
- [14] Okhotnikov O, Grudinin A, Pessa M. Ultra-fast fibre laser systems based on SESAM technology: new horizons and applications. *New J Phys.* 2004;6:177.
- [15] Set SY, Yaguchi H, Tanaka Y, Jablonski M, Sakakibara Y, Rozhin A et al. Mode-locked fiber lasers based on a saturable absorber incorporating carbon nanotubes. In: *Optical Fiber Communication Conference, 23–28 March 2003; Atlanta.* Optical Society of America; 2003. p. PD44.
- [16] Bao QL, Zhang H, Wang Y, Ni ZH, Shen ZX, Loh KP et al. Atomic layer graphene as saturable absorber for ultrafast pulsed laser. *Adv Funct Mater.* 2009;19:3077–3083.
- [17] Hasan T, Sun Z, Wang F, Bonaccorso F, Tan PH, Rozhin AG et al. Nanotube–polymer composites for ultrafast photonics. *Adv Mater.* 2009;21:3874–3899.
- [18] Ugolotti E, Schmidt A, Petrov V, Wan Kim J, Yeom D, Rotermund F et al. Graphene mode-locked femtosecond Yb:KLuW laser. *Appl Phys Lett.* 2012;101(16):161112
- [19] Di Dio Cafiso SD, Ugolotti E, Schmidt A, Petrov V, Griebner U, Agnesi A, Cho WB, Jung BH, Rotermund F, Bae S, Hong BH, Reali G, Pirzio F. Sub-100-fs Cr:YAG laser mode-locked by monolayer graphene saturable absorber. *Opt Lett.* 2013;38:1745–1747.
- [20] Baek I, Lee H, Bae S, Hong B, Ahn Y, Yeom D et al. Efficient mode-locking of sub-70-fs Ti:sapphire laser by graphene saturable absorber. *Appl Phys Express.* 2012;5(3):032701
- [21] Sobon G, Sotor J, Pasternak I, Grodecki K, Paletko P, Strupinski W et al. Er-doped fiber laser mode-locked by CVD-graphene saturable absorber. *J Lightwave Technol.* 2012;30:2770–2775.

- [22] Zhao C, Zhang H, Qi X, Chen Y, Wang Z, Wen S, Tang D. Ultra-short pulse generation by a topological insulator based saturable absorber," *Appl Phys Lett*. 2012;101:211106
- [23] Xu J, Liu J, Wu S, Yang QH, Wang P. Graphene oxide mode-locked femtosecond erbium-doped fiber lasers. *Opt Express*. 2012;20:15474–15480.
- [24] Xu J, Wu S, Li H, Liu J, Sun R, Tan F et al. Dissipative soliton generation from a graphene oxide mode-locked Er-doped fiber laser. *Opt Express*. 2012;20:23653.
- [25] Cunning B, Brown C, Kielpinski D. Low-loss flake-graphene saturable absorber mirror for laser mode-locking at sub-200-fs pulse duration. *Appl Phys Lett*. 2011;99:261109.
- [26] Lou F, Cui L, Li Y, Hou J, He J, Jia Z et al. High-efficiency femtosecond Yb:Gd₃Al₀₅Ga₄₅O₋₁₂ mode-locked laser based on reduced graphene oxide. *Opt Lett*. 2013;38:4189.
- [27] Xu J, Li X, Wu Y, Hao X, He J, Yang K. Graphene saturable absorber mirror for ultra-fast-pulse solid-state laser. *Opt Lett*. 2011;36(10):1948.
- [28] Xu J, Li X, He J, Hao X, Wu Y, Yang Y et al. Performance of large-area few-layer graphene saturable absorber in femtosecond bulk laser. *Appl Phys Lett*. 2011;99(26):261107.
- [29] Ma J, Huang H, Ning K, Xu X, Xie G, Qian L et al. Generation of 30 fs pulses from a diode-pumped graphene mode-locked Yb:CaYAlO₄ laser. *Opt Lett*. 2016;41:890.
- [30] Bonaccorso F, Sun Z. Solution processing of graphene, topological insulators and other 2d crystals for ultrafast photonics. *Opt Mater Express*. 2014;4:63–78.
- [31] Huang P, Lin S, Yeh C, Kuo H, Huang S, Lin G et al. Stable mode-locked fiber laser based on CVD fabricated graphene saturable absorber. *Opt Express*. 2012;20:2460.
- [32] Sotor J, Sobon G, Macherzynski W, Paletko P, Grodecki K, Abramski K. Mode-locking in Er-doped fiber laser based on mechanically exfoliated Sb₂Te₃ saturable absorber. *Opt Mater Express*. 2013;4:1.
- [33] Liu H, Zheng X, Liu M, Zhao N, Luo A, Luo Z et al. Femtosecond pulse generation from a topological insulator mode-locked fiber laser. *Opt Express*. 2014;22(6):6868.
- [34] Zhang H, Lu S, Zheng J, Du J, Wen S, Tang D et al. Molybdenum disulfide (MoS₂) as a broadband saturable absorber for ultra-fast photonics. *Opt Express*. 2014;22:7249.
- [35] Liu H, Luo A, Wang F, Tang R, Liu M, Luo Z et al. Femtosecond pulse erbium-doped fiber laser by a few-layer MoS₂ saturable absorber. *Opt Lett*. 2014;39:4591.
- [36] Sotor J, Sobon G, Macherzynski W, Paletko P, Abramski K. Black phosphorus saturable absorber for ultrashort pulse generation. *Appl Phys Lett*. 2015;107:051108.
- [37] Sotor J, Sobon G, Kowalczyk M, Macherzynski W, Paletko P, Abramski K. Ultrafast thulium-doped fiber laser mode locked with black phosphorus. *Opt Lett*. 2015;40:3885.

- [38] Song Y, Yamashita S, Goh C, Set S. Carbon nanotube mode lockers with enhanced nonlinearity via evanescent field interaction in D-shaped fibers. *Opt Lett.* 2006;32:148.
- [39] Song Y, Jang S, Han W, Bae M. Graphene mode-lockers for fiber lasers functioned with evanescent field interaction. *Appl Phys Lett.* 2010;96:051122.
- [40] Sotor J, Sobon G, Grodecki K, Abramski K. Mode-locked erbium-doped fiber laser based on evanescent field interaction with Sb₂Te₃ topological insulator. *Appl Phys Lett.* 2014;104:251112.
- [41] Jung M, Lee J, Park J, Koo J, Jhon Y, Lee J. Mode-locked, 1.94- μ m, all-fiberized laser using WS₂-based evanescent field interaction. *Opt Express.* 2015;23:19996.
- [42] Luo Z, Wang J, Zhou M, Xu H, Cai Z, Ye C. Multiwavelength mode-locked erbium-doped fiber laser based on the interaction of graphene and fiber-taper evanescent field. *Laser Phys Lett.* 2012;9:229–233.
- [43] Wang J, Luo Z, Zhou M, Ye C, Fu H, Cai Z et al. Evanescent-Light Deposition of graphene onto tapered fibers for passive Q-switch and mode-locker. *IEEE Photonics J.* 2012;4:1295–1305.
- [44] Kieu K, Mansuripur M. Femtosecond laser pulse generation with a fiber taper embedded in carbon nanotube/polymer composite. *Opt Lett.* 2007;32:2242.
- [45] Kashiwagi K, Yamashita S. Deposition of carbon nanotubes around microfiber via evanescent light. *Opt Express.* 2009;17:18364.
- [46] Du J, Wang Q, Jiang G, Xu C, Zhao C, Xiang Y et al. Ytterbium-doped fiber laser passively mode locked by few-layer molybdenum disulfide (MoS₂) saturable absorber functioned with evanescent field interaction. *Sci Rep.* 2014;4:6346.
- [47] Liu W, Pang L, Han H, Tian W, Chen H, Lei M et al. 70-fs mode-locked erbium-doped fiber laser with topological insulator. *Sci Rep.* 2016;5:19997.
- [48] Sotor J, Sobon G, Abramski K. Sub-130 fs mode-locked Er-doped fiber laser based on topological insulator. *Opt Express.* 2014;22:13244.
- [49] Jung M, Koo J, Park J, Song Y, Jhon Y, Lee K et al. Mode-locked pulse generation from an all-fiberized, Tm-Ho-codoped fiber laser incorporating a graphene oxide-deposited side-polished fiber. *Opt Express.* 2013;21:20062.
- [50] Park N, Jeong H, Choi S, Kim M, Rotermund F, Yeom D. Monolayer graphene saturable absorbers with strongly enhanced evanescent-field interaction for ultrafast fiber laser mode-locking. *Opt Express.* 2015;23:19806.
- [51] Bogusławski J, Soboń G, Zybala R, Mars K, Mikula A, Abramski K et al. Investigation on pulse shaping in fiber laser hybrid mode-locked by Sb₂Te₃ saturable absorber. *Opt Express.* 2015;23:29014.

- [52] Rusu M, Herda R, Kivistö S, Okhotnikov O. Fiber taper for dispersion management in a mode-locked ytterbium fiber laser. *Opt Lett*. 2006;31:2257.
- [53] Mueller T, Xia F, Avouris P. Graphene photodetectors for high-speed optical communications. *Nat Photonics*. 2010;4:297–301.
- [54] Liu M, Yin X, Ulin-Avila E, Geng B, Zentgraf T, Ju L et al. A graphene-based broadband optical modulator. *Nature*. 2011;474:64–67.
- [55] Kim J, Choi C. Graphene-based polymer waveguide polarizer. *Opt Express*. 2012;20:3556.
- [56] Shao Y, Wang J, Wu H, Liu J, Aksay IA, Lin Y. Graphene based electrochemical sensors and biosensors: a review. *Electroanalysis*. 2010;22:1027–1036.
- [57] Wang X, Zhi L, Müllen K. Transparent, Conductive graphene electrodes for dye-sensitized solar cells. *Nano Lett*. 2008;8:323–327.
- [58] Castro Neto A, Guinea F, Peres N, Novoselov K, Geim A. The electronic properties of graphene. *Rev Modern Phys*. 2009;81:109–162.
- [59] Xing G, Guo H, Zhang X, Sum T, Huan C. The physics of ultrafast saturable absorption in graphene. *Opt Express*. 2010;18:4564.
- [60] Newson R, Dean J, Schmidt B, van Driel H. Ultrafast carrier kinetics in exfoliated graphene and thin graphite films. *Opt Express*. 2009;17:2326.
- [61] Dawlaty J, Shivaraman S, Chandrashekar M, Spencer M, Rana F. Measurement of ultrafast carrier dynamics in epitaxial graphene. *MRS Proc*. 2008;1081.
- [62] Nair R, Blake P, Grigorenko A, Novoselov K, Booth T, Stauber T et al. Fine structure constant defines visual transparency of graphene. *Science* 2008;320:1308–1308.
- [63] Popa D, Sun Z, Torrisi F, Hasan T, Wang F, Ferrari A. Sub 200 fs pulse generation from a graphene mode-locked fiber laser. *Appl Phys Lett*. 2010;97:203106.
- [64] Cho W, Kim J, Lee H, Bae S, Hong B, Choi S et al. High-quality, large-area monolayer graphene for efficient bulk laser mode-locking near 125 μm . *Opt Lett*. 2011;36:4089.
- [65] Zaugg C, Sun Z, Wittwer V, Popa D, Milana S, Kulmala T et al. Ultrafast and widely tuneable vertical-external-cavity surface-emitting laser, mode-locked by a graphene-integrated distributed Bragg reflector. *Opt Express*. 2013;21:31548.
- [66] Schibli T, Thoen E, Kärtner F, Ippen E. Suppression of Q-switched mode locking and break-up into multiple pulses by inverse saturable absorption. *Appl Phys. B* 2000;70:S41–S49.
- [67] Sobon G, Sotor J, Pasternak I, Krajewska A, Strupinski W, Abramski K. Multilayer graphene-based saturable absorbers with scalable modulation depth for mode-locked Er- and Tm-doped fiber lasers. *Opt Mater Express*. 2015;5:2884.

- [68] Zhu S, Yuan S, Janssen G. Optical transmittance of multilayer graphene. *EPL* 2014;108:17007.
- [69] Liu H, Chow K. Enhanced stability of dispersion-managed mode-locked fiber lasers with near-zero net cavity dispersion by high-contrast saturable absorbers. *Opt Lett*. 2013;39:150.
- [70] Fu B, Hua Y, Xiao X, Zhu H, Sun Z, Yang C. Broadband graphene saturable absorber for pulsed fiber lasers at 1, 1.5, and 2 μm . *IEEE J. Sel. Top. Quantum Electron*. 2014;20:1100705.
- [71] Sotor J, Sobon G, Pasternak I, Krajewska A, Strupinski W, Abramski K. Simultaneous mode-locking at 1565 nm and 1944 nm in fiber laser based on common graphene saturable absorber. *Opt Express*. 2013;21:18994.
- [72] Sotor J, Sobon G, Tarka J, Pasternak I, Krajewska A, Strupinski W et al. Passive synchronization of erbium and thulium doped fiber mode-locked lasers enhanced by common graphene saturable absorber. *Opt Express*. 2014;22:5536.
- [73] Sobon G. Mode-locking of fiber lasers using novel two-dimensional nanomaterials: graphene and topological insulators [Invited]. *Photon Res*. 2015;3:A56.
- [74] Grelu P, Akhmediev N. Dissipative solitons for mode-locked lasers. *Nat Photonics*. 2012;6:84–92.
- [75] Shi R, Bai Y, Qi M, Chen X, Wei H, Ren Z et al. A passively mode-locked intracavity frequency doubled Nd:YVO₄ femtosecond green laser based on graphene. *Laser Phys Lett*. 2013;11:025001.
- [76] Cizmeciyan M, Kim J, Bae S, Hong B, Rotermund F, Sennaroglu A. Graphene mode-locked femtosecond Cr:ZnSe laser at 2500 nm. *Opt Lett*. 2013;38:341.
- [77] Ma J, Xie G, Lv P, Gao W, Yuan P, Qian L et al. Graphene mode-locked femtosecond laser at 2 μm wavelength. *Opt Lett*. 2012;37:2085.
- [78] Renninger W, Chong A, Wise F. Dissipative solitons in normal-dispersion fiber lasers. *Phys. Rev. A* 2008;77: 023814
- [79] Zhao L, Tang D, Zhang H, Wu X, Bao Q, Loh K. Dissipative soliton operation of an ytterbium-doped fiber laser mode locked with atomic multilayer graphene. *Opt Lett*. 2010;35:3622.
- [80] Liu J, Wei R, Xu X, Wang P. Mode-locked fiber laser with few-layer epitaxial graphene grown on 6H-SiC substrates. In: *CLEO:2011 – Laser Applications to Photonic Applications 2011*, 1–6 May 2011, Baltimore, USA; p. CMK3.
- [81] Liu J, Wu S, Yang Q, Song Y, Wang Z, Wang P. 163 nJ graphene mode-locked Yb-doped fiber laser. In: *CLEO:2011 – Laser Applications to Photonic Applications 2011*; 1–6 May 2011; Baltimore, USA; p. JWA23.

- [82] Li X, Wang Y, Wang Y, Zhang Y, Wu K, Shum P et al. All-normal-dispersion passively mode-locked Yb-doped fiber ring laser based on a graphene oxide saturable absorber. *Laser Phys Lett*. 2013;10:075108.
- [83] Chong A, Buckley J, Renninger W, Wise F. All-normal-dispersion femtosecond fiber laser. *Opt Express*. 2006;14:10095.
- [84] Chong A, Renninger W, Wise F. All-normal-dispersion femtosecond fiber laser with pulse energy above 20 nJ. *Opt Lett*. 2007;32:2408.
- [85] Szczepanek J, Kardaś T, Michalska M, Radzewicz C, Stepanenko Y. Simple all-PM-fiber laser mode-locked with a nonlinear loop mirror. *Opt Lett*. 2015;40:3500.
- [86] Chichkov N, Hapke C, Hausmann K, Theeg T, Wandt D, Morgner U et al. 05 μ J pulses from a giant-chirp ytterbium fiber oscillator. *Opt Express*. 2011;19:3647.
- [87] Lecourt J, Duterte C, Narbonneau F, Kinet D, Hernandez Y, Giannone D. All-normal dispersion, all-fibered PM laser mode-locked by SESAM. *Opt Express*. 2012;20:11918.
- [88] Sotor J, Pasternak I, Krajewska A, Strupinski W, Sobon G. Sub-90 fs stretched-pulse mode-locked fiber laser based on a graphene saturable absorber. *Opt Express*. 2015;23:27503.
- [89] Tarka J, Sobon G, Boguslawski J, Sotor J, Jagiello J, Aksienionek M et al. 168 fs pulse generation from graphene-chitosan mode-locked fiber laser. *Opt Mater Express*. 2014;4:1981.
- [90] Hudson D. Invited paper: Short pulse generation in mid-IR fiber lasers. *Opt Fiber Technol*. 2014;20:631–641.
- [91] Rudy C, Digonnet M, Byer R. Advances in 2- μ m Tm-doped mode-locked fiber lasers. *Opt Fiber Technol*. 2014;20:642–649.
- [92] Scholle K, Lamrini S, Koopmann P, Fuhrberg P. 2 μ m laser sources and their possible applications. In: *Frontiers in Guided Wave Optics and Optoelectronics*. InTech; 2010.
- [93] Inventory of U.S. Greenhouse Gas Emissions and Sinks: 1990–2011, EPA 430-R-13-001. U.S. Environmental Protection Agency; 2013.
- [94] Anderson B, Bartlett K, Frolking S, Hayhoe K, Jenkins J, Salas W. Methane and Nitrous Oxide Emissions from Natural Sources. U.S. Environmental Protection Agency; Washington, DC, USA; 2010.
- [95] Projected Greenhouse Gas Emissions. In: *Fourth Climate Action Report to the UN Framework Convention on Climate Change*. U.S. Department of State, Washington, DC, USA; 2007.
- [96] Zhang M, Kelleher E, Torrisi F, Sun Z, Hasan T, Popa D et al. Tm-doped fiber laser mode-locked by graphene-polymer composite. *Opt Express*. 2012;20:25077.

- [97] Wang Q, Chen T, Zhang B, Li M, Lu Y, Chen K. All-fiber passively mode-locked thulium-doped fiber ring laser using optically deposited graphene saturable absorbers. *Appl Phys Lett*. 2013;102:131117.
- [98] Sobon G, Sotor J, Pasternak I, Krajewska A, Strupinski W, Abramski K. Thulium-doped all-fiber laser mode-locked by CVD-graphene/PMMA saturable absorber. *Opt Express*. 2013;21:12797.
- [99] Sobon G, Sotor J, Pasternak I, Krajewska A, Strupinski W, Abramski K. All-polarization maintaining, graphene-based femtosecond Tm-doped all-fiber laser. *Opt Express*. 2015;23:9339.
- [100] Sobon G, Sotor J, Pasternak I, Krajewska A, Strupinski W, Abramski K. 260 fs and 1 nJ pulse generation from a compact, mode-locked Tm-doped fiber laser. *Opt Express*. 2015;23:31446.
- [101] Peng H, Dang W, Cao J, Chen Y, Wu D, Zheng W et al. Topological insulator nanostructures for near-infrared transparent flexible electrodes. *Nat Chem*. 2012;4:281–286.
- [102] Hajlaoui M, Papalazarou E, Mauchain J, Lantz G, Moisan N, Boschetto D et al. Ultrafast surface carrier dynamics in the topological insulator Bi₂Te₃. *Nano Lett*. 2012;12:3532–3536.
- [103] Kumar N, Ruzicka B, Butch N, Syers P, Kirshenbaum K, Paglione J et al. Spatially resolved femtosecond pump-probe study of topological insulator Bi₂Se₃. *Phys. Rev. B* 2011;83: 235306
- [104] Hsieh D, Mahmood F, McIver J, Gardner D, Lee Y, Gedik N. Selective probing of photoinduced charge and spin dynamics in the bulk and surface of a topological insulator. *Phys Rev Lett*. 2011;107
- [105] Lu S, Zhao C, Zou Y, Chen S, Chen Y, Li Y et al. Third order nonlinear optical property of Bi₂Se₃. *Opt Express*. 2013;21:2072.
- [106] Zhao C, Zou Y, Chen Y, Wang Z, Lu S, Zhang H et al. Wavelength-tunable picosecond soliton fiber laser with topological insulator: Bi₂Se₃ as a mode locker. *Opt Express*. 2012;20:27888.
- [107] Luo Z, Liu M, Liu H, Zheng X, Luo A, Zhao C et al. 2 GHz passively harmonic mode-locked fiber laser by a microfiber-based topological insulator saturable absorber. *Opt Lett*. 2013;38:5212.
- [108] Sotor J, Sobon G, Macherzynski W, Abramski K. Harmonically mode-locked Er-doped fiber laser based on a Sb₂Te₃ topological insulator saturable absorber. *Laser Phys Lett*. 2014;11:055102.
- [109] Wilson J, Yoffe A. The transition metal dichalcogenides discussion and interpretation of the observed optical, electrical and structural properties. *Adv Phys*. 1969;18:193–335.

- [110] Wang Q, Kalantar-Zadeh K, Kis A, Coleman J, Strano M. Electronics and optoelectronics of two-dimensional transition metal dichalcogenides. *Nat Nanotech* 2012;7:699–712.
- [111] Kumar A, Ahluwalia P. Electronic structure of transition metal dichalcogenides monolayers 1H-MX₂ (M = Mo, W; X = S, Se, Te) from ab-initio theory: new direct band gap semiconductors. *The European Physical Journal B* 2012;85:186
- [112] Wang K, Wang J, Fan J, Lotya M, O'Neill A, Fox D et al. Ultrafast saturable absorption of two-dimensional MoS₂ nanosheets. *ACS Nano* 2013;7:9260–9267.
- [113] Zhang M, Howe R, Woodward R, Kelleher E, Torrisi F, Hu G et al. Solution processed MoS₂-PVA composite for sub-bandgap mode-locking of a wideband tunable ultrafast Er:fiber laser. *Nano Res.* 2015;8:1522–1534.
- [114] Liu M, Zheng X, Qi Y, Liu H, Luo A, Luo Z et al. Microfiber-based few-layer MoS₂ saturable absorber for 2.5 GHz passively harmonic mode-locked fiber laser. *Opt Express.* 2014;22:22841.
- [115] Wu K, Zhang X, Wang J, Chen J. 463-MHz fundamental mode-locked fiber laser based on few-layer MoS₂ saturable absorber. *Opt Lett.* 2015;40:1374.
- [116] Mao D, Du B, Yang D, Zhang S, Wang Y, Zhang W et al. Nonlinear saturable absorption of liquid-exfoliated molybdenum/tungsten ditelluride nanosheets. *Small.* DOI: 10.1002/smll.201503348
- [117] Guoyu H, Song Y, Li K, Dou Z, Tian J, Zhang X. Mode-locked ytterbium-doped fiber laser based on tungsten disulphide. *Laser Phys Lett.* 2015;12:125102.
- [118] Mao D, Wang Y, Ma C, Han L, Jiang B, Gan X et al. WS₂ mode-locked ultrafast fiber laser. *Sci Rep.* 2015;5:7965.
- [119] Wu K, Zhang X, Wang J, Li X, Chen J. WS₂ as a saturable absorber for ultrafast photonic applications of mode-locked and Q-switched lasers. *Opt Express.* 2015;23:11453.
- [120] Nishii T, Maruyama Y, Inabe T, Shirotani I. Synthesis and characterization of black phosphorus intercalation compounds. *Synth Met.* 1987;18:559–564.
- [121] Baba M, Nakamura Y, Takeda Y, Shibata K, Morita A, Koike Y et al. Hall effect and two-dimensional electron gas in black phosphorus. *J Phys: Condens Matter.* 1992;4:1535–1544.
- [122] Xia F, Wang H, Jia Y. Rediscovering black phosphorus as an anisotropic layered material for optoelectronics and electronics. *Nature Communications* 2014;5:4458
- [123] Liu H, Neal A, Zhu Z, Luo Z, Xu X, Tománek D et al. Phosphorene: an unexplored 2D semiconductor with a high hole mobility. *ACS Nano.* 2014;8:4033–4041.
- [124] Cai Y, Zhang G, Zhang YW. Layer-dependent band alignment and work function of few-layer phosphorene. *Sci. Rep.* 2014;4:6677

- [125] Tran V, Soklaski R, Liang Y, Yang L. Layer-controlled band gap and anisotropic excitons in few-layer black phosphorus. *Phys. Rev. B* 2014;89: 235319.
- [126] Lu SB, Miao LL, Guo ZN, Qi X, Zhao CJ, Zhang H, Wen SC, Tang DY, Fan DY. Broadband nonlinear optical response in multi-layer black phosphorus: an emerging infrared and mid-infrared optical material. *Opt Express*. 2015;23:11183–11194.
- [127] Zheng X, Chen R, Shi G, Zhang J, Xu Z, X. Cheng, T. Jiang. Characterization of nonlinear properties of black phosphorus nanoplatelets with femtosecond pulsed Z-scan measurements. *Opt Lett*. 2015;40:3480–3483.
- [128] Sotor J, Sobon G, Macherzynski W, Paletko P, Abramski KM. Black phosphorus a new saturable absorber material for ultrashort pulse generation. arXiv:1504.04731 [cond-mat.mtrl-sci].
- [129] Yu H, Zheng X, Yin K, Cheng X, Jiang T. Thulium/holmium-doped fiber laser passively mode locked by black phosphorus nanoplatelets-based saturable absorber. *Appl Opt*. 2015;54:10290.
- [130] Wang Z, Zhao R, He J, Zhang B, Ning J, Wang Y et al. Multi-layered black phosphorus as saturable absorber for pulsed Cr:ZnSe laser at 2.4 μm . *Opt Express*. 2016;24:1598.

2D-Based Nanofluids: Materials Evaluation and Performance

Jaime Taha-Tijerina, Laura Peña-Parás and
Demófilo Maldonado-Cortés

Additional information is available at the end of the chapter

<http://dx.doi.org/10.5772/63806>

Abstract

Advancement in technology demands the successful utilization of energy and its management in a greater extent. Thermal energy management plays a crucial role from high-payload electrical instruments to ultra-small electronic circuitries. The advent of nanofluids that happened in the 1990s successfully addressed the low thermal efficiency of conventional fluids in a significant manner. The ground-breaking report on the concept of “nanofluids for thermal management” led to the development of numerous thermal fluids using nanofillers of ceramics, metals, semiconductors, various carbon nanostructures, and composite materials. Later, demonstration of two-dimensional (2D) nanomaterials and their successful bulk synthesis led to the development of highly efficient fluids with even very low filler fractions. Introduction of 2D materials into fluids also brought out the multifunctional aspects of fluids by using them in tribology. In this chapter, we narrate the advances in thermal nanofluids and the development of novel fluids with the discovery graphene. Multifunctional aspects of these fluids are discussed here. To support the experimental observation, a theoretical platform is discussed and its predictions are correlated on the basis of existing data. The chapter has been concluded with a brief discussion on futuristic aspects of nanofluids in real-life applications. This chapter aims to focus on the description of the thermal transport, tribological behavior, and aspects that involve the use of 2D-based nanofluids, from various 2D nanostructures such as h-BN, MoS₂, WS₂, graphene, among others. The homogeneous nanoparticle distribution within conventional fluids and the results from the thermal transport and tribological tests and observations are included. The nanofluids under investigation belong mainly to dielectric and metal-mechanic lubricants. Also, the mechanisms that promote these effects on the improvement of nanofluids properties are considered.

Keywords: 2D nanostructures, nanofluids, tribology, wear, scuffing, thermal conductivity

1. General overview

Energy, the input to impulse the world's future, has been pointed out as the most important issue facing humanity in the next 50 years and crucial to solve issues like mitigation of pollution, global warming, among others [1]. For instance, among diverse forms of energy used, over 70% is produced in or through the form of heat [2]. Heat is transferred either to input energy into a system or to remove the energy produced in a system. Considering the rapid increase in energy demand worldwide, intensifying heat transfer process and thereby reducing energy loss are becoming increasingly important tasks. That is why thermal management plays a crucial factor concerning apparatuses or machines performance; thermal dissipation role has been subjected to many investigations and is under the scope of the operational useful life of these devices and components.

Nanotechnology is a science that deals with diverse phenomenon's, properties', and materials' characteristics at the nanometric level (1 nanometer, nm = 10^{-9} m). Important and interesting discoveries have been realized in this field over the past 30 years. Among them, the discovery of Buckyball (C_{60}) [3], carbon nanotubes (CNTs) [4], and graphene isolation and identification [5] are just to mention some of them. During the last couple of decades, diverse techniques, equipment, and instrumentations have been devised, as well as various relevant and interesting characteristics and properties of these materials were sort out for the betterment of mankind.

Energy management becomes crucial for meeting the rising needs of mankind [2]. Nowadays, with increasing pressure of globalized markets and companies' profit race, a dramatic search is carried out for obtaining proper material performance; optimizing components and devices designs; improving efficiencies; reducing tools wear, materials consumption, and pollution; and obtaining the most possible revenue. In addition to issues regarding scrap materials, maintenance, and components wear among others, a hot topic in industry is the heat dissipation. Avoiding or reducing the use of resources for cooling equipment, or simply reflected in wear/friction issues among metal-mechanic processes, there is a high demand for successful heat management and energy-efficient fluid-based heat transfer systems, with aid of reinforced materials.

2. Introduction to nanofluids

Among diverse techniques to cool down or maintain certain temperature in these systems, vanes, fins, or radiators as well as forced air/fluids thru cooling channels are being used, even though they are costly. Some equipment and devices use inexpensive conventional heat transfer fluids to intensify heat dissipation, such as water (DiW), ethylene-glycol (EG), oils, and other lubricants. However, the inherent limitation of these fluids is the relatively low thermal conductivity; water, for instance, is roughly three orders of magnitude less conductive than copper or aluminum (**Table 1**). What these conventional fluids lack in thermal conductivity, however, is compensated by their ability to flow.

	Material	Thermal conductivity (W/m K)	Ref.
Conventional fluids	Water (DiW)	~0.598–0.609	[3, 10, 11]
	Ethylene glycol (EG)	~0.251	[12–14]
	Engine oil	~0.145	[12, 14]
	Mineral oil	~0.115	[15, 16]
	Kerosene	~0.139	[4]
	Toluene	~0.133	[4]
	R141b refrigerant	~0.089	[17]
Metallic solids	Aluminum	237	[18]
	Copper	398	[18]
	Gold	315	[18]
	Iron	80	[18]
	Nickel	91	[18]
	Silver	424	[18]
Carbon structures	Singlewall nanotubes (SWCNTs)	3000–6000	[19–22]
	Multiwall nanotubes (MWCNTs)	~3000	[23, 24]
	Carbon (diamond)	900–2320	[25, 26]
	Carbon (graphite)	119–165	[25]
	Graphene	~3000	[27, 28]
	Graphite	130–2000	[29]
Non-metallic solids	Alumina (Al ₂ O ₃)	31–41	[29–31]
	Aluminum nitride (AlN)	319–550	[32]
	Boron nitride (h-BN)	~300	[33, 34]
	Boron nitride nanotubes (BNNTs)	~600–960	[35–37]
	Boron nitride nanoribbons (BNNRs)	1700–2000	[42]
	Copper oxide (CuO)	76.5	[38]
	Molybdenum disulfide (MoS ₂)	34.5 ± 4	[39]
	Silicon carbide (SiC)	148	[18]
	Silicon oxide (SiO ₂)	1.4	[40, 41]
	Titania (TiO ₂)	8.4	[13]
Tungsten disulfide (WS ₂)	32–53	[42]	
	Zinc oxide (ZnO)	29	[13]

Table 1. Typical thermal conductivities for diverse conventional fluids and solid materials.

The primary mechanism for heat transfer in fluids is convection; its efficacy mostly depends on the thermo-physical properties of conventional fluids. Still, if the thermal conductivity of conventional fluids were enhanced, it would be much more effective. Hence, since the solid materials possess several orders higher thermal conductivity compared with that of conventional fluids, an idea to introduce conducting particles to fluids was considered. This idea occurred more than a century ago for Maxwell [6], where millimeter- or micrometer-sized solid particles were dispersed in conventional fluids to increase cooling rates, also a formulation of a method to calculate the effective conductivity of such suspensions was developed. Later, this technique was investigated and adapted for particle shape and composition by Hamilton and Crosser [7], but neither can predict the enhanced thermal conductivities of nanofluids (NFs) because their models do not include any dependence on particle size [8, 9]. Among diverse particle geometry, different particle shapes occur naturally or are engineered for specific applications (see **Figure 1**).

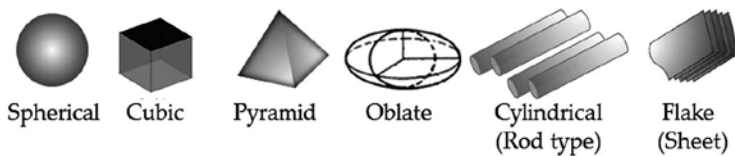


Figure 1. Diverse particle shapes and geometries.

Heat transfer using fluids is a very complicated phenomenon, and various factors such as fluid stability, composition, viscosity, surface charge, interface, and morphology of the dispersed particles influence the observed results [43–45]. Optimization and high efficiency of components and devices have gained great importance since these factors play a paramount role in diverse fields such as microelectronics, engine motors, fuel cells, air conditioning, power transmission systems, solar cells, medical therapy and diagnosis, biopharmaceuticals, components' and tools' wear, and nuclear reactors cooling, among others [15, 27, 46–49]. Solid materials such as metals, CNTs, oxide/nitride/carbide ceramics, semiconductors, and composite materials having higher thermal conductivity can be suspended within conventional fluids, resulting in better thermal transport performance composite fluids. Nevertheless, improvement in thermal conductivity cannot be achieved by just increasing the solid filler concentration because beyond a certain limit, increasing the filler fraction will also increase the viscosity, which will adversely affect the fluid properties and performance.

Most early studies used suspensions of millimeter- or micrometer-sized particles, which led to countless problems, such as a tendency to settle too rapidly, unless flow rate is increased; not only losing the enhancement in thermal conductivity but also forming sludge sediment, increasing the thermal resistance, and impairing the heat transfer capacity of the conventional fluids. In addition, increasing flow rate also increases erosion of pipelines or channels by the coarse and hard particles; outstanding thermal conductivity enhancement is based on high particle concentration, which leads to apparent increase in viscosity. Furthermore, fluids of this scale size could have considerably larger pressure drops, thus making flow through small

channels much more difficult since diverse parameters are critical for device performance, such as morphology and stability of dispersed particles or structures within these fluids, fluids composition, viscosity, fast sedimentation, channels clogging, wear or erosion, among others, which are often very serious for systems consisting of small channels [48–53]. Therefore, the search for nanofillers which can obtain high thermal conductivities at lower concentrations is desirable. Hence, extensive research has been done upon these conventional fluids, in order to develop improved materials to sublimely achieve all critical needs.

A revolution in the field of heat transfer fluids arose with the advent of NFs, a term introduced by Choi’s research group in the late 1990s at Argonne National Lab (ANL) [52]. First research was conducted by Masuda et al. [53] for $\gamma\text{-Al}_2\text{O}_3$ particles in water, and by Choi-Eastman group [52] for Cu in water as well. As depicted by **Figure 2**, nanofluids research has been increasing through time, reaching up to 1100 publications in 2015, according to scientific search engine “sciedirect.com” and keyword *Nanofluid*. On the inset of **Figure 2**, two keywords were applied *Nanofluid* and *2D*, where nearly 150 publications in 2015. Nanofluids are a new class of stable heat transfer liquid suspensions which are engineered containing homogeneously dispersed solid nanofillers (ultra-fine particles, fibers rods, or tubes <100 nm). Compared to micro- or milli-fluids, nanofluids tend to be more stable, since nanofillers possess unique properties, such as large surface area to volume ratio, as well as dimension-dependent physical properties, which make nanostructures better and more stably dispersed within conventional fluids. Nevertheless, some limitations of the effective incorporation of nanoparticles within conventional fluids are dispersion and solubility because these tend to aggregate and settle. In some cases, additives or surfactants are used to stabilize the nanoparticles within the fluids, even though the surfactants can decrease the thermal conductivity of the nanofluids, since surfactants introduce defects at the interfaces [54].

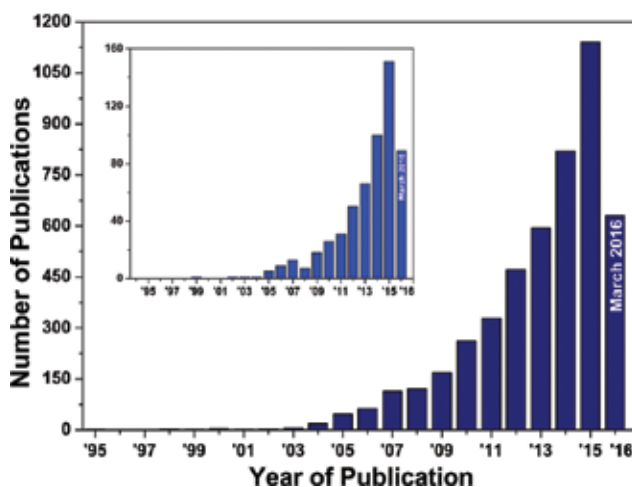


Figure 2. Number of publications with “Nanofluid” as search topic, according to Sciedirect.com; inset showing number of publications with keywords “Nanofluid” and “2D.”

Therefore, one of the main advantages of nanofluids is that they can be specially engineered to optimally fulfill particular objectives, such as enhanced thermal conductivity, a higher thermal energy storage capacity, a higher heat transfer coefficients, a better temperature stabilization, and less pressure drop, among others. Moreover, nanofluids are promising for practical application without clogging, sediment or such. Nanofluids will keep the fluidic properties of the conventional fluids, behave almost like conventional fluids, and incur in little or no extra penalty of pressure drop (i.e., the viscosity increase is small) due to the fact that dispersed nanoparticles are extremely small, which are very stably suspended in fluids with or without the aid of additives or surfactants [55]. Hence, search for new nanofillers which can get high thermal conductivities at lower filler fractions is important [15, 56].

It has been demonstrated that nanofluids for heat transfer applications have provided better thermal performance than conventional fluids [12, 15, 48, 49, 56–58]. Therefore, the advent of nanofluid-based heat transfer systems can make compact designs with highly efficient thermal, physical, and electrical performance for instruments and devices.

Experiments on convection heat transfer of nanofluids were conducted by several research groups [57, 59–61]. The results showed significant improvements in heat transfer rates of nanofluids. Meanwhile, the thermal conductivity enhancement of nanofluids shows a temperature-dependent characteristic—increase of enhancement with rising temperature, which makes the nanofluids more suitable for applications at elevated temperatures [15, 49, 62–66]. Additionally, previous research has shown that nanofluids display better performance in their thermo-physical and tribology properties, such as thermal conductivity, thermal diffusivity, viscosity, friction, etc., compared to conventional fluids [15, 46–49, 67–71]. Hence, nanofluids could be used for aforesaid engineering applications. From all these, a great variety of nanocomposite materials have been developed, using diverse techniques and methodologies, obtaining significant performance.

3. Synthesis and preparation of nanofluids

The manipulation of matter on the nanometer scale has become a central focus from both fundamental and technological perspectives. Unique, unpredictable, and highly intriguing physical, mechanical, optical, electrical, and magnetic phenomena result from the confinement of matter into nanoscale features. Morphology control in nanostructures has become a key issue in the preparation of electronic or mechanical nanodevices and functional materials [72]. A wide variety of combinations of nanostructures and conventional fluids can be used to synthesize and prepare stable nanofluids for diverse applications. Nanofluids could be manufactured by two methods:

- (a) *One-step method*: The one-step process simultaneously makes and disperses the nanostructures within the base fluid. This method avoids diverse processes such as particles drying, storage, handling, and dispersion, so the agglomeration of nanoparticles is minimized; therefore, stability of nanofluids is improved [73]. Thus, it is possible to obtain

uniformly dispersed and highly stable suspended nanostructures within the base fluids [74, 75].

- (b) *Two-step method*: Two-step method is the most widely used method for preparing nanofluids [15, 49, 76–82]. Various nanostructures such as nanofibers, nanotubes, nanosheets, among other nanomaterials used in this technique are initially produced by mechanical comminuting, chemical reaction, vapor condensation, or decomposition of organic complex [83–85] and finally obtained as dry powder. Then, it is followed by further dispersion of as-produced nanostructures within base fluids through magnetic force agitation (stirring), ball milling, ultrasonic agitation, and high-shear mixing, among others [77, 81, 86, 87]. This procedure is the most economic method to produce nanofluids in large scale since nanoparticle synthesis techniques are readily scaled up to mass production levels. Sonication is used to speed dissolution by breaking intermolecular interactions, and homogeneously dispersing nanoparticles within a fluid. It is especially useful when it is not possible or difficult to stir a sample.

3.1. Nanofluids: variables and features

Diverse features and challenges regarding the effect of nanoparticles on thermal transport, tribological performance, and energetic performance have been studied. The heat transfer enhancement in nanofluids, for example, has been attributed to many variables including nanoparticle size, shape, and filler fraction. However, as mentioned, diverse challenges have hindered their large-scale applications (Figure 3), such as nanoparticle dispersion, agglomeration, long-term stability, increase in nanofluid viscosity, cost increase, and scale-up capacity for industrial applications, which are presented in the following sections.

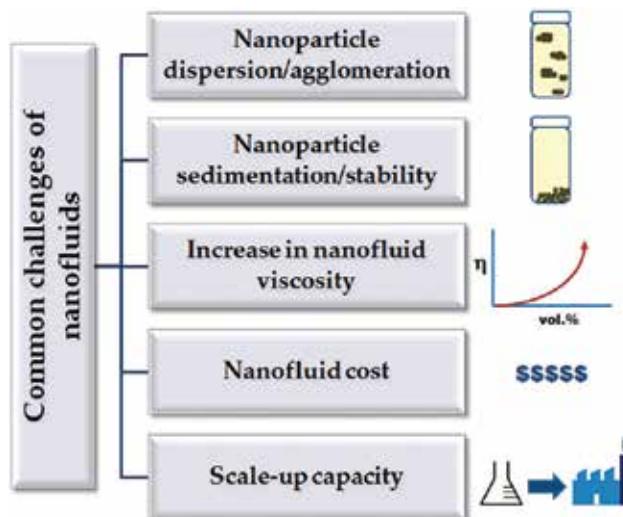


Figure 3. Common challenges of nanofluid developments.

3.1.1. Nanofiller size

Diverse studies have found that as nanoparticles are reduced in size, the effective thermal conductivity of the nanofluid increases [13, 64, 88–94]. As the nanoparticle size is reduced, Brownian motion is induced. Also, lighter and smaller nanoparticles are better at resisting sedimentation, one of the biggest technical challenges in experimenting with nanofluids [61]. Li et al. [88] investigated the thermal properties of $\text{Al}_2\text{O}_3/\text{DiW}$ nanofluids with particle sizes of 36 and 47 nm at various filler fractions. The nanofluid with 36-nm particles improved the effective thermal conductivity enhancement at $\sim 35^\circ\text{C}$, varying the filler fractions from 0.5 to 6.0 vol.% (~ 7 to $\sim 28\%$, respectively). Similar trend was observed for the nanofluid with 47 nm particles, but slightly lower thermal conductivity enhancement was shown compared to the smaller particles nanofluid (~ 4 to $\sim 25\%$, respectively). Nguyen et al. [95] and Minsta et al. [89] studied the heat transfer enhancement and behavior of Al_2O_3 -water nanofluid for microprocessors/electronic purposes. It is found that with smaller nanoparticles (36 nm in diameter), nanofluids showed higher convective heat transfer coefficients than with larger ones (47 nm in diameter). From Nguyen's research, thermal transport increased 40% at 6.8 vol.% filler fraction, as compared to water. Chopkar et al. [96] studied 0.20–2.0 vol.% $\text{Al}_{70}\text{Cu}_{30}$ nanoparticle reinforced EG, and also found that thermal conductivity strongly depends on the size of nanoparticles.

He et al. [97] studied the heat transfer behavior of TiO_2 -water nanofluids with diameters of 95, 145, and 210 nm at various filler fractions. For the 95-nm-particle-size nanofluid, the thermal conductivity showed an increase from 1 to $\sim 5\%$ at 1.0 and 4.9 wt.%, respectively, compared to water; as filler fraction increased, the thermal conductivity increased as well. It was shown that the effective thermal conductivity decreases as particle size increases. Research conducted by Hong et al. [77] achieved 18% increase in thermal conductivity with only 0.55 vol.% of Fe-nanoparticles (~ 10 nm size)-reinforced EG nanofluids. Showing as well that sonication of the nanofluid has an important effect on the thermal conductivity of the system indirectly proves the effect of particle size on the thermal conductivity of the nanofluid. Teng et al. [92] studied the effect of particle size, temperature, and weight fraction on the thermal conductivity ratio of Al_2O_3 /water nanofluid with filler fraction up to 2.0 wt.%, and different Al_2O_3 particle nominal diameters (20, 50, and 100 nm). The results showed a dependence relationship between high thermal conductivity ratios and enhanced sensitivity, small nanoparticle size, and higher temperature. Hence, nanofillers' size is a determinant variable for heat transfer nanofluids, since, as previously stated, its smaller size reduces or avoids critical issues of larger fillers.

Nevertheless, there have been a few reports on SiC, CeO_2 , and Al_2O_3 nanoparticles reinforcing water that stated a decrease of the effective thermal conductivity with increase in particle size [98–101]. As shown by Beck et al.'s [100] research on Al_2O_3 /water nanofluids with diverse particle sizes ranging from 8 to ~ 300 nm in diameter, the thermal conductivity enhancement decreases as the particle size decreases below ~ 50 nm. Beck et al. attribute this behavior to nanoparticles thermal conductivity, as the particle size becomes small enough to be affected by increased phonon scattering [100]. Similarly, studies performed on water-based CeO_2

nanofluids [101] showed an increase in the effective thermal conductivity with an increase of nanoparticle size, although only two particle sizes were studied (12 and 74 nm).

3.1.2. Particle shape/surface area

Several studies have found that rod-shaped nanoparticles, such as CNTs, remove more heat than spherical nanoparticles [78, 102–107], probably because rod-shaped particles have a larger aspect ratio (the ratio between a particle's surface area to volume) than spherical nanoparticles. Elias et al. [103] studied various boehmite alumina (γ -AlOOH) nanoparticle shapes (cylindrical, spherical, bricks, blades, and platelets) within EG/water (50/50%). Nanofluids at diverse filler fraction, up to 1.0 vol.%, showed a linear increase in thermal conductivity. Best performance was found for cylindrical-shaped nanoparticles, followed by bricks, blades, platelets, and spherical-shaped nanoparticles, respectively. Thermal conductivity enhancement of cylindrical-shaped nanoparticles is observed to be $\sim 2.5\%$ higher than the spherical shape with 1.0 vol.% filler fraction. Murshed et al. [104] investigated water reinforced with TiO₂ rod-type (10 nm in diameter and 40 nm in length) and spherical (15 nm) nanoparticles; an enhancement of thermal conductivity of ~ 30 and $\sim 33\%$, respectively, was observed at 5.0 vol.% filler fraction compared to base fluid. EG-based nanofluids with addition of SiC nanowhiskers (1.5 μm in diameter and 18 μm in length) and spherical particles (diameter $< 40 \mu\text{m}$) were investigated by Cherkasova et al. [106]. Nanowhiskers were prepared at various aspect ratios by ball milling from 0, 4, 12, and up to 28 h. At 2.5 vol.%, the thermal conductivity enhancement is observed to increase from 16.5 to 39.5% as the aspect ratio increases from 4.8 to 9.6. It is also observed that suspensions containing cylindrical particles showed significantly higher increase in thermal conductivity than suspensions with dispersed spherical particles. For 5.0 vol.%, a thermal conductivity enhancement of ~ 85 and $\sim 20\%$ was observed for suspensions containing SiC whiskers and spheres, respectively. Thermal conductivity increase for both types of particles is nearly linear with volume fraction of solids up to 5.0 vol.% as well. On other research on rod-type nanoparticles, Glory et al. [105] studied multiwall nanotubes (MWCNTs)/water nanofluids. An increase in thermal conductivity enhancement was observed with an increase of nanotube length. For instance, the relative increase of thermal conductivity of nanofluids at 2.0 wt.% with nanotubes with length of $\sim 0.5 \mu\text{m}$ was $\sim 14\%$, an 18% increase was observed for nanotubes with length of 1.0 μm , a 38% increase was observed for nanotubes with length of 1.7 μm , and finally, a $\sim 45\%$ increase was observed for the longest nanotubes tested with length of $\sim 5.0 \mu\text{m}$. As explained by Glory et al., this behavior is attributed to a mechanism where longer nanotubes diminish the number of nanotube-nanotube contacts, therefore favoring phonon transmission in the suspensions, giving an increase of the thermal conductivity. Other nanoparticles with morphology possessing large surface area are the 2D nanosheets, which are obtained by exfoliation layers in its structure [15, 108]. Moreover, little research has been conducted for 2D-nanoparticles reinforcing conventional fluids. Recently, it has been demonstrated by Taha-Tijerina et al. [15, 49] that 2D-based nanofluids have high impact in the thermal transport, as well as in physical, electrical, and tribological properties.

3.1.3. Filler fraction

Probably, the key variable for nanofluids' improvement is the nanofillers concentration homogeneously dispersed within conventional fluids. Filler fraction has been stated by volume and weight percentages in papers, patents, and reports. Effective thermal conductivity (k_{eff}) and coefficient of friction (COF), among other properties of nanofluids improve with increasing nanoparticles filler fraction [109], but as the nanoparticles filler fraction increases, it may no longer be valid to assume a well-suspended nanoparticles. Also, pressure drop has been observed in diverse conventional fluids as filler fraction of different nanoparticles is increased [10]. This is why it is more effective to use a very small filler fraction in nanofluids [15, 110–113]. At low filler fractions, nanostructures have more intense Brownian motion at higher temperatures, which can significantly enhance the effective thermal conductivity. But at high volume fractions, nanoparticles have high potential to be agglomerated at high temperatures.

3.1.4. Particles agglomeration

A key challenge with nanofluids is that nanoparticles tend to agglomerate due to molecular interactions, such as Van der Waals forces [99, 114]. Agglomeration of nanoparticles increases as filler fraction increases, due to closer particles and higher Van der Waals attraction. Similarly, this issue generates other problems such as viscosity increments (**Figure 4**). Agglomeration causes the effective surface area to volume ratio to decrease, which impacts the thermal conductivity performance of the fluid. Timofeeva et al. [99, 107] studied the thermal conductivity and viscosity of Al_2O_3 nanoparticles dispersed in water and EG. It is observed that the main parameters for controlling nanofluids' thermal conductivity enhancement are the geometry, agglomeration state, and surface resistance of nanoparticles. Karthikeyan et al. [109] identified that CuO nanoparticles and cluster size have a significant influence on thermal conductivity of water and EG. Similarly, it is found that nanoparticle agglomeration is time dependent; as time elapsed, agglomeration increased, which decreased the thermal conductivity. Wang et al. [115] performed studies on diverse fluids (water, pump fluid, engine oil, and EG) with the addition of Al_2O_3 and CuO with 28 and 23 nm in diameter, respectively. Viscosity of these systems increase as nanoparticles agglomerate, also thermal conductivity performance is observed to decrease, most probably an effect of the agglomeration of the nanoparticles. Moreover, particle agglomeration is exacerbated by the size of the reinforced fillers. Nasiri et al. observed a reduction in thermal conductivity with time for water-based CNT nanofluids due to agglomeration [114]. However, some reports show that aggregation in water-based Al_2O_3 nanofluids significantly increases the thermal conductivity of the fluid [116, 117]. In other studies, stable nanofluids showed no significant variation in thermal conductivity with time. Yu et al. observed that the thermal conductivity of EG-based ZnO nanofluids [118] and kerosene-based Fe_3O_4 nanofluids [119] were independent of time. Additionally, engine coolant-based Al_2O_3 nanofluid exhibited minimum change of thermal conductivity with time [120]. Yu et al. [121] conducted studies on EG-based graphene oxide nanosheets (GON). An enhancement in thermal conductivity at 5.0 vol.% of ~61% was observed. Thermal conductivity performance was invariable for ~7 days, reflecting high stability of GON/EG nanofluids.

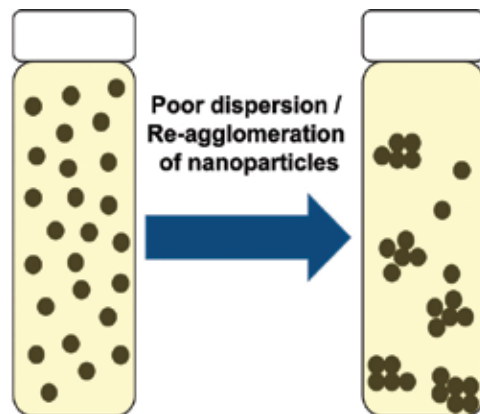


Figure 4. Scheme of nanoparticles sedimentation over time.

3.1.5. Stability

Because the reinforced particles are so small, weight is less, and the sedimentation probability is less too (**Figure 5**). This reduced nanostructures sedimentation can overcome one of the major drawbacks of suspensions, the settling of particles, and make the nanofluids more stable. In some cases, to enhance the stability of the nanofluids, surfactants or additives are used; nevertheless, there are certain drawbacks of using them.



Figure 5. Nanoparticles sedimentation; CuO-reinforced nanofluids over time.

3.1.6. Surfactants/additives

Surfactants are mainly used to stabilize the nanofillers within the conventional fluids, even though these surfactants can affect the nanofluids performance, since surfactants introduce defects at the molecular interfaces [54]. The use of surfactants and dispersion agents has shown to be effective providing repulsion between nanoparticles and reducing agglomeration [49, 81, 122, 123]. Additives are also incorporated to materials to enhance their mechanical properties. For instance, Chen et al. [124] found that the addition of stearic acid (SA) coated MWNTs, and performed as lubricant, improving the friction reduction and anti-wear properties of MWNTs. Non-ionic surfactants were found to strongly interact with graphite surfaces in case of CNTs

stabilization within aqueous suspensions [125]. Wang et al. [126] investigated oil with addition of graphite nanoparticles ($\sim 10\text{--}30\text{ nm}$), and also using a dispersant (CH-5) up to 12.0 wt.%. Graphite nanofluids at various filler fractions, from 0.5 to 4.0 wt.%, showed an increase in thermal conductivity from 0.5 to 20%, respectively. These increments were improved with the addition of dispersant (1.5–12.0 wt.%) from 2.4 to 36%. According to Wang et al., this behavior is due to the improvement in dispersibility of graphite with the aid of the dispersant. Oleic acid (OA)-modified TiO_2 nanostructures increased the maximum non-seizure load 6–10 times when added to water [127]. Recently, OA was added to h-BN/mineral oil nanofluids [49] showing a decrease of 8 and 3% COF and wear scar diameter (WSD), respectively, compared to the surfactant-less material. Similarly, the addition of OA surfactant in nanolubricants of CuO and MoS_2 in palm oil facilitated the reduction of agglomerates, thus improving the tribological properties [123]. In other cases, nanoparticles are used as additives to enhance their useful life, as well as antimicrobial agents. In metal-mechanic industry, for instance, diverse fluids are used to cut or lubricate stamping or metal-cutting processes. Nevertheless, some of them provide a breeding ground for large numbers of microorganisms (fungi/bacteria) which is hazardous to the machine operators [128, 129]. Kumar et al. used silver (Ag) nanoparticles dispersed in paints based on vegetable oil [130], since silver is highly antimicrobial by virtue of its antiseptic properties against several kinds of bacteria, fungi, and viruses [130, 131].

3.1.7. Viscosity

Viscosity is described as the internal resistance of a fluid to flow. Viscosities in nanofluids are dependent on both fillers geometry and surface properties of nanofillers. As mentioned by Timofeeva et al. [107], elongated particles and agglomerates result in higher viscosity at the same filler fraction due to structural limitation of rotational and transitional Brownian motions. Nguyen et al. [132] have investigated on particle size effect for Al_2O_3 aqueous-based nanofluids and observed that the particle size effects on viscosity are more significant for high particles concentration. Taha-Tijerina et al. [15] investigated mineral oil reinforced with 2D nanostructures of h-BN and graphene at very low filler fractions. It was observed that the viscosity of the nanofluids decreases significantly with temperature (from $16\text{ mm}^2/\text{s}$ at room temperature to $2.2\text{ mm}^2/\text{s}$ at 100°C), as expected; while the enhancement in viscosity with the addition of 2D-nanofillers is very small ($<2\%$ at 313 K). This is an additional advantage of the low filler fractions since the increase in viscosity will decrease the effective thermal conductivity values as well as flow characteristics of the fluid. Moreover, the relatively small increase in viscosity ($<30\%$) at 0.35 wt.% of h-BN is an evidence that the solution is not flocculating [133, 134]. Small deviations from the theoretical values of viscosity at higher concentrations of h-BN/MO may be as a result of a transition from a dilute to a semi-dilute phase or due to the onset of some small aggregation between the h-BN nanosheets [15].

3.1.8. Brownian motion

Researchers have found that Brownian motion, which is the random movement of particles (**Figure 6**), is one of the key heat transfer mechanisms in nanofluids [62, 115, 135–140]. Keblinski et al. stated possible micro-mechanisms for nanofluids thermal conductivity increase, among

which Brownian motion was the reason for this [45]. Moreover, Jang et al. proposed that particles' Brownian motion can induce nanoscale convection, which enhances the thermal conductivity of nanofluids [135]. Brownian motion only exists when the particles in the fluid are extremely small, and as the size of the particles gets larger, Brownian motion effects diminish [61].

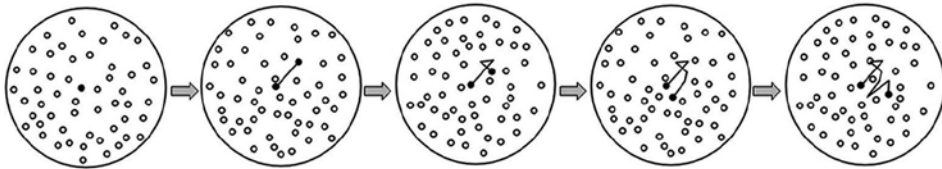


Figure 6. Representative scheme of Brownian (random) motion of nanoparticles.

3.1.9. Temperature dependence

Nanofluids' effective thermal conductivity and Brownian motion increase with temperature [11, 61–65, 141–143]. Das et al. [62], similarly to Lee et al. [144], observed that Al_2O_3 and CuO nanofluids thermal conductivity has temperature-dependent influence (in the range from 20 to 50°C); they posed motion of reinforced fillers as an important factor for that. Hu et al. showed a 20% increase in the thermal conductivity of ethanol with the addition of 4.0 vol.% of AlN at 273 K, and a strong temperature dependence of the thermal conductivity [145]. Similarly, Yu et al. [146] research on Al-N nanofluid showed an enhancement of $\sim 40\%$ with a little effect on temperature from 10 to 60°C . Wang et al. [40] measured thermal conductivity of TiO_2 (26 nm) and SiO_2 (23 nm) nanoparticles suspended in DiW, EG, and ethanol. The experiment was conducted with 1.0–4.0 vol.% filler fractions at temperatures ranging from 18 to 65°C . Results indicated that thermal conductivity of nanofluids was higher than the base fluids and increased with rise of temperature and filler fraction. For instance, from measurements taken at 18– 65°C , TiO_2/DiW nanofluid thermal conductivity improved from 3, 4, and 10% to 9, 10, and $\sim 20\%$ at filler fractions of 1.0, 2.0, and 4.0 vol.%, respectively. As seen from research conducted by Wen et al. [66], the effective thermal conductivity increases with increasing temperature, showing a non-linear dependence after temperatures above $\sim 30^\circ\text{C}$. On the other hand, studies by Das et al. [147] on $\text{Al}_2\text{O}_3/\text{water}$ nanofluids have shown that the thermal-conductivity ratio increased with temperature in a linear fashion.

Jyothirmayee et al. [141] observed a temperature dependence on graphene nanosheets (GnS)-reinforced EG and DiW, on temperatures ranging from 25 to 50°C . It was observed that the thermal conductivity increases with increasing graphene concentration and temperature. The thermal conductivity of the base fluids did not show much enhancement as the temperature increases, similar tendency as reported by Jha et al. [148]. An enhancement in thermal conductivity of $\sim 2.4\%$ is observed at 25°C with a very low filler fraction of 0.008 vol.% of the graphene/EG nanofluid, meanwhile, at 50°C , this increases to $\sim 17\%$. At 0.14 vol.%, the enhancement in thermal conductivity is 6.5% and 36% at 25 and 50°C , respectively. The behavior is similar as reported by Chon et al. [64] and Xie et al. [149]. For the 0.14 vol.%

graphene/DiW nanofluid, the enhancement is about 13.6% and 94.3% at 25 and 50°C, respectively. These high increments in thermal conductivity exhibited by the graphene-based nanofluids can be ascribed to the high aspect ratio of defect-free graphene sheets. Walvekar et al. [150] and Ding et al. [151] performed diverse studies on CNTs-water nanofluids, showing that thermal conductivity is highly dependent on temperature as well.

3.1.10. Interfacial layering on the liquid-nanostructure interface

Interfaces are ideal templates for assembling nanoparticles into 2D structures by the nature of the interfaces. At the interfaces, the nanoparticles are mobile and defects of the structures can be eliminated [152]. This ordered structure could have higher thermal conductivity than that of the conventional, therefore an enhancement of the effective thermal conductivity. However, some issues could be addressed when a surfactant or dispersant is used [66]. Interfacial layering refers to a phenomenon at the liquid-particle interface where liquid molecules are more ordered than those in the conventional liquid; therefore the interface effect could enhance the thermal conductivity by the layering of the liquid at the solid interface (giving that crystalline solids possess much better thermal transport than liquids) [45, 153], by which the atomic structure of the liquid layer is significantly more ordered than that of the conventional liquid. Various researchers have suggested that there is a liquid layering on the nanoparticles, which helps enhance the heat transfer properties of the nanofluid [151, 154–156]. Yu et al. [156] proved the formation of layers by the liquid molecules close to a solid surface, even though the thickness and thermal conductivity of the nanolayers are not well known yet. Ren et al. [157] found, through a theoretical model, that adding liquid layering on the nanoparticles an increase in layer thickness leads to higher thermal conductivity increment; as larger the size of the suspended particles, the weaker appear the effects of the nanolayer and the thermal motion.

4. Nanofluids application fields

Diverse studies on nanofluids have been carried out by many researchers. This section deals with literature reviews on nanofluids; nanofluids preparation and characterization; thermo-physical, electrical, and tribological properties; as well as nanofluids applications, which lays foundation and basis for further investigations. Some of the main fields of application for these systems are thermal management and tribological, which are described in the following sections.

4.1. Thermal performance of nanofluids

Heat transfer is classified into various mechanisms, such as thermal convection, thermal radiation, and thermal conduction. In diverse fields, thermal transport is a critical parameter to obtain efficient performance of components and devices. Heat convection occurs when bulk flow of a fluid (gas or liquid) carries heat along with the flow of matter in the fluid, this process could be “natural,” by density differences in the fluid occurring due to temperature gradients, or “forced,” where fluid motion is generated by an external source such as a pump, fan, or

other mechanical means. Radiation heat transfer is the transfer of energy by means of photons in electromagnetic waves in much the same way as electromagnetic light waves transfer light. On the other hand, heat conduction is the direct microscopic exchange of kinetic energy of particles through the boundary between two systems. When an object is at a different temperature from another body or its surroundings, heat flows so that the body and the surroundings reach the same temperature, at which point they are in thermal equilibrium. The thermal conductivity (k) of liquids can be successfully measured if the time taken to measure k is very small so that the convection current does not develop [158]. Effective thermal conductivity (k_{eff}) is described as the nanofluid thermal conductivity, compared to conventional fluid thermal conductivity. Diverse techniques have been proposed to measure nanofluids thermal conductivity over the past years. The most common techniques to measure the effective thermal conductivity of nanofluids are the transient hot-wire method [15, 47, 99, 126, 158–161], steady-state method [35, 88, 105, 115, 162], cylindrical cell method [163], temperature oscillation method [62, 164–166], and 3- ω method [40, 167–169] to name a few.

Heat transfer fluids have been explored in diverse systems. Argonne National Lab research group with Eastman et al. reported a 40% enhancement with only 0.40 vol.% of copper oxide (CuO) particles of 10 nm in diameter [83], while Choi et al. reported a remarkable 160% increase in thermal conductivity of MWCNTs/engine oil nanofluid at 1.0 vol.% filler fraction of nanotubes [170]. Marquis et al. [19] reported a thermal conductivity enhancement of 45% at 1.0 vol.% concentration of highly pure SWCNTs in 15W-40 oil. In this same investigation, a remarkable enhancement of 175% with 1.0 vol.% of MWCNTs in poly- α -olefin (BP Amoco Ds-166) oil is obtained, similar to Choi found at 1.0 vol.% of nanotubes in oil [170]. Similarly,, other researchers have investigated the effect of CNTs in diverse fluids with aid of dispersants. For instance, Liu et al. [14] measured the thermal conductivities of nanofluids containing MWCNTs dispersed in EG and synthetic engine oil. The increase of thermal conductivity for MWCNT/EG at 1.0 vol% was $\sim 12.5\%$, meanwhile, for MWCNT/synthetic engine oil, an improvement of ~ 9 and 30% for 1.0 and 2.0 vol.% filler fraction was observed. Wen et al. [66] investigated the effect of temperature on the thermal conductivity of MWCNTs/DiW (20–60 nm in diameter and micrometer size in length) nanofluids. In order to properly stabilize the MWCNTs within DiW, 20 wt.% of sodium dodecyl benzene sulfonate (SDBS) was added to all samples. At 0.84 vol.% filler fraction, thermal conductivity enhancements of ~ 24 and $\sim 31\%$ were achieved at 20 and 45°C , respectively. In general, an improvement on thermal conductivity enhancement was observed as filler fraction and temperature increased. Assael et al. [78] studied the MWCNTs/DiW nanofluids with addition of 0.10 wt.% sodium dodecyl sulfate (SDS) as a dispersant. According to Assael et al., SDS would interact with MWCNTs, affecting their outer surface, enhancing interactions with DiW. It was found that at 0.60 vol.% MWCNTs, the enhancement in thermal conductivity was $\sim 38\%$. Hwang et al. [41] investigated the thermal conductivity of DiW- and EG-based nanofluids. MWCNTs (10–30 nm in diameter and 10–50 μm in length), CuO, and SiO₂ (33 and 12 nm in diameter, respectively) were used. It was observed that thermal conductivity of nanofluids was improved almost linearly as filler fraction increased. For DiW-based systems, the addition of SiO₂, CuO, and MWCNTs at 1.0 vol.% filler fraction showed an increase of 3, 5, and $\sim 12\%$, respectively. Also, CuO/EG nanofluid at 1.0 vol.% showed an increase of $\sim 9\%$.

Ding et al. [66] also investigated the effects of MWCNTs dispersed in DiW, with addition of 0.25 wt.% gum Arabic (GA) dispersant. For MWCNTs at 0.50 and 1.0 wt.%, an increase in thermal conductivity was achieved up to ~30 and ~38% at 25°C, and ~35 and ~80% at 30°C, respectively. It was found that these improvements were slightly higher than that results reported by Liu et al. [14], Wen et al. [151], Assael et al. [78], and Xie et al. [171], but lower than that showed by Choi et al. [170]. There are diverse factors that cause these discrepancies among the different groups; as mentioned by Wang et al. [138], these discrepancies should rely on the dependency of thermal conductivity is on diverse factors such as the structure and properties of the CNTs, aspect ratio, clustering, addition of dispersants, temperature and the experimental errors as well. Hong et al. [58] successfully developed stable and homogeneous nanolubricants and nanogreases based on CNTs in polyolefin oils. Thermal conductivity experiments showed an increment of 20% at 0.10 wt.% filler fraction; similarly, at 3.0 and 10 wt.%, thermal conductivity increments were 50 and 80%, respectively. More recently, Walvekar et al. [150] analyzed the effect of CNTs on diverse temperatures ranging from 25 to 60°C. CNTs/DiW nanofluids were stabilized with the addition of GA as dispersant. Superb results showed improvements at diverse filler fractions, varying from 0.01 to 0.10 wt.%, and diverse temperatures, ranging from 25 to 60°C. A maximum thermal conductivity enhancement of ~288% was shown for 1.0 wt.% CNTs/DiW nanofluids at 60°C.

Research on oxide nanoparticles have been conducted as well. Das et al. [62], for instance, showed strong temperature dependence of nanofluids with Al_2O_3 and CuO particles as used by Lee et al. [144], which significantly improved the scope of nanofluids as an alternate for existing coolants. In 2005, Chon et al. [64] and Li et al. [172] confirmed this, but no temperature effect on thermal conductivity enhancement of nanofluids was observed in CNTs [173]. Li et al. [174] synthesized kerosene-based nanofluids with dispersed Cu nanoparticles (~40–60 nm in diameter). Temperature dependence on thermal conductivity for Cu/kerosene-based nanofluids showed that as nanofluid temperature increases, thermal conductivities increased as well. For measurements at 25, 40, and 50°C, the effective thermal conductivity increased by ~10, ~13, and 15%, respectively, with 1.0 wt.% Cu nanoparticles. In other investigations, nanodiamonds (<10 nm) dispersed in EG (with addition of poly (glycidol) polymer) and MO (with addition of OA) were studied by Branson et al. [175]. It was observed that addition of 0.88 vol.% of nanodiamonds enhanced the thermal conductivity by ~12%. In MO, for instance, with enhancements of ~6 and ~11%, filler fractions of 1.0 and 1.9 vol.% are achieved, respectively. According to Branson et al., the differences on enhancement efficiencies are attributable to divergence in thermal boundary resistance at nanoparticle/surfactant interfaces [175].

Several research studies have developed graphene-based nanofluids with high nanoparticle stability and significant enhancements [146, 176–183]. Shaikh et al. studied the effect of exfoliated graphite (2D sheets in micrometer size range) dispersed within poly- α -olefin (PAO) oil at various filler fractions, ranging from 0.10 to 1.0 vol.%. It was observed that addition of 2D structures improved the thermal conductivity from 18 to ~130%, respectively [176]. Moreover, Yu et al. [180] investigated EG/graphene sheets (0.20–2.0 μm range, and 0.43 nm of interplanar distance), obtaining up to ~86% increase in thermal conductivity with 5.0 vol.% concentration at 50°C. Hadadian et al. [184] prepared highly stable graphene oxide (GO)-based

nanosheets. Thermal transport of EG increased by 30% with 0.07 GO mass fraction. Other EG-based nanofluids synthesized by Yu et al. [121, 180] have shown better enhancements of 61 and 86% with graphene oxide [121] and graphene nanosheets [180], respectively, at 5.0 vol.% loading. Similarly, a different study by Yu et al. [146] with graphene oxide nanosheets found enhancements of up to 30.2, 62.3, and 76.8% for distilled water, propyl glycol, and liquid paraffin (LP), respectively. Kole et al. [159] obtained a 15% in thermal conductivity with 0.395 vol.% exfoliated GnP dispersed in distilled water. Moreover, Aravind et al. [178] synthesized graphene and graphene-MWCNT composite nanoparticles and dispersed them in polar base fluids. Enhancements in thermal conductivity of de-ionized water of 9.2 and 10.5% were found for graphene and graphene-MWCNT, respectively. According to this study, a synergistic effect was found for graphene-MWNT additives; furthermore, MWNTs prevented restacking of graphene sheets.

Diverse theories explain the mechanisms that could affect the behavior of nanofluids; the most accepted being Brownian motion [40, 137–140], percolation theory [137, 138, 154, 173, 185], micro-convection cell model [137–140, 154, 185], and liquid layering theory [45, 137, 138, 153, 154, 185]. **Table 2** shows the influence of oil-based nanofluids on thermal conductivity. Similarly, **Table 3** shows the results from diverse investigations on other water-based nanofluids, and various materials and sizes used as reinforced nanoparticles. **Table 4** shows the influence of various nanofluids in thermal management properties, as well.

Filler	Type of oil	Nanoparticles morphology	Filler fraction	TC enhancement	Ref.
Al ₂ O ₃	Engine oil (10W-30)	Spherical ~28 nm diam.	5.0 vol.%	~26%	[115]
			7.5 vol.%	~30%	
Al ₂ O ₃	Engine oil	Spherical ~80 nm diam.	0.5 vol.%	~9%	[186]
			1.0 vol.%	~12%	
Al ₂ O ₃	Mineral oil	Spherical ~13 nm diam.	4.0 vol.%	>20%	[187]
Al ₂ O ₃	Pump oil	Spherical ~28 nm diam.	5.0 vol.%	~12%	[115]
			7.0 vol.%	~20%	
Al ₂ O ₃	Engine oil	Spherical ~28 nm diam.	5.0 vol.%	~26%	[115]
			7.5 vol.%	~30%	
Al	Engine oil	Spherical ~80 nm diam.	1.0 vol.%	~20%	[186]
			3.0 vol.%	~37%	
AlN	Mineral oil	Spherical ~50 nm diam.	0.05 vol.%	~8%	[187]
CuO	Mineral oil	Spherical ~100 nm diam.	2.5 vol.%	~12%	[84]
			5.0 vol.%	~23%	
			7.5 vol.%	~43%	
CuO ₂	HE-200 oil (pumps)	Spherical ~36 nm diam.	0.052 vol.%	~44%	[12]

Filler	Type of oil	Nanoparticles morphology	Filler fraction	TC enhancement	Ref.
Diamond	Mineral oil	Spherical ~<10 nm diam.	1.0 vol.%	~5%	[188]
			1.9 vol.%	~11%	
Graphene	Mineral oil (50°C)	2D sheets ~500 by 500 nm ~8–10 atomic layer thick	0.01 wt.%	~10%	[15]
			0.10 wt.%	~80%	
Graphite	Heat transfer oil ¹ (LD320) at 30°C	Spherical ~10–30 nm diam.	0.34 vol.%	~5%	[126]
			0.68 vol.%	~12%	
			1.36 vol. %	~36%	
h-BN	Mineral oil (50°C)	2D sheets ~500 by 500 nm ~5 atomic layer thick	0.01 wt.%	~9%	[15]
			0.05 wt.%	~10%	
			0.10 wt.%	~80%	
h-BN	Synthetic fluid	2D sheets ~500 by 500 nm ~5 atomic layer thick	0.10 wt.%	8%	[49]
MWCNT	Engine oil (15W-40)	Rods ~ Length: 0.3–10 μm Diameter: 10–50 nm	0.25 vol.%	~10%	[19]
			0.5 vol.%	~17%	
			1.0 vol.%	~45%	
MWCNT	Mineral oil	Rods ~ Length: 10–50 μm Diameter: 10–30 nm	0.5 vol.%	~8.5%	[76]
MWCNT	Synthetic PAO oil	Rods ~ Length: 50 μm Diameter: 25 nm	1.0 vol.%	160%	[170]
MWCNT	Synthetic engine oil	Rods ~ Length: μm range Diameter: 10–50 nm	1.0 vol.%	~9%	[14]
			2.0 vol.%	~30%	
MWCNT	Poly-α-olefin (PAO)	Rods ~ Length: 1–100 μm Diameter: 20–300 nm	1.0 vol.%	~175%	[19]
MWCNT	Poly-α-olefin (PAO6)	Rods ~ Length: μm range Diameter: ~25 nm	0.04 vol.%	~9%	[189]
			0.25 vol.%	~100%	
			0.34 vol.%	~200%	
CNTs	Poly-α-olefin (PAO)	Rods ~ Length: μm range Diameter: ~15 nm	0.10 vol.%	~35%	[176]
			0.60 vol.%	~96%	
			1.0 vol. %	~161%	
Exfoliated graphite	Poly-α-olefin (PAO)	2D sheets ~ μm range	0.10 vol.%	~18%	[176]
			0.60 vol.%	~56%	
			1.00 vol.%	~130%	

Notes: If not specified, measurements were conducted at room temperature.

¹With addition of dispersant (CH-5).

Table 2. Influence of oil-based nanofluids in thermal management.

Filler	Conventional fluid	Nanoparticles morphology	Filler fraction	TC Enhancement	Ref.
Al ₂ O ₃	Water (RT ~25°C)	Spherical ~38 nm diam.	1.0 vol. %	~5%	[62]
	Water (50°C)		1.0 vol.%	~11%	
	Water (RT ~25°C)		4.0 vol.%	~12%	
	Water (50°C)		4.0 vol.%	~25%	
Al ₂ O ₃	Water (RT ~21°C)	Spherical ~11 nm diam.	1.0 vol.%	~10%	[64]
	Water (50°C)		1.0 vol.%	~13%	
	Water (70°C)		1.0 vol.%	~15%	
Al ₂ O ₃	Water (RT ~21°C)	Spherical ~47 nm diam.	1.0 vol.%	~3%	[64]
	Water (50°C)		1.0 vol.%	~6%	
	Water (50°C)		4.0 vol.%	~10%	
	Water (70°C)		4.0 vol.%	~10%	
Al ₂ O ₃	Water (RT ~21°C)	Spherical ~150 nm diam.	1.0 vol.%	~2%	[64]
	Water (50°C)		1.0 vol.%	~5%	
	Water (70°C)		4.0 vol.%	~8%	
Al ₂ O ₃	Water	Spherical ~60 nm diam.	5.0 vol.%	~20%	[190]
Al ₂ O ₃	Water (50°C)	Spherical ~131 nm diam.	1.0 vol.%	~11%	[191]
	Water (RT ~25°C)		4.0 vol.%	~10%	
	Water (50°C)		4.0 vol.%	~25%	
Al ₂ O ₃	Water	Spherical ~27–56 nm diam.	1.6 vol.%	~10%	[192]
Au	Water	Spherical ~10–20 nm diam.	0.00026 vol.%	~8%	[11]
Ag	Water	Spherical ~60–80 nm diam.	0.001 vol.%	~5%	[11]
Cu	Water ^l (+ CTAB)	Spherical ~60–100 nm diam.	1.0 vol.%	~48%	[193]
CuO	Water	Spherical ~36 nm diam.	1.0 vol.%	~12%	[12]
			5.0 vol.%	~60%	
CuO	Water	Spherical ~100 nm diam.	1.0 vol.%	~5%	[55]
			2.0 vol.%	~17%	
CuO	Water (RT ~25°C)	Spherical ~ 24 nm diam.	1.0 vol.%	~14%	[62]
	Water (50°C)		1.0 vol.%	~29%	
	Water (RT ~25°C)		4.0 vol.%	~15%	
	Water (50°C)		4.0 vol.%	~36%	
CuO	Water	Spherical ~ 100 nm diam.	2.5 vol.%	~24%	[84]
			5.0 vol.%	~55%	
			7.5 vol.%	~78%	
CuO	Water (RT ~25°C)	Spherical ~ 87 nm diam.	1.0 vol. %	~7%	[191]
	Water (50°C)		1.0 vol.%	~28%	
	Water (50°C)		4.0 vol. %	~15%	

Filler	Conventional fluid	Nanoparticles morphology	Filler fraction	TC Enhancement	Ref.
CuO	Water (50°C)		4.0 vol.%	~36%	
	Water	Spherical ~ 25 nm diam.	0.10 vol.%	~7%	[194]
			0.30 vol.%	~12%	
Graphene	Water	Sheets, 1 µm lateral	0.40 vol.%	~9%	[178]
Graphene & MWCNTs	Water	G sheets, 1 µm lateral; MWCNTs ~19 nm diam.	0.40 vol.%	~11%	[178]
Graphene nanoplatelets	Water	2D sheets, ~2 nm in thickness	0.01 wt.%	~28%	[179]
SiO ₂	Water	Spherical ~12 nm diam.	1.0 vol.%	~3 %	[76]
TiO ₂	Water	Spherical ~15 nm diam.	1.0 vol.%	~18%	[104]
			5.0 vol.%	~30%	
CNTs	Water (RT ~25°C)	Rods ~ Length: 35 µm	0.01 wt.%	~38%	[150]
	Water (60°C)	Diam.: 20 nm	0.10 wt.%	~126%	
	Water (60°C)		0.10 wt.%	~288%	
MWCNTs	Water	Rods ~ Length: 30 µm Diam.: 15 nm	1.0 vol.%	~7%	[171]

Notes: If not specified, measurements were conducted at room temperature.

¹With addition of cetrimonium bromide (CTAB).

Table 3. Influence of water-based nanofluids in thermal management.

Filler	Conventional fluid	Nanoparticles morphology	Filler fraction	TC enhancement	Ref.
Al ₂ O ₃	R141b refrigerant (20°C)	Spherical ~13 nm diam.	0.50 vol.%	~26%	[17]
			2.0 vol.%	~69%	
Al ₂ O ₃	Ethylene glycol	Spherical ~10 nm diam.	5.0 vol.%	~18 %	[83]
Al ₂ O ₃	Ethylene glycol	Spherical ~60 nm diam.	5.0 vol.%	~30%	[190]
Al ₂ O ₃	Ethylene glycol	Spherical ~28 nm diam.	5.0 vol.%	~25%	[115]
			8.0 vol.%	~40%	
AlN	Ethylene glycol	Spherical ~50 nm diam.	5.0 vol.%	~20%	[195]
			10.0 vol.%	~40%	
Au	Toluene	Spherical ~ 10–20 nm diam.	0.011 vol.%	~9%	[11]
Cu	Ethylene glycol ¹	Spherical ~ 10 nm diam.	~0.30 vol.%	~40%	[83]
Cu	Toluene	Spherical ~ 40–60 nm diam.	1.0 wt.%	~12%	[174]
			1.5 wt.%	~14%	
Cu	Kerosene (@25°C)	Spherical ~ 40–60 nm diam.	1.0 wt.%	10%	[174]

Filler	Conventional fluid	Nanoparticles morphology	Filler fraction	TC enhancement	Ref.
	Kerosene (@50°C)		1.0 wt.%	~15%	
CuO	Ethylene glycol	Spherical ~35 nm diam.	2.0 vol.%	~10%	[144]
			4.0 vol.%	~22%	
CuO	Ethylene glycol	Spherical ~23 nm diam.	~15.0 vol.%	~55%	[115]
Fe ₃ O ₄	Kerosene	Spherical ~15 nm diam.	0.50 vol.%	~15%	[119]
			1.0 vol.%	~34%	
Graphene	Ethylene glycol (20°C)	2D sheets, 500 nm by 600 nm	0.14 vol.%	6.5%	[141]
	Ethylene glycol (50°C)		0.14 vol.%	36%	
Graphene	Ethylene glycol (50°C) thickness of 0.7–1.3 nm	2D sheets ~0.2–2.0 μm,	2.0 vol.%	~40%	[180]
			5.0 vol.%	~86%	
h-BN	EcoDraw (50°C)	2D sheets ~500 by 500 nm ~5 atomic layer thick	0.01 wt.%	~25%	[49]
			0.10 wt.%	~30%	
h-BN	Montgomery (50°C)	2D sheets ~500 by 500 nm ~5 atomic layer thick	0.01 wt.%	~10%	[49]
			0.10 wt.%	~14%	
h-BN	Metkut (50°C)	2D sheets ~500 by 500 nm ~5 atomic layer thick	0.01 wt.%	~4%	[49]
			0.10 wt.%	~8%	
h-BN	Metkool (50°C)	2D sheets ~500 by 500 nm ~5 atomic layer thick	0.01 wt.%	~14%	[49]
			0.10 wt.%	~18%	
MWCNT	Ethylene glycol	Rods Length: 30 μm Diam.: 15 nm	0.05 vol.%	~7%	[196]
			1.0 vol.%	~13%	
MWCNT	Ethylene glycol	Rods Length: μm range Diam.: ~20–30 nm	0.50 vol.%	~8%	[14]
			1.0 vol.%	~13%	
SiC	Ethylene glycol	Whiskers Length ~18 μm Diam.: 1.5 μm	5.0 vol.%	~85%	[106]
SiO ₂	Ethylene glycol	Spherical ~23 nm diam.	1.0 vol.%	~4%	[40]
TiO ₂	Ethylene glycol/water (20/80 %)	Spherical ~21 nm diam.	4.0 vol.%	~15%	[197]

Notes: If not specified, measurements were conducted at room temperature.

¹With addition of <1 vol.% of thioglycolic acid.

Table 4. Influence of diverse nanofluids in thermal management.

4.2. Tribological performance

Tribology is a science and technology that describes the interaction between surfaces and their relative movement, practices and materials associated, including friction, lubrication, and wear. Friction and wear are two major causes of energy and material losses in mechanical processes. Friction plays a crucial role in diverse processes such as drilling, cutting, working pair components and mechanisms, among others; a measurement for this property, which is

becoming more relevant in today's life, is the COF (μ). Wear is a critical issue as components are in constant friction; a key measurement of the anti-wear properties of the lubricants and metal-cutting fluids is the WSD. Lubricants can be used to minimize contact friction between components, resulting in considerable energy and tooling savings [198]. The use of nanoparticles on lubricant nanofluids applications have the advantage of not to be temperature sensible and that tribo-chemical reactions are limited, compared to conventional additives [71, 199–201]. A great advantage is that in cooling applications, there could be higher energy savings and less pollution emissions. Moreover, it is very important to mention that some of these used nanoparticles are environmental friendly.

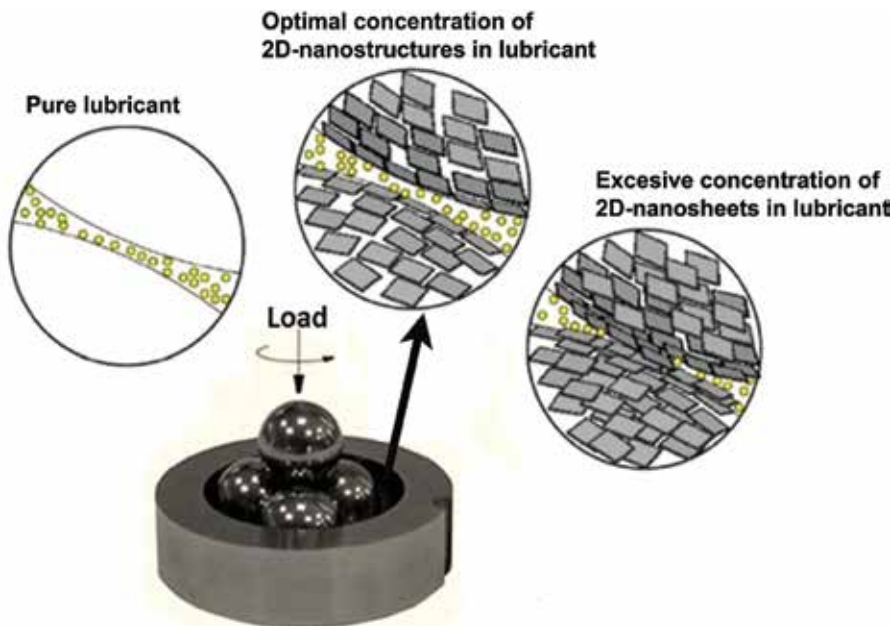


Figure 7. Schematic diagram of the tribological mechanism of nanosheets as lubricant additives.

The addition of nanoparticles (or nanoadditives) has been shown excellent enhancements in tribological properties in numerous fluids. Moreover, diverse mechanisms by which dispersed nanoparticles in lubricants result in lower friction and wear have been shown in the literature. These mechanisms include (i) reacting with the surfaces creating a transferred solid lubricant film from nanoparticles under the contact pressure [202, 203], (ii) rolling of nanoparticles in the contact zone, where the nanoparticles serve as a third body, which decrease the contact between the asperities of the two mating surfaces [204], (iii) reducing asperity contact by filling the valleys of contacting surfaces [71, 205, 206], (iv) shearing of trapped nanoparticles at the interface without the formation of an adhered film [207], and (v) tribosinterization of nanoparticles can occur on the wear surfaces forming a film which also prevent the direct contact of rubbing surfaces and reduce greatly the frictional force between the contacting surfaces [71, 208, 209]. As observed by Zhang et al. [204], a particular effect occurs when excessive concen-

tration of nanostructures is added to nanofluids. A threshold is reached and even though with higher filler fraction there is an improvement in tribological properties, there is an optimal filler fraction where wear is minimized, as it is explained by the tribological mechanism depicted in **Figure 7**. During tribological evaluation (four-ball tribotesting), components are in sliding contact, nanosheets can form a protective layer on the surface of each steel ball at lower concentrations, which introduces the enhanced anti-wear performance. However, as the nanosheets loading exceed a critical value, the fluid film will become discontinuous, degrading the anti-wear properties, finally leading to a dry friction.

Eswaraiah et al. [210] synthesized ultrafine graphene thru solar radiation exfoliation techniques (sheets ~ 300 nm by <2 nm thick). Nanofluids from these material and motor oil showed a decrease in COF of 80%, compared to base oil. This increase was attributed to the graphene tribological mechanism, which acted as nano-bearing within the oil, as well as for its excellent mechanical properties. It was explained by Hernández-Battez et al. [71] that nanoparticles could react with the surfaces, forming antifriction compounds and deposit on the wear surfaces by tribosinterization [71]. Moreover, Yu et al. [211] reported improved lubricating properties by adding 0.2 wt.% Cu nanoparticles to lubricant oil; in their study, Cu formed a soft film by friction-shearing and high pressure, reducing the COF up to 20%. As described by Peng et al. [212] during the friction process, a lubricating film of the nanoparticles is formed between the rubbed faces. The nanoparticles in the film not only bear the load but also separate the rubbing faces, dominating the reduction in the wear and friction.

Recently, Hu et al. [213] investigated the effects of MoS₂ nanosheets (30–70 nm in thickness) dispersed in LP. Average COF for 0.5 wt.% filler fraction of MoS₂/LP was reduced $\sim 60\%$, as well as WSD, which was reduced $\sim 8\%$, compared to pure LP. The anti-wear properties of the base fluid with MoS₂ nanosheets were improved remarkably by increasing the MoS₂ concentration up to 0.5 wt.%. According to Hu et al., due to the dimension and surface effect, it is ascribed that MoS₂ could enter into the gap of the friction pair, functioning as lubricator. Wu et al. [214] studied the effects of 2D nanosheets of MoS₂ with addition of 1.0 wt.% of span-80 (sorbitant monooleate) as a surfactant in LP. Results were also compared with MoS₂ microparticles (3–5 μm in diameter). It was shown that COF was reduced by $\sim 18\%$ at 1.5 wt.% MoS₂/LP; furthermore, the COF of nanosheets were lower and more stable than that of microparticles due to the surface area effect [215]. As explained by Wu et al., the lubrication mechanism of layered 2D-nanosheets of MoS₂ was associated with the shearing of the weak Van der Waals bonds between molecular layers. When MoS₂ is used as an additive in base oils, besides molecules of base oils, MoS₂ powder is also adsorbed on the surface of substrates. Then the adsorbed MoS₂ is burnished and forms stable films, which can endure high loads and improve tribological performances of the base oil. Therefore, with addition of MoS₂ particles, the COF of base oil is reduced significantly. Similarly, Kao et al. [216] used TiO₂ nanoparticles as additives in paraffin oil to reduce the friction between cast iron components. Tribological studies revealed an enhancement of $\sim 24\%$ in COF at 60°C; it was concluded that spherical nanoparticles provide good rolling to reduce friction between two parallel specimens, as nanoparticles could fill rough cracks in a metal wall surface to reduce the COF.

For the protection of mechanical components, from friction and wear in aerospace, automotive, military, and various industrial applications, an efficient lubricant is demanded; graphene is a widely known material for this purpose. More recently, BN has attracted attention, since it has similar properties as graphene. Among diverse applications, BN could improve lubricity properties of composites under friction or wear applications as well. Zhang et al. [217] and Saito et al. [218], for instance, have observed a decrease in COF with increasing temperature in composites containing BN and have attributed this to the lubricating nature of BN. Silver (Ag) is also used due to its relatively larger coefficient of diffusion and its nature to form low shearing stress junctions at sliding interfaces, resulting in good lubrication. However, h-BN high thermal stability, good chemical inertness, and high thermal conductivity, makes it suitable candidate to be a “clean” lubricant [217]. There are studies available in the literature on the coatings prepared by addition of h-BN. Leon et al. reported that Ni-P-hBN autocatalytic composite coating with 35 vol.% hBN sliding against steel ball at room temperature had a COF of ~ 0.2 [219], while steel on steel COF is ~ 0.8 . Avril et al. reported that laser melting hBN/ α -Fe(Cr) coating showed lower COF and better wear resistance than untreated steels under dry sliding within a temperature range of 25–500°C [220]. Spikes [221] stated that the most promising 2D sheet structures are carbon-based graphitic materials and the inorganic fullerenes. These showed low friction in boundary lubrication conditions in laboratory tests. Hence, for metal-mechanic and oil industry which deals with drilling, cutting, or other friction characteristics with working tools, this research will be suitable. **Table 5** shows the influence of 2D nanoparticles on tribological applications with COF and wear performance.

Filler	Type of Oil	Nanoparticles morphology	Filler fraction	COF decrease	Wear decrease	Ref.
CuO	Poly- α -olefin oil	Spherical ~ 30 – 50 nm diam.	2.0 wt.%	$\sim 54\%$	–	[71]
CuO	Poly- α -olefin (25°C)	Spherical ~ 20 nm diam.		$\sim 5\%$	$\sim 13\%$	
	Poly- α -olefin (80°C)		0.20 wt. %	$\sim 10\%$	$\sim 21\%$	[211]
	Poly- α -olefin (140°C)			$\sim 20\%$	$\sim 23\%$	
CuO	API-SF engine oil	Spherical ~ 5 nm diam.	~ 0.10 wt.%	$\sim 20\%$	$\sim 17\%$	[222]
CuO	SAE30 oil	Spherical ~ 5 nm diam.	~ 0.10 wt.%	$\sim 6\%$	$\sim 79\%$	[222]
Diamond	API-SF engine oil	Spherical ~ 10 nm diam.	<0.10 wt.%	$\sim 4\%$	$\sim 43\%$	[222]
Graphene	Engine oil	Sheets ~ 300 nm, <2 nm thick	0.025 wt.%	$\sim 80\%$	$\sim 33\%$	[210]
Graphene	Poly- α -olefin oil ¹	Sheets $\sim \mu\text{m}$ size	0.02 wt.%	$\sim 17\%$	$\sim 9\%$	
			0.06 wt.%	$\sim 13\%$	$\sim 14\%$	[204]
			1.00 wt.%	$\sim 12\%$	$\sim 12\%$	
MoS₂	Graphene solid lubricant	Flakes (10–20 nm)	7–10 wt.%	$\sim 23\%$	$\sim 56\%$	[223]
Graphene	Ionic liquid (IL)	Sheets (monolayer 3.819 nm)	23 wt.%	$\sim 56\%$	$\sim 94\%$	[224]
MoS₂	PAO	Nano sheets (5–10 nm thick)	5.0 wt.%	~ 30 – 40%	$\sim 75\%$	[225]
h-BN	CIMFLO 20 oil ²	Spherical ~ 70 nm diam.	1.0 wt.%	–	$\sim 55\%$	[205]
MoS₂	CIMFLO 20 oil ²	Spherical ~ 70 – 100 nm diam.	4.0 wt.%	$\sim 10\%^2$	$\sim 65\%$	[205]

Filler	Type of Oil	Nanoparticles morphology	Filler fraction	COF decrease	Wear decrease	Ref.
TiO ₂	API-SF engine oil	Spherical ~80 nm diam.	~0.10 wt.%	~15%	~40%	[222]
WS ₂	CIMFLO 20 oil ³	Spherical ~50 nm diam.	4.0 wt.%	–	~66%	[205]

Notes: If not specified, measurements were conducted at room temperature.

¹Oleic acid was added ~5 vol.%.

²On steel/440C systems.

³On titanium/440C pairs.

Table 5. Influence of nanofluids (oil-based) in tribological applications.

5. Two-dimensional nanostructures

Initial studies on 1-D nanostructures got immediate attention soon after the landmark paper by Iijima [4] on CNTs in 1991 and various types of organic-inorganic 1-D nanostructures were realized thereafter [226]. More recent advances in layered materials enable large-scale synthesis of various two-dimensional (2D) materials [5, 15, 108, 210, 227, 228], where atoms are arranged in flat layers, which can be stacked on top of each other. One of the most common naturally layered materials is graphene, which has been widely studied for its superb properties and applications in diverse fields. 2D materials can be good choices as nanofillers in heat transfer fluids, as they have high surface area available for heat transfer.

A common production route of these layered nanostructures is exfoliation, where material individual layers are separate out from each other, either chemically or mechanically (i.e., abrasion) [15, 49, 108, 229–231]. It is important to mention that even though exfoliation can be achieved mechanically on a small scale [229, 230], liquid phase methods are required for diverse applications such as nanoelectronics, micro-electromechanical systems (MEMS)/nanoelectromechanical systems (NEMS), chemical and pressure sensors, etc. [231]. Another possible route to obtain these 2D structures is by direct chemical growth of individual layers (i.e., graphene sheets) through chemical vapor deposition (CVD) technique on the surface of a metals catalyst (i.e., copper, silica) by heating at high temperatures (~600–1200°C) and passing a carbon-containing gas such as methane over the catalyst [227]. A breakthrough research by Coleman et al. [108] showed that they were able to synthesize diverse 2D materials (MoS₂, WS₂, BN, Bi₂Te₃, MoSe₂, MoTe₂, NiTe₂, etc.) by wet exfoliation technique. Exfoliation of 2D insulators such as Bi₂Te₃, Bi₂Se₃, and h-BN would reduce its residual bulk conductance, highlighting surface effects. Another important aspect is that changes in electronic properties, as the number of layers is reduced as expected [108, 232]. This class of materials represents a diverse and largely unexploited source of 2D systems with interesting physic-mechanical and electrical properties, with high specific surface areas that is important for sensing, catalysis, and energy storage applications [108]. Hence, like graphene [5, 233], layered materials must be exfoliated to achieve their full potential.

6. Hexagonal boron nitride (h-BN)

In our research, main focus is on a novel 2D material, hexagonal boron nitride (h-BN), which is a ceramic material that exhibits versatile properties such as outstanding mechanical stability, remarkable chemical inertness, anti-wear promotion, high electrical resistivity, and superb thermal conductivity [5, 46, 234–239]. On the other hand, h-BN is an effective solid lubricant, it is suitable for diverse applications such as metal-working processes where lubrication at high-temperatures is required and is widely used in high-temperature wear-sealing materials of aerospace engines [155, 239]. Boron and nitrogen atoms behave similarly to carbon when bonded with each other to form boron nitride, exhibiting many similar structures as carbon only with alternating B and N atoms instead of C atoms (see **Figure 8**). Because of this, there are many forms of boron nitride (BN) that coincide with carbon structures and have a variety of properties and functions. h-BN (so-called “white graphite” due to its structural similarity to graphite) is a common form of BN that has a similar configuration to graphite which has been recently studied [15, 49, 108, 133]. Like graphite, this honeycomb layered material has hexagonal ring layers separated by 3.33 Å, in which every boron atom is connected to three nitrogen atoms by strong covalent bonds and vice versa; the B-N distance is 1.44 Å. Between the layers, every boron interacts with a nitrogen atom through a Van der Waals force [237, 240]. Therefore, the strong B-N bond makes an h-BN atomic layer a mechanically strong material, quite analogous to graphene, and individual BN layers could be isolated from bulk h-BN crystals [15, 108, 229]. As an insulating material with very high thermal conductivity [241], h-BN surpasses other nanofillers and is an attractive material for high thermal transport and electrically insulating composites [15, 133, 236, 242]. Nevertheless, theoretical studies indicate that high thermal conductivities can only be achieved from the (002) planes (up to hundreds to thousands of W/m K) [50, 243]; through a synthesis process of wet exfoliation, h-BN can give maximum exposure to these (002) lattice planes. Meantime, some thermal management systems need electrically conducting fillers for static electric charge dissipation. Graphene-based systems are good for these applications where they can do both thermal and electrical management. This shows how h-BN will be specially applicable and useful in thermal management applications, where electrical insulation is also required. It is also important to mention that BN is environmentally and skin friendly; proof of this is that BN is widely used as the main ingredient for cosmetics. According to the Cosmetic Ingredient Review (CIR) report from 2012, BN is used in 483 cosmetic formulations. Products containing BN are reported to be used on baby skin (in a lotion, oil, powder, or cream), eye area, or mucous membranes. BN is reported to be used at up to 25% in eye product formulations, at 2% in lipstick formulations, up to 16% in powders, and at up to 0.9% in fragrance preparations [244]. Hence, since little research have been conducted on 2D nanostructures, and particularly on boron nitride, exfoliated h-BN, having a few layers in thickness has a remarkable opportunity to overcome the material of the future in the thermal management field for diverse applications, including electrical/electronic, since its nature allows it to be a thermal conductor but an electrical insulator.

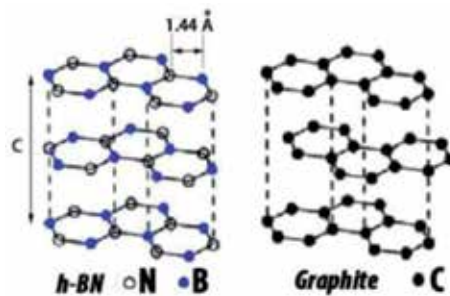


Figure 8. Scheme of h-BN and graphite structure.

7. Summary

The present work offers a general overview of the recent research and development on preparation and characterization of nanofluids for thermal management and tribological applications, with emphasis on experimental data, variables and features, as well as proposed mechanisms responsible for nanofluids improvement performance. Nowadays, many technologies search for the highest efficiency, mainly and more than ever before, on the cooling and anti-wear challenges within machines, devices and components. Several efforts have been made trying to homogeneously disperse nanostructures (oxides, metals, ceramics, CNTs, 2D-nanosheets and others) within conventional fluids to improve their properties, such as thermal transport, viscosity, lubrication, electrical behavior, among others. Nanofillers size has positive effect on conventional fluids performance, that is compared to larger dispersed solid particles making flow through small channels much more easier, also since diverse parameters are critical for devices performance, such as morphology and stability of dispersed nanostructures within conventional fluids, fluids composition, viscosity, fast sedimentation, channels clogging, wear or erosion, among others, which are often very serious for systems consisting of small channels. Furthermore, properties improvement is also dependent of various factors, such as filler fraction, temperature, chemical, and interfacial properties on the nanostructure-fluid interfaces. Some nanofluids are currently expensive, partly due to the difficulty in manufacturing. Hence, mass production of nanostructures could further decrease the cost, also low filler fraction is necessary to make nanofluids more affordable before they will see widespread applications.

Acknowledgements

Authors acknowledge the support from UDEM personnel, Department of Engineering at Universidad de Monterrey, the Institute for Sustainable Technologies (ITeE-PIB), Rice University, and CONACYT.

Author details

Jaime Taha-Tijerina*, Laura Peña-Parás and Demófilo Maldonado-Cortés

*Address all correspondence to: jose.taha@udem.edu

University of Monterrey, San Pedro Garza García, NL, México

References

- [1] Smalley RE. Future global energy prosperity: The Terawatt challenge. *MRS Bull.* 2005;30(06): 412–417. DOI:10.1557/mrs2005.124
- [2] Wen D, Lin G, Vafaei S, Zhang K. Review of nanofluids for heat transfer applications. *Particuology.* 2009;7(2): 141–150. DOI:10.1016/j.partic.2009.01.007
- [3] Kroto HW, Heath JR, O'Brien SC, Curl RF, Smalley RE. C₆₀: Buckminsterfullerene. *Nature.* 1985;318(6042): 162–163. DOI:10.1038/318162a0
- [4] Iijima S. Helical microtubules of graphitic carbon. *Nature.* 1991;354(6348): 56–58. DOI: 10.1038/354056a0
- [5] Geim AK, Novoselov KS. The rise of graphene. *Nat Mater.* 2007;6(3): 183–191.
- [6] Maxwell JC. *A Treatise on Electricity and Magnetism.* Courier Corporation. London: United Kingdom, 1881. 538 p.
- [7] Hamilton RL, Crosser OK. Thermal conductivity of heterogeneous two-component systems. *Ind Eng Chem Fundam.* 1962;1(3): 187–191. DOI: 10.1021/i160003a005
- [8] Beck MP, Sun T, Teja AS. The thermal conductivity of alumina nanoparticles dispersed in ethylene glycol. *Fluid Phase Equilib.* 2007;260(2): 275–278. DOI:10.1016/j.fluid.2007.07.034
- [9] Kakaç S, Pramuanjaroenkij A. Review of convective heat transfer enhancement with nanofluids. *Int J Heat Mass Transf.* 2009;52(13): 3187–3196. DOI:10.1016/j.ijheatmasstransfer.2009.02.006
- [10] Lee J, Mudawar I. Assessment of the effectiveness of nanofluids for single-phase and two-phase heat transfer in micro-channels. *Int J Heat Mass Transf.* 2007;50(3): 452–463. DOI:10.1016/j.ijheatmasstransfer.2006.08.001
- [11] Patel HE, Das SK, Sundararajan T, Nair AS, George B, Pradeep T. Thermal conductivities of naked and monolayer protected metal nanoparticle based nanofluids: Manifestation of anomalous enhancement and chemical effects. *Appl Phys Lett.* 2003;83: 2931. DOI: <http://dx.doi.org/10.1063/1.1602578>

- [12] Eastman JA, Choi US, Li S, Thompson LJ, Lee S. Enhanced thermal conductivity through the development of nanofluids. *MRS Proc.*; 1996;457. DOI: <http://dx.doi.org/10.1557/PROC-457-3>
- [13] Kim SH, Choi SR, Kim D. Thermal conductivity of metal-oxide nanofluids: Particle size dependence and effect of laser irradiation. *J Heat Transf.* 2006;129(3): 298–307. DOI: 10.1115/1.2427071
- [14] Liu M-S, Ching-Cheng Lin M, Huang I-T, Wang C-C. Enhancement of thermal conductivity with carbon nanotube for nanofluids. *Int Commun Heat Mass Transf.* 2005;32(9): 1202–1210. DOI: 10.1016/j.icheatmasstransfer.2005.05.005
- [15] Taha-Tijerina J, Narayanan TN, Gao G, Rohde M, Tsentalovich DA, Pasquali M, Ajayan PM. Electrically insulating thermal nano-oils using 2D fillers. *ACS Nano.* 2012;6(2): 1214–1220. DOI: 10.1021/nn203862p
- [16] Godfrey D, Herguth WR. Physical and chemical properties of industrial mineral oils affecting lubrication. *Lubr Eng.* 1995;51(6): 493–496.
- [17] Mahbulul IM, Saidur R, Amalina MA. Influence of particle concentration and temperature on thermal conductivity and viscosity of Al₂O₃/R141b nanorefrigerant. *Int Commun Heat Mass Transf.* 2013;43: 100–104. DOI:10.1016/j.icheatmasstransfer.2013.02.004
- [18] Perry RH, Green DW. *Perry's Chemical Engineers' Handbook*. 8th ed. New York: McGraw-Hill Education; 2007. 2704 p.
- [19] Marquis FDS, Chibante LPF. Improving the heat transfer of nanofluids and nanolubricants with carbon nanotubes. *JOM.* 2005;57(12): 32–43. DOI: 10.1007/s11837-005-0180-4
- [20] Berber S, Kwon Y-K, Tománek D. Unusually high thermal conductivity of carbon nanotubes. *Phys Rev Lett.* 2000;84(20): 4613–4616. DOI: <http://dx.doi.org/10.1103/PhysRevLett.84.4613>
- [21] Che J, Çagin T, Goddard WA. Thermal conductivity of carbon nanotubes. *Nanotechnology.* 2000;11(2): 65–69. DOI:10.1088/0957-4484/11/2/305
- [22] Osman MA, Srivastava D. Temperature dependence of the thermal conductivity of single-wall carbon nanotubes. *Nanotechnology.* 2001;12(1): 21. DOI: 10.1088/0957-4484/12/1/305
- [23] Kim P, Shi L, Majumdar A, McEuen PL. Thermal transport measurements of individual multiwalled nanotubes. *Phys Rev Lett.* 2001;87(21): 215502. DOI: <http://dx.doi.org/10.1103/PhysRevLett.87.215502>
- [24] Hong H, Zheng Y, Roy W. Nanomaterials for efficiently lowering the freezing point of anti-freeze coolants. *J Nanosci Nanotechnol.* 2007;7(9): 3180–3184. DOI: <http://dx.doi.org/10.1166/jnn.2007.662>

- [25] Speight JG. *Lange's Handbook of Chemistry*. 16th ed. New York: McGraw-Hill Inc; 2004. 1608 p.
- [26] Kang HU, Kim SH, Oh JM. Estimation of thermal conductivity of nanofluid using experimental effective particle volume. *Exp Heat Transf*. 2006;19(3): 181–191. DOI: 10.1080/08916150600619281
- [27] Balandin AA. Thermal properties of graphene, carbon nanotubes and nanostructured carbon materials. *Nat Mater*. 2011;10: 569–581. DOI: 10.1038/nmat3064
- [28] Ghosh S, Calizo I, Teweldebrhan D, Pokatilov EP, Nika DL, Balandin AA, Bao W, Miao F, Lau CN. Extremely high thermal conductivity of graphene: Prospects for thermal management applications in nanoelectronic circuits. *Appl Phys Lett*. 2008;92(15): 151911. DOI: <http://dx.doi.org/10.1063/1.2907977>
- [29] Callister WD, Rethwisch DG. *Materials Science and Engineering: An Introduction*. 9th ed. Wiley. New Jersey, USA 2014. 984 p.
- [30] Dodd AD, Murfin D. *Dictionary of Ceramics*. 3rd ed. London, UK: Maney Publishing; 1994. 384 p.
- [31] Shackelford JF, Alexander W. *Materials Science and Engineering Handbook*. 3rd ed. CRC Press; Florida, USA, 2000. 1980 p.
- [32] Slack GA, Tanzilli RA, Pohl RO, Vandersande JW. The intrinsic thermal conductivity of AlN. *J Phys Chem Solids*. 1987;48(7): 641–647. DOI: 10.1016/0022-3697(87)90153-3.
- [33] Xu Y, Chung DDL. Increasing the thermal conductivity of boron nitride and aluminum nitride particle epoxy-matrix composites by particle surface treatments. *Compos Interfaces*. 2000;7(4): 243–256. DOI: 10.1163/156855400750244969
- [34] Wang J, Lee CH, Bando Y, Golberg D, Yap YK. Multiwalled Boron Nitride Nanotubes: Growth, Properties, and Applications. *B-C-N Nanotubes and related Nanostructures*. New York: Springer; 2009. p. 23–44. DOI: 10.1007/978-1-4419-0086-9_2
- [35] Duclaux L, Nysten B, Issi J-P, Moore AW. Structure and low-temperature thermal conductivity of pyrolytic boron nitride. *Phys Rev B*. 1992;46(6): 3362–3367. DOI: <http://dx.doi.org/10.1103/PhysRevB.46.3362>
- [36] Lindsay L, Broido DA. Theory of thermal transport in multilayer hexagonal boron nitride and nanotubes. *Phys Rev B*. 2012;85(3): 035436. DOI: <http://dx.doi.org/10.1103/PhysRevB.85.035436>
- [37] Chang CW, Han W-Q, Zettl A. Thermal conductivity of B–C–N and BN nanotubes. *Appl Phys Lett*. 2005;86(17): 173102. DOI: 10.1063/1.1914963
- [38] Hwang Y, Lee JK, Lee CH, Jung YM, Cheong SI, Lee CG, Ku BC, Jang SP. Stability and thermal conductivity characteristics of nanofluids. *Thermochim Acta*. 2007;455(1-2): 70–74. DOI: 10.1016/j.tca.2006.11.036

- [39] Yan R, Simpson JR, Bertolazzi S, Brivio J, Watson M, Wu X, Kis A, Xing HG. Thermal conductivity of monolayer molybdenum disulfide obtained from temperature-dependent Raman spectroscopy. *ACS Nano*; 2014;8(1): 986–993. DOI: 10.1021/nn405826k
- [40] Wang ZL, Tang DW, Liu S, Zheng XH, Araki N. Thermal-conductivity and thermal-diffusivity measurements of nanofluids by 3ω method and mechanism. *Int J Thermophys*. 2007;28(4): 1255–1268. DOI: 10.1007/s10765-007-0254-3
- [41] Hwang YJ, Ahn YC, Shin HS, Lee CG, Kim GT, Park HS, Lee JK. Investigation on characteristics of thermal conductivity enhancement of nanofluids. *Curr Appl Phys*. 2006;6(6): 1068–1071. DOI: 10.1016/j.cap.2005.07.021
- [42] Peimyoo N, Shang J, Yang W, Wang Y, Cong C, Yu T. Thermal conductivity determination of suspended mono- and bilayer WS_2 by Raman spectroscopy. *Nano Res*. 2014;8(4): 1210–1221. DOI: 10.1007/s12274-014-0602-0
- [43] Krishnamurthy S, Bhattacharya P, Phelan PE, Prasher RS. Enhanced mass transport in nanofluids. *Nano Lett*. 2006;6(3): 419–423. DOI: 10.1021/nl0522532
- [44] Shima PD, Philip J, Raj B. Synthesis of aqueous and nonaqueous iron oxide nanofluids and study of temperature dependence on thermal conductivity and viscosity. *J Phys Chem C*; 2010;114(44): 18825–18833. DOI: 10.1021/jp107447q
- [45] Keblinski P, Phillpot S., Choi SU., Eastman J. Mechanisms of heat flow in suspensions of nano-sized particles (nanofluids). *Int J Heat Mass Transf*. 2002;45(4): 855–863. DOI: 10.1016/S0017-9310(01)00175-2
- [46] Zhi C, Xu Y, Bando Y, Golberg D. Highly thermo-conductive fluid with boron nitride nanofillers. *ACS Nano*; 2011;5(8): 6571–6577. DOI: 10.1021/nn201946x
- [47] Botha SS, Ndungu P, Bladergroen BJ. Physicochemical properties of oil-based nanofluids containing hybrid structures of silver nanoparticles supported on silica. *Ind Eng Chem Res*; 2011;50(6): 3071–3077. DOI: 10.1021/ie101088x
- [48] Baby TT, Sundara R. Synthesis and transport properties of metal oxide decorated graphene dispersed nanofluids. *J Phys Chem C*. ; 2011;115(17): 8527–8533. DOI: 10.1021/jp200273g
- [49] Taha-Tijerina J, Peña-Paras L, Narayanan TN, Garza L, Lapray C, Gonzalez J, Palacios E, Molina D, García A, Maldonado D, Ajayan PM. Multifunctional nanofluids with 2D nanosheets for thermal and tribological management. *Wear*. 2013;302(1-2): 1241–1248. DOI: 10.1016/j.wear.2012.12.010
- [50] Zhi C, Bando Y, Terao T, Tang C, Kuwahara H, Golberg D. Towards thermoconductive, electrically insulating polymeric composites with boron nitride nanotubes. *Adv Funct Mater*. 2009;19(12): 1857–1862. DOI: 10.1002/adfm.200801435
- [51] Aravind SSJ, Baskar P, Baby TT, Sabareesh RK, Das S, Ramaprabhu S. Investigation of structural stability, dispersion, viscosity, and conductive heat transfer properties of

- functionalized carbon nanotube based nanofluids. *J Phys Chem C.* ; 2011;115(34): 16737–16744. DOI: 10.1021/jp201672p
- [52] Choi SUS, Eastman JA. Enhancing thermal conductivity of fluids with nanoparticles. In: *ASME International Mechanical Engineering Congress and Exhibition (IMECE 1995)*. 12–17 November 1995. San Francisco, CA, USA p. 196525
- [53] Masuda H, Ebata A, Teramae K, Hishinuma N. Alteration of thermal conductivity and viscosity of liquid by dispersing ultra-fine particles (dispersion of γ -Al₂O₃, SiO₂ and TiO₂ ultra-fine particles. *Netsu Bussei*. 1993;7(4): 227–233.
- [54] Xie H, Chen L. Review on the preparation and thermal performances of carbon nanotube contained nanofluids. *J Chem Eng Data*; 2011;56(4): 1030–1041. DOI: 10.1021/je101026j
- [55] Xuan Y, Li Q. Investigation on convective heat transfer and flow features of nanofluids. *J Heat Transfer*. 2003;125(1): 151–155. DOI: 10.1115/1.1532008
- [56] Choi SUS. Nanofluids: From vision to reality through research. *J Heat Transfer*. 2009;131(3): 033106. DOI:10.1115/1.3056479
- [57] Wu D, Zhu H, Wang L, Liu L. Critical issues in nanofluids preparation, characterization and thermal conductivity. *Curr Nanosci*. 2009;5(1): 103–112. DOI: 10.2174/157341309787314548
- [58] Hong H, Wensel J, Roy W. Heat transfer nanolubricant and nanogrease based on carbon nanotubes. *ECS Trans*. 2007;2(12): 133–138. DOI: 10.1149/1.2408959
- [59] Das SK, Choi SU, Yu W, Pradeep T. *Nanofluids: Science and Technology*. Hoboken, NJ, USA: John Wiley & Sons, Inc.; 2007. 416 p.
- [60] Peterson GP, Li CH. Heat and Mass transfer in fluids with nanoparticle suspensions. *Adv Heat Transf*. 2006;39: 257–376. DOI: 10.1016/S0065-2717(06)39003-X
- [61] Prasher R, Bhattacharya P, Phelan PE. Brownian-motion-based convective-conductive model for the effective thermal conductivity of nanofluids. *J Heat Transfer*. 2006;128(6): 588. DOI: 10.1115/1.2188509
- [62] Das SK, Putra N, Thiesen P, Roetzel W. Temperature dependence of thermal conductivity enhancement for nanofluids. *J Heat Transfer*. 2003;125(4): 567. DOI: 10.1115/1.1571080.
- [63] Yang B, Han ZH. Temperature-dependent thermal conductivity of nanorod-based nanofluids. *Appl Phys Lett*; 2006;89(8): 083111. DOI: 10.1063/1.2338424.
- [64] Chon CH, Kihm KD, Lee SP, Choi SUS. Empirical correlation finding the role of temperature and particle size for nanofluid (Al₂O₃) thermal conductivity enhancement. *Appl Phys Lett*; 2005;87(15): 153107. DOI: 10.1063/1.2093936

- [65] Pil Jang S, Choi SUS. Effects of various parameters on nanofluid thermal conductivity. *J Heat Transfer*; 2007;129(5): 617. DOI: 10.1115/1.2712475
- [66] Wen D, Ding Y. Effective Thermal conductivity of aqueous suspensions of carbon nanotubes (carbon nanotube nanofluids). *J Thermophys Heat Transf*. 2004;18(4): 481–485. DOI: 10.2514/1.9934
- [67] Wong K V., De Leon O. Applications of nanofluids: Current and future. *Adv Mech Eng*. 2010;2: 519659. DOI: 10.1155/2010/519659
- [68] Hernández Battez A, González R, Viesca JL, Fernández JE, Díaz Fernández JM, Machado A, Chou R, Riba J. CuO, ZrO₂ and ZnO nanoparticles as antiwear additive in oil lubricants. *Wear*. 2008;265(3-4): 422–428. DOI: 10.1016/j.wear.2007.11.013
- [69] Lee P-H, Nam JS, Li C, Lee SW. An experimental study on micro-grinding process with nanofluid minimum quantity lubrication (MQL). *Int J Precis Eng Manuf*. 2012;13(3): 331–338. DOI: 10.1007/s12541-012-0042-2
- [70] Chang H, Li ZY, Kao MJ, Huang KD, Wu HM. Tribological property of TiO₂ nanolubricant on piston and cylinder surfaces. *J Alloys Compd. Elsevier B.V.*; 2010;495(2): 481–484. DOI: 10.1016/j.jallcom.2009.10.017
- [71] Hernández Battez A, Viesca JL, González R, Blanco D, Asedegbega E, Osorio A. Friction reduction properties of a CuO nanolubricant used as lubricant for a NiCrBSi coating. *Wear*. 2010;268(1-2): 325–328. DOI: 10.1016/j.wear.2009.08.018
- [72] Narayanan TN. Template assisted fabrication of I-D nanostructures of nickel, cobalt, iron oxide and carbon nanotubes and a study on their structural, magnetic and nonlinear optical properties for applications [PhD thesis]. India: Cochin University; 2009. <http://dyuthi.cusat.ac.in/xmlui/bitstream/handle/purl/2551/Dyuthi-T0695.pdf?sequence=1>
- [73] Li Y, Zhou J, Tung S, Schneider E, Xi S. A review on development of nanofluid preparation and characterization. *Powder Technol*. 2009;196(2): 89–101. DOI: 10.1016/j.powtec.2009.07.025
- [74] Munkhbayar B, Tanshen MR, Jeoun J, Chung H, Jeong H. Surfactant-free dispersion of silver nanoparticles into MWCNT-aqueous nanofluids prepared by one-step technique and their thermal characteristics. *Ceram Int*. 2013;39(6): 6415–6425. DOI: 10.1016/j.ceramint.2013.01.069
- [75] Zhu H, Lin Y, Yin Y. A novel one-step chemical method for preparation of copper nanofluids. *J Colloid Interface Sci*. 2004;277(1): 100–103. DOI: 10.1016/j.jcis.2004.04.026
- [76] Hwang Y, Park HS, Lee JK, Jung WH. Thermal conductivity and lubrication characteristics of nanofluids. *Curr Appl Phys*. 2006;6(SUPPL. 1): 67–71. DOI: 10.1016/j.cap.2006.01.014

- [77] Hong T-K, Yang H-S, Choi CJ. Study of the enhanced thermal conductivity of Fe nanofluids. *J Appl Phys*. 2005;97(6): 064311. DOI: 10.1063/1.1861145
- [78] Assael MJ, Chen C-F, Metaxa I, Wakeham WA. Thermal conductivity of suspensions of carbon nanotubes in water. *Int J Thermophys*. 2004;25(4): 971–985. DOI: 10.1023/B:IJOT.0000038494.22494.04
- [79] Sohel Murshed SM, Tan S-H, Nguyen N-T. Temperature dependence of interfacial properties and viscosity of nanofluids for droplet-based microfluidics. *J Phys D Appl Phys*; 2008;41(8): 085502. DOI: 10.1088/0022-3727/41/8/085502
- [80] Li D, Hong B, Fang W, Guo Y, Lin R. Preparation of well-dispersed silver nanoparticles for oil-based nanofluids. *Ind Eng Chem Res*. ; 2010;49(4): 1697–1702. DOI: 10.1021/ie901173h
- [81] Hwang Y, Lee J-K, Lee J-K, Jeong Y-M, Cheong S, Ahn Y-C, Kim SH. Production and dispersion stability of nanoparticles in nanofluids. *Powder Technol*. 2008;186(2): 145–153. DOI: 10.1016/j.powtec.2007.11.020
- [82] Ghozatloo A, Shariaty-Niasar M, Rashidi AM. Preparation of nanofluids from functionalized graphene by new alkaline method and study on the thermal conductivity and stability. *Int Commun Heat Mass Transf*. 2013;42: 89–94. DOI: 10.1016/j.icheatmasstransfer.2012.12.007
- [83] Eastman JA, Choi SUS, Li S, Yu W, Thompson LJ. Anomalously increased effective thermal conductivities of ethylene glycol-based nanofluids containing copper nanoparticles. *Appl Phys Lett*. 2001;78(6): 718.
- [84] Xuan Y, Li Q. Heat transfer enhancement of nanofluids. *Int J Heat Fluid Flow*. 2000;21(1): 58–64. DOI: 10.1016/S0142-727X(99)00067-3
- [85] Guo L, Yang S, Yang C, Yu P, Wang J, Ge W, Wong GKL. Highly monodisperse polymer-capped ZnO nanoparticles: Preparation and optical properties. *Appl Phys Lett*; 2000;76(20): 2901. DOI: 10.1063/1.126511
- [86] Chen M-L, Meng Z-D, Zhu L, Choi J-G, Park C-Y, Lee S-C, Hong D-S, Lee J-G, Jang W-K, Oh W-C. Dispersion stability of metal (oxide)-graphene nanofluids with electrical and thermal properties. *Sci Adv Mater*. 2011;3(6): 887–892. DOI: 10.1166/sam.2011.1213
- [87] Murshed SMS, de Castro CAN, Lourenço MJ V. Effect of Surfactant and nanoparticle clustering on thermal conductivity of aqueous nanofluids. *J Nanofluids*. 2012;1(2): 175–179. DOI: 10.1166/jon.2012.1020
- [88] Li CH, Peterson GP. The effect of particle size on the effective thermal conductivity of Al₂O₃-water nanofluids. *J Appl Phys*; 2007;101(4): 044312. DOI: 10.1063/1.2436472
- [89] Mintsa HA, Roy G, Nguyen CT, Doucet D. New temperature dependent thermal conductivity data for water-based nanofluids. *Int J Therm Sci*. 2009;48(2): 363–371. DOI: 10.1016/j.ijthermalsci.2008.03.009

- [90] Patel HE, Sundararajan T, Das SK. An experimental investigation into the thermal conductivity enhancement in oxide and metallic nanofluids. *J Nanoparticle Res.* 2009;12(3): 1015–1031. DOI: 10.1007/s11051-009-9658-2
- [91] Anoop KB, Sundararajan T, Das SK. Effect of particle size on the convective heat transfer in nanofluid in the developing region. *Int J Heat Mass Transf.* 2009;52(9-10): 2189–2195. DOI: 10.1016/j.ijheatmasstransfer.2007.11.063
- [92] Teng T-P, Hung Y-H, Teng T-C, Mo H-E, Hsu H-G. The effect of alumina/water nanofluid particle size on thermal conductivity. *Appl Therm Eng.* 2010;30(14-15): 2213–2218. DOI: 10.1016/j.applthermaleng.2010.05.036
- [93] Abbasian Arani AA, Amani J. Experimental investigation of diameter effect on heat transfer performance and pressure drop of TiO₂-water nanofluid. *Exp Therm Fluid Sci.* 2013;44: 520–533. DOI: 10.1016/j.expthermflusci.2012.08.014
- [94] Kwek D, Crivoi A, Duan F. Effects of temperature and particle size on the thermal property measurements of Al₂O₃-water nanofluids. *J Chem Eng Data.* ; 2010;55(12): 5690–5695. DOI: 10.1021/je1006407.
- [95] Nguyen CT, Roy G, Gauthier C, Galanis N. Heat transfer enhancement using Al₂O₃-water nanofluid for an electronic liquid cooling system. *Appl Therm Eng.* 2007;27(8-9): 1501–1506. DOI:10.1016/j.applthermaleng.2006.09.028
- [96] Chopkar M, Das PK, Manna I. Synthesis and characterization of nanofluid for advanced heat transfer applications. *Scr Mater.* 2006;55(6): 549–552. DOI:10.1016/j.scriptamat.2006.05.030
- [97] He Y, Jin Y, Chen H, Ding Y, Cang D, Lu H. Heat transfer and flow behaviour of aqueous suspensions of TiO₂ nanoparticles (nanofluids) flowing upward through a vertical pipe. *Int J Heat Mass Transf.* 2007;50(11-12): 2272–2281. DOI: 10.1016/j.ijheatmasstransfer.2006.10.024
- [98] Singh D, Timofeeva E, Yu W, Routbort J, France D, Smith D, Lopez-Cepero JM. An investigation of silicon carbide-water nanofluid for heat transfer applications. *J Appl Phys.* AIP Publishing; 2009;105(6): 064306. DOI: 10.1063/1.3082094
- [99] Timofeeva E V, Gavrilov AN, McCloskey JM, Tolmachev Y V, Sprunt S, Lopatina LM, Selinger J V. Thermal conductivity and particle agglomeration in alumina nanofluids: experiment and theory. *Phys Rev E;* 2007;76(6): 061203. DOI:10.1103/PhysRevE.76.061203
- [100] Beck MP, Yuan Y, Warriar P, Teja AS. The effect of particle size on the thermal conductivity of alumina nanofluids. *J Nanoparticle Res.* 2009;11(5): 1129–1136. DOI: 10.1007/s11051-008-9500-2
- [101] Beck MP, Yuan Y, Warriar P, Teja AS. The thermal conductivity of aqueous nanofluids containing ceria nanoparticles. *J Appl Phys;* 2010;107(6): 066101. DOI: 10.1063/1.3330506

- [102] Yu W, France DM, Routbort JL, Choi SUS. Review and comparison of nanofluid thermal conductivity and heat transfer enhancements. *Heat Transf Eng.* Taylor & Francis Group; 2008;29(5): 432–460. DOI: 10.1080/01457630701850851
- [103] Elias MM, Miqdad M, Mahbubul IM, Saidur R, Kamalisarvestani M, Sohel MR, Hepbasli A, Rahim NA, Amalina MA. Effect of nanoparticle shape on the heat transfer and thermodynamic performance of a shell and tube heat exchanger. *Int Commun Heat Mass Transf.* 2013;44: 93–99. DOI: 10.1016/j.icheatmasstransfer.2013.03.014
- [104] Murshed SMS, Leong KC, Yang C. Enhanced thermal conductivity of TiO₂–water based nanofluids. *Int J Therm Sci.* 2005;44(4): 367–373. DOI: 10.1016/j.ijthermalsci.2004.12.005
- [105] Glory J, Bonetti M, Helezen M, Mayne-L’Hermite M, Reynaud C. Thermal and electrical conductivities of water-based nanofluids prepared with long multiwalled carbon nanotubes. *J Appl Phys;* 2008;103(9): 094309. DOI: 10.1063/1.2908229
- [106] Cherkasova AS, Shan JW. Particle aspect-ratio effects on the thermal conductivity of micro- and nanoparticle suspensions. *J Heat Transfer;* 2008;130(8): 082406. DOI: 10.1115/1.2928050
- [107] Timofeeva E V., Routbort JL, Singh D. Particle shape effects on thermophysical properties of alumina nanofluids. *J Appl Phys.;* 2009;106(1): 014304. DOI: 10.1063/1.3155999
- [108] Coleman JN, Lotya M, O’Neill A, Bergin SD, King PJ, Khan U, Young K, Gaucher A, De S, Smith RJ, Shvets I V, Arora SK, Stanton G, Kim H-Y, Lee K, Kim GT, Duesberg GS, Hallam T, Boland JJ, Wang JJ, Donegan JF, Grunlan JC, Moriarty G, Shmeliov A, Nicholls RJ, Perkins JM, Grievson EM, Theuwissen K, McComb DW, Nellist PD, Nicolosi V. Two-dimensional nanosheets produced by liquid exfoliation of layered materials. *Science;* 2011;331(6017): 568–571. DOI:10.1126/science.1194975
- [109] Karthikeyan NR, Philip J, Raj B. Effect of clustering on the thermal conductivity of nanofluids. *Mater Chem Phys.* 2008;109(1): 50–55. DOI: 10.1016/j.matchemphys.2007.10.029
- [110] Peña-Parás L, Taha-Tijerina J, García A, Maldonado D, González JA, Molina D, Cantú P. Antiwear and extreme pressure properties of nanofluids for industrial applications. *Tribol Trans.* 2014;57(6): 1072–1076. DOI:10.1080/10402004.2014.933937
- [111] Peña-Parás L, Maldonado-Cortés D, Taha-Tijerina J, García P, Garza GT, Irigoyen M, Gutiérrez J, Sánchez D. Extreme pressure properties of nanolubricants for metal-forming applications. *Ind Lubr Tribol;* 2016;68(1): 30–34. DOI: 10.1108/ILT-05-2015-0069
- [112] Peña-Parás L, Taha-Tijerina J, García A, Maldonado D, Nájera A, Ortiz D. Thermal transport and tribological properties of nanogreases for metal-mechanic applications. *Wear.* Elsevier; 2015;332-333: 1322–1326. DOI:10.1016/j.wear.2015.01.062

- [113] Peña-Parás L, Taha-Tijerina J, Garza L, Maldonado D, Michalczewski R, Lapray C. Effect of CuO and Al₂O₃ nanoparticle additives on the tribological behavior of fully formulated oils. *Wear*. 2015;332-333: 1256–1261. DOI: 10.1016/j.wear.2015.02.038
- [114] Nasiri A, Shariaty-Niasar M, Rashidi A, Amrollahi A, Khodafarin R. Effect of dispersion method on thermal conductivity and stability of nanofluid. *Exp Therm Fluid Sci*. 2011;35(4): 717–723. DOI: 10.1016/j.expthermflusci.2011.01.006
- [115] Wang X, Xu X, S. Choi SU. Thermal conductivity of nanoparticle–fluid mixture. *J Thermophys Heat Transf*. 1999;13(4): 474–480. DOI: 10.2514/2.6486
- [116] Gharagozloo PE, Eaton JK, Goodson KE. Diffusion, aggregation, and the thermal conductivity of nanofluids. *Appl Phys Lett*; 2008;93(10): 103110. DOI: 10.1063/1.2977868
- [117] Gharagozloo PE, Goodson KE. Aggregate fractal dimensions and thermal conduction in nanofluids. *J Appl Phys*; 2010;108(7): 074309. DOI: 10.1063/1.3481423
- [118] Yu W, Xie H, Chen L, Li Y. Investigation of thermal conductivity and viscosity of ethylene glycol based ZnO nanofluid. *Thermochim Acta*. 2009;491(1-2): 92–96. DOI: 10.1016/j.tca.2009.03.007
- [119] Yu W, Xie H, Chen L, Li Y. Enhancement of thermal conductivity of kerosene-based Fe₃O₄ nanofluids prepared via phase-transfer method. *Colloids Surfaces A Physicochem Eng Asp*. 2010;355(1-3): 109–113. DOI: 10.1016/j.colsurfa.2009.11.044
- [120] Kole M, Dey TK. Thermal conductivity and viscosity of Al₂O₃ nanofluid based on car engine coolant. *J Phys D Appl Phys*. 2010;43(31): 315501. DOI: 10.1088/0022-3727/43/31/315501
- [121] Yu W, Xie H, Bao D. Enhanced thermal conductivities of nanofluids containing graphene oxide nanosheets. *Nanotechnology*. 2010;21(5): 055705. DOI: 10.1088/0957-4484/21/5/055705
- [122] Peng D, Kang Y, Chen S, Shu F, Chang Y. Dispersion and tribological properties of liquid paraffin with added aluminum nanoparticles. *Ind Lubr Tribol*; 2010;62(6): 341–348. DOI: 10.1108/00368791011076236
- [123] Gulzar M, Masjuki H, Varman M, Kalam M, Mufti RA, Yunus R, Zahid R. Improving the AW/EP ability of chemically modified palm oil by adding CuO and MoS₂ nanoparticles. *Tribol Int*. 2015;88: 271–279. DOI:10.1016/j.triboint.2015.03.035
- [124] Chen CS, Chen XH, Xu LS, Yang Z, Li WH. Modification of multi-walled carbon nanotubes with fatty acid and their tribological properties as lubricant additive. *Carbon*. 2005;43(8): 1660–1666. DOI: 10.1016/j.carbon.2005.01.044
- [125] Findenegg GH, Pasucha B, Strunk H. Adsorption of non-ionic surfactants from aqueous solutions on graphite: adsorption isotherms and calorimetric enthalpies of displacement for C₈E₄ and related compounds. *Colloids and Surfaces*. 1989;37: 223–233. DOI: 10.1016/0166-6622(89)80121-0

- [126] Wang B, Wang X, Lou W, Hao J. Thermal conductivity and rheological properties of graphite/oil nanofluids. *Colloids Surfaces A Physicochem Eng Asp.* 2012;414: 125–131. DOI: 10.1016/j.colsurfa.2012.08.008
- [127] Gao Y, Chen G, Oli Y, Zhang Z, Xue Q. Study on tribological properties of oleic acid-modified TiO₂ nanoparticle in water. *Wear.* 2002;252(5-6): 454–458.
- [128] Sluhan CA. Selecting the right cutting and grinding fluids. *Tool Prod.* 1994;60(2): 7.
- [129] Hoff ML. Cutting fluids: necessary nuisance to productivity tool. *Soc Manuf Eng.* 2002; 1–6.
- [130] Kumar A, Vemula PK, Ajayan PM, John G. Silver-nanoparticle-embedded antimicrobial paints based on vegetable oil. *Nat Mater;* 2008;7(3): 236–241. DOI: 10.1038/nmat2099
- [131] Anon HSE. Warnings for grinding coolants. *Metalwork Prod.* 2003;147(5): 44.
- [132] Nguyen CT, Desgranges F, Roy G, Galanis N, Maré T, Boucher S, Angue Mintsa H. Temperature and particle-size dependent viscosity data for water-based nanofluids—Hysteresis phenomenon. *Int J Heat Fluid Flow.* 2007;28(6): 1492–1506. DOI: 10.1016/j.ijheatfluidflow.2007.02.004
- [133] Taha-tijerina J, Narayanan TN, Avali S, Ajayan PM. 2D structures-based energy management nanofluids. In: *ASME International Mechanical Engineering Congress & Exposition (IMECE 2012).* 9–12 November. Houston, TX, USA; p. IMECE 2012–87890. DOI: 10.1115/IMECE2012-87890
- [134] Larson RG. *The Structure and Rheology of Complex Fluids.* New York, USA: Oxford University Press; 1998. 688 p.
- [135] Jang SP, Choi SUS. Role of Brownian motion in the enhanced thermal conductivity of nanofluids. *Appl Phys Lett.* 2004;84(21): 4316. DOI: 10.1063/1.1756684
- [136] Koo J, Kleinstreuer C. Impact analysis of nanoparticle motion mechanisms on the thermal conductivity of nanofluids. *Int Commun Heat Mass Transf.* 2005;32(9): 1111–1118. DOI: 10.1016/j.icheatmasstransfer.2005.05.014
- [137] Kleinstreuer C, Feng Y. Experimental and theoretical studies of nanofluid thermal conductivity enhancement: a review. *Nanoscale Res Lett.* 2011;6(1): 229. DOI: 10.1186/1556-276X-6-229
- [138] Singh A. Thermal Conductivity of Nanofluids. *Def Sci J.* 2008;58(5): 600–607. DOI: 10.14429/dsj.58.1682
- [139] Patel HE, Sundararajan T, Pradeep T, Dasgupta A, Dasgupta N, Das SK. A micro-convection model for thermal conductivity of nanofluids. *Pramana.* 2005;65(5): 863–869. DOI: 10.1007/BF02704086

- [140] Kumar DH, Patel HE, Kumar VRR, Sundararajan T, Pradeep T, Das SK. Model for heat conduction in nanofluids. *Phys Rev Lett. American Physical Society*; 2004;93(14): 144301. DOI: 10.1103/PhysRevLett.93.144301
- [141] Jyothirmayee Aravind SS, Ramaprabhu S. Surfactant free graphene nanosheets based nanofluids by in-situ reduction of alkaline graphite oxide suspensions. *J Appl Phys*; 2011;110(12): 124326. DOI: 10.1063/1.3671613
- [142] Paul G, Philip J, Raj B, Das PK, Manna I. Synthesis, characterization, and thermal property measurement of nano- $\text{Al}_{95}\text{Zn}_{05}$ dispersed nanofluid prepared by a two-step process. *Int J Heat Mass Transf.* 2011;54(15-16): 3783–3788. DOI: 10.1016/j.ijheatmasstransfer.2011.02.044
- [143] Wang B, Wang X, Lou W, Hao J. Ionic liquid-based stable nanofluids containing gold nanoparticles. *J Colloid Interface Sci.* 2011;362(1): 5–14. DOI: 10.1016/j.jcis.2011.06.023
- [144] Lee S, Choi SU-S, Li S, Eastman JA. Measuring thermal conductivity of fluids containing oxide nanoparticles. *J Heat Transfer.* 1999;121(2): 280. DOI:10.1115/1.2825978
- [145] Hu P, Shan W-L, Yu F, Chen Z-S. Thermal conductivity of AlN -ethanol nanofluids. *Int J Thermophys.* 2008;29(6): 1968–1973. DOI: 10.1007/s10765-008-0529-3
- [146] Yu W, Xie H, Chen W. Experimental investigation on thermal conductivity of nanofluids containing graphene oxide nanosheets. *J Appl Phys. AIP Publishing*; 2010;107(9): 094317. DOI: 10.1063/1.3372733
- [147] Das SK, Putra N, Roetzel W. Pool boiling characteristics of nano-fluids. *Int J Heat Mass Transf.* 2003;46(5): 851–862.
- [148] Jha N, Ramaprabhu S. Thermal conductivity studies of metal dispersed multiwalled carbon nanotubes in water and ethylene glycol based nanofluids. *J Appl Phys*; 2009;106(8): 084317. DOI: 10.1063/1.3240307
- [149] Xie H, Chen L. Adjustable thermal conductivity in carbon nanotube nanofluids. *Phys Lett A.* 2009;373(21): 1861–184. DOI: 10.1016/j.physleta.2009.03.037
- [150] Walvekar R, Faris IA, Khalid M. Thermal conductivity of carbon nanotube nanofluid-experimental and theoretical study. *Heat Transf Res.* 2012;41(2): 145–163. DOI: 10.1002/htj.20405
- [151] Ding Y, Alias H, Wen D, Williams RA. Heat transfer of aqueous suspensions of carbon nanotubes (CNT nanofluids). *Int J Heat Mass Transf.* 2006;49(1-2): 240–250. DOI: 10.1016/j.ijheatmasstransfer.2005.07.009
- [152] Du K. Self-Assembly of nanoparticles at liquid-liquid interfaces [PhD thesis]. University of Massachusetts, Amherst, MA, USA; 2010.
- [153] Henderson JR, van Swol F. On the interface between a fluid and a planar wall. *Mol Phys.* Taylor & Francis Group; 2007;51(4): 991–1010. DOI: 10.1080/00268978400100651

- [154] Ding Y, Chen H, Wang L, Yang C-Y, He Y, Yang W, Lee WP, Zhang L, Huo R. Heat transfer intensification using nanofluids. *KONA Powder Part J.* 2007;25: 23–38.
- [155] Li L, Zhang Y, Ma H, Yang M. Molecular dynamics simulation of effect of liquid layering around the nanoparticle on the enhanced thermal conductivity of nanofluids. *J Nanoparticle Res.* 2009;12(3): 811–821. DOI: 10.1007/s11051-009-9728-5
- [156] Yu C-J, Richter AG, Datta A, Durbin MK, Dutta P. Observation of molecular layering in thin liquid films using X-ray reflectivity. *Phys Rev Lett*; 1999;82(11): 2326–2329. DOI: 10.1103/PhysRevLett.82.2326
- [157] Ren Y, Xie H, Cai A. Effective thermal conductivity of nanofluids containing spherical nanoparticles. *J Phys D Appl Phys.* 2005;38(21): 3958–3961. DOI: 10.1088/0022-3727/38/21/019
- [158] Duangthongsuk W, Wongwises S. Measurement of temperature-dependent thermal conductivity and viscosity of TiO₂-water nanofluids. *Exp Therm Fluid Sci.* 2009;33(4): 706–714. DOI: 10.1016/j.expthermflusci.2009.01.005
- [159] Kole M, Dey TK. Investigation of thermal conductivity, viscosity, and electrical conductivity of graphene based nanofluids. *J Appl Phys*; 2013;113(8): 084307. DOI: 10.1063/1.4793581
- [160] Aravind SSJ, Ramaprabhu S. Graphene–multiwalled carbon nanotube-based nanofluids for improved heat dissipation. *RSC Adv.*; 2013;3(13): 4199. DOI: 10.1039/c3ra22653
- [161] Yan X, Jiang Y, Jiang M, Hong H. ZnO Nanorod based nanofluids. *J Nanofluids.* 2013;2(1): 63–68. DOI: 10.1166/jon.2013.1037
- [162] Challoner AR, Powell RW. Thermal conductivities of liquids: New determinations for seven liquids and appraisal of existing values. *Proc R Soc A Math Phys Eng Sci.* 1956;238(1212): 90–106. DOI: 10.1098/rspa.1956.0205
- [163] Kurt H, Kayfeci M. Prediction of thermal conductivity of ethylene glycol–water solutions by using artificial neural networks. *Appl Energy.* 2009;86(10): 2244–2248. DOI: 10.1016/j.apenergy.2008.12.020
- [164] Santucci A, Verdini L, Verdini PG. Data-acquisition system for measurement of thermal diffusivity and propagation properties of thermal waves by a non-steady-state method. *Rev Sci Instrum*; 1986;57(8): 1627. DOI: 10.1063/1.1138541
- [165] Bhattacharya P, Nara S, Vijayan P, Tang T, Lai W, Phelan PE, Prasher RS, Song DW, Wang J. Characterization of the temperature oscillation technique to measure the thermal conductivity of fluids. *Int J Heat Mass Transf.* 2006;49(17-18): 2950–2956. DOI: 10.1016/j.ijheatmasstransfer.2006.02.023

- [166] Czarnetzki W, Roetzel W. Temperature oscillation techniques for simultaneous measurement of thermal diffusivity and conductivity. *Int J Thermophys.* 1995;16(2): 413–414. DOI: 10.1007/BF01441907
- [167] Cahill DG. Thermal conductivity measurement from 30 to 750 K: The 3ω method. *Rev Sci Instrum.* 1990;61(2): 802. DOI: 10.1063/1.1141498
- [168] Oh D-W, Jain A, Eaton JK, Goodson KE, Lee JS. Thermal conductivity measurement and sedimentation detection of aluminum oxide nanofluids by using the 3ω method. *J Heat Fluid Flow.* 2008;29(5): 1456–1461. DOI:10.1016/j.ijheatfluidflow.2008.04.007
- [169] Wang H, Sen M. Analysis of the 3-omega method for thermal conductivity measurement. *Int J Heat Mass Transf.* 2009;52(7-8): 2102–2109. DOI: 10.1016/j.ijheatmasstransfer.2008.10.020
- [170] Choi SUS, Zhang ZG, Yu W, Lockwood FE, Grulke EA. Anomalous thermal conductivity enhancement in nanotube suspensions. *Appl Phys Lett.* 2001;79(14): 2252. DOI: 10.1063/1.1613374
- [171] Xie H, Lee H, Youn W, Choi M. Nanofluids containing multiwalled carbon nanotubes and their enhanced thermal conductivities. *J Appl Phys.* AIP Publishing; 2003;94(8): 4967. DOI: 10.1063/1.2191571
- [172] Li CH, Peterson GP. Experimental investigation of temperature and volume fraction variations on the effective thermal conductivity of nanoparticle suspensions (nanofluids). *J Appl Phys.* 2006;99(8): 084314. DOI: 10.1063/1.2191571
- [173] Venkata Sastry NN, Bhunia A, Sundararajan T, Das SK. Predicting the effective thermal conductivity of carbon nanotube based nanofluids. *Nanotechnology;* 2008;19(5): 055704. DOI: 10.1088/0957-4484/19/05/055704
- [174] Li D, Xie W, Fang W. Preparation and properties of copper-oil-based nanofluids. *Nanoscale Res Lett;* 2011;6(1): 373. DOI: 10.1186/1556-276X-6-373
- [175] Branson BT, Beauchamp PS, Beam JC, Lukehart CM, Davidson JL. Nanodiamond nanofluids for enhanced thermal conductivity. *ACS Nano;* 2013;7(4): 3183–3189. DOI: 10.1021/nn305664x
- [176] Shaikh S, Lafdi K, Ponnappan R. Thermal conductivity improvement in carbon nanoparticle doped PAO oil: An experimental study. *J Appl Phys.* 2007;101(6): 064302. DOI: 10.1063/1.2710337
- [177] Yu W, Xie H, Chen L, Zhu Z, Zhao J, Zhang Z. Graphene based silicone thermal greases. *Phys Lett A.* 2014;378(3): 207–211. DOI: 10.1016/j.physleta.2013.10.017
- [178] Aravind SSJ, Ramaprabhu S. Graphene–multiwalled carbon nanotube-based nanofluids for improved heat dissipation. *RSC Adv.* 2013;3(13): 4199. DOI: 10.1039/c3ra22653k

- [179] Mehrali M, Sadeghinezhad E, Latibari ST, Kazi SN, Metselaar HSC. Investigation of thermal conductivity and rheological properties of nanofluids containing graphene nanoplatelets. *Nanoscale Res Lett*. 2014;9(1): 15. DOI: 10.1186/1556-276X-9-15
- [180] Yu W, Xie H, Wang X, Wang X. Significant thermal conductivity enhancement for nanofluids containing graphene nanosheets. *Phys Lett A*. 2011;375(10): 1323–1328. DOI: 10.1016/j.physleta.2011.01.040
- [181] Baby TT, Ramaprabhu S. Enhanced convective heat transfer using graphene dispersed nanofluids. *Nanoscale Res Lett*; 2011;6(1): 289. DOI: 10.1186/1556-276X-6-289
- [182] Kole M, Dey TK. Investigation of thermal conductivity, viscosity, and electrical conductivity of graphene based nanofluids. *J Appl Phys*. 2013;113(8): 0–8. DOI: 10.1063/1.4793581
- [183] Mehrali M, Sadeghinezhad E, Tahan Latibari S, Mehrali M, Togun H, Zubir MNM, Kazi SN, Metselaar HSC. Preparation, characterization, viscosity, and thermal conductivity of nitrogen-doped graphene aqueous nanofluids. *J Mater Sci*. 2014;49(20): 7156–7171. DOI: 10.1007/s10853-014-8424-8
- [184] Hadadian M, Goharshadi EK, Youssefi A. Electrical conductivity, thermal conductivity, and rheological properties of graphene oxide-based nanofluids. *J Nanoparticle Res*. 2014;16(12): 2788. DOI: 10.1007/s11051-014-2788-1
- [185] Wang X-Q, Mujumdar AS. Heat transfer characteristics of nanofluids: a review. *Int J Therm Sci*. 2007;46(1): 1–19. DOI:10.1016/j.ijthermalsci.2006.06.010
- [186] Murshed SMS, Leong KC, Yang C. Investigations of thermal conductivity and viscosity of nanofluids. *Int J Therm Sci*. 2008;47(5): 560–568. DOI: 10.1016/j.ijthermalsci.2007.05.004
- [187] Choi C, Yoo HS, Oh JM. Preparation and heat transfer properties of nanoparticle-in-transformer oil dispersions as advanced energy-efficient coolants. *Curr Appl Phys*. 2008;8(6): 710–712. DOI:10.1016/j.cap.2007.04.060
- [188] Branson BT, Beauchamp PS, Beam JC, Lukehart CM, Davidson JL, Science IM, Engineering M, Engineering E, States U. Nanodiamond nano fluids for enhanced thermal conductivity. 2013;(4): 3183–3189. DOI: 10.1021/nn305664x
- [189] Yang Y, Grulke EA, Zhang ZG, Wu G. Thermal and rheological properties of carbon nanotube-in-oil dispersions. *J Appl Phys*; 2006;99(11): 114307. DOI: <http://dx.doi.org/10.1063/1.2193161>
- [190] Xie H, Wang J, Xi T, Liu Y. Thermal conductivity of suspensions containing nanosized SiC particles. *Int J Thermophys*; 2002;23(2): 571–780. DOI: 10.1023/A:1015121805842
- [191] Putra N, Roetzel W, Das SK. Natural convection of nano-fluids. *Heat Mass Transf*. 2002;39(8-9): 775–784.

- [192] Wen D, Ding Y. Experimental investigation into convective heat transfer of nanofluids at the entrance region under laminar flow conditions. *Int J Heat Mass Transf.* 2004;47(24): 5181–5188. DOI: 10.1016/j.ijheatmasstransfer.2004.07.012
- [193] Saterlie M, Sahin H, Kavlicoglu B, Liu Y, Graeve O. Particle size effects in the thermal conductivity enhancement of copper-based nanofluids. *Nanoscale Res Lett.* 2011;6(1): 217. DOI: 10.1186/1556-276X-6-217
- [194] Lee D, Kim J-W, Kim BG. A new parameter to control heat transport in nanofluids: surface charge state of the particle in suspension. *J Phys Chem B;* 2006;110(9): 4323–4328. DOI: 10.1021/jp057225m
- [195] Yu W, Xie H, Li Y, Chen L. Experimental investigation on thermal conductivity and viscosity of aluminum nitride nanofluid. *Particuology.* 2011;9(2): 187–191. DOI: 10.1016/j.partic.2010.05.014
- [196] Eswaraiiah V, Jyothirmayee Aravind SS, Ramaprabhu S. Top down method for synthesis of highly conducting graphene by exfoliation of graphite oxide using focused solar radiation. *J Mater Chem;* 2011;21(19): 6800. DOI: 10.1039/c1jm10808e
- [197] Yiamsawasd T, Dalkilic AS, Wongwiset S. Measurement of the thermal conductivity of titania and alumina nanofluids. *Thermochim Acta.* 2012;545: 48–56. DOI: 10.1016/j.tca.2012.06.026
- [198] Stachowiak G, Batchelor AW. *Engineering Tribology.* 3rd ed. Oxford, UK: Elsevier Butterworth-Heinemann; 2005. 832 p.
- [199] Hu KH, Liu M, Wang QJ, Xu YF, Schraube S, Hu XG. Tribological properties of molybdenum disulfide nanosheets by monolayer restacking process as additive in liquid paraffin. *Tribol Int.* 2009;42(1): 33–39. DOI:10.1016/j.triboint.2008.05.016
- [200] Setti D, Ghosh S, Rao P V. Application of nano cutting fluid under minimum quantity lubrication (MQL) technique to improve grinding of Ti – 6Al – 4V alloy. *World Acad Sci Eng Technol Int Sci Index 70, Int J Mech Aerospace, Ind Mechatron Manuf Eng.* 2012;6(10): 2107–2111.
- [201] Kedzierski MA. Effect of Al₂O₃ nanolubricant on R134a pool boiling heat transfer. *Int J Refrig.* 2011;34(2): 498–508. DOI: 10.1016/j.ijrefrig.2010.10.007
- [202] Black AL, Dunster RW. Comparative study of surface deposits and behaviour of MoS₂ particles and molybdenum dialkyl-dithio-phosphate. *Wear.* 1969;13(2): 119–132. DOI: 10.1016/0043-1648(69)90507-9
- [203] Günsheimer J, Holinski R. A study of solid lubricants in oils and greases under boundary conditions. *Wear.* 1972;19(4): 439–449. DOI: 10.1016/0043-1648(72)90317-1
- [204] Zhang W, Zhou M, Zhu H, Tian Y, Wang K, Wei J, Ji F, Li X, Li Z, Zhang P, Wu D. Tribological properties of oleic acid-modified graphene as lubricant oil additives. *J Phys D Appl Phys;* 2011;44(20): 205303. DOI: 10.1088/0022-3727/44/20/205303

- [205] Mosleh M, Atnafu ND, Belk JH, Nobles OM. Modification of sheet metal forming fluids with dispersed nanoparticles for improved lubrication. *Wear*. 2009;267(5-8): 1220–1225. DOI: 10.1016/j.wear.2008.12.074
- [206] Rapoport L, Leshchinsky V, Lapsker I, Volovik Y, Nepomnyashchy O, Lvovsky M, Feldman Y, Tenne R. Tribological properties of WS₂nanoparticles under mixed lubrication. *Wear*. 2003;255(7-12): 785–793. DOI: 10.1016/S0043-1648(03)00044-9
- [207] Hisakado T, Tsukizoe T, Yoshikawa H. Lubrication mechanism of solid lubricants in oils. *J Lubr Technol*; 1983;105(2): 245. DOI: 10.1115/1.3254585.
- [208] Chiñas-Castillo F, Spikes HA. Mechanism of action of colloidal solid dispersions. *J Tribol*; 2003;125(3): 552. DOI:10.1115/1.1537752
- [209] Senthilraja S, Karthikeyan M, Gangadevi R. Nanofluid applications in future automobiles: Comprehensive review of existing data. *Nano-Micro Lett*. 2011;2(4): 306–310. DOI: 10.1007/BF03353859
- [210] Eswaraiyah V, Sankaranarayanan V, Ramaprabhu S. Graphene-based engine oil nanofluids for tribological applications. *ACS Appl Mater Interfaces*; 2011;3(11): 4221–4227. DOI: 10.1021/am200851z
- [211] Yu H, Xu Y, Shi P, Xu B, Wang X, Liu Q. Tribological properties and lubricating mechanisms of Cu nanoparticles in lubricant. *Trans Nonferrous Met Soc China*. 2008;18(3): 636–641. DOI: 10.1016/S1003-6326(08)60111-9
- [212] Peng DX, Kang Y, Hwang RM, Shyr SS, Chang YP. Tribological properties of diamond and SiO₂ nanoparticles added in paraffin. *Tribol Int*. 2009;42(6): 911–917. DOI: 10.1016/j.triboint.2008.12.015
- [213] Hu KH, Liu M, Wang QJ, Xu YF, Schraube S, Hu XG. Tribological properties of molybdenum disulfide nanosheets by monolayer restacking process as additive in liquid paraffin. *Tribol Int*. 2009;42(1): 33–39. DOI: 10.1016/j.triboint.2008.05.016
- [214] Wu Z, Wang D, Wang Y, Sun A. Preparation and tribological properties of MoS₂ nanosheets. *Adv Eng Mater*. 2010;12(6): 534–538. DOI: 10.1002/adem.201000127
- [215] Huang HD, Tu JP, Gan LP, Li CZ. An investigation on tribological properties of graphite nanosheets as oil additive. *Wear*. 2006;261(2): 140–144. DOI: 10.1016/j.wear.2005.09.010
- [216] Kao M-J, Lin C-R. Evaluating the role of spherical titanium oxide nanoparticles in reducing friction between two pieces of cast iron. *J Alloys Compd*. 2009;483(1-2): 456–459. DOI: 10.1016/j.jallcom.2008.07.223
- [217] Zhang S, Zhou J, Guo B, Zhou H, Pu Y, Chen J. Friction and wear behavior of laser cladding Ni/hBN self-lubricating composite coating. *Mater Sci Eng A*. 2008;491(1-2): 47–54.
- [218] Saito T, Honda F. Chemical contribution to friction behavior of sintered hexagonal boron nitride in water. *Wear*. 2000;237(2): 253–260. DOI: 10.1016/S0043-1648(99)00346-4

- [219] León OA, Staia MH, Hintermann HE. Wear mechanism of Ni–P–BN(h) composite autocatalytic coatings. *Surf Coatings Technol.* 2005;200(5-6): 1825–1829. DOI: 10.1016/j.surfcoat.2005.08.061
- [220] Avril L, Courant B, Hantzpergue J-J. Tribological performance of α -Fe(Cr)-Fe₂B-FeB and α -Fe(Cr)-h-BN coatings obtained by laser melting. *Wear.* 2006;260(4-5): 351–360. DOI: 10.1016/j.wear.2005.04.012
- [221] Spikes H. Friction modifier additives. *Tribol Lett.* 2015;60(1): 5. DOI: 10.1007/s11249-015-0589-z
- [222] Wu YY, Tsui WC, Liu TC. Experimental analysis of tribological properties of lubricating oils with nanoparticle additives. *Wear.* 2007;262(7–8): 819–825. DOI: 10.1016/j.wear.2006.08.021
- [223] Ben Difallah B, Kharrat M, Dammak M, Monteil G. Improvement in the tribological performance of polycarbonate via the incorporation of molybdenum disulfide particles. *Tribol Trans;* 2014;57(5): 806–813. DOI: 10.1080/10402004.2014.913751
- [224] Fan X, Wang L, Li W. In situ fabrication of low-friction sandwich sheets through functionalized graphene crosslinked by ionic liquids. *Tribol Lett.* 2015;58(1): 12. DOI: 10.1007/s11249-015-0485-6
- [225] Tomala A, Vengudusamy B, Rodríguez Ripoll M, Naveira Suarez A, Remškar M, Rosentsveig R. Interaction between selected MoS₂ nanoparticles and ZDDP tribofilms. *Tribol Lett.* 2015;59(1): 26. DOI: 10.1007/s11249-015-0552-z
- [226] Rao CNR, Nath M. Inorganic nanotubes The illustration of John Dalton (reproduced courtesy of the Library and Information Centre, Royal Society of Chemistry) marks the 200th anniversary of his investigations which led to the determination of atomic weights for hydrogen, nitrogen, carbon, oxygen, phosphorus and sulfur. *Dalt Trans;* 2003;(1): 1–24. DOI:10.1039/b208990b
- [227] Yaya A, Agyei-Tuffour B, Dodoo-Arhin D, Nyankson E, Annan E, Konadu DS, Sinayobye E, Baryeh EA, Ewels CP. Layered nanomaterials—A review. *Glob J Eng Des Technol.* 2012;1(2): 32–41.
- [228] Lin Y, Connell JW. Advances in 2D boron nitride nanostructures: nanosheets, nanoribbons, nanomeshes, and hybrids with graphene. *Nanoscale. The Royal Society of Chemistry;* 2012;4(22): 6908–6939. DOI: 10.1039/c2nr32201c
- [229] Novoselov KS, Jiang D, Schedin F, Booth TJ, Khotkevich V V, Morozov S V, Geim AK. Two-dimensional atomic crystals. *Proc Natl Acad Sci U S A.* 2005;102(30): 10451–10453. DOI: 10.1073/pnas.0502848102
- [230] Ayari A, Cobas E, Ogundadegbe O, Fuhrer MS. Realization and electrical characterization of ultrathin crystals of layered transition-metal dichalcogenides. *J Appl Phys;* 2007;101(1): 014507. DOI: <http://dx.doi.org/10.1063/1.2407388>

- [231] Ruoff R. Graphene: calling all chemists. *Nat Nanotechnol*; 2008;3(1): 10–11. DOI: 10.1038/nnano.2007.432
- [232] Splendiani A, Sun L, Zhang Y, Li T, Kim J, Chim C-Y, Galli G, Wang F. Emerging photoluminescence in monolayer MoS₂. *Nano Lett*; 2010;10(4): 1271–1275. DOI: 10.1021/nl903868w
- [233] Geim AK. Graphene: status and prospects. *Science*; 2009;324(5934): 1530–1534. DOI: 10.1126/science.1158877
- [234] Sudduth RD. A new approach to controlling the viscosity of a coating with a blend of particles with significantly different. *Pigment Resin Technol*. 2008;37(6): 362–374. DOI: <http://dx.doi.org/10.1108/03699420810915067>
- [235] Pakdel A, Zhi C, Bando Y, Nakayama T, Golberg D. Boron nitride nanosheet coatings with controllable water repellency. *ACS Nano*; 2011;5(8): 6507–6515. DOI: 10.1021/nn201838w
- [236] Golberg D, Bando Y, Tang CC, Zhi CY. Boron nitride nanotubes. *Adv Mater*. 2007;19(18): 2413–2432. DOI:10.1002/adma.200700179
- [237] Terrones H, Terrones M, Moran-Lopez JL. Curved nanomaterials. *Curr Sci*. 2001;81(8): 1011–1029.
- [238] Song L, Ci L, Lu H, Sorokin PB, Jin C, Ni J, Kvashnin AG, Kvashnin DG, Lou J, Yakobson BI, Ajayan PM. Large scale growth and characterization of atomic hexagonal boron nitride layers. *Nano Lett*; 2010;10(8): 3209–3215. DOI: 10.1021/nl1022139
- [239] Kimura Y, Wakabayashi T, Okada K, Wada T, Nishikawa H. Boron nitride as a lubricant additive. *Wear*. 1999;232(2): 199–206. DOI: 10.1016/S0043-1648(99)00146-5
- [240] Lin Y, Williams T V., Connell JW. Soluble, exfoliated hexagonal boron nitride nanosheets. *J Phys Chem Lett*; 2010;1(1): 277–283. DOI: 10.1021/jz9002108
- [241] Chang CW, Fennimore AM, Afanasiev A, Okawa D, Ikuno T, Garcia H, Li D, Majumdar A, Zettl A. Isotope effect on the thermal conductivity of boron nitride nanotubes. *Phys Rev Lett*; 2006;97(8): 085901. DOI: 10.1103/PhysRevLett.97.085901
- [242] Gao R, Yin L, Wang C, Qi Y, Lun N, Zhang L, Liu Y-X, Kang L, Wang X. High-yield synthesis of boron nitride nanosheets with strong ultraviolet cathodoluminescence emission. *J Phys Chem C*; 2009;113(34): 15160–15165. DOI: 10.1021/jp904246j
- [243] Kumar A, Pal D. Lattice thermal conductivity of boron nitride crystals at temperatures 1.5 to 300 K. *Phys Status Solidi*. 1985;129(1): K9–12. DOI: 10.1002/pssb.2221290150
- [244] Fiume MM. Safety Assessment of Boron Nitride as Used in Cosmetic. Washington, DC: *Cosmet Ingrid Rev. (CIR)*; 2013; 9 p.

Diverse Thermal Transport Properties of Two-Dimensional Materials: A Comparative Review

Guangzhao Qin and Ming Hu

Additional information is available at the end of the chapter

<http://dx.doi.org/10.5772/64298>

Abstract

The discovery of graphene led to an upsurge in exploring two-dimensional (2D) materials, such as silicene, germanene, phosphorene, hexagonal boron nitride (*h*-BN), and transition metal dichalcogenides (TMDCs), which have attracted tremendous attention due to their unique dimension-dependent properties in the applications of nanoelectronics, optoelectronics, and thermoelectrics. The phonon transport properties governing the heat energy transfer have become a crucial issue for continuing progress in the electronic industry. This chapter reviews the state-of-the-art theoretical and experimental investigations of phonon transport properties of broad 2D nanostructures in various forms, with graphene, silicene and phosphorene as representatives, all of which consist of single element. Special attention is given to the effect of different physical factors, such as sample size, strain, and layer thickness. The effect of substrate and the phonon transport properties in heterostructures are also discussed. We find that the phonon transport properties of 2D materials largely depend on their atomic structure and interatomic bonding nature, showing a diverse intrinsic phonon behavior and disparate response to external environment.

Keywords: two-dimensional materials, thermal conductivity, phonon transport, strain, substrate, first-principles

1. Introduction

Graphene, a two-dimensional (2D) atomic thin honeycomb lattice, exhibits numerous striking physical properties, and can, in principle, be considered as an elementary building block for all carbon allotropes. Ever since the recent developments in 2004, the field of graphene research took off rapidly. These developments in the science of graphene prompted an unprecedented

surge of activity and demonstration of new physical phenomena. Despite its success, graphene still faces some severe problems in its nature of semi-metal or zero band-gap semiconductor and its incompatibility with the current Si-based semiconductor technology. Given that the honeycomb geometry is related to some of the exceptional properties of graphene, there is strong motivation to investigate whether changing carbon to other atom type might give rise to novel physical phenomena as well. An intuitive idea is to study similar 2D materials, such as silicene and phosphorene. Actually, silicene, the Si counterpart of graphene, can solve the above-mentioned problems smoothly and thus has received intense interest lately. Given the fact that thermal transport plays a critical role in many applications such as heat dissipation in nanoelectronics and thermoelectric energy conversion, there has been an emerging demand in characterizing thermal (mainly phonons) transport property of silicene structures. Moreover, research results have shown that silicene exhibits a few novel thermal transport properties, which are fundamentally different from that of graphene, despite the similarity of their honeycomb lattice structure. Therefore, the abnormal physical property, primarily stemming from its unique low buckling structure, may enable silicene to open up entirely new possibilities for revolutionary electronic devices and energy conversion materials.

With the state of the art, this book chapter aims to present theoretical investigations of thermal transport of broad 2D nanostructures in various forms, which have been carried out in our research group in the past few years. Heat transfer in such structures is not only directly relevant to optimizing the device performance such as improved thermal management for nanoelectronics and thermoelectric energy conversion efficiency, but also is a scientifically fundamental problem for many other similar two-dimensional systems (**Figure 1**).

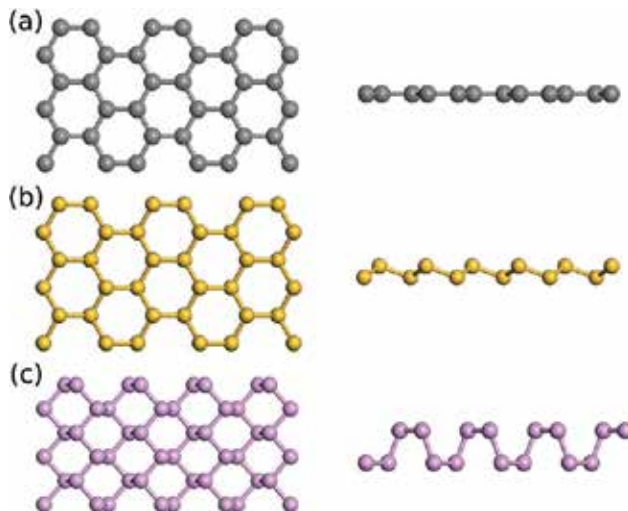


Figure 1. Comparison of the crystal structures (top view and side view) among (a) graphene, (b) silicene, and (c) phosphorene. Graphene possesses perfect planar structure, silicene possesses low buckling structure, and phosphorene possesses pucker (hinge-like) structure.

2. Thermal conductivity

Two-dimensional (2D) materials have been extensively studied in the past decade because of their novel physical and chemical properties [1, 2] and potential applications [3, 4]. For example, it has been found that graphene has extremely high thermal conductivity [5], which has great potential in the applications including electronic cooling and composite materials. In this section, we summarize the available experimental data and theoretical calculations on the phonon transport properties of several typical 2D materials consisting of only one type of element, including graphene, silicene, and phosphorene (Figure 2).

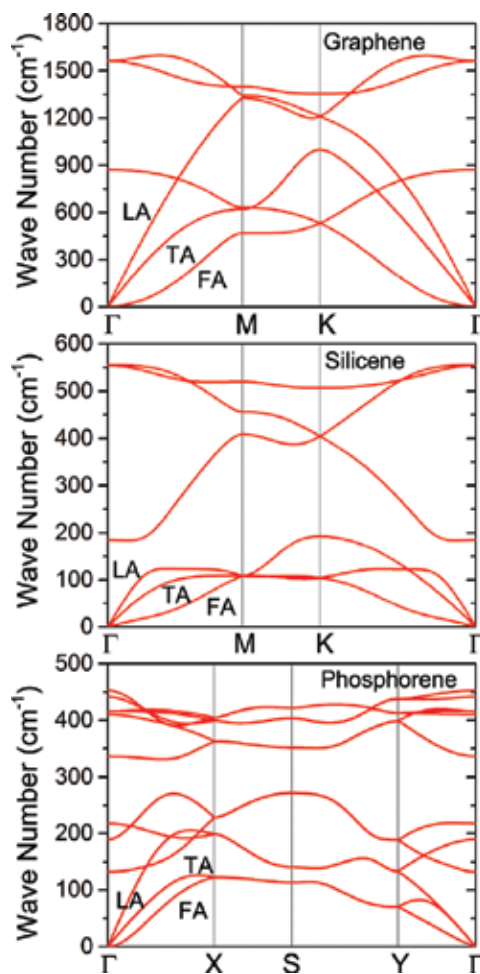


Figure 2. The phonon dispersion curves along the path passing through the main high-symmetry k -points in the irreducible Brillouin zone of graphene, silicene, and phosphorene. Three acoustic phonon modes (LA, TA, and FA) are labeled.

2.1. Graphene

Graphene, the first two-dimensional atomic crystal available to us, has attracted great attention due to its supreme mechanical, electronic, and optical properties. Besides these properties, thermal and thermoelectric properties of graphene are also very fascinating. Experiments have shown that the thermal conductivity of graphene reaches as high as about 3000 W/mK, which makes graphene very promising for thermal management applications such as heat dissipation in electronics [5]. In addition to the heat dissipation applications, due to its extremely high electrical conductivity, graphene has also been explored to be used as thermoelectric material by largely reducing its thermal conductivity by varieties of functionalization, such as constructing graphene nanoribbons, hydrogenation, defects, and doping.

There have been a long time for an intriguing open question on the phonon transport in graphene: what is the relative contribution to heat conduction of LA, TA, and FA phonon polarization branches? The focused point is the importance of FA phonons from negligible to dominant. Klemens' theory states that thermal energy is mainly carried by longitudinal acoustic (LA) and transverse acoustic (TA) phonons, and contributions from out-of-plane flexural acoustic (FA) phonons are negligible due to their small group velocity in the Brillouin zone center and large Grüneisen parameter [6–8]. However, based on recent studies, the arguments for the dominant contributions of FA modes are made on the basis of the symmetry-based phonon-phonon scattering selection rule [9–11]. As for graphene, because of the reflectional symmetry of the structure, the phonon scattering processes involving odd number of FA modes are not allowed, which restricts the phase space for phonon-phonon scattering [9]. The suppression of scattering of FA leads to its extremely low scattering rate which is equivalent to a very large phonon lifetime, which results in the huge contribution to thermal conductivity from FA modes. The selection rule can be broken by placing graphene on any substrate or due to the presence of nanoscale corrugations. Therefore, it is intuitive to see that thermal conductivity of supported graphene is dramatically reduced.

2.2. Silicene

Silicene, the silicon counterpart of graphene, possesses a two-dimensional structure that leads to a host of interesting physical and chemical properties of significant utility. Compared to graphene, silicene is more compatible with silicon-based semiconductor devices and technologies, and therefore has greater potential in nanoelectronic applications. In particular, in terms of thermoelectric application, silicene is even more exciting than graphene as the charge carrier of silicene is massless fermion, and the electrical conductivity of silicene is as high as that of graphene. At the same time, the thermal conductivity of silicene is expected to be much lower than that of graphene due to its buckled atomic structure. In addition to thermoelectric applications, silicene, with supreme electronic properties similar to those of graphene, has also shown great potential for other applications, such as nanoelectronics. For example, in contrast to graphene, the buckled atomic structure breaks the symmetry of the silicene, making it possible to open a band gap by applying electric field [12–14]. Monolayer silicene has been successfully fabricated on substrates such as Ag(1 1 0) [15], Ir(1 1 1) [16], and Ag(1 1 1) [17] surfaces. Recently, Tao et al. have demonstrated silicene-based transistors can operate at room

temperature [4]. Although the performance is still moderate and the lifetime of this transistor is only a few minutes, it has attracted significant research interest in silicene-based devices [18–20]. Therefore, there is an urgent demand to quantify the thermal transport property of silicene, and it is of great interest to explore the role of buckled lattice on phonon transport mechanisms compared with the planar graphene.

The intrinsic physical properties of silicene, such as lattice thermal conductivity, have been an active area of research. Although the thermal conductivity of silicene has not been measured in experiments due to the difficulty of synthesizing freestanding silicene, several numerical simulations have predicted the thermal conductivity of silicene and the results at 300 K range from 5 to 69 W/mK [21–23]. Most of the numerical simulations are based on classical molecular dynamics and the discrepancy of results mainly arises from the different interatomic interaction potentials used. Notably, first-principles-based lattice dynamics predicted that the thermal conductivity of silicene is in the range of 20–30 W/mK [23, 24], which should be more reliable.

From the aspect of theoretical study, the widely used classical molecular dynamics simulation is an appropriate way to investigate the transport phenomena and mechanisms in silicene. Based on the optimized SW potential of SW1 and SW2 obtained by Zhang et al. [21], the thermal conductivity of silicene calculated from non-equilibrium molecular dynamics (NEMD) is 8.64 W/mK (SW1) and 11.77 W/mK (SW2) at 230 K. One would notice that the results for the equilibrium molecular dynamics (EMD) and NEMD methods are not the same, even after the thermal conductivity was extrapolated to infinitely long in the case of NEMD simulation. Nevertheless, the results confirm that the thermal conductivity of monolayer silicene is ultra-low, which is one order of magnitude lower than the value of bulk silicon (about 150 W/mK from experiments).

The thermal conductivity was also calculated by Xie et al. using the single-mode relaxation time (SMRT) model derived from Boltzmann transport equation (BTE), where the scattering of certain phonon mode is irrelevant to the condition of other phonon modes, but other phonon modes are assumed to stay in their equilibrium condition. The interactions for silicon atoms are described by the SW1/SW2 potentials, and the single-point energies are calculated using the Large-scale Atomic/Molecular Massively Parallel Simulator (LAMMPS) package. The thermal conductivity values at 300 K are 3.33 W/mK for the optimized SW1 parameters and 5.43 W/mK for the optimized SW2 parameters. The thermal conductivity calculated by anharmonic lattice dynamics (ALD) is smaller than that calculated by molecular dynamics (MD) simulations. The discrepancy was argued to be mainly attributed to the strong normal scattering near the zone center in two-dimensional materials, as also seen in graphene. After that, first-principles-based ALD method is combined with BTE to accurately calculate the lattice thermal conductivity of silicene by Xie et al. [24]. The main difference from the previous study is that the interactions among atoms are described based on first-principles calculations, and the accuracy should be much higher. The temperature dependence of thermal conductivity was explicitly considered and mode-specific contribution to overall thermal conductivity was analyzed and discussed. Due to the buckling structure of silicene, the flexural mode is not purely out-of-plane vibration, but also contains small components in the in-plane directions.

The intrinsic lattice thermal conductivity of silicene is 9.4 W/mK at 300 K. Later on, due to the development of the calculation method, the BTE can be iteratively solved, where the thermal conductivity becomes unbounded and the iterative procedure reflects the process of the redistribution of phonon modes driven by the heat flux [11, 25–27]. However, the underlying mechanisms are still not well understood. Based on the iterative solution of BTE, the thermal conductivity of silicene is in the range of 15–30 W/mK for three finite sizes of 0.3, 3, and 30 μm [28]. Gu and Yang and Kuang et al. also calculated the thermal conductivity of silicene using the first-principles-based BTE approach, and obtained similar magnitude of thermal conductivity [23, 29].

2.3. Phosphorene

Black phosphorus (BP) is another emerging material which has a puckered layered structure with intra-layer interaction dominated by van der Waals forces [30–32]. Few-layer BP has recently been successfully fabricated by mechanical exfoliation [33, 34] and has generated tremendous interest among scientists [33–44]. Phosphorene, the single layer counterpart of BP, is another interesting 2D structure with high carrier mobility proved by experiments [33, 34, 36] and a large fundamental direct band gap (~ 1.5 eV) [39], which makes BP promising for lots of nanoelectronic applications [32]. For example, some previous theoretical and experimental works have illustrated that phosphorene can be used as nanoelectronic devices, such as field-effect transistors and photo-transistors [33, 34, 36–38]. Besides the extensive studies on its electrical properties, there are also a lot of explorations on its potential applications in thermoelectrics [35, 42, 43]. All these electrical and thermoelectrical applications are closely related to thermal properties. Considering the potential valuable applications of phosphorene as nano-/opto-electronic and thermoelectric devices, it is necessary to fundamentally study the phonon transport properties of this new 2D material.

There have been some experiment works on the measurement of the thermal conductivity of bulk BP [45] and phosphorene films with different thicknesses [46–48]. The thermal conductivity of monolayer phosphorene was also reported theoretically by several independent groups using various methods, such as analytical estimations [35, 49], MD simulation with optimized Stillinger-Weber potential [50–52], relaxation time approximation (RTA) [45, 53–55], and iterative method for solving BTE [45, 54]. However, the exact value of the lattice thermal conductivity of monolayer phosphorene is still unclear, since these results are even one order of magnitude different from each other. For example, the thermal conductivity of monolayer phosphorene along zigzag direction ranges from 30 $\text{W m}^{-1} \text{K}^{-1}$ to 152.7 $\text{W m}^{-1} \text{K}^{-1}$, while that along armchair direction ranges from 9.9 $\text{W m}^{-1} \text{K}^{-1}$ to 63.9 $\text{W m}^{-1} \text{K}^{-1}$ [35, 50–52]. The huge deviation might be due to the different calculation methods or parameters. For example, Jain et al. calculated the thermal conductivity using similar iterative method based on ALD/BTE as employed in this work, and the test for the convergence of thermal conductivity was performed with respect to the interactions cutoff [54]. However, the thermal conductivity does not show a distinct convergence trend versus the interactions cutoff while jumps in a quite wide range, which might lie in that: (1) the lacking of long-range electrostatic interactions in their work, which are taken into account by adding to the dynamical matrix a correction

from dielectric tensor and Born effective charges; (2) the scalar relativistic pseudopotential used in their work does not involve the van der Waals interactions, which are considered having significant effect on the properties of bulk BP and phosphorene [31, 56]. In another work by Zhu et al. [53] based on RTA, the interactions range of third-order Interatomic force constants (IFCs) is truncated up to 4.4 Å, with which the interaction is only taken into account up to 7th nearest neighbors. Therefore, to end the confusing situation, it is necessary to perform systematic study to precisely quantify the phonon transport properties of phosphorene, which would be of significance to its further applications in nano-/opto-electronics and thermoelectrics (**Figure 3**).

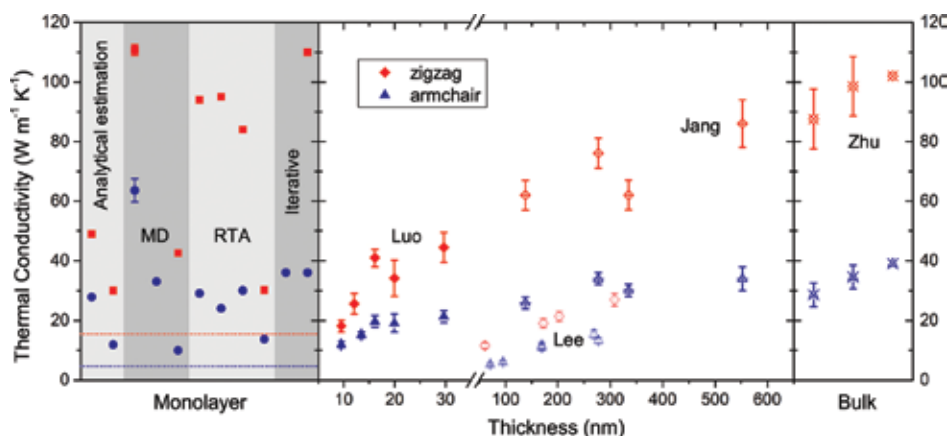


Figure 3. The comparison of the thermal conductivity obtained from experiments and theoretically reported results. The left box shows the thermal conductivity of monolayer phosphorene from different methods [35, 45, 49–55]. The middle box shows the thermal conductivity of phosphorene films with different thicknesses from experiments [46–48]. The right box shows the thermal conductivity of bulk BP from both experiment and theoretical calculation [45].

The thermal conductivity of monolayer phosphorene is in the same order of magnitude as that of silicene ($\sim 20 \text{ W m}^{-1} \text{ K}^{-1}$) [21–24, 28], while two orders of magnitude lower than that of graphene ($3000\text{--}5000 \text{ W m}^{-1} \text{ K}^{-1}$) [9, 11]. The thermal conductivity is mainly contributed by phonon modes below the gap which separates the phonon branches into two regions with each region containing six branches. The phonon modes in the region below the gap contribute more than 85% to the thermal conductivity, and dominate the anisotropy. The thermal conductivity along armchair direction is mainly contributed by LA, while along zigzag direction, TA/FA also contribute a lot to the thermal conductivity besides LA. The contributions to thermal conductivity along zigzag and armchair directions from FA are 16% and 8% at room temperature, respectively, which is close to that of silicene (7.5%) but much smaller than that of graphene (75%) [11, 23]. As for graphene, because of the reflectional symmetry of the structure, the phonon scattering processes involving odd number of FA modes are not allowed, which is the so-called symmetry-based phonon-phonon scattering selection rule [9]. Compared with graphene, the symmetry-based phonon-phonon scattering selection rule is broken by the hinge-like structure of phosphorene, resulting in a large scattering rate of FA,

which thus leads to its small contribution to the thermal conductivity. Note that FA contributes to the thermal conductivity along zigzag direction more than that along armchair direction. The reason might lie in the feature of the hinge-like structure that it is more “uneven” along armchair direction because of the up and down of the sublayers chains.

3. Effect of different physical factors

3.1. Length dependence

As for the length dependence of the thermal conductivity of silicene, regarding the convergence with respect to the q mesh, it seems that for infinite size (without boundary scattering), the thermal conductivity tends to diverge with denser q mesh, while for finite size the thermal conductivity converges. The possible divergence of thermal conductivity for 2D materials has raised a lot of debate recently. For example, in [23] it was claimed that the thermal conductivity of silicene would diverge with the sample size. Similar conclusions have been drawn in some other literature for graphene [57]. However, there have been strong debates on the possible divergence of thermal conductivity of graphene. On the other hand, Fugallo et al. argue that the thermal conductivity of graphene converges when the simulated sampling size goes up to 1 mm [58]. In their work, exact phonon BTE is solved and first-principles calculations are employed to extract harmonic and anharmonic IFCs. Barbarino et al. also reach the same conclusion with approach-to-equilibrium molecular dynamics simulations for graphene sample of 0.1 mm in size [59]. By using a finite q mesh, the extremely long wavelength acoustic phonon modes are actually excluded, which are believed to be responsible for the possible divergence of the thermal conductivity [57]. For finite sample size, the boundary scattering imposes a limit on the phonon mean free path (MFP) to avoid divergence. For real applications, a finite sample has to be used, and the wrinkles and defects are generally unavoidable, so the sample cannot have diverged thermal conductivity.

As for monolayer phosphorene, Zhu et al. claimed that there exists a compelling coexistence of size-dependent and size-independent thermal conductivities along zigzag and armchair directions, respectively [53], which is distinctly different from isotropic and divergent thermal conductivities in two-dimensional graphene and silicene. The size-dependent thermal conductivity is due to the lifetime of acoustic phonon modes quickly blowing up approaching the Γ point of the Brillouin zone [57]. The contributions of FA, TA, LA, and optical phonon modes to the total thermal conductivity are plotted to further understand the dependence of κ_{zz} on the size of the q mesh. It is found that the thermal conductivities contributed by FA, LA, and all optical phonons do not change with the increasing size of the q mesh. The divergent κ_{zz} is mainly due to the contribution from TA branch.

3.2. Strain

Despite recent efforts to describe the properties of unstrained materials, in real applications, nanoscale devices usually contain residual strain after fabrication [60]. It is thus important to

investigate possible strain effects on the properties of materials, especially phonon transport properties.

As for graphene, the application of tensile strain will give three noticeable changes that can affect κ : (1) lowered TO and LO phonon branches; (2) linearized zone-center ZA phonon branch; (3) weakened anharmonic IFCs [11]. Full solution of the BTE gives κ relatively strain independent up to 1% isotropic strain, which is a balanced result of the following aspects. With the increase of tensile strain, the ZA branch near the zone center becomes linear with increasing slope, leading to the increase of near zone center ZA phonon velocities and the decrease of density of ZA phonons. The character of the acoustic phonon-phonon scattering also changes due to these changes of the phonon dispersion. In addition, the tensile strain weakens the anharmonic IFCs, which acts to increase κ , but this is balanced by the changes in the phonon dispersion that tend to decrease κ . Furthermore, the lowered TO and LO branches play only a minor role in reducing κ through increased *acoustic + acoustic* \leftrightarrow *optic* three-phonon scattering.

It was found that a mechanical tensile strain less than 5% could tune the electronic structure of silicene [61] and larger tensile strain (7.5%) could induce a semimetal-metal transition [62]. On the other hand, using first-principles it has been demonstrated that the silicene structure remains buckled even when 12.5% tensile strain is applied [62, 63]. In comparison to the structural and electronic properties, the strain effect on the lattice thermal conductivity of silicene is also investigated. Pei et al. [64] and Hu et al. [22] investigated the effect of uniaxial strain on the thermal conductivity based on the classical NEMD method. Pei et al. studied tensile strain up to 12% and concluded that the thermal conductivity first increases slightly (around 10% increment) and then decreases with an increased amount of tensile strain. Hu et al. found that the thermal conductivity of silicene sheet and silicene nanoribbon experiences monotonic increase by a factor of two with tensile strain up to 18%. The modified embedded-atom method (MEAM) [65] and original Tersoff potential [66] were used in their simulations, respectively. However, both potentials are developed for bulk silicon, thus directly applying those potentials to the new 2D silicene structure is questionable. For example, the Tersoff potential cannot even reproduce the buckled structure of silicene and the MEAM potential seems to overestimate the buckling distance. It is well known that the interatomic potential directly determines the quality of classical molecular dynamics simulation. Therefore, in order to precisely predict the strain effect on the lattice thermal conductivity of silicene and identify the underlying mechanism, it is necessary to calculate the lattice thermal conductivity of silicene under different strains using a more accurate method.

The strain-dependent thermal conductivity of monolayer silicene was recently studied based on single mode RTA and iterative solution of the BTE by Xie et al. [28], where the harmonic and anharmonic force constants are determined using first-principles calculations. Both methods yield a similar trend in the change of thermal conductivity with respect to tensile strain. It is shown that within 10% tensile strain, the thermal conductivity of silicene first increases dramatically and then decreases slightly. The maximum thermal conductivity was found when 4% tensile strain was applied, and the value was about 7.5 times that of the unstrained case. Such a dramatic change is quite unusual for solid materials, and could be used

as a thermal switch together with thermal diodes to build thermal circuits. This trend is mainly due to the strain-dependent phonon lifetime, which is related to the variations of both harmonic and anharmonic force constants under strain. FA phonon lifetimes increase significantly under tensile strain because the structure becomes more planar, which leads to a large increase of their contribution to overall thermal conductivity, but is not the major reason for the significant change of overall thermal conductivity within 4% strain. The significant enhancement of thermal conductivity from 0 to 4% strain is mainly due to the reduced scattering of TA and LA phonons with FA phonons. The result suggests that other 2D materials with intrinsic buckling may have similar strain dependence of thermal conductivity, which is left for further investigation. Almost at the same time, Kuang et al. used a similar method to study the phonon transport properties of silicene with strain applied, and obtained similar results [29]. They also found a strong size dependence of κ for silicene with tensile strain, i.e., divergent κ with increasing system size. However, based on their calculations, the intrinsic room temperature κ for unstrained silicene converges with system size to 19.34 W/mK at 178 nm. They analyzed that the convergence behavior of thermal conductivity may be significantly affected by the out-of-plane acoustic phonon branch. The divergence of thermal conductivity with respect to system size is resulted from the linear behavior of FA at low frequencies, which is very different from the familiar quadratic nature for the corresponding branch in unstrained graphene. The origin of the size effect stems from nonzero contributions of FA modes at the long wavelength limit. Although physically this still demands further careful investigation, technologically speaking, using a larger supercell for the calculations of harmonic IFCs and the phonon dispersion should effectively suppress the divergence of thermal conductivity with respect to system size.

As for phosphorene, the strain effect on the thermal conductance was studied by Ong et al. using the first-principles-based non-equilibrium Green's function (NEGF) method, which yields the thermal transport behavior in the ballistic limit [67]. They find that the thermal conductance anisotropy with the orientation can be tuned by applying strain. In particular, the thermal conductance of phosphorene in zigzag direction is found to be enhanced when the strain is applied, but decreases when the strain is applied in the armchair direction; whereas the thermal conductance in armchair direction always decreases regardless of the strain direction.

Besides, Zhang et al. performed NEMD simulations to study the strain effect on the thermal conductivity of phosphorene [52]. The results show a clear trend that the thermal conductivity increases with the tensile strain and decreases with the compressive strain, which can be explained from the buckling deformation and is consistent with that of graphene. Moreover, the thermal conductivity along the zigzag direction increases slightly when the tensile strain is 0.01, and thereafter reaches a plateau until the strain level of 0.04, which may be attributed to the tension-induced elongation of the phosphorene sample.

3.3. Thickness dependence

For the thermal conductivity of few-layer films, there are two aspects affecting the phonon transport: (1) intrinsic properties of few layers, that is, crystal anharmonicity; (2) extrinsic

effects such as phonon-boundary or defect scattering. The optothermal Raman study found that κ of suspended uncapped few-layer graphene decreases with increasing number of layers, approaching the bulk graphite limit, which was explained by considering the intrinsic quasi-2D crystal properties described by the phonon Umklapp scattering. As the thickness increases, the phonon dispersion changes and more phase-space states become available for phonon scattering, resulting in the decrease of thermal conductivity. The small thickness (< 4) also means that phonons do not have a transverse component of group velocity, leading to weak phonon scattering from the top and bottom boundaries, especially if constant n is maintained over the whole area of the flake. The boundary scattering will increase if $n > 4$, because the transverse component of the group velocity is not equal to zero, and it is harder to maintain constant n through the whole area of an FLG flake, resulting in κ below the graphite limit. The graphite value recovers for thicker films.

The layer effect on the thermal conductivity of phosphorene was studied by Zhang et al. based on NEMD simulations [52]. It was found that the thermal conductivities along the two in-plane directions are insensitive to the number of layers, which is in sharp contrast to that of graphene, as it was shown that the thermal conductivity in multi-layer graphene decreases with increasing layer number. The underlying physical origin of the layer-independent thermal conductivity of multi-layer phosphorene was explained that unlike graphene with only one-atom thickness, the atoms in single-layer phosphorene are arranged in two sub-layers and formed a puckered geometry, which hinders the out-of-plane (flexural) phonon mode and thus diminishes the layer effect in multi-layer phosphorene. It is worth pointing out that the Lennard-Jones (LJ) potential is used for the van der Waals (vdW) interactions across different layers in multi-layer phosphorene in their work. Based on the studies of Qiao et al. and Hu et al. [31, 56], as confirmed with the real-space wave functions, the coupling between layers in few-layer black phosphorus is mediated by interactions that are much stronger than van der Waals (vdW) as in graphene or TMDCs. Considering the significant effect of interlayer interactions on the thermal conductivity, the use of vdW to quantify the interactions in the MD is questionable. Further works based on accurate first-principles calculations are needed to address the layer-dependent thermal conductivity of few-layers black phosphorus (phosphorene) in detail, which is ongoing in our group currently.

3.4. Effect of substrate

Supported silicene is, in fact, a common form in realistic applications. For example, it can be transferred onto an insulating substrate and gated electrically. The effects of different substrates on the thermal transport of silicene were studied by Zhang et al. recently based on NEMD simulations using the optimized SW potential for silicene [68]. They observe that the thermal conductivity of silicene can be bilaterally changed with different surface crystal plane of the substrate. The phenomenon found here is fundamentally different from our general understanding of monolayer graphene supported on substrate, where the substrate always has a negative effect on the in-plane thermal transport. The discrepancy between monolayer graphene and silicene can be explained in terms of different effects induced by the substrate on the phonon transport, specifically, the competition between the out-of-plane flexural modes

and the in-plane modes. This mechanism is further linked to the different atomic structure, i.e., for graphene, it is planar (no buckling distance), while silicene has a buckling distance of about 0.42 Å. By performing phonon polarization and spectral energy density (SED) analysis, the authors further revealed the underlying physics of the novel phenomenon in terms of the different impacts on the dominant phonons in the thermal transport of silicene induced by the substrate. These results indicate that by choosing different substrates, the thermal conductivity of 2D silicene can be largely tuned, which paves the way for manipulating the thermal transport properties of silicene for future emerging applications.

Very recently, the thermal conductivity of silicene supported in an amorphous silicon dioxide (SiO₂) for temperature ranging from 300 to 900 K was studied by Wang et al. from MD simulations [69]. They found that the thermal conductivity of silicene has a substantial reduction with increasing temperature, and putting silicene on amorphous SiO₂ leads to 78% reduction in the overall thermal conductivity of silicene at room temperature. They further compared model-level phonon properties, such as phonon relaxation times and phonon mean free paths (MFPs) of freestanding and supported silicene at 300 K. It is found that the phonon relaxation time in the case of supported silicene is reduced from 1–13 ps to 1 ps, and corresponding MFPs decrease from 10–120 nm to 0–20 nm. The thermal conductivities of freestanding and supported silicene are mainly (more than 85%) contributed by the longitudinal and transverse acoustic phonons, while the out-of-plane acoustic phonons have a negligible contribution of less than 3%. These results are in line with those found previously [68].

4. Heterostructures

In electronics, especially for nanoelectronics, interfacial thermal resistance is a key factor that affects heat dissipation in devices and researchers have shown that the interfacial thermal transport can be largely enhanced using graphene-based nanocomposites as thermal interface materials. Graphene and its bilayer structure are the two-dimensional crystalline forms of carbon, whose extraordinary electron mobility and other unique features hold great promise for nanoscale electronics and photonics. Their realistic applications in emerging nanoelectronics usually call for thermal transport manipulation in a controllable and precise manner. Equilibrium molecular dynamics simulations were performed by Zhang et al. to investigate the effect of interlayer *sp*³ bonding density on the thermal conductivity of bilayer graphene, especially the results of the randomly and regularly bonded bilayer graphene structures were compared in detail [70]. The thermal conductivity of randomly bonded bilayer graphene decreases monotonically with the increase of interlayer bonding density, which follows the same trend as that obtained in the literature. However, for the regularly bonded bilayer graphene structure, They observed the unexpected non-monotonic interlayer bonding density dependence of thermal conductivity. The phonon spectral energy density, participation ratio, and mode weight factor analyses were performed to explore the underlying mechanism of this counterintuitive phenomenon. It is found that the lifetimes of low-frequency (<5 THz) phonons for randomly and regularly bonded bilayer graphene are nearly the same, which is consistent with the general knowledge that the low-frequency phonons are not sensitive to the detailed

interfacial bonding configuration, considering that the characteristic size of the covalent bonding is in the order of only a few angstroms, which is much shorter than the typical wavelength of the low frequency phonons. In contrast, for medium-frequency (5–30 THz) and high-frequency (30–50 THz) phonons, the lifetimes in the regularly bonded bilayer graphene are quite larger than that of randomly bonded structure, especially for the medium-frequency phonon modes which have a rather large contribution to the higher thermal conductivity of the regularly bonded bilayer graphene than the randomly bonded structure. By evaluating the relative importance of the contributions of phonon lifetime and square of phonon group velocity, we conclude that compared with random bonding, the much higher thermal conductivity of the regularly bonded bilayer graphene is mainly due to the large enhancement in the group velocity of the phonon modes in the medium-frequency range (5–30 THz). In addition, the thermal conductivity of bilayer graphene depends not only on the interlayer bonding density, but also the detailed topological arrangement of the interlayer sp^3 bonds. Comparing the regularly bonded bilayer graphene between different bonding densities, the change of phonon lifetime, instead of the change of group velocity, is the main reason for the non-monotonic thermal conductivity dependence. The phonon mode localization is characterized by calculating the participation ratio and provides evidence that the participation ratio at different bonding density resembles the non-monotonic dependent thermal conductivity. Again this can be correlated with their atomic structure, where the regular bonding density of 6.25% and 12.5% has more homogeneous sp^3 bonding than that of other bonding densities, which should be responsible for their different phonon band structure.

5. Concluding remarks and perspectives

The present chapter has surveyed the recent advancements in understanding the phonon transport properties of some representative two-dimensional materials, which are one of the fastest growing emerging fields in nanostructured semiconductors and nanocrystals. The thriving expansion of new capabilities of two-dimensional semiconductors has progressed rapidly during the last few years. While physical fundamentals for electronic properties of this class of nanomaterials have been well understood and explored extensively, limited understanding has been achieved in thermal transport properties. Although most of two-dimensional materials have as simple as honeycomb lattice structure, revealing the phonon transport mechanism in such atomic thin materials seems not an easy task. Phonon transport in graphene is the first success in this line. However, the previous understanding achieved for graphene cannot be straightforwardly extended to other similar two-dimensional materials. In this chapter, we demonstrated a comparative study of the phonon transport properties between graphene, silicene, and phosphorene and found that these three materials could have fundamentally different governing mechanism in heat conduction. We also analyze the detailed mechanism from different aspects.

Despite the significant accomplishment that has been gained in understanding different behavior of phonon transport in two-dimensional materials in the last few years, some important physical fundamentals still remain to be clarified. For example, the thickness-

dependent thermal conductivity of few-layer two-dimensional structures and phonon interactions between two-dimensional monolayer and substrate demand further systematic study. In addition, the two-dimensional materials-based heterostructures could possess even more diverse and fantastic phonon transport behavior, which could open up new building blocks for the next generation of advanced functional 3D devices.

Acknowledgements

The authors acknowledge the support by the Deutsche Forschungsgemeinschaft (DFG) (project number: HU 2269/2-1).

Author details

Guangzhao Qin¹ and Ming Hu^{1,2*}

*Address all correspondence to: hum@ghi.rwth-aachen.de

1 Institute of Mineral Engineering, Division of Materials Science and Engineering, Faculty of Georesources and Materials Engineering, RWTH Aachen University, Aachen, Germany

2 Aachen Institute for Advanced Study in Computational Engineering Science (AICES), RWTH Aachen University, Aachen, Germany

References

- [1] Novoselov, K. S. et al. Electric field effect in atomically thin carbon films. *Science*, 2004;306:666–669. DOI: 10.1126/science.1102896
- [2] Seol, J. H. et al. Two-dimensional phonon transport in supported graphene. *Science*, 2010;328:213–216. DOI: 10.1126/science.1184014
- [3] Xu, X. et al. Length-dependent thermal conductivity in suspended single-layer graphene. *Nat. Commun.*, 2014;5:4689. DOI: 10.1038/ncomms4689
- [4] Tao, L. et al. Silicene field-effect transistors operating at room temperature. *Nat. Nano*, 2015;10:227–231. DOI: 10.1038/nnano.2014.325
- [5] Balandin, A. A. et al. Superior thermal conductivity of single-layer graphene. *Nano Lett.*, 2008;8:902–907. DOI: 10.1021/nl0731872
- [6] Balandin, A. A. Thermal properties of graphene and nanostructured carbon materials. *Nat. Mater.*, 2011;10:569–581. DOI: 10.1038/nmat3064

- [7] Klemens, P. G. Theory of thermal conduction in thin ceramic films. *Int. J. Thermophys.*, 2001;22:265–275. DOI: 10.1023/A:1006776107140
- [8] Klemens, P. G. Theory of the a-plane thermal conductivity of graphite. *J. Wide Bandgap Mater.*, 2000;7:332–339. DOI: 10.1106/7FP2-QBLN-TJPA-NC66
- [9] Lindsay, L., Broido, D. A. & Mingo, N. Flexural phonons and thermal transport in graphene. *Phys. Rev. B*, 2010;82:115427. DOI: 10.1103/PhysRevB.82.115427
- [10] Lindsay, L., Broido, D. A. & Mingo, N. Flexural phonons and thermal transport in multilayer graphene and graphite. *Phys. Rev. B*, 2011;83:235428. DOI: 10.1103/PhysRevB.83.235428
- [11] Lindsay, L. et al. Phonon thermal transport in strained and unstrained graphene from first principles. *Phys. Rev. B*, 2014;89:155426. DOI: 10.1103/PhysRevB.89.155426
- [12] Drummond, N. D., Zlyomi, V. & Fal'ko, V. I. Electrically tunable band gap in silicene. *Phys. Rev. B*, 2012;85:075423. DOI: 10.1103/PhysRevB.85.075423
- [13] Ni, Z. et al. Tunable bandgap in silicene and germanene. *Nano Lett.*, 2012;12:113–118. DOI: 10.1021/nl203065e
- [14] Kaloni, T. P., Cheng, Y. C. & Schwingenschlgl, U. Hole doped dirac states in silicene by biaxial tensile strain. *J. Appl. Phys.*, 2013;113:104305. DOI: 10.1063/1.4794812
- [15] Aufray, B. et al. Graphene-like silicon nanoribbons on Ag(1 1 0): a possible formation of silicene. *Appl. Phys. Lett.*, 2010;96:183102. DOI: 10.1063/1.3419932
- [16] Meng, L. et al. Buckled silicene formation on Ir(1 1 1). *Nano Lett.*, 2013;13:685–690. DOI: 10.1021/nl304347w
- [17] Lalmi, B. et al. Epitaxial growth of a silicene sheet. *Appl. Phys. Lett.*, 2010;97:223109. DOI: 10.1063/1.3524215
- [18] Nguyen, N.-T. Silicene transistors: silicon-based nanoelectronics from a single atom layer. *Micro Nanosyst.*, 2014;6:205–206. DOI: 10.2174/187640290604150302115649
- [19] Lian, C. & Ni, J. The effects of thermal and electric fields on the electronic structures of silicene. *Phys. Chem. Chem. Phys.*, 2015;17:13366. DOI: 10.1039/C5CP01557J
- [20] Schwierz, F., Pezoldt, J. & Granzner, R. Two-dimensional materials and their prospects in transistor electronics. *Nanoscale*, 2015;7:8261–8283. DOI: 10.1039/C5NR01052G
- [21] Zhang, X. et al. Thermal conductivity of silicene calculated using an optimized Stillinger-Weber potential. *Phys. Rev. B*, 2014;89:054310. DOI: 10.1103/PhysRevB.89.054310
- [22] Hu, M., Zhang, X. & Poulidakos, D. Anomalous thermal response of silicene to uniaxial stretching. *Phys. Rev. B*, 2013;87:195417. DOI: 10.1103/PhysRevB.87.195417

- [23] Gu, X. & Yang, R. First-principles prediction of phononic thermal conductivity of silicene: a comparison with graphene. *J. Appl. Phys.*, 2015;117(2):025102. DOI: 10.1063/1.4905540
- [24] Xie, H., Hu, M. & Bao, H. Thermal conductivity of silicene from first-principles. *Appl. Phys. Lett.*, 2014;104:131906. DOI: 10.1063/1.4870586
- [25] Lindsay, L. & Broido, D. A. Three-phonon phase space and lattice thermal conductivity in semiconductors. *J. Phys.: Condens. Matter*, 2008;20(16):165209. DOI: 10.1088/0953-8984/20/16/165209
- [26] Li, W. et al. Thermal conductivity of diamond nanowires from first principles. *Phys. Rev. B*, 2012;85:195436. DOI: 10.1103/PhysRevB.85.195436
- [27] Li, W., Lindsay, L., Broido, D. A., Stewart, D. A. & Mingo, N. Thermal conductivity of bulk and nanowire $\text{mg}_2\text{sixsn}1\text{x}$ alloys from first principles. *Phys. Rev. B*, 2012;86:174307. DOI: 10.1103/PhysRevB.86.174307
- [28] Xie, H. et al. Large tunability of lattice thermal conductivity of monolayer silicene via mechanical strain. *Phys. Rev. B*, 2016;93:075404. DOI: 10.1103/PhysRevB.93.075404
- [29] Kuang, Y. D., Lindsay, L., Shi, S. Q. & Zheng, G. P. Tensile strains give rise to strong size effects for thermal conductivities of silicene, germanene and stanene. *Nanoscale*, 2016;8:3760–3767. DOI: 10.1039/C5NR08231E
- [30] Rodin, A. S., Carvalho, A. & Castro Neto, A. H. Strain-induced gap modification in black phosphorus. *Phys. Rev. Lett.*, 2014;112:176801. DOI: 10.1103/PhysRevLett.112.176801
- [31] Qiao, J., Kong, X., Hu, Z.-X., Yang, F. & Ji, W. High-mobility transport anisotropy and linear dichroism in few-layer black phosphorus. *Nat. Commun.*, 2014;5(4475):4475. DOI: 10.1038/ncomms5475
- [32] Churchill, H. O. H. & Jarillo-Herrero, P. Two-dimensional crystals: Phosphorus joins the family. *Nat. Nanotech.*, 2014;9(5):330–331. DOI: 10.1038/nnano.2014.85
- [33] Liu, H. et al. Phosphorene: an unexplored 2D semiconductor with a high hole mobility. *ACS Nano*, 2014;8(4):4033–4041. DOI: 10.1021/nn501226z
- [34] Li, L. et al. Black phosphorus field-effect transistors. *Nat. Nanotech.*, 2014;9(5):372–377. DOI: 10.1038/nnano.2014.35
- [35] Fei, R. et al. Enhanced thermoelectric efficiency via orthogonal electrical and thermal conductances in phosphorene. *Nano Lett.*, 2014;14:6393–6399. DOI: 10.1021/nl502865s
- [36] Xia, F., Wang, H. & Jia, Y. Rediscovering black phosphorus as an anisotropic layered material for optoelectronics and electronics. *Nat. Commun.*, 2014;5(4458):4458. DOI: 10.1039/C4CC05752J

- [37] Low, T., Engel, M., Steiner, M. & Avouris, P. Origin of photoresponse in black phosphorus phototransistors. *Phys. Rev. B*, 2014;90:081408. DOI: 10.1103/PhysRevB.90.081408
- [38] Koenig, S. P., Doganov, R. A., Schmidt, H., Castro Neto, A. H. & Zyilmaz, B. Electric field effect in ultrathin black phosphorus. *Appl. Phys. Lett.*, 2014;104(10):103106. DOI: 10.1063/1.4868132
- [39] Tran, V., Soklaski, R., Liang, Y. & Yang, L. Layer-controlled band gap and anisotropic excitons in few-layer black phosphorus. *Phys. Rev. B*, 2014;89:235319. DOI: 10.1103/PhysRevB.89.235319
- [40] Wei, Q. & Peng, X. Superior mechanical flexibility of phosphorene and few-layer black phosphorus. *Appl. Phys. Lett.*, 2014;104(25):251915. DOI: 10.1063/1.4885215
- [41] Jiang, J.-W. & Park, H. S. Negative poisson's ratio in single-layer black phosphorus. *Nat. Commun.*, 2014;5(4727):4727. DOI: 10.1038/ncomms5727
- [42] Qin, G. et al. Hinge-like structure induced unusual properties of black phosphorus and new strategies to improve the thermoelectric performance. *Sci. Rep.*, 2014;4(6946):6946. DOI: 10.1039/C4CP04858J
- [43] Lv, H. Y., Lu, W. J., Shao, D. F. & Sun, Y. P. Enhanced thermoelectric performance of phosphorene by strain-induced band convergence. *Phys. Rev. B*, 2014;90:085433. DOI: 10.1103/PhysRevB.90.085433
- [44] Zhu, Z. & Tománek, D. Semiconducting layered blue phosphorus: A computational study. *Phys. Rev. Lett.*, 2014;112:176802. DOI: 10.1103/PhysRevLett.112.176802
- [45] Zhu, J. et al. Revealing the origins of 3d anisotropic thermal conductivities of black phosphorus. *Adv. Electron. Mater.*, 2016;1600040. DOI: 10.1002/aelm.201600040
- [46] Luo, Z. et al. Anisotropic in-plane thermal conductivity observed in few-layer black phosphorus. *Nat. Commun.*, 2015;6:9572. DOI: 10.1038/ncomms9572
- [47] Lee, S. et al. Anisotropic in-plane thermal conductivity of black phosphorus nanoribbons at temperatures higher than 100 K. *Nat. Commun.*, 2015;6:9573. DOI: 10.1038/ncomms9573
- [48] Jang, H., Wood, J. D., Ryder, C. R., Hersam, M. C. & Cahill, D. G. Anisotropic thermal conductivity of exfoliated black phosphorus. *Adv. Mater.*, 2015;27:8017–8022. DOI: 10.1002/adma.201503466
- [49] Liu, T.-H. & Chang, C.-C. Anisotropic thermal transport in phosphorene: effects of crystal orientation. *Nanoscale*, 2015;7:10648–10654. DOI: 10.1039/C5NR01821H
- [50] Hong, Y., Zhang, J., Huang, X. & Zeng, X. C. Thermal conductivity of a two-dimensional phosphorene sheet: a comparative study with graphene. *Nanoscale*, 2015;7:18716–18724. DOI: 10.1039/C5NR03577E

- [51] Xu, W., Zhu, L., Cai, Y., Zhang, G. & Li, B. Direction dependent thermal conductivity of monolayer phosphorene: parameterization of Stillinger-Weber potential and molecular dynamics study. *J. Appl. Phys.*, 2015;117:214308. DOI: 10.1063/1.4922118
- [52] Zhang, Y.-Y., Pei, Q.-X., Jiang, J.-W., Wei, N. & Zhang, Y.-W. Thermal conductivities of single- and multi-layer phosphorene: a molecular dynamics study. *Nanoscale*, 2016;8:483–491. DOI: 10.1039/C5NR05451F
- [53] Zhu, L., Zhang, G. & Li, B. Coexistence of size-dependent and size-independent thermal conductivities in phosphorene. *Phys. Rev. B*, 2014;90:214302. DOI: 10.1103/PhysRevB.90.214302
- [54] Jain, A. & McGaughey, A. J. H. Strongly anisotropic in-plane thermal transport in single-layer black phosphorene. *Sci. Rep.*, 2015;5(8501):8501. DOI: 10.1039/C5NR04366B
- [55] Qin, G. et al. Anisotropic intrinsic lattice thermal conductivity of phosphorene from first principles. *Phys. Chem. Chem. Phys.*, 2015;17:4854. DOI: 10.1039/C4CP04858J
- [56] Hu, Z.-X., Kong, X., Qiao, J., Normand, B. & Ji, W. Interlayer electronic hybridization leads to exceptional thickness-dependent vibrational properties in few-layer black phosphorus. *Nanoscale*, 2016;8:2740–2750. DOI: 10.1039/C5NR06293D
- [57] Bonini, N., Garg, J. & Marzari, N. Acoustic phonon lifetimes and thermal transport in free-standing and strained graphene. *Nano Lett.*, 2012;12:2673–2678. DOI: 10.1021/nl202694m
- [58] Fugallo, G. et al. Thermal conductivity of graphene and graphite: Collective excitations and mean free paths. *Nano Lett.*, 2014;14:6109–6114. DOI: 10.1021/nl502059f
- [59] Barbarino, G., Melis, C. & Colombo, L. Intrinsic thermal conductivity in monolayer graphene is ultimately upper limited: a direct estimation by atomistic simulations. *Phys. Rev. B*, 2015;91:035416. DOI: 10.1103/PhysRevB.91.035416
- [60] Bhowmick, S. & Shenoy, V. B. Effect of strain on the thermal conductivity of solids. *J. Chem. Phys.*, 2006;125:164513. DOI: 10.1063/1.2361287
- [61] Yan, J.-A., Gao, S.-P., Stein, R. & Coard, G. Tuning the electronic structure of silicene and germanene by biaxial strain and electric field. *Phys. Rev. B*, 2015;91:245403. DOI: 10.1103/PhysRevB.91.245403
- [62] Xu, G. L., Wu, M. S., Ouyang, C. Y. & B. Strain-induced semimetal-metal transition in silicene. *Europhys. Lett. (EPL)*, 2012;99:17010. DOI: 10.1186/1556-276X-9-521
- [63] Lian, C. & Ni, J. Strain induced phase transitions in silicene bilayers: a first principles and tight-binding study. *AIP Adv.*, 2013;3:052102. DOI: 10.1063/1.4804246
- [64] Pei, Q.-X., Zhang, Y.-W., Sha, Z.-D. & Shenoy, V. B. Tuning the thermal conductivity of silicene with tensile strain and isotopic doping: a molecular dynamics study. *J. Appl. Phys.*, 2013;114:033526. DOI: 10.1063/1.4815960

- [65] Baskes, M. I. Modified embedded-atom potentials for cubic materials and impurities. *Phys. Rev. B*, 1992;46:2727–2742. DOI: 10.1103/PhysRevB.46.2727
- [66] Tersoff, J. Modeling solid-state chemistry: interatomic potentials for multicomponent systems. *Phys. Rev. B*, 1989;39:5566–5568. DOI: 10.1103/PhysRevB.39.5566
- [67] Ong, Z.-Y., Cai, Y., Zhang, G. & Zhang, Y.-W. Strong thermal transport anisotropy and strain modulation in single-layer phosphorene. *J. Phys. Chem. C*, 2014;118:25272–25277. DOI: 10.1021/jp5079357
- [68] Zhang, X., Bao, H. & Hu, M. Bilateral substrate effect on the thermal conductivity of two-dimensional silicon. *Nanoscale*, 2015;7:6014–6022. DOI: 10.1039/C4NR06523A
- [69] Wang, Z., Feng, T. & Ruan, X. Thermal conductivity and spectral phonon properties of free-standing and supported silicene. *J. Appl. Phys.*, 2015;117(8):084317. DOI: 10.1063/1.4913600
- [70] Zhang, X., Gao, Y., Chen, Y. & Hu, M. Robustly engineering thermal conductivity of bilayer graphene by interlayer bonding. *Sci. Rep.*, 2016;6:22011. DOI: 10.1038/srep22011

Mechanical Properties and Applications of Two-Dimensional Materials

Rui Zhang and Rebecca Cheung

Additional information is available at the end of the chapter

<http://dx.doi.org/10.5772/104209>

Abstract

Two-dimensional (2D) materials have attracted increasing attention recently due to their extraordinarily different material properties compared with conventional bulk materials. The 2D materials possess ultralow weight, high Young's modulus, high strength, outstanding carrier mobility, as well as high anisotropy between the in-plane and out-of-plane mechanical properties. The nearby atoms in the same plane of layered 2D materials are connected via covalent bonding, while the interlayers are stacked together via weak van der Waals interactions. In this article, we review the in-plane mechanical properties (including the in-plane Young's modulus, pretension, breaking strength/strain) and out-of-plane mechanical properties (including the perpendicular-to-plane Young's modulus, shear force constant, and shear strength) of different 2D materials, varying from conductors, semiconductors, to insulators. The different fabrication methods for suspended 2D material structures are presented. The experimental methods and principles for mechanical properties characterization are reviewed. A comparison of the mechanical properties among different 2D materials is summarized. Furthermore, electrical output change as a result of mechanical deformation (piezoresistive and piezoelectric effects) is introduced briefly. By exploiting the unique mechanical and mechanoelectric transduction properties, 2D materials can be used in wide-ranging applications, including flexible electronics, strain sensors, nanogenerators, and innovative nanoelectromechanical systems (NEMS).

Keywords: 2D materials, mechanical properties, suspended structure, strain sensors, nanoelectromechanical systems (NEMS)

1. Introduction

Since the first successful preparation of graphene by mechanical exfoliation from graphite crystals in 2004 [1], two-dimensional (2D) materials have attracted dramatic attention due to their extraordinary physical properties (ultralow weight, high Young's modulus, and high strength) [2–7] and outstanding electrical properties [1] compared with conventional bulk materials. In the past few years, graphene, with the highest measured Young's modulus (~1 TPa) [3], is the most widely studied 2D material. Studies have shown that graphene filled into the polymer matrices can reinforce the mechanical properties of the composites significantly [8]. However, pristine graphene does not have a bandgap [9], which limits its applications in certain fields requiring a semiconducting material. As a potential substitute material of graphene, the transition metal dichalcogenides (TMDCs, e.g., MoS₂ and WSe₂) and black phosphorus (BP) with an intrinsic bandgap [10, 11] possess the potential for electronics and optoelectronics applications [12–15] and open a new field for 2D materials study. Moreover, the existence of piezoelectricity and the more sensitive piezoresistive effect in TMDCs compared with graphene under mechanical deformation make them more interesting for innovative applications including tactile strain sensors [16], nanogenerators [17], and advanced nanoelectromechanical systems (NEMS).

In this review, first, we introduce the common approaches used for fabricating suspended 2D material structures. Then, characterization methods for extracting the in-plane and out-of-plane mechanical properties of 2D materials are presented. A summary of the experimental results is given. In the last section, we introduce the electrical output change of 2D materials induced by mechanical deformation—piezoresistive and piezoelectric effects. In addition, we provide some example applications of 2D materials that make use of their extraordinary mechanical as well as mechanoelectric transduction properties.

2. Fabrication of suspended 2D materials

Generally, to measure the mechanical properties of 2D materials experimentally, a suspended structure needs to be fabricated. There are mainly two ways of fabricating a structure suspended with 2D materials. One approach is to transfer the 2D materials directly onto the prepatterned substrates [3, 7, 18–23]. The other approach is to transfer the 2D materials on the substrate first and then remove the sacrificial layer beneath the transferred 2D materials [24–31]. **Figure 1(a)** and **(b)** shows the two schematics of the first fabrication approach, while **Figure 1(c)** shows the second approach.

In the first approach, taking SiO₂/Si substrate for example, holes or cavities are patterned in the SiO₂ layer with lithography and wet/dry etching techniques, as shown in the first step of **Figure 1(a)**. Then, 2D materials are transferred onto the prepatterned SiO₂/Si substrate by the exfoliation method, forming suspended 2D materials structure (second step of **Figure 1(a)**). With this method, the suspended structure can be fabricated theoretically on various kinds of substrates. However, with the conventional mechanical exfoliation method, since the 2D

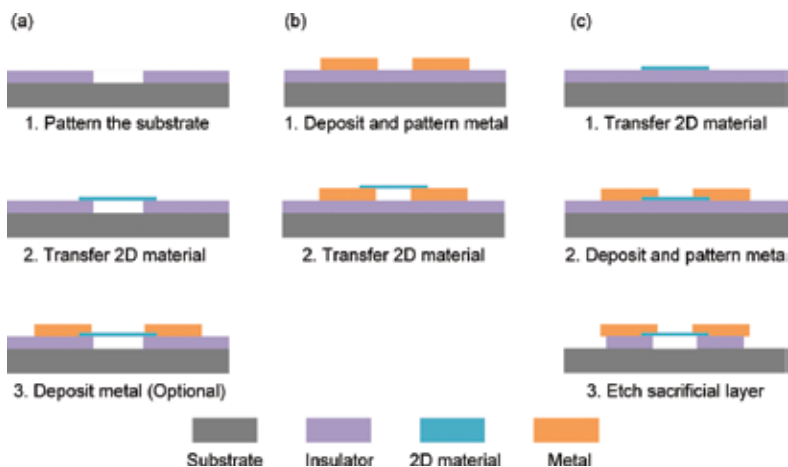


Figure 1. Schematic of two representative approaches of suspended structures fabrication. (a, b) Transfer of the 2D materials directly onto the prepatterned substrates; (c) Suspension of the 2D materials by etching the sacrificial layer underneath.

material sheets distribute randomly onto the substrates, the 2D material sheets may not cover necessarily the specific hole in the SiO₂ layers, bringing the challenge of improving the production rate. Normally, two methods can be employed to address this problem. One method is to fabricate repeatable patterns (e.g., hole arrays) in the substrate [3, 7, 22] to enhance the probability of producing the suspended structures, as shown in **Figure 2(a)**. Another method is to employ a modified exfoliation method (transfer printing/stamping [20, 32]), with a transparent viscoelastic material as the carrier for the 2D materials, which enables a precise transfer of 2D materials to the desirable location [19, 21].

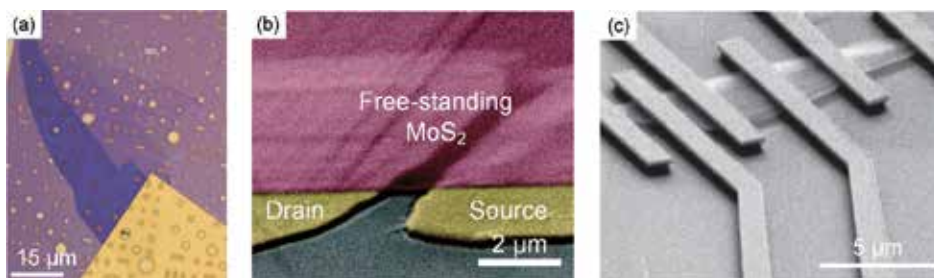


Figure 2. (a) Optical image of graphene suspended over hole arrays [35]. (b) SEM images of a MoS₂ bridge supported on Au electrodes [23]. (c) SEM image of suspended graphene stripe under Au electrodes [25].

In most cases, electrical signal needs to be applied to the suspended 2D materials; therefore, metal contacts need to be made to contact the suspended 2D materials, as shown in the third step of **Figure 1(a)**. In order to avoid the common wet process inducing the collapse of 2D membranes, the shadow mask method [27] instead of lithography should be used. In addition,

by combining conventional lithography, lift-off of deposited metal and transfer printing/stamping of 2D materials, one can realize the fabrication of suspended 2D materials supported on patterned metal contacts, as depicted in **Figures 1(b)** and **2(b)**.

The schematic of the second approach of fabricating a suspended 2D material structure is presented in **Figure 1(c)**. After the transfer of 2D material onto substrate and metal contacts deposition, the 2D material is suspended by etching the underlying sacrificial layer with the predeposited metal contacts acting as the etching mask and clamping of the 2D materials. In this method, SiO_2 has been used widely as the sacrificial layer, which is removed commonly by anisotropic wet etching with buffered hydrofluoric acid (BOE). In order to prevent the 2D materials from collapsing due to the surface tension between the 2D materials and BOE, the drying process is operated normally in a critical point dryer (CPD) [25, 29, 30]. In addition, the etching time needs to be adjusted carefully to control the undercut of SiO_2 beneath the metal contacts to prevent the metal from collapsing. Although a more complex structure can be fabricated with this approach, as shown in **Figure 2(b)**, the wet etching involved in the fabrication process may introduce some contamination in the 2D materials, which may degrade the performance of the devices. Moreover, the acids used in this process are not suitable for some 2D materials, such as Bi_2Se_3 [33] and metals (e.g., Ti, Al). Thus, to avoid acid etching in the fabrication process, photoresist can be used as the sacrificial layer instead of SiO_2 which can be removed with photoresist developers [33, 34].

3. Mechanical properties

As mentioned earlier, 2D materials possess high anisotropy between the in-plane and out-of-plane mechanical properties. In pristine-layered 2D materials, the nearby atoms in the same plane are bonded covalently with low defects density resulting in strong in-plane mechanical properties. While the interlayers are stacked together via weak van der Waals interactions, allowing layers to slide easily when shear stress is applied, the effect can give rise to lubrication properties. In this section, the experimental methods used to characterize the mechanical properties of 2D materials are introduced, and the corresponding empirical results are summarized.

3.1. In-plane properties

The in-plane mechanical properties (including the in-plane Young's modulus, pretension, and breaking strength/strain) of 2D materials have been studied extensively in bending experiments on suspended 2D sheets. In the bending experiments, atomic force microscope (AFM) is used widely to characterize the deformation of the suspended sheets under a certain amount of force. The force applied during the experiments can be divided into two categories: concentrated force and distributed force. In the following subsections, all the mechanical properties mentioned indicate the in-plane properties, unless stated otherwise.

3.1.1. Applying concentrated force

The indentation experiment conducted under AFM is one of the most popular methods for measuring the mechanical properties of 2D materials. In most cases, an AFM probe indents toward the center of the circular suspended 2D materials, as shown in **Figure 3(a)**. During the indentation, the displacement of piezoelectric scanner ΔZ (when the AFM probe starts to contact with the membrane) and the deflection of AFM probe d are recorded. The indentation depth at the center of a membrane can be determined by $\delta = \Delta Z - d$, and the force applied from the AFM tip onto the membrane can be derived from $F = k \times d$, where k is the spring constant of the AFM probe, which can be calibrated via a reference cantilever [36] or calculated using the Sader method [37, 38]. Then, the force F versus deformation δ curves of a suspended 2D material can be extracted, as shown in **Figure 3(b)**. When the radius of the AFM tip r_{tip} is far smaller than that of the hole r and the bending stiffness of the measured 2D material is negligible (monolayer or few-layer), the $F - \delta$ curves can be approximated using the Schwering-type solution, as Eq. (1) [3, 39, 40]:

$$F = (\sigma_0^{2D} \pi) \delta + \left(E^{2D} \frac{q^3}{r^2} \right) \delta^3, \quad (1)$$

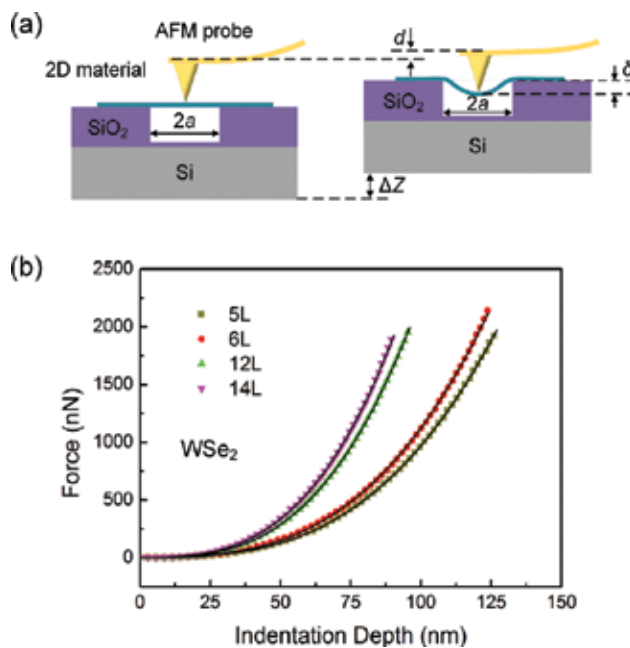


Figure 3. (a) Side view schematic of the indentation experiment on a suspended 2D membrane. (b) Representative force–deformation curves for multilayer WSe₂. The fitted curves using the Schwering-type solution agree well with the experimental results [42].

where σ_0^{2D} is the pretension, E^{2D} is the 2D elastic modulus, ν is the Poisson's ratio, and q is a dimensionless constant determined by $q = 1/(1.05 - 0.15\nu - 0.16\nu^2)$. By fitting the experimental curves with Eq. (1), the pretension σ_0^{2D} and 2D elastic modulus E^{2D} of the membranes can be derived. Due to the increasing thickness of 2D material (>15 nm) [41], the mechanical behavior of 2D materials undergoes a membrane-to-plate regime transition, and therefore, the bending stiffness should be taken into consideration by adding another term into Eq. (1), thus, forming a modified model [6] which gives a better estimation of the pretension σ_0^{2D} :

$$F = \left[\frac{4\pi E^{2D}}{3(1-\nu^2)} \cdot \left(\frac{t}{r} \right)^2 \right] \delta + (\sigma_0^{2D} \pi) \delta + \left(E^{2D} \frac{q^3}{r^2} \right) \delta^3, \quad (2)$$

where t is the thickness of the measured 2D material.

During an indentation experiment with a spherical indenter, the maximum stress for a circular and linear elastic membrane as a function of the applied force F can be derived with the expression as follows [43]:

$$\sigma_{\max}^{2D} = \sqrt{\frac{FE^{2D}}{4\pi r_{\text{tip}}}}, \quad (3)$$

where σ_{\max}^{2D} is the maximum stress at the center of the film (under the AFM tip). Thus, the breaking stress of the 2D material can be estimated by acquiring the force which breaks the 2D material during the indentation. Assuming the stress of the 2D material has a linear relationship with its strain, the breaking strain can be predicted by $\varepsilon_{\max} = \sigma_{\max}^{2D} / E^{2D}$.

Apart from the circular membrane, the indentation experiment can be operated also at the center of a beam-structured 2D material with two ends fixed [4, 44, 45]. In this case, the relation between applied force F and deformation at the center of the 2D material δ can be modeled with the expression [46]:

$$F = \frac{16E^{2D}wt^2}{l^3} \delta + \sigma_0^{2D} \delta + \frac{8wE^{2D}}{3l^3} \delta^3, \quad (4)$$

where l and w are the length and width of the suspended beam, respectively.

It is worth noting that it is extremely important to identify the zero displacement/force point precisely for nanoindentation experiments [47]. An inaccuracy of 2–5 nm in determining this point may lead to a 10% error in the extracted E^{2D} [35]. In order to compare the elastic properties of a particular 2D material with its bulk counterpart as well as other 2D materials, the 2D elastic modulus E^{2D} sometimes needs to be converted to the normal 3D Young's modulus E_Y by dividing the 2D value by the thickness of the 2D material t .

From the models of Eqs. (1), (2), and (4), we can see that the applied load has an approximate linear relationship with the indentation depth when the membrane deformation is small, and significantly follows a cubic relationship under large deformation. Thus, in the linear regime (small deformation of membrane), the effective spring constant of circular and beam-structured membrane can be extracted as

$$\begin{aligned}
 k_{\text{circular}} &= \frac{4\pi t^3}{3(1-\nu^2)r^2} E_Y + \sigma_0^{2D} \pi, \\
 k_{\text{beam}} &= \frac{16wt^3}{l^3} E_Y + \sigma_0^{2D}.
 \end{aligned}
 \tag{5}$$

By measuring the effective spring constant of the same kind of 2D material with different design, thickness t , or dimensions (r , w , or l), the Young's modulus E_Y and pretension σ_0^{2D} can be extracted. Note that this method is only valid under the assumption that E_Y and σ_0^{2D} are independent on the thickness or dimension of the 2D material, assumptions of which are under debate at present [48, 49].

3.1.2. Applying distributed force

Apart from the concentrated force applied with an indenter, distributed force (such as electrostatic force [50] or pressure force [51]) can be applied on suspended 2D material to measure the mechanical properties. In order to produce an electrostatic force, metal contacts need to be made on/below 2D membrane, so that a voltage can be applied between the membrane and the back-gate electrode, as shown in **Figure 4(a)** and **(b)**. Moreover, by creating a pressure difference between the inside of microcavities covered by the 2D membrane p_{int} and the outside atmosphere p_{ext} a pressure force Δp can be produced, as depicted in **Figure 4(c)** and **(d)**. The deformation of a membrane under distributed force can be characterized directly via tapping mode AFM (**Figure 4(e)**). In addition, by measuring the Raman shift of 2D material under loading and without loading, the local strain of 2D material can be extracted indirectly [49]. After building a specific mechanical model which describes the relationship of the deformation of the membrane due to the voltage bias [50] or pressure difference [51, 52], the mechanical properties can be extracted by fitting the experimental results with the appropriate model.

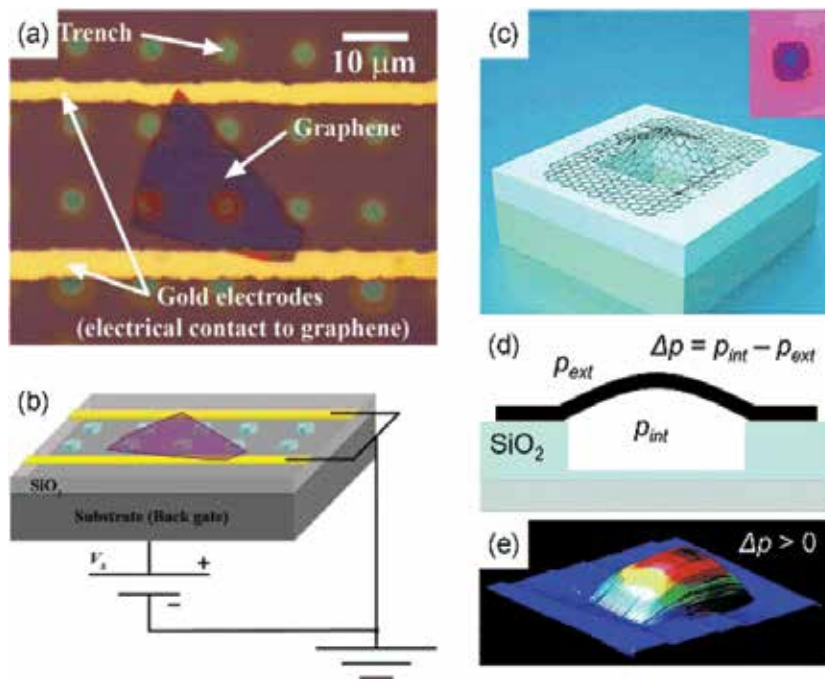


Figure 4. (a) Top view optical image of a graphene suspended over hole arrays. (b) Schematic of producing electrostatic force by applying a voltage V_s across the back gate and graphene [50]. (c) Schematic of a graphene-sealed microchamber. Inset: Optical image of a graphene membrane over a hole. (d) Side view schematic of the graphene-sealed microchamber. (e) Tapping mode AFM image of a graphene membrane with $\Delta p > 0$ [52].

3.1.3. Results summary

Table 1 summarizes the mechanical properties of 2D material families ranging from conductors (graphene), semiconductors (semiconducting TMDCs and BP), to dielectrics (graphene oxide [GO], mica, and h-BN). Overall, the Young's modulus of 2D materials is larger than that of the corresponding bulk materials, due to the lower crystal defects and interlayer stacking faults in 2D materials [6].

Material	Number of layers	Young's modulus (GPa)	Pretension (mN/m)	Breaking stress (GPa)	Breaking strain (%)	Characterization method	Ref.
Graphene (Mechanical exfoliated)	1	1000 ± 100	70–740	130 ± 10	~12	Indentation on circular membrane	[3]
	23–43	~1000	N/A	N/A	N/A	Electrostatic force	[50]
	4	930 ± 48	N/A	N/A	N/A	Pressurizing membranes	[52]
	1–5	1000 ± 31	N/A	N/A	N/A	Pressurizing membranes	[51]

Material	Number of layers	Young's modulus (GPa)	Pretension (mN/m)	Breaking stress (GPa)	Breaking strain (%)	Characterization method	Ref.
Graphene (Mechanical exfoliated + Ar plasma irradiation)	1, 2	2400 ± 400 (1 L) 2000 ± 500 (2 L)	N/A	N/A	N/A	Pressurizing membranes	[49]
	3–14	~800	N/A	N/A	N/A	Indentation on beam	[46]
	1	~1550	200–800	80–94	N/A	Indentation on circular membrane	[35]
	Graphene (GO reduced)	1	250 ± 150	N/A	N/A	N/A	Spring constant of beam
Graphene (CVD growth)	1	~157	~85	~35	N/A	Indentation on circular membrane	[55]
	1	~1000	N/A	~121 (small grains) ~140 (large grains)	N/A	Indentation on circular membrane	[56]
	1	~800	~100	~55	N/A	Indentation on circular membrane	[47]
MoS ₂ (Mechanical exfoliated)	1, 2	270 ± 100 (1 L) 200 ± 60 (2 L)	20–100	22 ± 4 (1 L) 21 ± 6 (2 L)	6–11	Indentation on circular membrane	[7]
	5–25	300 ± 10	0.15 ± 0.15	N/A	N/A	Spring constant of circular membrane	[59]
	5–25	330 ± 70	50 ± 20	N/A	N/A	Indentation on circular membrane	[6]
MoS ₂ (CVD growth)	1, 2	260 ± 18 (1 L) 231 ± 10 (2 L)	110 ± 40 (1 L)	N/A	N/A	Indentation on circular membrane	[48]
WS ₂ (CVD growth)	1	272 ± 18	150 ± 30	N/A	N/A	Indentation on circular membrane	[48]
WSe ₂ (Mechanical exfoliated)	5, 6, 12, 14	170 ± 7 (5 L) 166 ± 6 (6 L) 168 ± 7 (12 L) 165 ± 6 (14 L)	638 ± 22 (5 L) 691 ± 37 (6 L) 499 ± 34 (12 L) 137 ± 26 (14 L)	>12	>7.3	Indentation on circular membrane	[42]
BP (Mechanical exfoliated)	17–35	27 ± 4 (armchair direction) 59 ± 12 (zigzag direction)	N/A	2.2 (armchair direction) 4.2 (zigzag direction)	7.2 (armchair direction) 6.5 (zigzag direction)	Spring constant of beam	[54]

Material	Number of layers	Young's modulus (GPa)	Pretension (mN/m)	Breaking stress (GPa)	Breaking strain (%)	Characterization method	Ref.
	17, 37	276 ± 32 (17 L) 90 ± 6.4 (37 L)	180–1200	>25	>8	Indentation on circular membrane	[41]
GO (Solution-based deposition)	1–3	208 ± 23 (1 L) 224 ± 18 (2 L) 230 ± 27 (3 L)	54 ± 14 (1 L) 32 ± 6 (2 L) 28 ± 4 (3 L)	N/A	N/A	Indentation on circular membrane	[57]
Mica (Mechanical exfoliated)	2–14	202 ± 22	140 ± 80	4–9	2–4.5	Indentation on circular membrane	[60]
h-BN (CVD growth)	2, 4, 5	279 ± 20 (2 L) 269 ± 13 (4 L) 252 ± 15 (5 L)	8.8 ± 1.2 (2 L) 12.8 ± 1.3 (4 L) 15.7 ± 1.5 (5 L)	~9	2.2	Indentation on circular membrane	[2]

Table 1. Summary of the in-plane mechanical properties of 2D materials measured from experiments.

3.1.3.1. Young's modulus

Pristine monolayer graphene (prepared by mechanical exfoliation from bulk graphite) is reported to be the stiffest 2D material on earth so far with a Young's modulus of approximately 1 TPa [3, 49, 51], because of the strong in-plane covalent carbon-carbon bonds. For 2D TMDCs— MX_2 ($M = \text{Mo}, \text{W}$; $X = \text{S}, \text{Se}$) with the same crystal structure (chalcogen atoms in two hexagonal planes separated by a plane of transition metal atoms) [11], a smaller Young's modulus of WSe_2 has been observed compared with MoS_2 and WS_2 [42]; due to a decrease in the charge transfer and an increase in the lattice constant, resulting in a weakened binding between the metal and chalcogen [53], as M changes from Mo to W and X changes from S to Se .

Meanwhile, the Young's modulus of some 2D materials (e.g., MoS_2 , BP, and h-BN) [2, 7, 41, 48] have been found to decrease with an increase in their thickness (number of layers), which is caused mainly by interlayer stacking errors. The occurrence of interlayer sliding in multi-layer 2D materials during indentation is also a factor for underestimating the intrinsic Young's modulus [7]. However, the Young's modulus of WSe_2 remains unchanged statistically with increasing number of layers, which possibly results from the strong interlayer interaction in WSe_2 [42]. As stated earlier, for 2D materials with thickness-dependent Young's modulus, precaution needs to be taken when using model Eq. (5) to derive the Young's modulus. Furthermore, the highly anisotropic atomic structure in 2D materials, such as BP, presents an anisotropic Young's modulus along the different crystal orientations [54].

In addition, the mechanical properties of 2D materials largely depend on the density of crystal defects and thus are related to the preparation methods. For instance, the larger number of vacancy defects in the GO-reduced graphene and the existence of voids at the grain boundaries, together with wrinkles in polycrystalline graphene prepared by the CVD method, can contribute to the weaker mechanical properties [4, 55]. In addition, the presence of a larger

number of grain boundaries can affect the Young's modulus of 2D materials negatively [56]. By optimizing the processing steps of suspended 2D materials fabrication, the quantity of crystal defects and wrinkles in 2D materials can be reduced, thus leading to an improvement of the mechanical properties [56]. Research has shown that the elastic properties can be recovered by flattening the wrinkles in CVD graphene with a small prestretch [47]. The mechanical properties of 2D materials can be improved also by introducing controlled density of defects, such as Ar⁺ plasma irradiation [35].

3.1.3.2. Pretension

The factors that can affect the pretension in 2D materials are quite complicated. The pretension not only depends on the intrinsic mechanical properties of 2D materials, but also on the fabrication process of the suspended structure (e.g., the method of transferring 2D material onto the substrates). Therefore, the pretension values of suspended 2D materials in **Table 1** vary greatly. Generally, the dry transfer process with scotch tape or viscoelastic stamp introduces higher pretension compared with wet transfer process such as solution-based deposition [57]. Suspended structures fabricated by etching sacrificial layer (method shown in **Figure 1(c)**) normally possess less pretension than 2D materials transferred directly onto prepatterned substrates (method shown in **Figure 1(a)** and **(b)**). Annealing, as a common method to remove the residue on 2D materials left over by a fabrication process, can introduce thermal stress due to the different thermal expansion coefficients between the substrates and the 2D materials.

3.1.3.3. Breaking strength

As presented in **Table 1**, the 2D materials with higher Young's modulus normally possess higher breaking strength. Many reports have found that the breaking stress of 2D materials can reach the theoretical upper limit ($E_V/9$) [7], due to low disorder and impurities in the characterized 2D materials. The existence of anisotropic breaking strength along armchair and zigzag directions has been found in BP, possibly resulting from its anisotropic Young's modulus [54]. Except for the 2D dielectrics (mica and h-BN), the breaking strain of most 2D materials is above 7%, which is comparable with the common materials used as substrates for flexible electronics, namely polyimide (PI) or polydimethylsiloxane (PDMS) [58], implying that most of the 2D materials are compatible with flexible electronic devices.

3.2. Out-of-plane properties

The research on the out-of-plane mechanical properties of 2D materials includes characterizing the elasticity perpendicular to the plane's direction and the interlayer shear force constant/strength parallel to the plane's direction. Unlike the experiments already conducted in characterizing the in-plane mechanical properties of 2D materials, experimental investigations on quantifying the out-of-plane properties are still quite scarce, mainly because of the technical difficulties in characterization [61]. Overall, out-of-plane properties can be explored directly by applying normal/shear force to 2D materials or indirectly via Raman spectroscopy. This

section introduces the various experiments conducted thus far related to the measurements of out-of-plane properties.

3.2.1. Direct characterization

3.2.1.1. Perpendicular-to-plane elasticity

Direct investigation of the perpendicular-to-plane elasticity of few-layer 2D materials remains challenging, because extremely small indentations need to be conducted on supported 2D sheets. Since the interlayer distance of 2D materials is so small (<1 nm), the maximum indentation depth should be only a few angstroms (smaller than the interlayer distance) [62].

An unconventional AFM-based method (modulated nanoindentation, as shown in **Figure 5(a)**) with a high indentation depth resolution of 0.1 Å [63, 64] has been employed to measure the perpendicular-to-plane elasticity of highly oriented pyrolytic graphite (HOPG), epitaxial graphene (EG), epitaxial graphene oxide (EGO), and conventional GO successfully [62]. During the indentation, the AFM tip oscillates at 1 kHz frequency with an amplitude of approximately 0.1 Å (ΔZ_{piezo}) controlled by a piezoelectric tube. The AFM feedback loop sets a normal force F_z applied on the 2D materials from the AFM tip by setting the position of the piezoelectric tube vertically. A tip oscillation with an amplitude of ΔZ_{piezo} results in a variation of the normal force ΔF_z monitored via the deflection of a cantilever. At a certain normal force F_z , the tip–2D material contact stiffness k_{contact} can be obtained via the expression below:

$$\frac{\Delta F_z}{\Delta Z_{\text{piezo}}} = \left(\frac{1}{k_{\text{lever}}} + \frac{1}{k_{\text{contact}}(F_z)} \right)^{-1}, \quad (6)$$

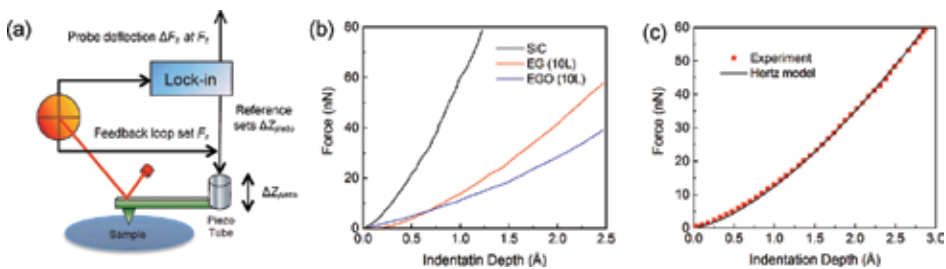


Figure 5. (a) Schematic of modulated nanoindentation on 2D materials. (b) Force–indentation curves for SiC, 10-layer EG, and 10-layer EGO extracted from the nanoindentation. (c) Force–indentation curve for HOPG and the Hertzian fitting. Adapted from Gao et al. [62].

where k_{lever} is the spring constant of the AFM cantilever. Then, the force F_z versus indentation depth Z_{indent} curves (as shown in **Figure 5(b)**) can be derived by integrating $dF_z = k_{\text{contact}}(F_z) dZ_{\text{indent}}$ as

$$Z_{\text{indent}} = \int_0^{F_z} \frac{dF_z}{k_{\text{contact}}(F_z)}. \quad (7)$$

When the indentation depth is in the subnanometer regime, the perpendicular Young's modulus can be extracted by fitting the $F_z - Z_{\text{indent}}$ curves with the Hertz model (as shown in **Figure 5(c)**):

$$F = \frac{4}{3} E^* r^{1/2} Z_{\text{indent}}^{2/3}, \quad (8)$$

where $E^* = (1 - (\nu^{\text{sample}})^2) / E_Y^{\text{sample}} + (1 - (\nu^{\text{tip}})^2) / E_Y^{\text{tip}}$, with ν^{sample} , ν^{tip} , E_Y^{sample} , and E_Y^{tip} being the Poisson's ratio and Young's modulus of the measured 2D material and AFM tip, respectively. With this approach, the perpendicular Young's modulus of HOPG, EG, EGO, and conventional GO is measured to be 33 ± 3 GPa, 36 ± 3 GPa, 23 ± 4 GPa, and 35 ± 10 GPa, respectively, which is far smaller than the in-plane Young's modulus. In addition, the intercalated water between GO layers can affect the perpendicular Young's modulus significantly. This method is very sensitive to the 2D material/substrate interaction and the number of layers of 2D material, and thus is useful for investigating 2D material/substrate interaction [62].

3.2.1.2. Shear force constant/strength

To measure the interlayer shear force constant/strength, proper shear stress should be applied to the interlayer interface of a 2D material using a probe. Oviedo et al. [61] have measured the interlayer shear strength of MoS₂ with a shearing strength test under in situ transmission electron microscopy (TEM) characterization, as shown in **Figure 6**. During the test, a multilayer MoS₂ flake sandwiched between a 3.5 μm thick focused ion beam (FIB)-deposited platinum (Pt) cap and a SiO₂/Si substrate has been attached to a piezoelectric manipulator, as shown in **Figure 6(a)**. Then, the sample has been moved toward a static indenter probe (attached to a force sensor) to apply force to the side of the Pt cap, thus creating shear stress in the MoS₂ flake (**Figure 6(b)**). During the test, the force versus distance plot has been recorded, as depicted in **Figure 6(c)**. With the force triggering the shear $F = 498.8 \pm 1.6$ μN and the sheared area $A = 19.7 \pm 0.5$ μm² (inset of **Figure 6(c)**), the shear strength of MoS₂ is calculated to be 25.3 ± 0.6 MPa, about 0.1% of in-plane Young's modulus (~260 GPa).

Another method to apply shear stress is to conduct friction force microscopy (FFM) measurements. In contrast to the approach mentioned earlier, the probe, applying normal force to the planes, is placed on the top surface of the 2D material sheets. Only when the probe-layer interactions are stronger than the interlayer interactions, shear stress can be applied in the 2D material by moving the probe laterally. The challenge of this approach is whether shear stress can be transferred from the probe to the interlayer interface of the measured samples efficiently. In addition, this method is not suitable to measure the shear strength with zero normal load. With this approach, shear strengths of graphite have been measured to be 0.27–0.75 MPa

depending on the sliding direction [65]. Meanwhile, the self-retracting motion of graphite, when the probe is removed away after loading, has been observed (shown in **Figure 7(a)** and **(b)**). Moreover, a set of lock-in states has been observed at certain rotation angles with 60° intervals, which requires an external force to unlock a lock-in state [66], as shown in **Figure 7(c)** and **(d)**. The interlayer shear strength of graphite where the lock-in appears is measured to be approximately 0.14 GPa [67].

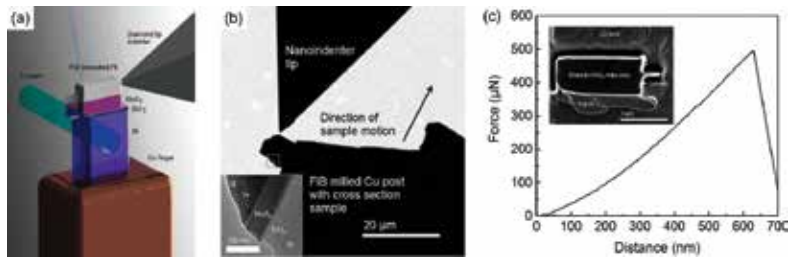


Figure 6. (a) Schematic of the in situ TEM shearing test. (b) Low-magnification TEM image of the indenter tip pointing to the test sample. Inset: High-magnification TEM image of the test sample. (c) Force versus distance plot recorded during the test. Inset: Top-view SEM image of the sheared surface. Adapted from Oviedo et al. [61].

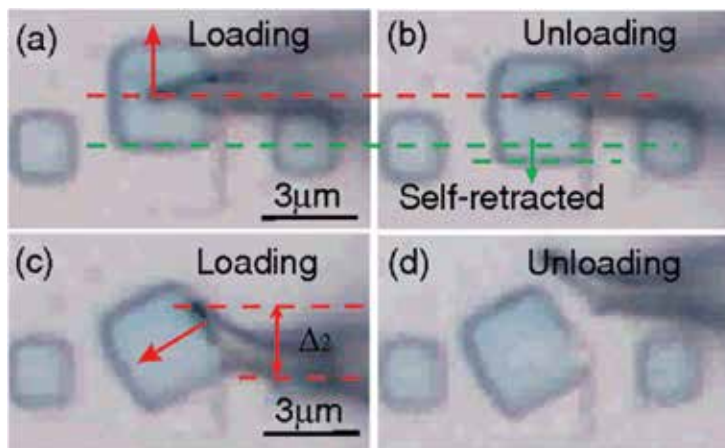


Figure 7. (a, b) Motion of a graphite flake that self-retracts after unloading. (c, d) Motion of a graphite that is in a lock-in state [66].

3.2.2. Raman spectroscopy

Furthermore, the interlayer interaction of 2D materials can be investigated using Raman spectroscopy. By probing the interlayer phonons modes, both the parallel-to-plane (shear) and perpendicular-to-plane (breathing) interlayer force constants can be extracted from the Raman spectrum. Since interlayer vibrational modes are usually in the low-frequency regime, due to the weak interlayer van der Waals restoring force, a special filter in Raman spectroscopy needs

to be used to suppress the Rayleigh scattering background [68, 69]. Alternatively, the interlayer interaction can be investigated from the Raman spectrum of folded 2D sheets with enhanced interlayer vibrational modes response [70]. The interlayer breathing mode or shear mode force constants can be obtained by fitting the experimental frequency of the i th vibrational mode, with the expression below [68]:

$$\omega_i = \sqrt{\frac{k}{2\mu\pi^2c^2} \left(1 - \cos\left(\frac{(i-1)\pi}{N}\right) \right)}, \quad (9)$$

where k is the breathing/shear mode force constant per unit area; c is the speed of light; μ and N are the mass per unit area and the number of layers of the 2D material, respectively. **Table 2** summarizes the shear and breathing mode force constants measured with this method. Generally, breathing mode force constant is about two to three times larger than that of shear mode, which is possibly the reason why shear exfoliation can enhance the exfoliation efficiency significantly compared with conventional exfoliation methods [71]. The interlayer interaction of multilayer graphene is reported to be the weakest so far. On the other hand, the large difference in the shear elastic modulus along two different in-plane directions reflects the strong anisotropic elastic properties of BP [72].

Materials	Number of layers	Force constants ($\times 10^{19}$ N/m ³)		Ref.
		Shear mode	Breathing mode	
Graphene	2–5	1.28	NA	[68]
MoS ₂	2–9	2.72	8.62	[69]
WSe ₂	2, 4	3.07	8.63	
BP	4–14	1.70 (armchair direction) 3.82 (zigzag direction)	12.3	[72]
Bi ₂ Te ₃	2–8	4.57	13.33	[73]
Bi ₂ Se ₃	2–6	2.27	5.26	

Table 2. Interlayer shear/breathing mode force constants extracted from Raman spectroscopy.

4. Applications

4.1. Flexible transistor

The combination of high breaking strain, low thickness, and versatile electronic properties of 2D materials make them competitive contenders for flexible electronics applications. Because of the semiconducting properties, certain TMDCs (such as MoS₂, WS₂, and WSe₂) and BP can be used as channel materials in flexible transistors, while pristine graphene with relative high

conductivity is suitable as an electrode material. Mica and h-BN with large bandgaps can be used for 2D gate dielectrics [74, 75]. **Figure 8(a)** shows a flexible and transparent thin film transistor (TFT) fabricated from all 2D materials on a polyethylene terephthalate (PET)-flexible substrate [76]. The structure of the TFT is depicted in the inset of **Figure 8(b)**. As shown in **Figure 8(b)**, the current On/Off ratio has been found to be about 7.5×10^3 , exhibiting p-type FET characteristics, and the device characteristics have been unaltered within a mechanical strain of 2%. **Figure 8(c)** shows the output characteristics of the flexible TFT with the characteristic of current saturation similar to conventional Si transistors, uncovering the great potential application of 2D materials in flexible transistors.

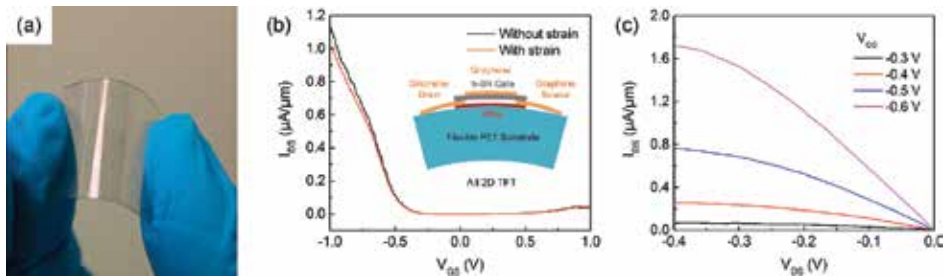


Figure 8. (a) All 2D materials-based TFTs on a flexible PET substrate. (b) Transfer characteristics of the TFT with and without 2% strain. Inset: Side-view schematic of the flexible TFT. (c) Output characteristics of the TFT. Adapted from Das et al. [76].

4.2. Strain sensor

The 2D materials [77, 78] have been found to undergo band structure change under applied strain. In addition, the distortion of the 2D films may result in additional scattering, thus reducing the carrier mobility [79]. The above factors contribute to a piezoresistive effect, in which the resistivity of 2D materials is modulated by mechanical deformation. Thus, 2D materials can be used as strain or pressure sensor [80, 81], by taking advantage of the piezoresistive effects. The sensitivity of a strain sensor is characterized usually by its gauge factor (GF), defined as $[\Delta R(\varepsilon)/R_0]/\varepsilon$, where R_0 is the total resistance of the unstrained device and $\Delta R(\varepsilon)$ is the resistance change under strain ε . The GF of pristine graphene has been characterized to be about 2 [81–85] due to the zero bandgap and the large strain required to open the bandgap, which can be a disadvantage for strain sensors. On the other hand, the GF of MoS₂ can reach approximately -200 [17, 29], resulting from the higher sensitivity of the decreasing bandgap and the direct–indirect bandgap transition under tensile strain, making MoS₂ more suitable for strain-sensing systems. The sensing performance of the 2D strain sensor can be enhanced by optimizing the structure design, such as the piezopotential-gated graphene matrix sensor arrays (GF = 389, as shown in **Figure 9(a)**) [16], quasi-continuous nanographene film sensor (GF = 507, as shown in **Figure 9(b)**) [86, 87], and graphene-woven fabric sensor (GF = 1000) [88, 89].

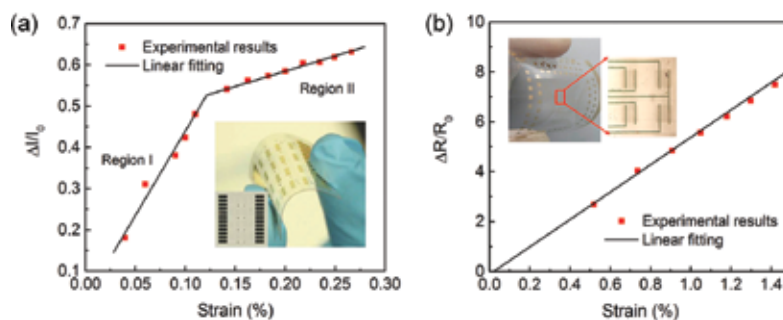


Figure 9. Sensing characteristics of the (a) piezopotential-gated graphene matrix strain sensor (Adapted from Sun et al. [16]) and (b) quasi-continuous nanographene film strain sensor (Adapted from Zhao et al. [86]).

Moreover, the piezoresistive effect, combined with the high breaking strain of 2D materials enable the design of wearable strain sensors for human motion detection. **Figure 10(a)** shows a prototype of tactile sensor fabricated with graphene films on a PDMS substrate attached on the human wrist. As shown in **Figure 10(b)**, the test subject's motions can be captured clearly with the strain sensor by outputting varying current response under different motions [16].

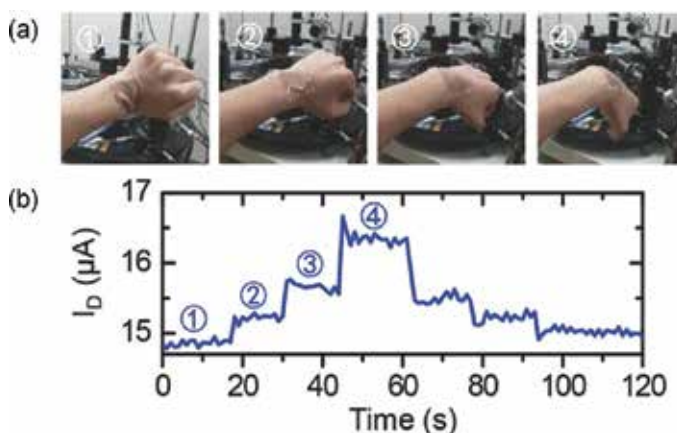


Figure 10. (a) A graphene tactile strain sensor attached on the wrist detecting the hand motion. (b) The electrical response of the tactile strain sensor in different hand motions shown in (a) [16].

4.3. Nanogenerator

Research has shown that odd-layer TMDCs possess piezoelectric property due to the absence of inversion symmetry [17, 34]. **Figure 11(a)** shows a flexible device with the monolayer MoS_2 flake outlined with black dashed line. When the substrate is bent from the two ends mechanically, the MoS_2 flake will be stretched, and piezoelectric polarization charges will be induced at the zigzag edges of the MoS_2 flake which can drive the flow of electrons in an external circuit as depicted in **Figure 11(e)**. When the substrate is released, electrons flow back

in the opposite direction as shown in **Figure 11(f)**. **Figure 11(b)** and **(c)** show that periodic stretching and releasing of the substrate can generate piezoelectric outputs in the external circuit with alternating polarity, which converts mechanical energy into electricity. A maximum mechanical-to-electrical energy conversion efficiency of 5.08% can be achieved from the device [17]. The existence of piezoelectricity, coupled with the mechanical flexibility of some 2D materials, demonstrates their potential applications in wearable power-generated nano-devices.

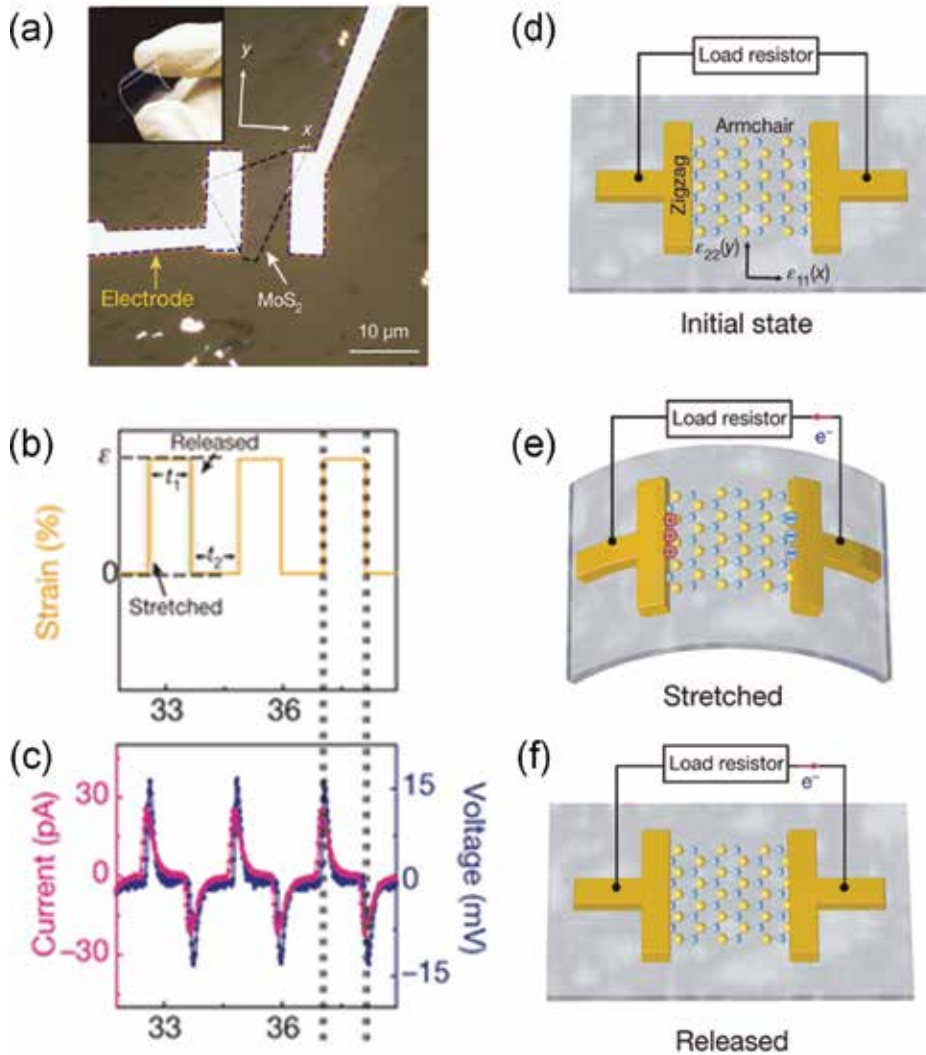


Figure 11. (a) A flexible device with a monolayer MoS₂ flake and metal electrodes at its zigzag edges. (b) Applied periodic strain as a function of time. (c) Corresponding piezoelectric outputs when strain is applied along the armchair direction. Operation of the MoS₂-based piezoelectric device in initial state (d), stretched state (e), and released state (f) [17].

4.4. Resonator

Nanoelectromechanical systems (NEMS) resonator, offering the potential for extreme mass and force sensitivity [25, 90], has triggered intense interest in recent years. The resonant frequency of the resonators depends greatly on their geometry and the mechanical properties of the vibrational materials (such as Young's modulus and mass density) [91]. As the sensitivity of resonators improves with increase in resonant frequency, 2D materials are prospective materials for highly sensitive NEMS due to their extraordinary mechanical properties and low mass. Among the family of 2D materials, graphene resonator has been studied most so far. **Figure 12(a)** shows a schematic and a SEM image of a graphene resonator. **Figure 12(b)** shows a schematic of the electrical actuation and detection of mechanical vibrations of the graphene resonator. A dc voltage V_g applied to the gate causes static deflection of the graphene toward the gate. The resonant motion is actuated by ac voltage with an amplitude of V_a and frequency of ω_a applied to the drain electrode, and read out by the current mixing method [25] using a lock-in amplifier. As shown in **Figure 12(c)**, when $V_g = 0$ V and $V_a = 250$ mV, the fundamental resonance frequency (Peak A) is approximately 1 MHz, and the second vibration mode (Peak B) is measured to be approximately 2 MHz. The amplitude of vibrational modes increases with increasing V_a . However, the resonant frequency decreases as V_a increases due to nonlinear damping effects at higher resonance amplitudes [92]. By operating the graphene resonant sensors in the second mode regime, the detection sensitivity can be improved significantly [93].

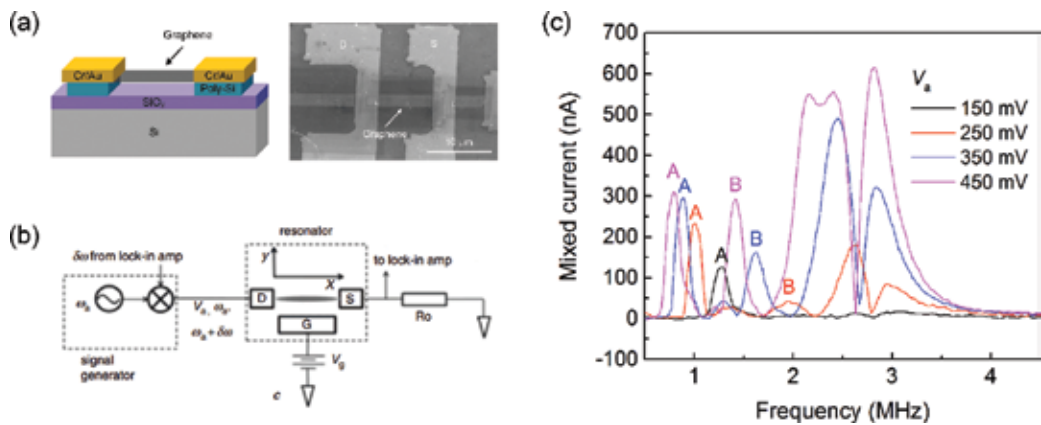


Figure 12. (a) Schematic and SEM image of a graphene resonator. (b) Circuit diagram of current-mixing characterization setup. (c) The mixed current versus driving frequency for different amplitudes of actuation voltages. Adapted from Chen et al. [93].

NEMS with low resonant frequency can be used for acoustic electronics, such as acoustic sensor [94] and loudspeakers [95]. Since the resonant frequencies of resonators can be tuned inversely by increasing the dimensions of vibrational parts, resonators with lower resonant frequencies can be fabricated on 2D membranes with larger dimensions. **Figure 13** shows the response of a graphene resonator working in the low-frequency regime [94]. The resonator has been actuated with a piezoelectric disk driven with a sinusoidal signal and detected using a Laser

Doppler Vibrometer (LDV). The fundamental resonant frequency has been measured to be approximately 16 kHz for a $3 \times 3 \text{ mm}^2$ graphene membrane.

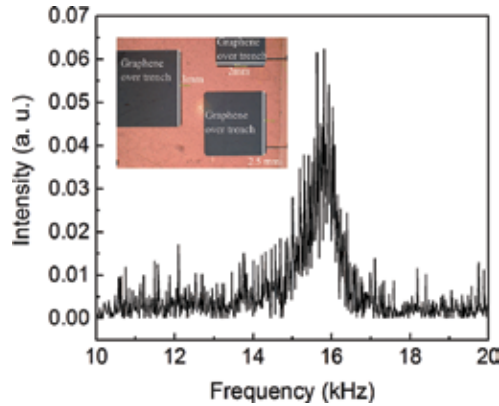


Figure 13. Measured resonant frequency for a $3 \times 3 \text{ mm}^2$ membrane over the cavity using LDV. Adapted from Grady et al. [94].

5. Conclusions

In this article, we have reviewed the experimental study of in-plane and out-of-plane mechanical properties of 2D materials ranging from conductors (e.g., graphene), semiconductors (e.g., TMDCs and BP), to insulators (e.g., h-BN). First, various approaches for fabricating suspended 2D material devices have been demonstrated, whose advantages and disadvantages have been compared. Then, the various characterization methods and the corresponding results have been summarized, with special focus being paid to the mechanical differences among the different 2D materials. With the extraordinary mechanical properties (ultralow weight, high Young's modulus, and high strength), 2D materials possess the potential for applications in flexible electronics and highly sensitive resonating mass sensors. The associated piezoresistive and piezoelectric effects under mechanical strain in 2D materials extend their applications to strain sensors, nanogenerators, and advanced NEMS.

Acknowledgements

The authors would like to thank the financial support of UK Engineering and Physical Sciences Research Council (EPSRC) for this work.

Author details

Rui Zhang and Rebecca Cheung*

*Address all correspondence to: r.cheung@ed.ac.uk

Scottish Microelectronics Centre, The University of Edinburgh, Edinburgh, United Kingdom

References

- [1] Novoselov KS, Geim AK, Morozov SV, Jiang D, Zhang Y, Dubonos SV, et al. Electric field effect in atomically thin carbon films. *Science*. 2004;306:666–669. DOI: 10.1126/science.1102896
- [2] Song L, Ci L, Lu H, Sorokin PB, Jin C, Ni J, et al. Large scale growth and characterization of atomic hexagonal boron nitride layers. *Nano Letters*. 2010;10:3209–3215. DOI: 10.1021/nl1022139
- [3] Lee C, Wei X, Kysar JW, Hone J. Measurement of the elastic properties and intrinsic strength of monolayer graphene. *Science*. 2008;321:385–388. DOI: 10.1126/science.1157996
- [4] Gomez-Navarro C, Burghard M, Kern K. Elastic properties of chemically derived single graphene sheets. *Nano Letters*. 2008;8:2045–2049. DOI: 10.1021/nl801384y
- [5] Song XF, Oksanen M, Sillanpaa MA, Craighead HG, Parpia JM, Hakonen PJ. Stamp transferred suspended graphene mechanical resonators for radio frequency electrical readout. *Nano Letters*. 2012;12:198–202. DOI: 10.1021/nl203305q
- [6] Castellanos-Gomez A, Poot M, Steele GA, van der Zant HSJ, Agrait N, Rubio-Bollinger G. Elastic properties of freely suspended MoS₂ nanosheets. *Advanced Materials*. 2012;24:772–775. DOI: 10.1002/adma.201103965
- [7] Bertolazzi S, Brivio J, Kis A. Stretching and breaking of ultrathin MoS₂. *ACS Nano*. 2011;5:9703–9709. DOI: 10.1021/nn203879f
- [8] Zhao X, Zhang Q, Chen D, Lu P. Enhanced mechanical properties of graphene-based poly(vinyl alcohol) composites. *Macromolecules*. 2010;43:2357–2363. DOI: 10.1021/ma902862u
- [9] Zhang Y, Tan Y-W, Stormer HL, Kim P. Experimental observation of the quantum Hall effect and Berry's phase in graphene. *Nature*. 2005;438:201–204. DOI: 10.1038/nature04235

- [10] Zhao W, Ghorannevis Z, Chu L, Toh M, Kloc C, Tan P-H, et al. Evolution of electronic structure in atomically thin sheets of WS_2 and WSe_2 . *ACS Nano*. 2013;7:791–797. DOI: 10.1021/nn305275h
- [11] Wang QH, Kalantar-Zadeh K, Kis A, Coleman JN, Strano MS. Electronics and optoelectronics of two-dimensional transition metal dichalcogenides. *Nature Nanotechnology*. 2012;7:699–712. DOI: 10.1038/nnano.2012.193
- [12] Yoon J, Park W, Bae G-Y, Kim Y, Jang HS, Hyun Y, et al. Highly flexible and transparent multilayer mos_2 transistors with graphene electrodes. *Small*. 2013;9:3295–3300. DOI: 10.1002/smll.201300134
- [13] Wang H, Yu LL, Lee YH, Shi YM, Hsu A, Chin ML, et al. Integrated circuits based on bilayer MOS_2 transistors. *Nano Letters*. 2012;12:4674–4680. DOI: 10.1021/nl302015v
- [14] Bertolazzi S, Krasnozhan D, Kis A. Nonvolatile memory cells based on mos_2 /graphene heterostructures. *ACS Nano*. 2013;7:3246–3252. DOI: 10.1021/nn3059136
- [15] Lopez-Sanchez O, Lembke D, Kayci M, Radenovic A, Kis A. Ultrasensitive photodetectors based on monolayer MoS_2 . *Nature Nanotechnology*. 2013;8:497–501. DOI: 10.1038/nnano.2013.100
- [16] Sun Q, Seung W, Kim BJ, Seo S, Kim S-W, Cho JH. Active matrix electronic skin strain sensor based on piezopotential-powered graphene transistors. *Advanced Materials*. 2015;27:3411–3417. DOI: 10.1002/adma.201500582
- [17] Wu W, Wang L, Li Y, Zhang F, Lin L, Niu S, et al. Piezoelectricity of single-atomic-layer MoS_2 for energy conversion and piezotronics. *Nature*. 2014;514:470–474. DOI: 10.1038/nature13792
- [18] Bunch JS, van der Zande AM, Verbridge SS, Frank IW, Tanenbaum DM, Parpia JM, et al. Electromechanical resonators from graphene sheets. *Science*. 2007;315:490–493. DOI: 10.1126/science.1136836
- [19] Choi K, Lee YT, Min S-W, Lee HS, Nam T, Kim H, et al. Direct imprinting of MoS_2 flakes on a patterned gate for nanosheet transistors. *Journal of Materials Chemistry C*. 2013;1:7803–7807. DOI: 10.1039/c3tc31796j
- [20] Castellanos-Gomez A, Buscema M, Molenaar R, Singh V, Janssen L, van der Zant HSJ, et al. Deterministic transfer of two-dimensional materials by all-dry viscoelastic stamping. *2D Materials*. 2014;1:011002. DOI: 10.1088/2053-1583/1/1/011002
- [21] Yang R, Zheng X, Wang Z, Miller CJ, Feng PXL. Multilayer MoS_2 transistors enabled by a facile dry-transfer technique and thermal annealing. *Journal of Vacuum Science & Technology B*. 2014;32:061203. DOI: 10.1116/1.4898117
- [22] Li B, He Y, Lei S, Najmaei S, Gong Y, Wang X, et al. Scalable transfer of suspended two-dimensional single crystals. *Nano Letters*. 2015;15:5089–5097. DOI: 10.1021/acs.nanolett.5b01210

- [23] Qiu D, Lee DU, Park CS, Lee KS, Kim EK. Transport properties of unrestricted carriers in bridge-channel MoS₂ field-effect transistors. *Nanoscale*. 2015;7:17556–17562. DOI: 10.1039/c5nr04397b
- [24] van der Zande AM, Barton RA, Alden JS, Ruiz-Vargas CS, Whitney WS, Pham PHQ, et al. Large-scale arrays of single-layer graphene resonators. *Nano Letters*. 2010;10:4869–4873. DOI: 10.1021/nl102713c
- [25] Chen CY, Rosenblatt S, Bolotin KI, Kalb W, Kim P, Kymissis I, et al. Performance of monolayer graphene nanomechanical resonators with electrical readout. *Nature Nanotechnology*. 2009;4:861–867. DOI: 10.1038/nnano.2009.267
- [26] Bolotin KI, Sikes KJ, Jiang Z, Klima M, Fudenberg G, Hone J, et al. Ultrahigh electron mobility in suspended graphene. *Solid State Communications*. 2008;146:351–355. DOI: 10.1016/j.ssc.2008.02.024
- [27] Bao W, Liu G, Zhao Z, Zhang H, Yan D, Deshpande A, et al. Lithography-free fabrication of high quality substrate-supported and freestanding graphene devices. *Nano Research*. 2010;3:98–102. DOI: 10.1007/s12274-010-1013-5
- [28] Wang F, Stepanov P, Gray M, Lau CN. Annealing and transport studies of suspended molybdenum disulfide devices. *Nanotechnology*. 2015;26:105709. DOI: 10.1088/0957-4484/26/10/105709
- [29] Manzeli S, Allain A, Ghadimi A, Kis A. Piezoresistivity and strain-induced band gap tuning in atomically thin MoS₂. *Nano Letters*. 2015;15:5330–5335. DOI: 10.1021/acs.nanolett.5b01689
- [30] Jin T, Kang J, Su Kim E, Lee S, Lee C. Suspended single-layer MoS₂ devices. *Journal of Applied Physics*. 2013;114:164509. DOI: 10.1063/1.4827477
- [31] Wang F, Stepanov P, Gray M, Lau CN, Itkis ME, Haddon RC. Ionic liquid gating of suspended mos₂ field effect transistor devices. *Nano Letters*. 2015;15:5284–5288. DOI: 10.1021/acs.nanolett.5b01610
- [32] Meitl MA, Zhu ZT, Kumar V, Lee KJ, Feng X, Huang YY, et al. Transfer printing by kinetic control of adhesion to an elastomeric stamp. *Nature Materials*. 2006;5:33–38. DOI: 10.1038/nmat1532
- [33] Velasco J, Jr., Zhao Z, Zhang H, Wang F, Wang Z, Kratz P, et al. Suspension and measurement of graphene and Bi₂Se₃ thin crystals. *Nanotechnology*. 2011;22:285305. DOI: 10.1088/0957-4484/22/28/285305
- [34] Zhu H, Wang Y, Xiao J, Liu M, Xiong S, Wong ZJ, et al. Observation of piezoelectricity in free-standing monolayer MoS₂. *Nature Nanotechnology*. 2015;10:151–155. DOI: 10.1038/nnano.2014.309

- [35] Lopez-Polin G, Gomez-Navarro C, Parente V, Guinea F, Katsnelson MI, Perez-Murano F, et al. Increasing the elastic modulus of graphene by controlled defect creation. *Nature Physics*. 2015;11:26–31. DOI: 10.1038/nphys3183
- [36] Gates RS, Reitsma MG. Precise atomic force microscope cantilever spring constant calibration using a reference cantilever array. *Review of Scientific Instruments*. 2007;78:086101. DOI: 10.1063/1.2764372
- [37] Sader JE, Chon JWM, Mulvaney P. Calibration of rectangular atomic force microscope cantilevers. *Review of Scientific Instruments*. 1999;70:3967–3969. DOI: 10.1063/1.1150021
- [38] Sader JE, Sanelli JA, Adamson BD, Monty JP, Wei X, Crawford SA, et al. Spring constant calibration of atomic force microscope cantilevers of arbitrary shape. *Review of Scientific Instruments*. 2012;83:103705. DOI: 10.1063/1.4757398
- [39] Komaragiri U, Begley MR, Simmonds JG. The mechanical response of freestanding circular elastic films under point and pressure loads. *Journal of Applied Mechanics*. 2005;72:203–212. DOI: 10.1115/1.1827246
- [40] Begley MR, Mackin TJ. Spherical indentation of freestanding circular thin films in the membrane regime. *Journal of the Mechanics and Physics of Solids*. 2004;52:2005–2023. DOI: 10.1016/j.jmps.2004.03.002
- [41] Wang J-Y, Li Y, Zhan Z-Y, Li T, Zhen L, Xu C-Y. Elastic properties of suspended black phosphorus nanosheets. *Applied Physics Letters*. 2016;108:013104. DOI: 10.1063/1.4939233
- [42] Zhang R, Koutsos V, Cheung R. Elastic properties of suspended multilayer WSe₂. *Applied Physics Letters*. 2016;108:042104. DOI: 10.1063/1.4940982
- [43] Bhatia NM, Nachbar W. Finite indentation of an elastic membrane by a spherical indenter. *International Journal of Non-Linear Mechanics*. 1968;3:307–324. DOI: 10.1016/0020-7462(68)90004-8
- [44] Lindahl N, Midtvedt D, Svensson J, Nerushev OA, Lindvall N, Isacson A, et al. Determination of the bending rigidity of graphene via electrostatic actuation of buckled membranes. *Nano Letters*. 2012;12:3526–3531. DOI: 10.1021/nl301080v
- [45] Frank IW, Tanenbaum DM, van der Zande AM, McEuen PL. Mechanical properties of suspended graphene sheets. *Journal of Vacuum Science & Technology B*. 2007;25:2558–2561. DOI: 10.1116/1.2789446
- [46] Li P, You Z, Haugstad G, Cui T. Graphene fixed-end beam arrays based on mechanical exfoliation. *Applied Physics Letters*. 2011;98:253105. DOI: 10.1063/1.3594242
- [47] Lin Q-Y, Jing G, Zhou Y-B, Wang Y-F, Meng J, Bie Y-Q, et al. Stretch-induced stiffness enhancement of graphene grown by chemical vapor deposition. *ACS Nano*. 2013;7:1171–1177. DOI: 10.1021/nn3053999

- [48] Liu K, Yan QM, Chen M, Fan W, Sun YH, Suh J, et al. Elastic properties of chemical-vapor-deposited monolayer MoS_2 , WS_2 , and their bilayer heterostructures. *Nano Letters*. 2014;14:5097–5103. DOI: 10.1021/nl501793a
- [49] Lee J-U, Yoon D, Cheong H. Estimation of young's modulus of graphene by raman spectroscopy. *Nano Letters*. 2012;12:4444–4448. DOI: 10.1021/nl301073q
- [50] Wong CL, Annamalai M, Wang ZQ, Palaniapan M. Characterization of nanomechanical graphene drum structures. *Journal of Micromechanics and Microengineering*. 2010;20:115029. DOI: 10.1088/0960-1317/20/11/115029
- [51] Koenig SP, Boddeti NG, Dunn ML, Bunch JS. Ultrastrong adhesion of graphene membranes. *Nature Nanotechnology*. 2011;6:543–546. DOI: 10.1038/nnano.2011.123
- [52] Bunch JS, Verbridge SS, Alden JS, van der Zande AM, Parpia JM, Craighead HG, et al. Impermeable atomic membranes from graphene sheets. *Nano Letters*. 2008;8:2458–2462. DOI: 10.1021/nl801457b
- [53] Zeng F, Zhang W-B, Tang B-Y. Electronic structures and elastic properties of monolayer and bilayer transition metal dichalcogenides MX_2 (M= Mo, W; X= O, S, Se, Te): a comparative first-principles study. *Chinese Physics B*. 2015;24:097103. DOI: 10.1088/1674-1056/24/9/097103
- [54] Tao J, Shen W, Wu S, Liu L, Feng Z, Wang C, et al. Mechanical and electrical anisotropy of few-layer black phosphorus. *ACS Nano*. 2015;9:11362–11370. DOI: 10.1021/acsnano.5b05151
- [55] Ruiz-Vargas CS, Zhuang HL, Huang PY, van der Zande AM, Garg S, McEuen PL, et al. Softened elastic response and unzipping in chemical vapor deposition graphene membranes. *Nano Letters*. 2011;11:2259–2263. DOI: 10.1021/nl200429f
- [56] Lee G-H, Cooper RC, An SJ, Lee S, van der Zande A, Petrone N, et al. High-strength chemical-vapor-deposited graphene and grain boundaries. *Science*. 2013;340:1073–1076. DOI: 10.1126/science.1235126
- [57] Suk JW, Piner RD, An J, Ruoff RS. Mechanical properties of monolayer graphene oxide. *ACS Nano*. 2010;4:6557–6564. DOI: 10.1021/nn101781v
- [58] Kim D-H, Ahn J-H, Choi WM, Kim H-S, Kim T-H, Song J, et al. Stretchable and foldable silicon integrated circuits. *Science*. 2008;320:507–511. DOI: 10.1126/science.1154367
- [59] Castellanos-Gomez A, Poot M, Steele GA, van der Zant HSJ, Agrait N, Rubio-Bollinger G. Mechanical properties of freely suspended semiconducting graphene-like layers based on MoS_2 . *Nanoscale Research Letters*. 2012;7:1–4. DOI: 10.1186/1556-276x-7-233
- [60] Castellanos-Gomez A, Poot M, Amor-Amoros A, Steele GA, van der Zant HSJ, Agrait N, et al. Mechanical properties of freely suspended atomically thin dielectric layers of mica. *Nano Research*. 2012;5:550–557. DOI: 10.1007/s12274-012-0240-3

- [61] Oviedo JP, Kc S, Lu N, Wang J, Cho K, Wallace RM, et al. In situ TEM characterization of shear-stress-induced interlayer sliding in the cross section view of molybdenum disulfide. *ACS Nano*. 2015;9:1543–1551. DOI: 10.1021/nl506052d
- [62] Gao Y, Kim S, Zhou S, Chiu H-C, Nelias D, Berger C, et al. Elastic coupling between layers in two-dimensional materials. *Nature Materials*. 2015;14:714–720. DOI: 10.1038/nmat4322
- [63] Lucas M, Mai W, Yang R, Wang ZL, Riedo E. Aspect ratio dependence of the elastic properties of ZnO nanobelts. *Nano Letters*. 2007;7:1314–1317. DOI: 10.1021/nl070310g
- [64] Palaci I, Fedrigo S, Brune H, Klinke C, Chen M, Riedo E. Radial elasticity of multiwalled carbon nanotubes. *Physical Review Letters*. 2005;94:175502. DOI: 10.1103/PhysRevLett.94.175502
- [65] Zheng Q, Jiang B, Liu S, Weng Y, Lu L, Xue Q, et al. Self-retracting motion of graphite microflakes. *Physical Review Letters*. 2008;100:067205. DOI: 10.1103/PhysRevLett.100.067205
- [66] Liu Z, Yang J, Grey F, Liu JZ, Liu Y, Wang Y, et al. Observation of microscale superlubricity in graphite. *Physical Review Letters*. 2012;108:205503. DOI: 10.1103/PhysRevLett.108.205503
- [67] Liu Z, Zhang S-M, Yang J-R, Liu JZ, Yang Y-L, Zheng Q-S. Interlayer shear strength of single crystalline graphite. *Acta Mechanica Sinica*. 2012;28:978–982. DOI: 10.1007/s10409-012-0137-0
- [68] Tan PH, Han WP, Zhao WJ, Wu ZH, Chang K, Wang H, et al. The shear mode of multilayer graphene. *Nature Materials*. 2012;11:294–300. DOI: 10.1038/nmat3245
- [69] Zhao Y, Luo X, Li H, Zhang J, Araujo PT, Gan CK, et al. Inter layer breathing and shear modes in few-trilayer MoS₂ and WSe₂. *Nano Letters*. 2013;13:1007–1015. DOI: 10.1021/nl304169w
- [70] Cong C, Yu T. Enhanced ultra-low-frequency interlayer shear modes in folded graphene layers. *Nature Communications*. 2014;5:4709. DOI: 10.1038/ncomms5709
- [71] Chen M, Nam H, Rokni H, Wi S, Yoon JS, Chen P, et al. Nanoimprint-assisted shear exfoliation (NASE) for Producing multilayer MoS₂ structures as field-effect transistor channel arrays. *ACS Nano*. 2015;9:8773–8785. DOI: 10.1021/acs.nano.5b01715
- [72] Luo X, Lu X, Koon GKW, Neto AHC, Ozyilmaz B, Xiong QH, et al. Large frequency change with thickness in interlayer breathing mode-significant interlayer interactions in few layer black phosphorus. *Nano Letters*. 2015;15:3931–3938. DOI: 10.1021/acs.nanolett.5b00775
- [73] Zhao Y, Luo X, Zhang J, Wu J, Bai X, Wang M, et al. Interlayer vibrational modes in few-quintuple-layer Bi₂Te₃ and Bi₂Se₃ two-dimensional crystals: Raman spectroscopy

- and first-principles studies. *Physical Review B*. 2014;90:245428. DOI: 10.1103/PhysRevB.90.245428
- [74] Lee G-H, Cui X, Kim YD, Arefe G, Zhang X, Lee C-H, et al. Highly Stable, dual-gated mos_2 transistors encapsulated by hexagonal boron nitride with gate-controllable contact, resistance, and threshold voltage. *ACS Nano*. 2015;9:7019–7026. DOI: 10.1021/acsnano.5b01341
- [75] Roy T, Tosun M, Kang JS, Sachid AB, Desai SB, Hettick M, et al. Field-effect transistors built from all two-dimensional material components. *ACS Nano*. 2014;8:6259–6264. DOI: 10.1021/nn501723y
- [76] Das S, Gulotty R, Sumant AV, Roelofs A. All two-dimensional, flexible, transparent, and thinnest thin film transistor. *Nano Letters*. 2014;14:2861–2866. DOI: 10.1021/nl5009037
- [77] Dou X, Ding K, Jiang D, Sun B. Tuning and identification of interband transitions in monolayer and bilayer molybdenum disulfide using hydrostatic pressure. *ACS Nano*. 2014;8:7458–7464. DOI: 10.1021/nn502717d
- [78] Wang Y, Cong C, Yang W, Shang J, Peimyoo N, Chen Y, et al. Strain-induced direct–indirect bandgap transition and phonon modulation in monolayer WS_2 . *Nano Research*. 2015;8:2562–2572. DOI: 10.1007/s12274-015-0762-6
- [79] Fu X-W, Liao Z-M, Zhou J-X, Zhou Y-B, Wu H-C, Zhang R, et al. Strain dependent resistance in chemical vapor deposition grown graphene. *Applied Physics Letters*. 2011;99:213107. DOI: 10.1063/1.3663969
- [80] Bae S-H, Lee Y, Sharma BK, Lee H-J, Kim J-H, Ahn J-H. Graphene-based transparent strain sensor. *Carbon*. 2013;51:236–242. DOI: 10.1016/j.carbon.2012.08.048
- [81] Zhu S-E, Ghatkesar MK, Zhang C, Janssen GCAM. Graphene based piezoresistive pressure sensor. *Applied Physics Letters*. 2013;102:161904. DOI: 10.1063/1.4802799
- [82] Huang M, Pascal TA, Kim H, Goddard WA, III, Greer JR. Electronic-mechanical coupling in graphene from in situ nanoindentation experiments and multiscale atomistic simulations. *Nano Letters*. 2011;11:1241–1246. DOI: 10.1021/nl104227t
- [83] He X, Gao L, Tang N, Duan J, Xu F, Wang X, et al. Shear strain induced modulation to the transport properties of graphene. *Applied Physics Letters*. 2014;105:083108. DOI: 10.1063/1.4894082
- [84] Smith AD, Niklaus F, Paussa A, Vaziri S, Fischer AC, Sterner M, et al. Electromechanical piezoresistive sensing in suspended graphene membranes. *Nano Letters*. 2013;13:3237–3242. DOI: 10.1021/nl401352k
- [85] Choi MK, Park I, Kim DC, Joh E, Park OK, Kim J, et al. Thermally controlled, patterned graphene transfer printing for transparent and wearable electronic/optoelectronic

- system. *Advanced Functional Materials*. 2015;25:7109–7118. DOI: 10.1002/adfm.201502956
- [86] Zhao J, Wang G, Yang R, Lu X, Cheng M, He C, et al. Tunable piezoresistivity of nanographene films for strain sensing. *ACS Nano*. 2015;9:1622–1629. DOI: 10.1021/nn506341u
- [87] Zhao J, He C, Yang R, Shi Z, Cheng M, Yang W, et al. Ultra-sensitive strain sensors based on piezoresistive nanographene films. *Applied Physics Letters*. 2012;101:063112. DOI: 10.1063/1.4742331
- [88] Wang Y, Wang L, Yang T, Li X, Zang X, Zhu M, et al. Wearable and highly sensitive graphene strain sensors for human motion monitoring. *Advanced Functional Materials*. 2014;24:4666–4670. DOI: 10.1002/adfm.201400379
- [89] Yang T, Wang Y, Li X, Zhang Y, Li X, Wang K, et al. Torsion sensors of high sensitivity and wide dynamic range based on a graphene woven structure. *Nanoscale*. 2014;6:13053–13059. DOI: 10.1039/c4nr03252g
- [90] Ekinici KL, Roukes ML. Nanoelectromechanical systems. *Review of Scientific Instruments*. 2005;76:061101. DOI: 10.1063/1.1927327
- [91] Chen C, Hone J. Graphene nanoelectromechanical systems. *Proceedings of the IEEE*. 2013;101:1766–1779. DOI: 10.1109/JPROC.2013.2253291
- [92] Eichler A, Moser J, Chaste J, Zdrojek M, Wilson-Rae I, Bachtold A. Nonlinear damping in mechanical resonators made from carbon nanotubes and graphene. *Nature Nanotechnology*. 2011;6:339–342. DOI: 10.1038/nnano.2011.71
- [93] Chen T, Mastropaolo E, Bunting A, Cheung R. Observation of second flexural mode enhancement in graphene resonators. *Electronics Letters*. 2015;51:1014–1016. DOI: 10.1049/el.2015.0361
- [94] Grady E, Mastropaolo E, Chen T, Bunting A, Cheung R. Low frequency graphene resonators for acoustic sensing. *Microelectronic Engineering*. 2014;119:105–108. DOI: 10.1016/j.mee.2014.02.036
- [95] Suk JW, Kirk K, Hao Y, Hall NA, Ruoff RS. Thermoacoustic sound generation from monolayer graphene for transparent and flexible sound sources. *Advanced Materials*. 2012;24:6342–6347. DOI: 10.1002/adma.201201782

Design, Assembly, and Fabrication of Two-Dimensional Nanomaterials into Functional Biomimetic Device Systems

Chengyi Hou, Minwei Zhang and Qijin Chi

Additional information is available at the end of the chapter

<http://dx.doi.org/10.5772/64127>

Abstract

Diverse functioning biosystems in nature have inspired us and offered unique opportunities in developing novel concepts as well as new class of materials and devices. The design of bioinspired functional materials with tailored properties for actuation, sensing, electronics, and communication has enabled synthetic devices to mimic natural behavior. Among which, artificial muscle and electronic skin that enable to sense and respond to various environmental stimuli in a human-like way have been widely recognized as a significant step toward robotics applications. Polymer materials have previously been dominant in fabricating such functional biomimetic devices owing to their soft nature. However, lacking multifunctionality, handling difficulty, and other setbacks have limited their practical applications. Recently, versatile and high-performance two-dimensional (2D) materials such as graphene and its derivatives have been studied and proven as promising alternatives in this area. In this chapter, we highlight the recent efforts on fabrication and assembly of 2D nanomaterials into functional biomimetic systems. We discuss the structure-function relationships for the development of 2D materials-based biomimetic devices, their tailoring property features, and their variety of applications. We start with a brief introduction of artificial functional biomimetic materials and devices, then summarize some key 2D materials-based systems, including their fabrication, properties, advantages and demonstrations, and finally present concluding remarks and outlook.

Keywords: 2D nanomaterials, biomimetics, smart device systems, graphene, functional design and fabrication

sophistication has been enhanced significantly. Biomimetic materials made today are routinely information rich and incorporate biologically active components derived from nature, and have found use in a wide variety of nonmedical applications [2]. Advancements in materials science, manufacturing process, and continual miniaturization of components have enabled biomimetic materials to have the ability of sensing, actuation, communication, and even computation [3]. Engineers have employed such intelligent materials to fabricate precise, predictable robotic devices and systems, which learned from studying biological systems are now culminating in the definition of a new class of machines that researchers refer to as soft robots [4], which connects strongly with biomimetics (**Figure 1**).

Similar to humans, such robots will, in addition to hard components such as bones, have soft bodies made of soft materials, and will be capable of soft movements and soft interactions with people (**Figure 2**). A recent trend in soft robotics is to simplify the typically computationally intensive, neutrally inspired control through smart morphological design and use of functional materials [5–7]. There is no doubt that soft biomimetic materials enable most of the automation of tasks beyond the capacities of current robotic technology. The full integration of biomimetic materials and devices into complete robotic systems is of significant interest in science and technologies, but is full of complex challenges.

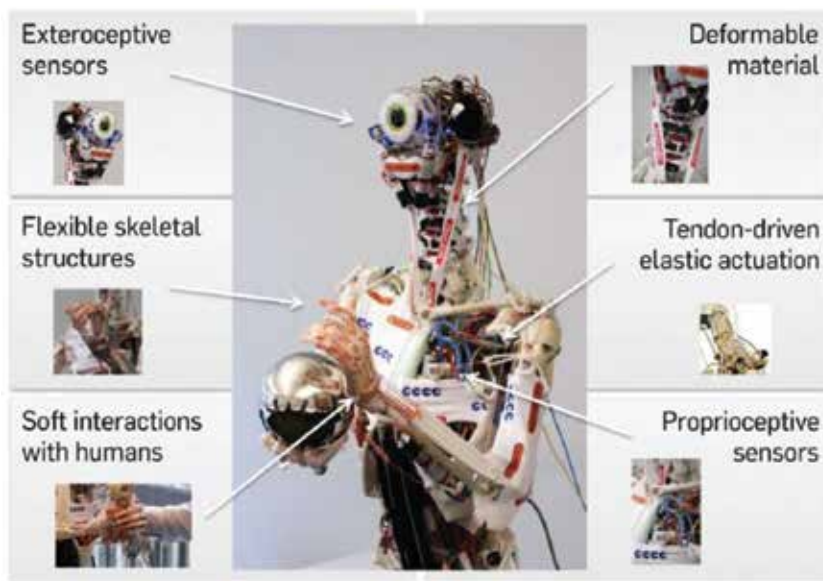


Figure 2. An anthropomorphic humanoid robot ECCE (Embodied Cognition in a Compliantly Engineered Robot) [8].

1.2. Design and synthesis of 2D materials

In a biomimetic material, biomimetic behaviors refer to changing the material properties of the underlying base material to actuating, sensing, and communicating. Some possible mechanisms involve changes of stiffness, volume and shape, electronic properties, or color

(Figure 3). For example, inorganic nanowires such as single-walled carbon nanotube (SWCNT), ZnO, Cu, In_2O_3 , and etc. offer new material basis and opportunities for flexible electronics that enables many biomimetic applications, including sensors, display devices, and logic gates [9]. All-dielectric meta-materials that can respond to both the electric and magnetic fields of light, support large optical chirality and anisotropy, have promising potential to be used in fabrication of biomimetic meta-surfaces [10]. Ionic polymer-metal composites show large deformation in the presence of low applied voltage and therefore have been widely used as highly active actuators and sensors [11]. Shape-memory polymers are an important class of stimuli-responsive soft materials for which shape-shifting behavior can be programmed, enabling the application as artificial muscles [12]. Overall, from inorganic to organic, from nanoscale to macroscale, various range of materials can be fabricated into designable biomimetic devices including electronic skins [13, 14], artificial muscles [15, 16], etc.

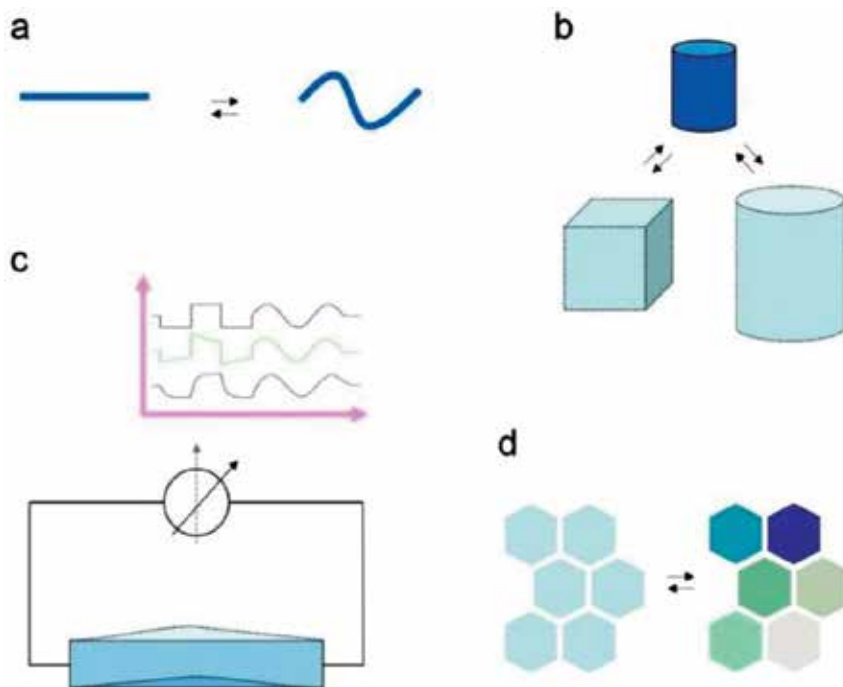


Figure 3. Examples of a biomimetic material working toward changing the crucial properties of the base material. Changes in (a) stiffness and (b) shape/volume could enable shape-changing actuation materials. Robotic skins could utilize changes in (c) electronic responses and (d) appearance to sense and communicate.

Particularly, due to their inherent flexibility and novel properties, 2D-layered nanomaterials as the *in situ* unit of biomimetic materials hold great promise in flexible and versatile biomimetic devices. Here we summarized the reported alternative 2D materials, and the description has been organized in an order according to their synthesis methods.

In addition to graphene, micromechanical exfoliation has been extended to prepare other 2D inorganic materials. In fact, following this approach, individual crystal sheets from a variety of layered materials have been isolated. Monolayers of BN, MoS₂, NbSe₂, and Bi₂Sr₂CaCu₂O_x have been prepared by rubbing a layered crystal against a substrate and leaving random flakes on it [17]. Among the resulting flakes, single layers were always found. This method leads to high crystal quality and macroscopic continuity, and is considered as one of the easiest and the fastest ways, as in the case of well-known graphene. However, a serious drawback is noticed: monolayers obtained by micromechanical exfoliation are in a great minority among accompanying thicker flakes. Despite allowing the first example of characterization of one-atom-thick monolayers, this is not a feasible procedure for large-scale production of 2D materials for technological applications. Therefore, in the last few years, new methods have been developed to approach scalable synthesis of 2D inorganic materials.

Vapor deposition techniques have been most extensively explored due to their potential for high scalability and morphological control. By balancing the production cost and the above prerequisites, chemical vapor deposition (CVD) is the most promising route to produce large-area device-grade graphene. Normally, the procedure involves two steps: *first*, pyrolysis of a precursor to form carbon and disassociation of carbon atoms, and then the formation of the graphene. The pyrolysis to disassociate carbon atoms must be carried out on selected substrates to prevent the precipitation of carbon clusters during the gas phase. This leads to a problem and metal catalysts must be used to reduce the reaction temperature required for pyrolytic decomposition of precursors. During the reaction, the metal substrate not only works as a catalyst to lower the energy barrier of the reaction, but also determines the graphene deposition mechanism, which ultimately affects the quality of graphene [18]. Graphene growth has been demonstrated on a variety of transition metals such Ni, Pd, Ru, Ir, or Cu, and is also achievable on insulating SiC [19]. In a similar process, metal containing precursors [e.g., MoO₃, WO₃, or (NH₄)₂MoS₄] are vaporized and reacted with chalcogen elements through vapor-solid reactions, leading to the growth of 2D materials beyond graphene on a substrate downstream [20]. Alternatively, 2D material bulk powders can also be used as the precursor directly [21]. For example, Feng et al. [22] employed a tree-zone furnace to synthesize large-area 2D MoS_{2(1-x)}Se_{2x} semiconductor alloys.

Liquid-phase exfoliation is Low-cost and scalable method which has been widely used for preparing individual sheets of 2D materials. Typically, this method requires homogeneous dispersion of 2D materials in diverse solvents or aqueous solutions. With the assistance of sonication, the weak van der Waals bonds between the layers are broken and individual layers are obtained. Shen et al. [23] have reported an effective strategy to exfoliate 2D materials in a high yield. In addition to the total surface tension, efficient solvents for liquid-phase exfoliation were found to be those which have a similar ratio of polar components to dispersive components of surface tension to the 2D materials. Mono- to few-layer graphene, WS₂, MoS₂ h-BN, MoSe₂, Bi₂Se₃, TaS₂, and SnS₂ were prepared with low-toxic and low-boiling point solvents, such as 1:1 IPA/water for graphene, WS₂, h-BN, and MoSe₂; 1:4 IPA/water for Bi₂Se₃, and SnS₂; 7:3 IPA/water for MoS₂, acetonitrile for TaS₂.

2. 2D materials enable sensing, actuation, and communication

Smart advanced materials that are flexible, adaptable, multifunctional, and meanwhile “green” are essential for biomimetic approaches. Since it was *first* isolated in 2004 [24], graphene has attracted tremendous attention because of its extraordinary electrical, thermal, and mechanical properties [25–27]. It is not surprising that graphene leads to 2D material research and has developed *rapidly* to several important applications such as energy technologies [28, 29], electronics [30, 31], and biomedicine [32, 33]. Among these applications, graphene-based intelligent devices that can spontaneously detect and respond to external stimuli are of broad practical interest and importance. Inspired by the great success achieved through the research of graphene-based materials, the similar ideas and methodologies have also been extended to study other layered materials. This is well indicated by the number of new 2D inorganic nanomaterials blossomed in the past few years. In this section, we offer a brief overview of the successes reported on the biomimetic performance of 2D materials.

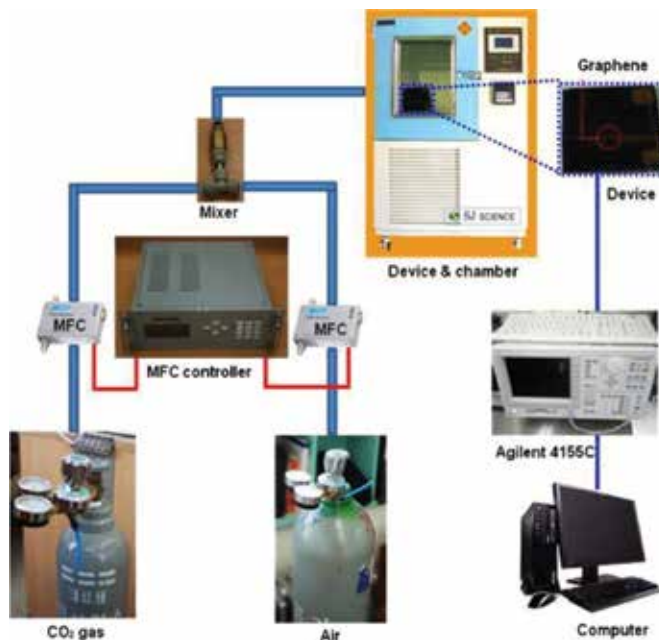


Figure 4. Experimental setup for measurements performed using the graphene CO₂ gas sensor [35].

2.1. Sensing

2D materials are usually good candidates for gas sensors due to their large surface-to-volume ratio and the associated charge transfer between gas molecules and the substrates [34]. Graphene has very high electron mobility at room temperature, and hence, its gas sensitivity

is very high. Yoon et al. [35] fabricated a graphene-based CO₂ gas sensor by mechanical cleavage and micromachining. The graphene sensor shows significant conductance changes when exposed to various concentrations of CO₂ in air. The response time of the sensor is less than 10 s. The overall system is illustrated in **Figure 4**. They have shown the principle idea, but the sensing systems might need to be upgraded to wearable devices in order to meet the fashion applications. Late et al. [36] reported a comprehensive suite of sensing behavior of atomically thin-layered MoS₂ structures in a transistor-like configuration. MoS₂-based field emission transistor (FET) showed outstanding sensitive response to NH₃, NO₂, as well as water vapor at room temperature and atmospheric pressure. 2D material-based FET showed improved mobility and wearable capability, due to its nanoscale size and facile and precise testing systems. Kou et al. [34] reported first-principles calculations that examine the adsorption of several typical molecules, CO, CO₂, NH₃, NO, and NO₂ on phosphorene. They determined their preferential binding positions and the corresponding binding energy. Their results show that the strength of binding is highly dependent on the extent of charge transfer between the adsorbed molecules and the phosphorene layer, which is similar to that observed in graphene and MoS₂. However, the adsorption of gas molecules on phosphorene is notably stronger resulting in a more pronounced effect on the sensitivity.

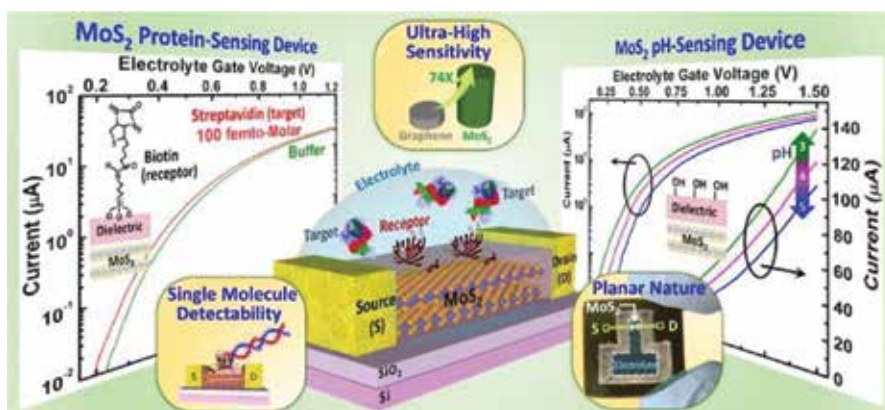


Figure 5. MoS₂-based FET biosensors, which provides high sensitivity and at the same time offers possibility for facile patterning and device fabrication [38].

Biosensors based on 2D material FETs have also attracted much attention, as they offer rapid, inexpensive, and label-free detection of biologically related signals. Development of 2D material FETs may bridge the technological gap between signal transduction, conditioning, processing, and wireless transmission in a wearable biosensing device, by merging plastic-based sensors that interface the skin with silicon-integrated circuits on a flexible circuit board for complex signal processing [37]. Sarkar et al. [38] demonstrated a FET biosensor based on MoS₂. This sensor shows ultrahigh sensitivity (713 for a pH change of 1 unit) and wide operation range (pH of 3–9) (**Figure 5**). It also demonstrates specific detection of protein as well as an extremely high sensitivity of 196 even at 100 femtomolar concentration.

In addition to the examples described above, sensing platforms equipped or integrated with temperature, strain, and humidity sensors have attracted more and more attention due to their natural skin-like biomimetic sensing behavior [39–41]. Trung et al. [42] developed a very simple fabrication process to realize the all-elastomeric temperature sensor array. They integrated a strain sensor on a platform which can be attached as a patch to objects or human skin (**Figure 6**). Reduced graphene oxide (rGO) nanosheets embedded in an elastomeric polyurethane matrix were used as the temperature sensing layer. Notably, most function layers of the device are intrinsically transparent and stretchable.

Wu et al. [43] reported an experimental observation of piezoelectricity in single-atomic-layer 2D MoS₂ and explored its application in mechanical energy harvesting and piezotronic sensing (**Figure 7**). Cyclic stretching and releasing of odd-layer MoS₂ flakes produced oscillating electrical outputs, which could convert mechanical energy into electricity. The strain-induced polarization charges in single-layer MoS₂ can also modulate charge carrier transport at the MoS₂–metal barrier and enables enhanced strain sensing. This study has demonstrated the potential of 2D nanomaterials for powering nanodevices, adaptive bioprobes, and tunable/stretchable electronics/optoelectronics.

In short, these sensors have shown great potential for their adaptability to wearable skin electronics for recognition of human activity and environmental changes.

2.2. Actuation

The crumpling of materials is widely observed in various objects as small as biological membranes, in objects as thin as a piece of paper, and in systems as large as the Earth's crust. 2D actuation systems responsive to electrochemical, light, and other external stimuli can convert different energy forms (electric, chemical, photonic, thermal, etc.) to mechanical energy that is potentially profitable for diverse applications ranging from robots, sensors to memory chips [15, 44]. Theoretically, Roger et al. [45] have studied the electrochemical actuation of monolayer graphene upon charge injection and ionic liquid (IL) electrolyte immersion. They have concluded that the electrostatic double layer could induce strains of more than 1% and its contribution to the overall strain was always equal to or higher than that of the quantum-mechanical strain (~0.2%) from charge injection of -0.1 e per C atom. Based on these theoretical predictions, GO is in principle an excellent material for actuators and artificial muscles.

Zhang, et al. [46] performed molecular dynamics simulation to create a nanosized graphene origami box. By warping the top graphene layer downward and the bottom graphene layer upward, the cross-shaped cubic graphene nanocage could encapsulate nano objects such as biomolecules (**Figure 8**). This paradigm opens up a new avenue to control the 3D architecture of 2D-layered materials and provides a feasible way to exploit and fabricate the 2D nanosized actuators.

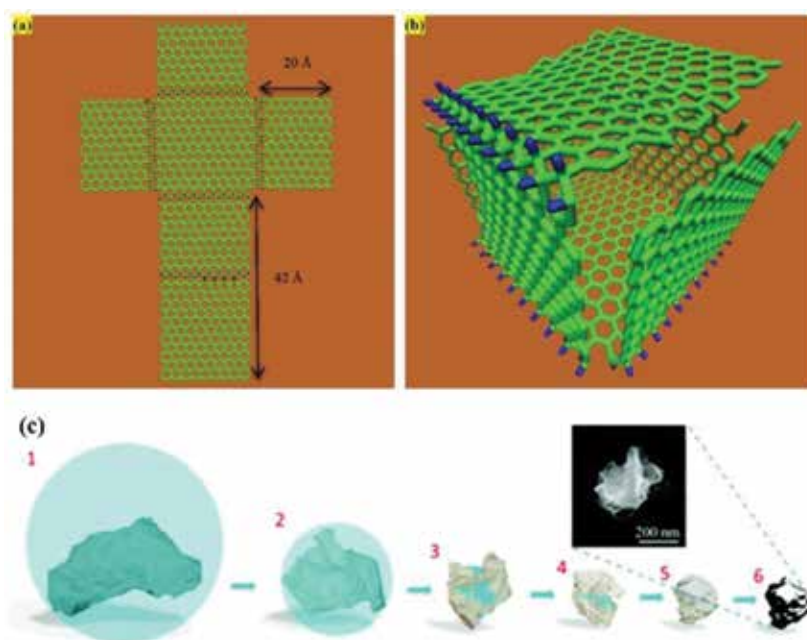


Figure 8. Programmable graphene folding with designed morphology. (a) and (b) represent the initial and final configurations of a graphene nanocage, respectively. (c) Schematic illustrating rapid loss of H_2O in GO and subsequent crumpling of GO nanosheets [46, 47].

Ma et al. [47] experimentally proved that GO in aqueous solution could be aerosolized and dried to produce crumpled nanopaper-like sheets, which are similar to the graphene nanocage. They used online size selection and aerosol mass analysis to determine the fractal dimension (D) of crumpled GO nanosheets. D is able to be tuned by altering solvent conditions. Typically, a 10% acetone mixture increases D to 2.68 ± 0.02 from 2.54 ± 0.04 . Calculations of the confinement force indicate that crumpling of GO nanosheets is driven by the capillary force associated with rapid loss of the solvent.

Similarly, a fluidic motion of alcohol molecules which across the interlayer gap in layered double hydroxide (LDH) could enable rapid and reversible tuning of interlayer spacing of the LDH at sub-Å precision, reported by Ishihara et al. [48]. This so-called hydrogen bond-driven “homogeneous intercalation” mechanism could be used in rapid, reversible, and ultraprecise actuation of LDH materials.

Similar approaches could also be applied to magadiite [49] and layered potassium hexaniobate [50]. Novel photoactivated artificial muscle model units could be obtained as they reported. For example, as seen in **Figure 9**, it is clearly observed on a cross-cut section of the layered hybrid film that upon photoirradiation of a layered hexaniobate intercalated with a polyfluoroalkyl azobenzene derivative, a very large magnitude lateral movement (sliding) of the nanosheets was reversibly induced. By applying this strategy, organic/inorganic hybrid nanosheets reversibly and horizontally slide on a macroscale upon on/off photoirradiation, which results in vertically shrinking and expansion of the interlayer spaces in the layered

hybrid structure. The sliding movement of the structure on such a giant scale is the first example of an artificial muscle model unit having remarkable similarity to that in natural muscle fibrils.

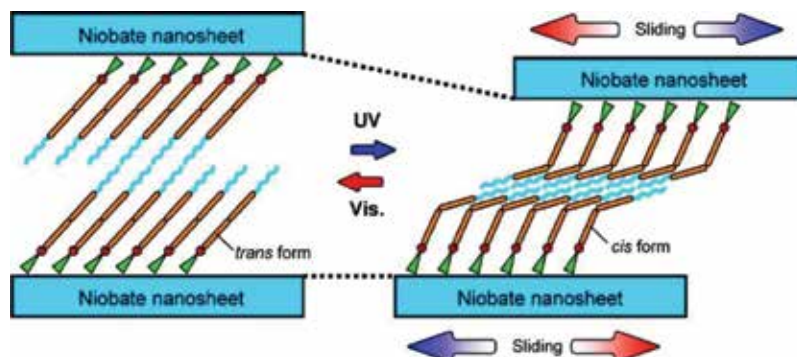


Figure 9. Schematic diagram of the niobate nanosheet sliding movement and interlayer distance change induced by photochemical trans–cis isomerization of the azobenzene molecules [50].

2.3. Communication

Emotional (or feeling) communication skills are natural behavior in biological systems. However, similar communication between humans and autonomous robots is a tremendous challenge to be achieved.

Appearance and texture identification in an artificial skin allows creating and broadcasting emotional cues, which may facilitate the acquisition of the robot’s emotional behavior. The fabrication of a network consisting of mechanically flexible sensors is the key to achieve artificial intelligence that comes into direct contact with humans for biomedical applications such as prosthetic skin. To mimic the interaction behavior such as tactile sensing properties of natural skin, large arrays of pixel sensors on a flexible and stretchable substrate are usually required [51]. The integration of 2D materials in FET arrays as the dielectric layer leads to a new type of active sensing devices which not only have high sensitivity but also enable to initiate responsive interactive behavior. In this context, there are several cases reported. For example, Wang et al. [52] integrated various electronic, sensor, and light-emitting components (involving both organic and inorganic materials) on a thin plastic substrate (**Figure 10**). This work demonstrated a possibly practical technology platform serving as a flexible user-interactive system that could not only detect and spatially map external stimuli such as pressure, but also respond with a seamlessly integrated display. The responsive pressure profile is instantaneously visible without the need of sophisticated data acquisition circuits and electronic boards on such systems. Such approach based on integration of 2D functional materials into a flexible thin film device could lead to an emerging and hot research topic, i.e., electronic skin, or e-skin.

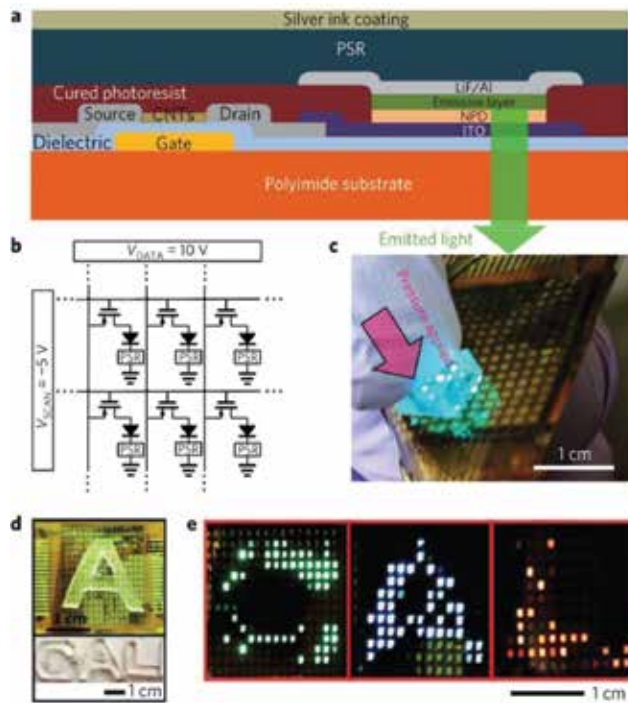


Figure 10. (a) Cross-sectional schematic showing one pixel of the interactive e-skin device, consisting of various components. (b) Schematic of the e-skin circuit matrix. (c) Photograph of an integrated device showing that light is locally emitted when the device surface is touched. (d) PDMS slabs with C, A, and L shapes are prepared and used to apply pressure onto the sensor array. (e) Green, blue, and red color interactive e-skins are used to spatially map and display the pressure [52].

3. Functional biomimetic devices based on 2D materials

As described above, the development of integrated intelligent devices is essential to the realization of biomimetic systems. In this section, we discuss the two most promising classes of biomimetic devices: e-skins and artificial muscles based on 2D materials.

3.1. e-Skins

The skin, as the largest organ in the human body, is mechanically self-healing and can provide a variable degree of touch sensitivity. Mimicking the functions of natural skins is therefore widely accepted to be very important in the future for robots used by humans in daily life for numerous applications. Thus, the development of an artificial skin, also known as electronic skin (e-skin) that is flexible and stretchable [51–54], sensitive enough to perceive touch [55–57], and yet able to heal itself following damage [58, 59] is in high demand in robotic applications.

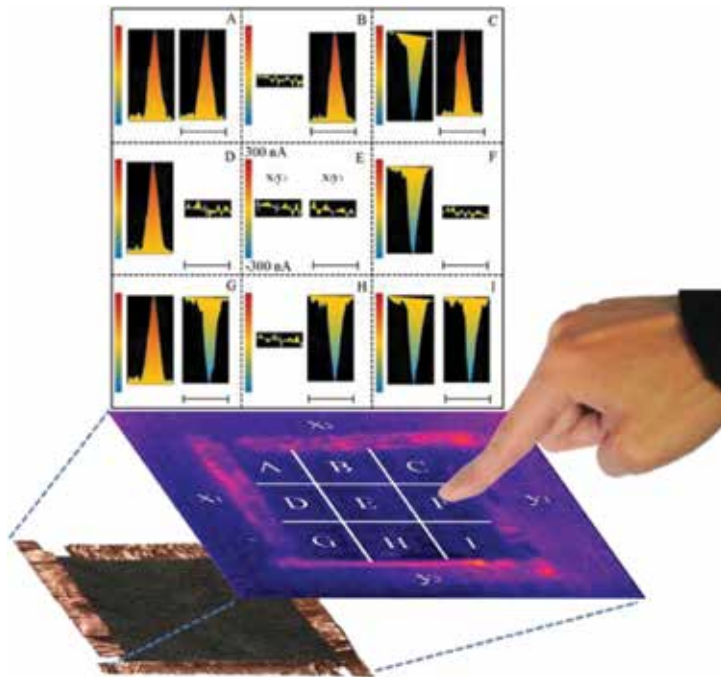


Figure 11. Real-time current curves of the sensor pad during a finger touch/remove cycle on its surface [60].

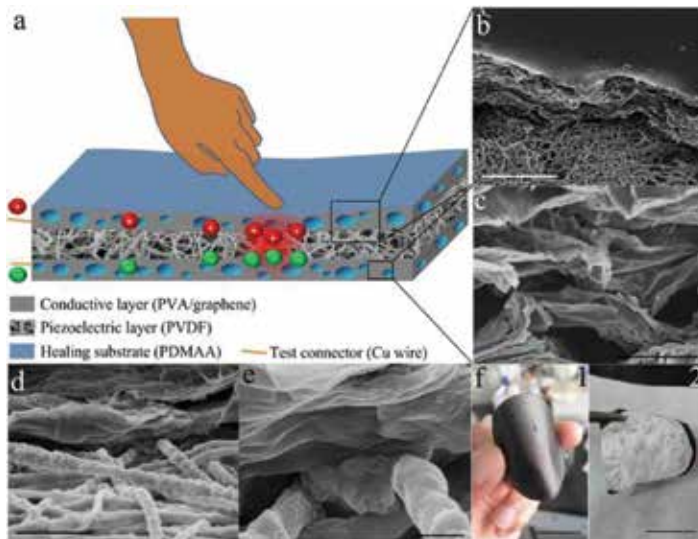


Figure 12. (a) Schematic of the hybrid e-skin and its pressure sensitivity.(b–e) Cross-sectional FESEM images of the hybrid e-skin showing microscopic structures and the boundary between functional layers. Scale bars are 30 μm , 5 μm , 3 μm , and 500 nm, respectively.(f) Photographs of the hybrid e-skin. Scale bar is 2 cm [59].

Hou et al. [60] designed and fabricated a novel reduced graphene oxide foam (rGOF) that is free-standing, flexible, and elastic. As shown in **Figure 11**, the rGOF shows temperature sensitivity based on thermoelectric effects in the graphene with assistance of its good electrical properties. The rGOF can respond rapidly to finger pressure owing to the finger heating effects. As a proof of concept, the authors also produced rGOF pressure sensor pad that can locate finger pressure points and measure the pressure level. Most importantly, all sensing abilities of this device can operate by itself without the need of any additional power supply.

Hou et al. [59] also presented the first self-healing, mechanically strong and stretchable, self-activated pressure-sensing device based on rGO. The device is composed of various functional components including piezoelectric and electrically conductive layers as well as a healing substrate **Figure 12**. Poly(N,N-dimethylacrylamide), poly(vinyl alcohol), rGO, and polyvinylidene difluoride are employed in this hybrid device. It is suggested that preparing flexible and porous hybrid foams with interconnected 3D networks is a practical way to fabricate stretchable and self-healing thin film e-skin.

In order to improve the texture resolution of e-skin, FET technology is usually involved in the design and fabrication of sensors. Mannsfeld et al. [51] reported an organic thin film pressure sensor, which employs a key organic FET structure consisting of a thin, regularly structured rubber. The dielectric capacitance in organic FET devices directly depends on the output current, which enables the sensing of an applied pressure. This device provides high sensitivity in both medium- and low-pressure regimes. Besides, unprecedentedly fast response and relaxation times ($\ll 1$ s) are also reported.

Sun et al. [61] reported a piezopotential-powered active matrix strain sensor arrays which combined coplanar gate graphene transistors and piezoelectric nanogenerators. The strain sensor demonstrated excellent performances including a high sensitivity (gauge factor = 389) and a minimum detectable strain as low as 0.008%. Excellent device durability was also observed after 3000 bending-releasing cycles. This transparent and conformal strain sensor could be mounted onto a human hand for continuous monitoring of hand movements.

In addition to graphene, other 2D nanomaterials, such as MoS₂, WS₂, and vanadium disulfide (VS₂), have also been recently explored for effective conversion of environmental stimuli into electric signals.

For example, The VS₂ nanosheets with a quasi-two-dimensional electronic structure are very promising building block material for high moisture responsiveness. Intriguingly, the structural characteristics and calculation results indeed revealed theoretical feasibility to achieve VS₂ material in ultrathin structures with only a few atomic layers. Feng et al. [62] synthesized ultrathin VS₂ nanosheets and assembled them into a highly cooriented structure, which had a maximum resistance response of almost two orders of magnitude toward moisture. Using VS₂ nanosheets as the sole functional material, a new concept, flexible touchless positioning interface based on the spatial mapping of moisture distribution was demonstrated (**Figure 13**). This moisture-based positioning interface provides a new conceptual approach to practical real-time moisture mapping matrix or noncontact control interfaces for advanced man-made interactive systems.

Considering the excellent photothermal properties of rGO and GO [68], as well as its high flexibility and mechanical robustness, a rGO/GO hybrid paper holds great potential for photo-thermoreponsive actuator applications. Mu et al. exploited these properties to yield GM paper with reversible, fast (~ 0.3 s), powerful (7.5×10^5 N/kg force output), and controllable mechanical deformation and recovery, in response to moisture, heat, and light. The response of this water-driven actuator to multiple stimuli allows the artificial muscles and electric generators to be fabricated. Furthermore, it was found that with a programmed dual-gradient (vertical and lateral) structure, a self-folding all-graphene origami was also developed to demonstrate three types of capability: (i) producing predesigned shapes, (ii) walking, and (iii) turning a corner (Figure 14) [69].

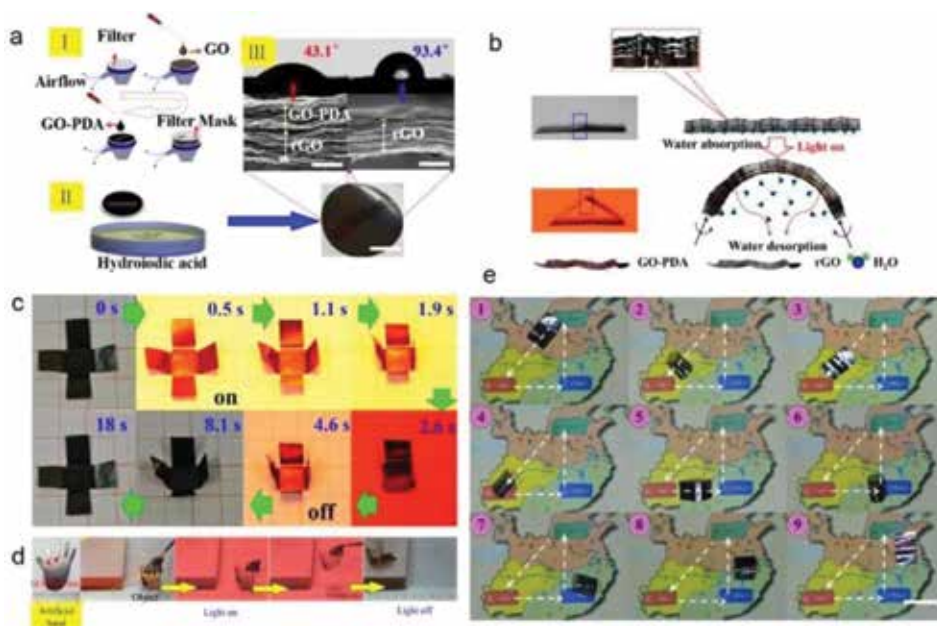


Figure 14. (a) I. Illustration of the mask-assisted filtration process, scale bar is 2 cm; II. Cross-sectional SEM images of different regions of the actuator, scale bar is 1 μm ; III. CA measurement of the opposite surfaces of the actuator. (b) Schematic representations of the structures and mechanisms of the actuator paper. (c) Time profiles of self-folding movements of a cross-shaped piece of paper with and without NIR light irradiation. (d) Optical images showing artificial/robotic hand holding an object driven by light irradiation. (e) Optical images showing the “micro robot” walking and turning on a map driven by light irradiation [69].

The hydration-triggered actuation of GO materials opens up a new possibility to synthesize graphene-based actuators responsive to changes in environmental water and/or relative humidity. Cheng et al. [70] designed and fabricated the region-asymmetric graphene/graphene oxide (G/GO) fiber actuators in virtue of the laser positioning reduction of the freshly spun GO fibers. The graphene-based fiber actuators display complex and well-controlled motion and deformation in a predetermined manner in response to moisture changes. This work offers a strategy for producing region-asymmetric G/GO fibers which can be deformed deliberately

and can walk as a single-fiber robot along a channel. The fiber-based actuator with such a unique structure provides a new platform for the development of the wearable devices such as smart textiles.

Differently, the mechanisms based on ionic liquid (IL) electrolyte immersion have also been reported for graphene-based actuators. Lu et al. [71] showed that IL could be inserted to separate the layers of paralleled graphene nanosheets. The rGO-IL with 66.7 wt% of IL displayed a 98% variation in the thickness upon a 2 V electrical voltage stimulation.

Alternatively, graphene can be used as electrodes [73], fillers [74, 75], and conductive substrates [72] for actuators rather than being as the solo functional material. These have been well reviewed elsewhere. We next focus on other 2D materials themselves in biomimetic actuation applications. However, the successful examples are still very few up to date.

Yang et al. [76] tailored magnetic, optical, and electrical properties of ReSe₂ nanosheets by local strain engineering through formation of ReSe₂ wrinkles on elastomeric substrates. Local strain induced by generation of wrinkles could perform several actions: (1) to modulate the optical gap as evidenced by red-shifted photoluminescence peaks, (2) to enhance light emission, (3) to induce magnetism, and (4) to adjust electrical properties. Their work not only shows how to create materials with vastly different properties at the nanoscale, but also enables a wide range of applications based on 2D materials, including strain sensors, stretchable electrodes, flexible field-effect transistors, artificial-muscle actuators, solar cells, and other spintronic, electromechanical, piezoelectric, photonic devices.

Yang et al. [77] analyzed electromechanical coupling effects in suspended doubly clamped single-layer MoS₂ structures, by which they designed suspended-channel FETs and vibrating-channel nanoelectromechanical resonators. In direct current gating scenario, signal transduction processes (such as deflection, electrostatic actuation, mobility, straining on bandgap, carrier density, and their intricate cross-interactions) have been analyzed with considering the strain-enhanced mobility (by up to 4 times), in order to determine the transfer characteristics.

Yuan et al. [78] reported synthesis of monolayer perovskite-like KCa₂Nb₃O₁₀ nanosheets, and therefore they were able to study the size-dependent properties of these nanosheets as monolayer nanosheet seed layers to grow functional thin films for piezo-microelectromechanical systems (piezo-MEMS). Their results implied that larger Ca₂Nb₃O₁₀ nanosheets can be useful for constructing scale-up piezo-MEMS devices, such as microactuators.

4. Outlook and perspective

Over the past 5 years, advances in 2D material fabrication, 3D assembly, and biological analysis have accelerated development of soft materials in biomimetic applications. In the future, integration of other sensor components can be predicted using a similar platform to enable more sophisticated human-surface interfacing. Additional circuits, sensors (e.g., strain gauges, thermal flux sensors), and actuators (LEDs, pacing/ablation electrodes) have been designed with these design considerations in order to enable conformal integration with soft and

curvilinear organs (**Figure 15**) [39, 79]. We believe that these 2D material-based biomimetic platforms would find a wide range of applications in automotive control panels, interactive input devices, robotics, and medical and health monitoring devices.

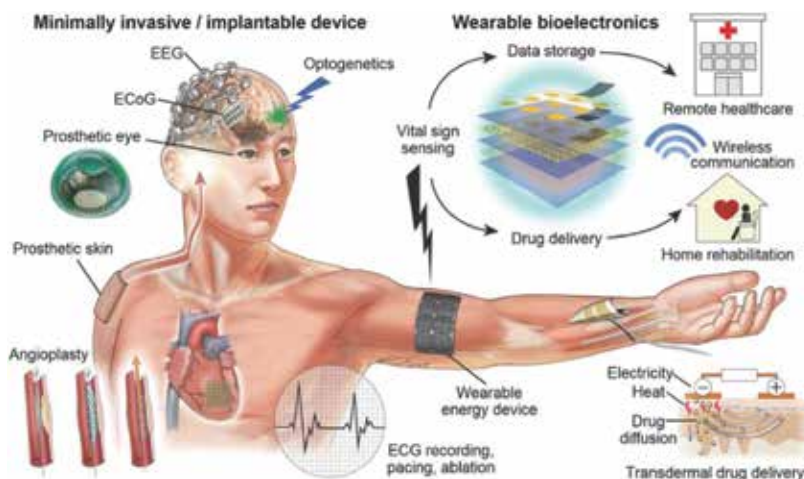


Figure 15. Bio-integrated flexible and stretchable systems: schematic illustration of bio-integrated electronics in development today across a broad range of biomedical applications. Minimally invasive and implantable devices include electrophysiological sensors (ECoG, ECG), angioplasty tools, prosthetic eye/skin, and optoelectronic nerve stimulator, etc. Wearable bioelectronics include physiological sensors (pressure, strain, temperature sensors) integrated with transdermal drug delivery devices and data storage devices. Continuous monitoring and real-time feedback therapy are performed in conjunction with the wireless communication. Energy supply module is an essential component to bioelectronics systems for mobile and personalized healthcare [34, 38, 73, 76, 77].

Author details

Chengyi Hou, Minwei Zhang and Qijin Chi*

*Address all correspondence to: cq@kemi.dtu.dk

Department of Chemistry, Technical University of Denmark, Kongens Lyngby, Denmark

References

- [1] Lepora NF, Verschure P, Prescott TJ, The state of the art in biomimetics. *Bioinspiration & Biomimetics*. 2013; 8: 013001. Doi:10.1088/1748-3182/8/1/013001.
- [2] Huebsch N, Mooney DJ, Inspiration and application in the evolution of biomaterials. *Nature*. 2009; 462: 426–432. Doi:10.1038/nature08601

- [3] McEvoy MA, Correll N, Materials that couple sensing, actuation, computation, and communication. *Science*. 2015; 347: 1261689. DOI: 10.1126/science.1261689.
- [4] Rus D, Tolley MT, Design, fabrication and control of soft robots. *Nature*. 2015; 521: 467–475. DOI: 10.1038/nature14543
- [5] Kim S, Laschi C, Trimmer B, Soft robotics: a bioinspired evolution in robotics. *Trends in Biotechnology*. 2013; 31: 23–30. DOI:10.1016/j.tibtech.2013.03.002
- [6] Studart AR, Additive manufacturing of biologically-inspired materials. *Chemical Society Reviews*. 2016; 45: 359–376. DOI: 10.1039/c5cs00836k
- [7] Case JC, White EL, Kramer RK, Soft material characterization for robotic applications. *Soft Robotics*. 2015; 2: 80–87. DOI: 10.1089/soro.2015.0002.
- [8] Pfeifer R, Lungarella M, Iida F, The challenges ahead for bio-inspired 'soft' robotics. *Communications of the Acm*. 2012; 55: 76–87. DOI:10.1145/2366316.2366335.
- [9] Liu Z, Xu J, Chen D, Shen GZ, Flexible electronics based on inorganic nanowires. *Chemical Society Reviews*. 2015; 44: 161–192. DOI: 10.1039/C4CS00116H.
- [10] Jahani S, Jacob Z, All-dielectric metamaterials. *Nature Nanotechnology*. 2016; 11: 23–36. DOI: 10.1038/NNANO.2015.304
- [11] Bhandari B, Lee GY, Ahn SH, A review on IPMC material as actuators and sensors: fabrications, characteristics and applications. *International Journal of Precision Engineering and Manufacturing*. 2012; 13: 141–163. DOI: 10.1007/s12541-012-0020-8
- [12] Zhao Q, Qi HJ, Xie T, Recent progress in shape memory polymer: new behavior, enabling materials, and mechanistic understanding. *Progress in Polymer Science*. 2015; 50: 79–120. Doi:10.1016/j.progpolymsci.2015.04.001
- [13] Bauer S, Simona BG, Graz I, Kaltenbrummer M, Keplinger C, Schwödiauer R, 25th anniversary article: a soft future: from robots and sensor skin to energy harvesters. *Advanced Materials*. 2014; 26: 149–162. DOI: 10.1002/adma.201303349
- [14] Park M, Park J, Jeong U, Design of conductive composite elastomers for stretchable electronics. *Nano Today*. 2014; 9: 244–260. DOI:10.1016/j.nantod.2014.04.009
- [15] Zhao Y, Song L, Zhang ZP, Qu LT, Stimulus-responsive graphene systems towards actuator applications. *Energy & Environmental Science*. 2013; 6: 3520–3536. DOI: 10.1039/C3EE42812E
- [16] Fleischmann EK, Zentel R, Liquid-crystalline ordering as a concept in materials science: from semiconductors to stimuli-responsive devices. *Angewandte Chemie-International Edition*. 2013; 52: 8810–8827. DOI: 10.1002/anie.201300371
- [17] Mas-Balleste R, Gomez-Navarro C, Gomez-Herrero J, Zamora F, 2D materials: to graphene and beyond. *Nanoscale*. 2011; 3: 20–30. DOI: 10.1039/C0NR00323A

- [18] Zhang Y, Zhang LY, Zhou CW, Review of chemical vapor deposition of graphene and related applications. *Accounts of Chemical Research*. 2013; 46: 2329–2339. DOI: 10.1021/ar300203n
- [19] Mattevi C, Kim H, Chhowalla M, A review of chemical vapour deposition of graphene on copper. *Journal of Materials Chemistry*. 2011; 21: 3324–3334. DOI: 10.1039/c0jm02126a
- [20] Bhimanapati GR, et.al., Recent advances in two-dimensional materials beyond graphene. *Acs Nano*. 2015; 9: 11509–11539. DOI:10.1021/acsnano.5b05556.
- [21] Wang F, Wang ZX, Wang QS, Wang FM, Yin L, Xu K, Huang Y, He J, Synthesis, properties and applications of 2D non-graphene materials. *Nanotechnology*. 2015; 26: 292001. DOI:10.1088/0957-4484/26/29/292001.
- [22] Yang L, Wang WH, Huang J, Huang JL, Zhang JY, Xiang B, Large-area synthesis of monolayered $\text{MoS}_2(1-x)\text{Se}_2x$ with a tunable band gap and its enhanced electrochemical catalytic activity. *Nanoscale*. 2015; 7: 10490–10497. DOI: 10.1039/c5nr02652k
- [23] Shen JF, He YM, Wu JJ, Gao CT, Keyshar K, Zhang X, Yang YC, Ye MG, Vajtai R, Lou J, Ajayan PM, Liquid phase exfoliation of two-dimensional materials by directly probing and matching surface tension components. *Nano Letters*. 2015; 15: 5449–5454. DOI: 10.1021/acs.nanolett.5b01842
- [24] Novoselov KS, Geom AK, Morozov SV, Jiang D, Zhang Y, Dubonos SV, Grigorieva IV, Firsov AA, Electric field effect in atomically thin carbon films. *Science*. 2004; 306: 666–669. DOI:10.1126/science.1102896
- [25] Katsnelson MI, Graphene: carbon in two dimensions. *Materials Today*. 2007; 10: 20–27. DOI:10.1016/S1369-7021(06)71788-6
- [26] Park S, Ruoff RS, Chemical methods for the production of graphenes. *Nature Nanotechnology*. 2009; 4: 217–224. DOI: 10.1038/NNANO.2009.58
- [27] Berger C, et al., Electronic confinement and coherence in patterned epitaxial graphene. *Science*. 2006; 312: 1191–1196. DOI: 10.1126/science.1125925
- [28] El-Kady MF, et al., Laser scribing of high-performance and flexible graphene-based electrochemical capacitors. *Science*. 2012; 335(6074): 1326–1330.
- [29] Yang XW, Cheng C, Wang YF, Qiu L, Li D, Liquid-mediated dense integration of graphene materials for compact capacitive energy storage. *Science*. 2013; 341: 534–537. DOI: 10.1126/science.1239089
- [30] Dean CR, et al., Boron nitride substrates for high-quality graphene electronics. *Nature Nanotechnology*. 2010; 5: 722–726. DOI:10.1038/NNANO.2010.172
- [31] Wei ZQ, et al., Nanoscale tunable reduction of graphene oxide for graphene electronics. *Science*. 2010; 328: 1373–1376. DOI:10.1126/science.1188119

- [32] Yang K, Feng LZ, Shi XZ, Liu Z, Nano-graphene in biomedicine: theranostic applications. *Chemical Society Reviews*. 2013; 42: 530–547. DOI: 10.1039/c2cs35342c
- [33] Byun J, Emerging frontiers of graphene in biomedicine. *Journal of Microbiology and Biotechnology*. 2015; 25: 145–151. DOI: 10.4014/jmb.1412.12045
- [34] Kou LZ, Frauenheim T, Chen CF, Phosphorene as a superior gas sensor: selective adsorption and distinct I-V response. *Journal of Physical Chemistry Letters*. 2014; 5: 2675–2681. DOI:10.1021/jz501188k
- [35] Yoon HJ, Jun DH, Yang JH, Zhou ZX, Yang SS, Cheng MMM, Carbon dioxide gas sensor using a graphene sheet. *Sensors and Actuators B-Chemical*. 2011; 157: 310–313. DOI: 10.1016/j.snb.2011.03.035
- [36] Late DJ, et al., Sensing behavior of atomically thin-layered MoS₂ transistors. *ACS Nano*. 2013; 7: 4879–4891. DOI: 10.1021/nn400026u
- [37] Gao W, et al. Fully integrated wearable sensor arrays for multiplexed in situ perspiration analysis. *Nature*. 2016; 529: 509–514. DOI:10.1038/nature16521
- [38] Sarkar D, Liu W, Xiun XJ, Anselmo AC, Mitragotri S, Banerjee K, MoS₂ field-effect transistor for next-generation label-free biosensors. *ACS Nano*. 2014; 8: 3992–4003. DOI: 10.1021/nn5009148
- [39] Kim J, et al., Stretchable silicon nanoribbon electronics for skin prosthesis. *Nature Communications*. 2014; 5. DOI: 10.1038/Ncomms6747
- [40] Hattori Y, et al., Multifunctional skin-like electronics for quantitative, clinical monitoring of cutaneous wound healing. *Advanced Healthcare Materials*. 2014; 3: 1597–1607. DOI: 10.1002/adhm.201400073
- [41] Yeo WH, et al., Multifunctional epidermal electronics printed directly onto the skin. *Advanced Materials*. 2013; 25: 2773–2778. DOI: 10.1002/adma.201204426
- [42] Trung TQ, Ramasundaram S, Hwang BU, Lee NE, An all elastomeric transparent and stretchable temperature sensor for body attachable wearable electronics. *Advanced Materials*. 2016; 28: 394–394. DOI: 10.1002/adma.201504441
- [43] Wu WZ, et al., Piezoelectricity of single-atomic-layer MoS₂ for energy conversion and piezotronics. *Nature*. 2014; 514: 470–477. DOI:10.1038/nature13792
- [44] Stuart MAC, et al., Emerging applications of stimuli-responsive polymer materials. *Nature Materials*. 2010; 9: 101–113. DOI: 10.1038/NMAT2614
- [45] Rogers GW, Liu JZ, Graphene actuators: quantum-mechanical and electrostatic double-layer effects. *Journal of the American Chemical Society*. 2011; 133: 10858–10863. DOI: 10.1021/ja201887r
- [46] Zhang LY, Zeng XW, Wang XQ, Programmable hydrogenation of graphene for novel nanocages. *Scientific Reports*. 2013; 3. DOI:10.1038/Srep03162

- [47] Ma XF, Zachariah MR, Zangmeister CD, Crumpled nanopaper from graphene oxide. *Nano Letters*. 2012; 12: 486–489. DOI: 10.1021/nl203964z
- [48] Ishihara S, et al., Hydrogen-bond-driven 'homogeneous intercalation' for rapid, reversible, and ultra-precise actuation of layered clay nanosheets. *Chemical Communications*. 2013; 49: 3631–3633. DOI:10.1039/c3cc40398j
- [49] Ogawa M, Ishii T, Miyamoto N, Kuroda K, Photocontrol of the basal spacing of azobenzene-magadiite intercalation compound. *Advanced Materials*. 2001; 13: 1107–1110. DOI:10.1002/1521-4095(200107)
- [50] Nabetani Y., et al., A photoactivated artificial muscle model unit: reversible, photoinduced sliding of nanosheets. *Journal of the American Chemical Society*. 2011; 133: 17130–17133. DOI: 10.1021/ja207278t
- [51] Mannsfeld SCB, et al., Highly sensitive flexible pressure sensors with microstructured rubber dielectric layers. *Nature Materials*. 2010; 9: 859–864. DOI: 10.1038/NMAT2834
- [52] Wang C, et al., User-interactive electronic skin for instantaneous pressure visualization. *Nature Materials*. 2013; 12: 899–904. DOI: 10.1038/NMAT3711
- [53] Someya T, Sekitani T, Kato Y, Kawaguchi H, Sakurai T, A large-area, flexible pressure sensor matrix with organic field-effect transistors for artificial skin applications. *Proceedings of the National Academy of Sciences of the United States of America*. 2004; 101: 9966–9970. DOI: 10.1073/pnas.0401918101
- [54] Liu X, Long YZ, Duan XF, Fan ZY, Large-scale integration of semiconductor nanowires for high-performance flexible electronics. *ACS Nano*. 2012; 6: 1888–1900. DOI: 10.1021/nn204848r
- [55] Takei K, et al., Nanowire active-matrix circuitry for low-voltage macroscale artificial skin. *Nature Materials*. 2010; 9: 821–826. DOI: 10.1038/NMAT2835
- [56] Maheshwari V, Saraf RF, Tactile devices to sense touch on a par with a human finger. *Angewandte Chemie-International Edition*. 2008; 47: 7808–7826. DOI:10.1002/anie.200703693
- [57] Maheshwari V, Saraf RF, High-resolution thin-film device to sense texture by touch. *Science*. 2006; 312: 1501–1504. DOI: 10.1126/science.1126216
- [58] Toohey KS, Sottos N, Lewis JA, Moorw JS, White SR, Self-healing materials with microvascular networks. *Nature Materials*. 2007; 6: 581–585. DOI:10.1038/nmat1934
- [59] Hou CY, Huang T, Wang HZ, Yu H, Zhang QH, Li YG, A strong and stretchable self-healing film with self-activated pressure sensitivity for potential artificial skin applications. *Scientific Reports*. 2013; 3. DOI:10.1038/Srep03138
- [60] Hou CY, Wang HZ, Zhang QH, Li YG, Zhu FM, Highly conductive, flexible, and compressible all-graphene passive electronic skin for sensing human touch. *Advanced Materials*. 2014; 26: 5018–5024. DOI: 10.1002/adma.201401367

- [61] Sun Q, Seung W, Kim BJ, Seo S, Kim SW, Cho JH, Active matrix electronic skin strain sensor based on piezopotential-powered graphene transistors. *Advanced Materials*. 2015; 27: 3411–3417. DOI: 10.1002/adma.201500582
- [62] Feng J, et al., Giant moisture responsiveness of VS₂ ultrathin nanosheets for novel touchless positioning interface. *Advanced Materials*. 2012; 24: 1969–1974. DOI: 10.1002/adma.201104681
- [63] Sidorenko A, Krupenkin T, Taylor A, Fratzl P, Aizenberg J, Reversible switching of hydrogel-actuated nanostructures into complex micropatterns. *Science*. 2007; 315: 487–490. DOI: 10.1126/science.1135516
- [64] Lu W, et al., Use of ionic liquids for pi-conjugated polymer electrochemical devices. *Science*. 2002; 297: 983–987. DOI:10.1126/science.1072651
- [65] Lendlein A, Kelch S, Shape-memory polymers. *Angewandte Chemie-International Edition*. 2002; 41: 2034–2057. Doi 10.1002/1521-3773(20020617)
- [66] Smela E, Conjugated polymer actuators for biomedical applications. *Advanced Materials*. 2003; 15: 481–494. DOI:10.1002/adma.200390113
- [67] Mu JK, et al., A multi-responsive water-driven actuator with instant and powerful performance for versatile applications. *Scientific Reports*. 2015; 5. DOI:10.1038/Srep09503
- [68] Balandin AA, Thermal properties of graphene and nanostructured carbon materials. *Nature Materials*. 2011; 10: 569–581. DOI: 10.1038/NMAT3064
- [69] Mu JK, Hou CY, Wang HZ, Li YG, Zhang QH, Zhu FM, Origami-inspired active graphene-based paper for programmable instant self-folding walking devices. *Science Advance*. 2016; 1: e1500533. DOI: 10.1126/sciadv.1500533
- [70] Cheng HH, et al., Graphene fibers with predetermined deformation as moisture-triggered actuators and robots. *Angewandte Chemie-International Edition*. 2013; 52: 10482–10486. DOI: 10.1002/anie.201304358
- [71] Lu LH, Liu JH, Hu Y, Chen W, Large volume variation of an anisotropic graphene nanosheet electrochemical–mechanical actuator under low voltage stimulation. *Chemical Communication*. 2012; 48: 3978–3980. DOI: 10.1039/C2CC18165G
- [72] Jang H, Park YJ, Chen X, Das T, Kim MS, Ahn Jh, Graphene-based flexible and stretchable electronics. *Advanced Materials*. 2016; 28: 4184–4202. DOI:10.1002/adma.201504245
- [73] Liang JJ, et al., Electromechanical actuators based on graphene and graphene/Fe₃O₄ hybrid paper. *Advanced Functional Materials*. 2011; 21: 3778–3784. DOI: 10.1002/anie.201304358

- [74] Lian YF, Liu YX, Jiang T, Shu J, Lian HQ, Cao MH, Enhanced electromechanical performance of graphite oxide-nafion nanocomposite actuator. *Journal of Physical Chemistry C*. 2010; 114(21): 9659–9663. DOI: 10.1021/jp101337h
- [75] Bakhtiarpour P, Parvizi A, Müller M, Shahinpoor M, Marti O, Amirkhani M, An external disturbance sensor for ionic polymer metal composite actuators. *Smart Materials and Structures*. 2016; 25. DOI:10.1088/0964-1726/25/1/015008
- [76] Yang S, Kang J, Yue Q, COey JMD, Jiang CB, Defect-modulated transistors and gas-enhanced photodetectors on ReS₂ Nanosheets. *Advanced Materials Interfaces*. 2016; 1500707. DOI: 10.1002/admi.201500707
- [77] Yang R, Islam A, Feng PXL, Electromechanical coupling and design considerations in single-layer MoS₂ suspended-channel transistors and resonators. *Nanoscale*. 2015; 7: 19921–19929. DOI:10.1039/c5nr06118k
- [78] Yuan HY, Nguyen M, Hammer T, Koster G, Rijnders Elshof JE, Synthesis of KCa₂Nb₃O₁₀ crystals with varying grain sizes and their nanosheet mono layer films as seed layers for piezoMEMS applications. *ACS Applied Materials & Interfaces*. 2015; 7: 27473–27478. DOI: 10.1021/acsami.5b09456
- [79] Ko HC, et al., A hemispherical electronic eye camera based on compressible silicon optoelectronics. *Nature*. 2008; 454: 748–753. DOI:10.1038/nature07113



Edited by Pramoda Kumar Nayak

There are only a few discoveries and new technologies in materials science that have the potential to dramatically alter and revolutionize our material world. Discovery of two-dimensional (2D) materials, the thinnest form of materials to ever occur in nature, is one of them. After isolation of graphene from graphite in 2004, a whole other class of atomically thin materials, dominated by surface effects and showing completely unexpected and extraordinary properties, has been created. This book provides a comprehensive view and state-of-the-art knowledge about 2D materials such as graphene, hexagonal boron nitride (*h*-BN), transition metal dichalcogenides (TMD) and so on. It consists of 11 chapters contributed by a team of experts in this exciting field and provides latest synthesis techniques of 2D materials, characterization and their potential applications in energy conservation, electronics, optoelectronics and biotechnology.

Photo by Rost9 / Can Stock

IntechOpen

